

# MISSISSIPPI ACADEMY OF SCIENCES



**Supplemental Issue  
31<sup>st</sup> Annual Southern Biomedical Engineering Conference  
Digest of Papers**

**April 30- May 2, 2015**

**Crowne Plaza New Orleans Airport,  
Kenner, LA**

**Majpr Sponsor  
Mississippi Academy of Science**

# Journal of the Mississippi Academy of Sciences

Volume 60

April 2015

Supplemental Issue 1



## Editor

Michelle Tucci  
University of Mississippi Medical Center

## Associate Editors

Hamed Benghzui  
University of Mississippi Medical Center

Kenneth Butler  
University of Mississippi Medical Center

## Editorial Board

Gregorio Begonia  
Jackson State University

Maria Begonia  
Jackson State University

Ibrahim O. Farah  
Jackson State University

Robin Rockhold  
University of Mississippi Medical Center

## Program Editors

Michelle Tucci  
University of Mississippi Medical Center

Kenneth Butler  
University of Mississippi Medical Center

The *Journal of the Mississippi Academy of Sciences* (ISSN 0076-9436) is published in January (annual meeting abstracts), April, July, and October, by the Mississippi Academy of Sciences. Members of the Academy receive the journal as part of their regular (nonstudent) membership. Inquiries regarding subscriptions, availability of back issues, and address changes should be addressed to The Mississippi Academy of Sciences, Post Office Box 55709, Jackson, MS 39296-5709, telephone 601-977-0627, or email [msacademyofscience@comcast.net](mailto:msacademyofscience@comcast.net).

## Contents

- 165 SOUTHERN BIOMEDICAL ENGINEERING CONFERENCE
- 168 OVERVIEW OF ANNUAL MEETING
- PAPAERS
- 179 ROBOTIZED METHOD FOR COMPARATIVE TESTING OF BACK SUPPORT DEVICE  
Denis DiAngelo and John Simmons,  
The University of Tennessee Health Science Center, Memphis, TN
- 187 SCOLIOSIS ANALOG MODEL FOR THE EVALUATION OF BRACING TECHNOLOGY  
Cloe Chung, and Denis DiAngelo,  
The University of Tennessee Health Science Center, Memphis, TN
- 193 TOWARDS THE DESIGN OF A DISTRACTIVE AND MOBILITY-ENABLING BACK SUPPORT DEVICE  
Denis DiAngelo and John Sims  
The University of Tennessee Health Science Center, Memphis, TN
- 201 ROLE OF PDE ISOFORMS IN REGULATING CAMP COMPARTMENTALIZATION AND PULMONARY MICROVASCULAR ENDOTHELIAL CELL (PMVEC) BARRIER PERMEABILITY  
Naga Srilakshmi Annamdevula, Andrea Britain, Thomas C. Rich, and Silas Leavesley  
University of South Alabama, Mobile, AL
- 207 DIFFERENTIAL DIAGNOSIS OF SLEEP DISORDERS BASED ON EEG ANALYSIS  
Sai Mohan Rudrashetty, Ashmit Pyakurel, Rui, Lui, Bharat R Karumuri, Ioannis Vlachos, and Leonidas Iaesmidis  
Louisiana Tech University, Rushton LA, and Louisiana State University Medical School, Shreveport, LA
- 211 SPATIO-TEMPORAL DYNAMICS OF EPILEPTIC SPIKES  
Balu Krishnan<sup>1</sup>, Ioannis Vlachos<sup>2</sup>, Aaron Faith<sup>4</sup>, Stephen Mullane<sup>5</sup>, Korwyn Williams<sup>3</sup>and Leonidas Iasemidis.  
<sup>1</sup>Cleveland Clinic Foundation, Cleveland, OH, <sup>2</sup>Louisiana Tech University, Rushton, LA, <sup>3</sup>Phoenix Children's Hospital, Phoenix, AZ, <sup>4</sup> Arizona State University, Tempe, AZ, and <sup>5</sup> Biotronik Lake Oswego, OR
- 217 IMPULSE OSCILLOMETRY REFERENCE VALUES IN ANGLO AND HISPANIC CHILDREN  
Roya Edalapour<sup>1</sup>, Homer Nazeran<sup>1</sup>, Carlos Rodrigues<sup>1</sup>, and Erika Meraz<sup>2</sup>  
<sup>1</sup>The University of Texas at El Paso and <sup>2</sup>Universidad Autonoma de Ciudad Juarez, Chihuahua, Mexiico
- 220 HOTSPOT ANALYSIS FOR EXAMINING THE ASSOCIATION BETWEEN SPATIAL AIR POLLUTANTS AND ASTHMA IN NEW YORK STATE, USA USING KERNEL DENSITY ESTIMATION (KDE)  
<sup>1</sup>Francis Tuluri and <sup>2</sup>A.K. Gorai  
<sup>1</sup>Department of Technology, Jackson State University, Jackson, MS and <sup>2</sup>Department of Mining Engineering, National Institute of Technology, Rourkela, Odisha, India

## **Contents Continued**

- 227 IMPACT OF COMMON ORGANICS ON CELLULAR GLYCOLYSIS AND THE DIFFERENTIAL SURVIVAL OF LUNG FIBROBLAST AND LUNG CARCINOMA CELL LINES  
Ibrahim Farah  
Jackson State University, Jackson, MS
- 236 A HYBRID SEQUENCE-SPECIFIC OLIGONUCLEOTIDE ELISA METHOD FOR RAPID DETECTION OF BACTEREMIA  
D. Olga McDaniel<sup>1</sup> Jason Guillot<sup>1</sup>, Larry McDaniel<sup>1</sup>, William Turner<sup>1,2</sup>, Ross Fremin<sup>1</sup>, Gita Subramony<sup>1</sup>, and Mark Williams<sup>1,3</sup>  
<sup>1</sup>University of Mississippi medical Center, Jackson, MS, <sup>2</sup> University of Texas Health Science Center, Dallas, TX, and <sup>3</sup>University of Colorado, Colorado Spring, CO
- 240 THE SYNERGISTIC EFFECT OF THYMOQUINONE AND EPIGALLOCATECHIN-3-GALLATE ON THE FUNCTIONAL CAPACITY OF CAOV-3 OVARIAN CANCER CELLS.  
Jennifer Harpole, Michelle Tucci, and Hamed Benghuzzi  
University of Mississippi Medical Center, Jackson, MS
- 244 FREQUENCY DEPENDENCE OF FOCUS LOCALIZATION FROM EEG BY DIRECTIONAL INFORMATION MEASURES  
Joshua Adkinson, Ioannis Vlachos, and Leonidas Iasemidis  
Louisiana Tech University, Rushton, LA
- 249 INFLAMMATORY MOLECULES RELEASED DURING ISCHEMIA/REPERFUSION IN A RAT MODEL OF CARDIAC LAD OCCLUSION  
D. Olga McDaniel<sup>1,2</sup>, Lance Majors<sup>1,2</sup>, Larry S. McDaniel<sup>2,3</sup>, Danielle A. Redd<sup>1,3</sup>, Taolin Fang<sup>1</sup>, Alan A. Simeone<sup>1,2</sup>  
<sup>1</sup>Department of Surgery, <sup>2</sup>School of Medicine, <sup>3</sup>Department of Microbiology  
University of Mississippi Medical Center, Jackson, Mississippi
- 254 OSTEOCHONDRAL XENOGRAFT DEVELOPMENT FOR ARTICULAR CARTILAGE REPAIR  
Andrew Garza and Steven Elder  
Mississippi State University, Starkville, MS
- 260 THE EFFECTS OF INSULIN AND EGCG ON PANC-1 CELL SURVIVAL  
Victoria Hodges, Michelle Tucci, and Hamed Benghuzzi  
University of Mississippi Medical Center, Jackson, MS
- 266 SODIUM INTAKE AND ARTERIAL PRESSURE IN NORMOTENSIVE AND DOCA-SALT HYPERTENSIVE RATS DURING CHRONIC MINOXIDIL TREATMENT  
Min Huang<sup>1</sup>, Hamed Benghuzzi<sup>2</sup>, Michelle Tucci<sup>3</sup>, and Robert L .Hester<sup>4</sup>,  
Departments of Physical Therapy<sup>1</sup>, Diagnostics and Clinical, Health Sciences<sup>2</sup>, Orthopedics<sup>3</sup>, and Physiology<sup>4</sup>  
University of Mississippi Medical Center, Jackson, MS
- 272 MORPHOLOGICAL ALTERATION OF THE LIVER AND ADRENAL BY STATIN RELEASED BY MEANS OF TRICALCIUM PHOSPHATE LYSINE DELIVERY SYSTEM IN A DEFECT AND SEGMENTAL FEMORAL INJURY IN AN ANIMAL MODEL  
Felix Adah<sup>1</sup>, Hamed Benghuzzi<sup>1</sup>, Michelle Tucci<sup>1</sup>, and Barry England<sup>2</sup>.  
1University of Mississippi Medical Center, Jackson, MS and 2University of Michigan Medical School, Ann Arbor, MI
- 279 D-GLUCOSE-INDUCED CYTOGENOTOXICITY AND APOPTOSIS OF HUMAN BREAST ADENOCARCINOMA (MCF-7) CELLS  
Clement G. Yedjou, Christine K. Tchounwou, Ibrahim Farah, and Paul B. Tchounwou  
Natural Chemotherapeutics Research Laboratory, NIH-Center for Environmental Health, College of Science, Engineering and Technology, Jackson State University, 1400 Lynch Street, Box 18540, Jackson, Mississippi

# **Program**

**31<sup>st</sup> ANNUAL SOUTHERN BIOMEDICAL ENGINEERING CONFERENCE**

**April 30- May 2, 2015**

.....  
**Program Co-Chairs**

Hamed A. Benghuzzi, Ph.D., FBSE, FAIMBE  
Department of Diagnostic and Clinical Health Sciences  
University of Mississippi Medical Center  
Jackson, MS 39216

Michelle A. Tucci, MS, Ph.D.  
University of Mississippi Medical Center  
Jackson, MS 39216

## **Program Committee**

Amol Janorkar, Ph.D.	Aaron Puckett, Ph.D.	LaShan Simpson, Ph.D.	Adel Mohamed, M.D
Ibrahim Farah, Ph.D.	Ken Butler, Ph.D.	Jafar Vossoughi, Ph.D.	Gerri Wilson, PhD,
Joseph A. Cameron, Ph.D.	Lynne Jones, Ph.D.	Elgenaid Hamadain, Ph.D.	Lisa McCammon
Zelma J. Cason, Ph.D.			

Subrata Saha, Ph.D. Founder and SBEC Steering Committee Chairman

## **SBEC HISTORY**

The Southern Biomedical Engineering Conference (SBEC) series was conceived by bioengineering professionals from academia and industry located primarily in the South of the United States in 1982. The first Southern Biomedical Engineering Conference was held at the LSU Medical Center, Shreveport, Louisiana, in 1982. Since then it has been held annually in different cities, mostly in the southern United States, and has grown to become a global event that regularly attracts attendees from all over the world. Submitted Papers are peer-reviewed, and those papers accepted for presentation and publication appear in the yearly issue of SBEC proceedings.

The SBEC serves a special purpose by emphasizing participation from young professionals and advanced students. Since established investigators present papers in the same sessions with the students, it encourages a high level of professionalism as a standard for young investigators and students. Submission of papers from individuals from around the world is encouraged. However, if their papers are accepted, an author or co-author must attend the conference to present their work and to interact with other attendees. In keeping with the emphasis on student participation, the SBEC presents best paper and presentation awards to undergraduate, graduate, and professional students.

### ***Conference Information***

The format of the conference is to have two concurrent sessions, with each presentation limited to 15 minutes (12-minute presentation and three minute discussions). Room assignments for each session is posted in the program contents,

The Conference will be held at the **Crowne Plaza New Orleans Airport, Kenner, LA**, which is located approximately 10 miles west of New Orleans, LA on interstate 10, and 1.5 miles from New Orleans International Airport.

## Airport

### **Louis Armstrong New Orleans International Airport (MSY)**

- Distance from hotel: 1.5 MI/ 2.41 KM North East 1
- Complimentary hotel shuttle available
- Driving directions: Take Airport Service Road going northeast to Veterans Blvd. Turn right; the hotel is on the left.

## Train

### **AMTRAK**

- Distance from hotel: ~15 MI/ 24.14 KM East
- Head on Williams Blvd toward Veterans Blvd. Make a U-turn at Veterans Blvd 0.1 mi. Merge onto I-10 E via the ramp to New Orleans Take the exit toward Superdome. Turn right at Girod St/W Stadium Dr Continue to follow Girod St. Turn right at Loyola Ave.

## **Registration and Fees**

Initial on-site registration will be held from 4:00–8:00 p.m., Thursday, April 30, 2015. Participants are encouraged to preregister by April 4, 2015 to take advantage of the reduced registration rates.

### **Fees before April 4, 2015**

Students:	\$190
Faculty/Staff:	\$280

### **Fees after April 4, 2015**

Students:	\$225
Faculty/Staff:	\$375

**Student Awards:** There will be 8 students' awards given as follows: 1. First Place Outstanding Student Presentation; 2. Second Place Outstanding Student Presentation; 3. Third Place Outstanding Student Presentation; 4. First Place Outstanding Student Poster Presentation; 5. Second Place Outstanding Student Poster Presentation; 6. Third Place Outstanding Student Poster Presentation; 7. Outstanding Student Manuscript Award, Subrata Saha Outstanding Student Award.

## **Session Chairs**

### **Session I: Animal Models**

Session Chair: Dr. Lynne Jones

### **Session II: Tissue Engineering**

Session Chair: Dr. LaShan Simpson      Co-Chair: Dr. Amol Janorkar

### **Session III: Imaging I & Bioinstrumentation**

Session Co-Chair: Dr. Thomas Rich Co-Chair: Dr. Hongtao Yu

### **Session IV: Drug Delivery Systems**

Session Co-Chair: Dr. Joseph A. Cameron      Co-Chair: Dr. Kenneth Butler

### **Session V: Respiratory/Imaging II**

Session Co-Chair: Dr. Ramesh Patel      Co-Chair: Dr. Samarendra K Mohanty

### **Poster Session**

Session Co-Chairs: Drs. Zelma Cason, Aaron Puckett, Ken Heard, Min Huang, Hamed Benghuzzi, Felix Adah

### **Session VI: Inflammation/Injury/Health Care**

Session Chair: Dr. Olga McDaniel Co-Chair: Dr. Larry McDaniel

### **Session VII: Tissue Engineering/ Scaffolds/Bone**

Session Co-Chair: Dr. Subrata Saha Co-Chair: Dr. Jafar Vossoughi

### **Session VIII: Modeling**

Session Co-Chair: Dr. Elgenaid Hamadain Co-Chair: Dr. Jens Rosenberg

### **Session IX: Cancer Research**

Session Co-Chair: Dr. Pradip Biswas Co-Chair: Dr. Ibrahim Farah

# **31<sup>st</sup> Annual Meeting**

*Program*

**Major Sponsor of 31<sup>st</sup> SBEC**



**Mississippi Academy of Sciences**



**Thursday**  
**April 30, 2015**

**4:00 PM-8:00 PM    Registration and Reception**  
**Hotel Lobby**

**Friday**  
**May 1, 2015**

**8:00 AM-4:00 PM:    Registration (Hotel Lobby)**

**8:45-8:55 AM:**              **Opening of the Meeting**  
**Dr. Ham Benguzzi, Program Chair**

**May 1, 2015**

*Scientific Sessions*

<b>Friday Morning</b>	<b>Talk #</b>	<b>Conference Room: Salon 3</b>
<b>Time</b>		<b>Session I: Animal Models</b> <b>Session Chair: Dr. Lynne Jones</b>
9:00-9:05	1	Opening Remarks Dr. Lynne Jones
9:05-9:25	2	Hip Dogs: A Canine Model for Coxofemoral Joint Pathogenesis and Therapy <b>Mandi J. Lopez, DVM, MS, PhD</b> <i>Diplomat, American College of Veterinary Surgeons</i> <i>Professor &amp; Director</i> <i>Laboratory for Equine &amp; Comparative Orthopedic Research</i>  <i>Department of Veterinary Clinical Sciences</i>
9:25-9:40	3	Animal Models of Osteopenia and Osteoporosis <b>Michelle Tucci, PhD</b> <b>University of Mississippi Medical Center</b> <b>Jackson, MS,</b>
9:40-10:00	4	Biotechnology and Orthopaedic Research: Selecting the Most Appropriate Animal Model Lynne C. Jones, Ph.D. Associate Professor, Orthopaedic Surgery Director of Resident Research Johns Hopkins University School of Medicine Baltimore, MD
10:00		<b>BREAK</b>

<b>Friday Morning</b>	<b>Talk #</b>	<b>Conference Room: Salon 3</b>
<b>Time</b>	<b>5</b>	<b>Session II: Tissue Engineering:</b> <b>Session Chair: Dr. LaShan Simpson Co-Chair: Dr. Amol Janorkar</b>
10:15	6	Genetic Switching of Vascular Smooth Muscle Cells  <b>Amber Kay, Joshua Grant, C. LaShan Simpson</b> Department of Agricultural and Biological Engineering, Mississippi State University, Mississippi State, MS
10:30	7	<b>3D Diabetic Matrix Mediates Fibroblast Phenotypic and Functional Differentiation Through AGE/RAGE and PKC-Zeta Signaling</b> CM Cerovsky, ZN Syed, S Kundu, JA Stewart, Jr Department of Biological Sciences, and Bagley School of Engineering, Mississippi State University, Starkville, MS
10:45	8	<b>Isolation and Analysis of Exosomes from Conditioned Media of Suprachiasmatic Nuclei Cells</b> Dan Zhao <sup>1</sup> , Jiaxu Li <sup>1</sup> , David Earnest <sup>2</sup> , Morgan Farnell <sup>3</sup> , and Yuhua Farnell <sup>1</sup> <sup>1</sup> Department of Biochemistry, Molecular Biology, Entomology, and Plant Pathology, Mississippi State University, Starkville, MS, <sup>2</sup> Department of Neuroscience and Experimental Therapeutics, Texas A&M Health Science Center, Bryan, TX, and Department of Poultry Science, Mississippi State University Extension Service, Mississippi State, MS
11:00	9	<b>Functionalized Polylactide Scaffolds for Bone Tissue Engineering Application</b> Cheryl Gomillion <sup>1,4</sup> , Rubinder Lakhman <sup>2</sup> , Rajeswari Kasi <sup>2</sup> , RA Weiss <sup>3</sup> , Liisa Kuhn <sup>1</sup> , and A. Jon Goldberg <sup>1</sup> <sup>1</sup> Department of Reconstructive Sciences, University of Connecticut Health Center, Farmington, CT, <sup>2</sup> Institute of Material Sciences, University of Connecticut, Storrs, CT, <sup>3</sup> Department of Polymer Engineering, University of Georgia, Athens, GA
11:15	10	<b>Engineered Cartilage on Chitosan Phosphate Scaffolds for Osteochondral Defects</b> Anuhyaa Gottipati and Steven Elder Department of Agricultural and Biological Engineering, Mississippi State University, Mississippi State, MS
11:30	11	<b>Anisotropic Compressive Properties of Porcine Muscle Tissue</b> Renee Pielich, Benjamin Wheatley, Tammy Haut-Donahue, Ryan Gilbrech, Raj Prabu, Jun Liao, and Lakiesha Williams Department of Agricultural and Biological Engineering, Mississippi State University, Mississippi State, MS
		<b>BREAK</b>

<b>Friday Morning</b>	<b>Talk #</b>	<b>Conference Room: Salon 5-6</b>
<b>Time</b>	<b>12</b>	<b>Session III: Imaging I and Bioinstrumentations</b> <b>Session Co-Chair: Dr. Thomas Rich Co-Chair: Dr. Jens Rosenberg</b>
10:15	13	<b>Efficacy of Real-Time Optical Measurement System</b> Nicholas Carroll, Emily Gould, Sung Kim, Jon Morrison University of South Alabama, Mobile, AL
10:30	14	<b>Hyperspectral Illumination Device for Microscopic and Endoscopic Applications</b>  <b>Sam Mayes<sup>1</sup>, Silas Levesley<sup>1,2</sup>, Thomas Rich<sup>2,3</sup></b> <sup>1</sup> University of South Alabama Department of Chemical and Biomolecular Engineering, Mobile AL, University of South Alabama Department of Pharmacology, Mobile, AL, and University of South Alabama Center for Lung Biology, Mobile, AL
10:45	15	<b>Single and Multiple CoAxial Inputs to Excite a Cylindrical Waveguide for Traveling Wave MRI at 21.1 T</b>

		Samuel Grant <sup>1,2</sup> , Smiriti Sagaran <sup>2,3</sup> , Jose Muniz <sup>1,2</sup> , and Jens Rosenberg <sup>1</sup> <sup>1</sup> Chemical and Biomedical Engineering, Florida State University, Tallahassee, FL, National High Magnetic Field Laboratory, Florida State University, Tallahassee, FL, and Electrical and Computer Engineering, Florida State University, Tallahassee, FL
11:00	16	<b>Metabolic Confinements in Normal and Stroked CNS in vivo Revealed by Localized Double Pulse-Field Gradient MRS at 21.1 T</b> Jens Rosenberg <sup>1</sup> , Noam Shemesh <sup>3</sup> , Jean Nicolas Dumez <sup>2</sup> , Lucio Frydman <sup>1,2</sup> and Samuel Grant <sup>1</sup> <sup>1</sup> Florida State University, <sup>2</sup> Weizmann Institute of Science, Rehovot Israel, and <sup>3</sup> Champalimaud neuroscience programme, Lisbon Portugal
11:15	17	<b>Spatio-Temporal Dynamics of Epileptic Spikes</b> Balu Krishnan <sup>1</sup> , Ioannis Vlachos <sup>2</sup> , Aaron Faith <sup>4</sup> , Stephen Mullane <sup>5</sup> , Korwyn Williams <sup>3</sup> and Leonidas Iasemidis. <sup>1</sup> Cleveland Clinic Foundation, Cleveland, OH, <sup>2</sup> Louisiana Tech University, Rushton, LA, <sup>3</sup> Phoenix Children's Hospital, Phoenix, AZ, <sup>4</sup> Arizona State University, Tempe, AZ, and <sup>5</sup> Biotronik Lake Oswego, OR
11:30	18	<b>Differential Diagnosis of Sleep Disorders Based on EEG Analysis</b> Sai Mohan Rudrashtety, Ashmit Pyakurel, Rui, Lui, Bharat R Karumuri, Ioannis Vlachos, and Leonidas Iasemidis Louisiana Tech University, Rushton LA, and Louisiana State University Medical School, Shreveport, LA
		<b>BREAK</b>

## 12:00 -1:00 PM: Lunch & Keynote Speaker

**Keynote Speaker: Dr. Rodney Baker**

**Title: Contribution of Phosphatidic Acid to Intracellular Signaling**

Friday Afternoon	Talk #	Conference Room: Salon 3
Time		<b>Session IV: Drug Delivery Systems</b> <b>Session Co-Chair: Dr. Joseph A. Cameron Co-Chair: Dr. Kenneth Butler</b>
1:00	19	<b>Ex vivo System for Pharmacokinetic Analysis of Catheter-Based, Vascular Drug Delivery</b> Emily Turner, Marzieh Atigh, Saami Yazdani University of South Alabama, Mobile, AL
1:15	20	<b>Development of Environmentally Responsive Micro and Nanosystems for Targeted Drug Delivery Applications</b> Nehal Patel, Luke Villermi, Neesha Sirivardane, Cam Tran, Abitha Hemibuck and Caldorera-Moore Louisiana Tech University, Rushton, LA
1:30	21	<b>Site Specific Delivery of Antibiotics During Experimental Otitis Media</b> Larry McDaniel Department of Microbiology, University of Mississippi Medical Center, Jackson, MS
1:45	22	<b>Effect of Chain Length, Number of Chains and Charge on the In vitro Cytotoxicity of Surface Coating Agents Used on Nanoparticles</b> Ying Zhang, Salma Begum, Makiesha James, and Hongtao Yu, Department of Chemistry and Biochemistry, Jackson, State University, Jackson, MS
2:00	23	<b>The Synergistic Effect of Thymoquinone and Epigallocatechin-3-Gallate on the Functional Capacity of CaOV-3 Ovarian Cancer Cells.</b> Jennifer Harpole, Michelle Tucci, and Hamed Benghuzzi University of Mississippi Medical Center, Jackson, MS
2:15	24	<b>D-Glucose-Induced Cytogenotoxicity and Apoptosis of Human Breast Adenocarcinoma (MCF-7) Cells</b>

		Clement G. Yedjou, Christine K. Tchounwou, Ibrahim Farah, and Paul B. Tchounwou  Natural Chemotherapeutics Research Laboratory, NIH-Center for Environmental Health, College of Science, Engineering and Technology, Jackson State University, 1400 Lynch Street, Box 18540, Jackson, Mississippi
		BREAK

<b>Friday Afternoon</b>	<b>Talk #</b>	<b>Conference Room: Salon 5-6</b>
<b>Time</b>		<b>Session V: Respiratory/Imaging II</b> <b>Session Co-Chair: Dr. Rameesh Patel    Co-Chair: Dr. Samarendra K. Mohanty</b>
1:00	26	<b>Role of PDE Isoforms in Regulating cAMP Compartmentalization and Pulmonary Microvascular Endothelial Cell (PMVEC) Barrier Permeability</b>  Naga Srilakshmi Annamdevula, Andrea Britain, Thomas C. Rich, and Silas Leavesley University of South Alabama, Mobile, AL
1:15	27	<b>Excitation Scanning Hyperspectral Imaging of Autofluorescence in Decellularized Rat Lungs</b> Peter Favreau <sup>1</sup> , Lauren Cichon <sup>1</sup> , Diego F. Alvarez <sup>2</sup> , Thomas C. Rich <sup>1</sup> , and Silas J Leavesley <sup>1</sup> <sup>1</sup> University of South Alabama, Mobile, AL and <sup>2</sup> Center for Lung Biology, Mobile, AL
1:30	28	Skin Blood Flow Measurement Using Millimeter Wave Energy: Modeling and in vitro Experiments Erin Lowery, Todd Hamlin, Silas Leavesly, and David Nelson University of South Alabama, Mobile, AL
1:45	29	<b>Impulse Oscillometry Reference Values in Anglo and Hispanic Children</b> Roya Edalapour <sup>1</sup> , Homer Nazeran <sup>1</sup> , Carlos Rodrigues <sup>1</sup> , and Erika Meraz <sup>2</sup> <sup>1</sup> The University of Texas at El Paso and <sup>2</sup> Universidad Autonoma de Ciudad Juarez, Chihuahua, Mexico
2:00	30	<b>Hotspot Analysis for Examining the Association Between Spatial Air Pollutants and Asthma in New York State, USA Using Kernel Density Estimation (KDE)</b> <sup>1</sup> Francis Tuluri and <sup>2</sup> A.K. Gorai <sup>1</sup> Department of Technology, Jackson State University, Jackson, MS and <sup>2</sup> Department of Mining Engineering, National Institute of Technology, Rourkela, Odisha, India
2:15	31	<b>Optical Sensing Of Citrate By A Macrocycle-Based Synthetic Receptor In Water</b> Md. Alamgir Hossain* <sup>1</sup> , Md Mhabubur Rhaman, <sup>1</sup> Azmain Alamgir, <sup>1</sup> Chinyere D. Jones, <sup>1</sup> and Douglas R. Powell <sup>2</sup>  Department of Chemistry and Biochemistry, Jackson State University, Jackson, MS <sup>2</sup> University of Oklahoma, Norman, OK
		BREAK

## 2:30-5:00 PM: Poster Session (Student Posters Judging)

*Scientific Sessions-Poster Session will be held in Salon 4*

<b>Session Co-Chairs: Zelma Cason, Aaron Puckett, Felix Adah, Min Huang, and Hamed Benguzzzi</b>	<b>P#</b>
<b>Sodium Intake And Arterial Pressure In Normotensive And Doca-Salt Hypertensive Rats During Chronic Minoxidil Treatment</b> Min Huang <sup>1</sup> , Hamed Benguzzzi <sup>2</sup> , Michelle Tucci <sup>3</sup> , and Robert L .Hester <sup>4</sup> , Departments of Physical Therapy <sup>1</sup> , Diagnostics and Clinical, Health Sciences <sup>2</sup> , Orthopedics <sup>3</sup> , and Physiology <sup>4</sup> University of Mississippi Medical Center, Jackson, MS	P1

<b>Tumor Necrosis Alpha Temporally Regulates micro-RNA-181a and its Target in A549 Cells</b> Maricica Pacurari Department of Biology, Jackson State University, Jackson, MS	P2
<b>Manipulation of the Macrophage Response Using Amino Acid Coated UHMW-PE Implanted Subcutaneously</b> Kenneth R. Butler, Jr., PhD, Hamed Benghuzzi, PhD, Michelle Tucci, PhD, Aaron Puckett, PhD University of Mississippi Medical Center, Jackson, MS	P3
<b>Impact of Some Common Organics on Cellular Glycolysis and the Differential Survival of Lung Fibroblast and Lung Carcinoma Cell Lines</b> Ibrahim Farah Jackson State University, Jackson, MS	P4
<b>Examining the Structural Integrity of Human Gingival Fibroblasts after Exposure to Dental Adhesives Combined with Nifedipine or Cortisol in an Infectious Environment</b> Angelia Garner, Hamed Benghuzzi <sup>1</sup> , and Michelle Tucci <sup>2</sup> <sup>1</sup> School of Health Related Professions and <sup>2</sup> Department of Orthopedic Surgery University of Mississippi Medical Center, Jackson, MS 39216	P5
<b>Modified PEGDF and PEDGI Polymers for Non-Viral Gene Delivery in HEK 293 Cells</b> Anh. Le, Xizi Dai, and Yen-Chih Huang Florida International University, Miami, FL	P6
<b>Paper-based 3D Cell Culture Devices for Rapid, Antibiotic Assays</b> Alexander. Williams, Chenzhong Li and Mehenur Sarwar Florida International University, Miami, FL	P7
<b>Intervention to Reduce <i>Pseudomonas aeruginosa</i> Related Infections in Neonatal Intensive Care Unit</b> Elham Ghonim and Hamed Benghuzzi University of Mississippi Medical Center, Jackson, MS 39216	P8
<b>GFP Transfected Autologous Schwann Cells Are Rejected After Transplantation In The Spinal Cord Injury in a Minipig Model</b> AJ Santamaría <sup>1</sup> , J.T. Rosenberg <sup>2</sup> , FC Benavides <sup>1</sup> , Y Nunez <sup>1</sup> , AE Brooks <sup>1</sup> , JP Solano <sup>1</sup> , JD Guest <sup>1</sup> , SC Grant <sup>1</sup> <sup>1</sup> University of Miami, Miami, FL and <sup>2</sup> Florida State University, Tallahassee, FL	P9
<b>Restoration Of Spermatogenesis In Testosterone Acetate Induced Azoospermic Rats</b> Ham Benghuzzi* and Michelle Tucci Department of Diagnostic and Clinical Health Sciences and Department of Orthopaedic Surgery and Rehabilitation , University of Mississippi Medical Center, Jackson, MS	P10
<b>Frequency Dependence of Focus Localization from EEG by Directional Information Measures</b> Joshua Adkinson, Ioannis Vlachos, and Leonidas Iasemidis Louisiana Tech university, Rushton, LA	P11
<b>Demonstration of the Safety of the Neonatal Airflow Perturbation Device</b> Jafar Vossoughi <sup>1,2</sup> , Arthur Johnson <sup>2</sup> , Khushbu Shukla <sup>3</sup> , Alyse Laliberte <sup>3</sup> , Martin Keszler <sup>3</sup> <sup>1</sup> ESRA (Vvossoughi@verizon.net), <sup>2</sup> Bioengineering Department, Maryland, and <sup>3</sup> Women and Infant Hospital of Rhode Island RI	P12
<b>Noninvasive Evaluation of Neonatal Respiratory Resistance</b> Jafar Vossoughi <sup>1,2</sup> , Arthur Johnson <sup>2</sup> , Khushbu Shukla <sup>3</sup> , Alyse Laliberte <sup>3</sup> , Martin Keszler <sup>3</sup> <sup>1</sup> ESRA (Vvossoughi@verizon.net), <sup>2</sup> Bioengineering Department, Maryland, and <sup>3</sup> Women and Infant Hospital of Rhode Island, RI	P13
<b>The Effect Of Neuropeptide Y On The Female Rat Reproductive Tract</b> Zelma Cason, Hamed Benghuzzi, and Michelle Tucci University of Mississippi Medical Center, Jackson, MS 39216	P14
<b>Arsenic-Induced Changes In Human-Induced Pluripotent Stem Cells (IPSC)</b> BE Graham and K Ndebele Laboratory of Cancer Immunology, Target Identification and Validation, Department of Biology, Center of Environmental Health, RCMI Center of Environmental Health, Department of Biology (BEG, KN.), Jackson State University, Jackson, MS	P15
<b>Phthalate (DEHP) Modulates Cell Invasion, Migration, and Anchorage Independent Growth Through Targeting s100P in Glioblastoma Cells</b> Jennifer Sims, Barbara Graham, Paul Tchounwou and Kenneth Ndebele Laboratory of Cancer Immunology Target Identification and Validation, College of Science and Engineering and Technology, Jackson State University, Jackson, MS	P16
<b>Towards the Design of a Distractive and Mobility-Enabling Back Support Device</b> Denis DiAngelo and John Sims The University of Tennessee Health Science Center, Memphis, TN	P17
<b>Treatment Depth Effects Of The Zavation Lumbar Bone Growth Stimulator</b> Gerri A. Wilson, Jonathan M. Mitchell, Michelle A. Tucci, and Hamed A. Benghuzzi, University of Mississippi Medical Center, Jackson, MS	P18
<b>Antinociceptive Efficacy Of Chronic Fluoxetine Treatment</b>	P19

Gerri A. Wilson, Jonathan M. Mitchell, J. Scott. Bittle, Yatrik J. Patel, Jennifer E. Naylor, Kevin B. Freeman, Michelle A. Tucci, and Hamed A. Benguzzi, University of Mississippi Medical Center, Jackson, MS	
<b>Evidence of Structural Alteration of Caov-3 Ovarian Like Cell Line Upon the Exposure to Potential Herbal Antioxidants</b> Jennifer Harpole, Hamed Benguzzi <sup>1</sup> , and Michelle Tucci <sup>2</sup> <sup>1</sup> School of Health Related Professions and <sup>2</sup> Department of Orthopedic Surgery University of Mississippi Medical Center, Jackson, MS	P20
<b>AGES AND AGING: ELIMINATING RAGE EXTENDS LIFESPAN</b> Carter G Holland, Jack Sudduth, Paul Hogue, Donna Gordon, and James Stewart Mississippi State University, Starkville, MS USA	P21
<b>Proliferation, Cell Viability, Toxicity, And Protein Expression Analysis Of MCF7 Breast Ductal Epithelial Adenocarcinoma Cells Cultured With <i>Pseudognaphalium Obtusifolium</i> Dichloromethane-Derived Extract Indicates A Possible Anti-Carcinogenic Treatment Alternative</b> Mary McDonnell Mississippi College, Clinton, MS	P22
<b>The Effects Of Insulin And EGCG on Panc-1 Cell Survival</b> Victoria Hodges, Michelle Tucci, and Hamed Benguzzi University of Mississippi Medical Center, Jackson, MS	P23
<b>Structure Elucidation of G-Quadruplex within the Mid-Region of the kRAS Promoter and Identification of Stabilizing Small Molecules as Promising Transcriptional Silencers</b> Rhianna Morgan <sup>1</sup> Khondaker Miraz Rahman <sup>2</sup> ,and Tracy Brooks <sup>1</sup> University of Mississippi, University, MS and <sup>2</sup> Institute of Pharmaceutical Sciences, King's College London, England	P24
<b>PROLIFERATION OF ENDOGENOUS T-REG CELLS IMPORVES THE PATHO-PHYSIOLOGY ASSOCIATED WITH PLACENTAL ISCHEMIA OF PREGNANCY</b> Tarek Ibrahim, Lukasz Przybyl, Ashlyn Harmon, Lorena Amaral, Denise Cornelius, Janae Moseley, Jessica Faulkner, Babbette LaMarca, and Ralf Dechend University of Mississippi Medical Center, Jackson,MS	P25
<b>Verruca Localization Predominately In Black Tattoo Ink</b> Kristen Ramey, Robert Brodell, And Jamil Ibrahim University of Mississippi Medical Center Jackson, MS	P26

## 5:00-7:30 PM: Banquet Event/Salon 3

**Saturday**

**May 2, 2015**

Scientific Sessions

Saturday Morning	Talk #	Conference Room: Salon 3
Time		<b>Session VI (Inflammation/Injury/Health-Care)</b> Session Chair: Dr. Olga McDaniel      Co-Chair: Dr. Larry McDaniel
8:30	32	<b>Tracking Stem Cells in Irradiated Traumatic Brain Injury Models using <sup>1</sup>H MRI at 11.75 T</b> Nastaren Abad <sup>1</sup> , Abdol Aziz Ould Ismail <sup>2</sup> , Ali Darkazalli <sup>3,4</sup> , Cathy Levenson <sup>3</sup> , and Samuel Grant <sup>1</sup> <sup>1</sup> Chemical and Biomedical Engineering, Florida State University, Tallahassee, FL, <sup>2</sup> National High Magnetic Field Laboratory, Florida State University, Tallahassee, FL, <sup>3</sup> Neuroscience Program, Florida State University, Tallahassee, FL, and <sup>4</sup> Biomedical Sciences, Florida State University, Tallahassee, FL
8:45	33	<b>Discovering Unknown Genes</b> Michael Robinson, Florida International University, Miami, FL
9:00	34	<b>A Hybrid Sequence-Specific Oligonucleotide ELISA Method for Rapid Detection of Bacteremia</b> D. Olga McDaniel <sup>1</sup> Jason Guillot <sup>1</sup> , Larry McDaniel <sup>1</sup> , William Turner <sup>1,2</sup> , Ross Fremin <sup>1</sup> , Gita Subramony <sup>1</sup> , and Mark Williams <sup>1,3</sup> <sup>1</sup> University of Mississippi medical Center, Jackson, MS, <sup>2</sup> University of Texas Health Science Center, Dallas, TX, and <sup>3</sup> University of Colorado, Colorado Spring, CO
9:15	35	<b>Morphological Alteration of the Liver and Adrenal by Statin Released by Means of</b>

		<b>Tricalcium Phosphate Lysine Delivery System in a Defect and Segmental Femoral Injury in an Animal Model</b> Felix Adah <sup>1</sup> , Hamed Benguzzi <sup>1</sup> , Michelle Tucci <sup>1</sup> , and Barry England <sup>2</sup> . <sup>1</sup> University of Mississippi Medical Center, Jackson, MS and <sup>2</sup> University of Michigan Medical School, Ann Arbor, MI
9:30	36	<b>Inflammatory Molecules Released During Ischemia/Reperfusion in a Rat Model of Cardiac LAD Occlusion</b> Danielle Redd <sup>1</sup> , Larry McDaniel <sup>2</sup> , Lance Majors <sup>2</sup> , Alan Simeone <sup>2</sup> , and D. Olga McDaniel <sup>2</sup> <sup>1</sup> Tougaloo College, Jackson, MS and <sup>2</sup> University of Mississippi Medical Center, Jackson, MS
9:45	37	<b>Morphometric Evaluation Of The Tissue Implant Response Surrounding Subcutaneous TCP, HA, And ALCAP Bioceramic Implants</b> Kenneth R. Butler, Jr., PhD, Hamed Benguzzi, PhD, Michelle Tucci, PhD, Aaron Puckett, PhD University of Mississippi Medical Center, Jackson, MS
10:00	38	<b><math>\beta</math>-Estradiol Induces Cytotoxic Effects To Human T-Lymphoma (Jurkat) Cells Through Oxidative Stress</b> Clement Yedjou, Joseph Cameron, Ariane T. Mbemi, and Paul Tchounwou Natural Chemotherapeutics Research Laboratory, NIH-Center for Environmental Health, College of Science, Engineering and Technology, Jackson State University, 1400 Lynch Street, P.O. Box 18540, Jackson, Mississippi
10:15	39	<b>Toxicity of Gold Nanoparticles and Gold Ions to Bacteria</b> Thabitha Shareena Dasari, Neil Hammond, and Hongtao Yu Department of Chemistry and Biochemistry, Jackson State University, Jackson
		<b>BREAK</b>

<b>Saturday Morning</b>	<b>Talk #</b>	<b>Conference Room: Salon 5-6</b>
<b>Time</b>		<b>Session VII: Tissue Engineering/ Scaffolds/Bone</b> <b>Session Co- Chair: Dr. Subrata Saha Co-Chair: Dr. Jafar Vossoughi</b>
8:30	40	<b>Comparing Scaffold Formulation for Three Dimensional Bone Tissue Engineering</b> Patrick Bierdeman, Bhuvaneswari Gurumurthy, Amol Janorkar University of Mississippi Medical Center, Jackson, MS
8:45	41	<b>Regional Variations on Microstructure and Biomechanical Properties of the human Vertebral Endplate and Trabecular Bone</b> Fred Xavier, Rozen Wynter, Martin Pendola, Gavriel Feuer, Westley Hayes, Subrata Saha Department of Orthopaedic Surgery and Rehabilitation Medicine SUNY Downstate Medical Center, Brooklyn NY
9:00	42	<b>A Three Dimensional Tissue Engineering Approach to Generate Functional Cardiac Muscle from Mouse Embryonic Stem cells in vitro</b> Sasmith Rath, Florida International University, Miami, FL
9:15	43	<b>Hubigel Enriched Fibro-porous Scaffolds for Tissue Engineering</b> Vinoy Thomas <sup>1</sup> , Harsh Patel <sup>1</sup> , Steven Pogwizd <sup>1</sup> , Raj Singh <sup>2</sup> , Yogesh Vohras <sup>1</sup> <sup>1</sup> University of Alabama at Birmingham, Birmingham, AL and <sup>2</sup> Vivo Bioscience Inc, Birmingham, AL
9:30	44	<b>Role of Physical Cues in Axonal Guidance</b> Samarendra K. Mohanty Biophysics and Physiology Group, Department of Physics, The University of Texas at Arlington, Arlington, TX

9:45	45	Material and Mechanical Properties of Osteophytes and Non-Osteophytic Cortical Bone: A Preliminary Study Fred Xavier, Rozen Wynter, Martin Pendola, Gavriel Feuer, Westley Hayes, Subrata Saha Department of Orthopaedic Surgery and Rehabilitation Medicine SUNY Downstate Medical Center, Brooklyn, NY
10:00	46	<b>Osteochondral Xenograft Development for Articular Cartilage Repair</b> Andrew Garza and Steven Elder Mississippi State University, Starkville, MS
10:15	47	<b>Robotized Method for Comparative Testing of Back Support Device</b> Denis DiAngelo and John Simmons, The University of Tennessee Health Science Center, Memphis, TN
10:30-11:00		<b>BREAK</b>

<i>Saturday Morning</i>	Talk #	<b>Conference Room: Salon 3</b>
<b>Time</b>		<b>Session VIII: Modeling</b> <b>Session Co-Chair: Dr. Elgenaid Hamadain Co-Chair: Dr. Hongtao Yu</b>
11:00	48	<b>MREPT at 21.1 T</b> Ghoncheh Amouzandeh <sup>1,2</sup> , Jens Rosenberg <sup>2,3</sup> , and Samuel Grant <sup>2</sup> <sup>1</sup> Physics, Florida State University, Tallahassee, FL , <sup>2</sup> National High Magnetic Field Laboratory, Florida State University, Tallahassee, FL, and <sup>3</sup> Chemical and Biomedical Engineering, Florida State University, Tallahassee, FL
11:15	49	<b>Ultrafast in vivo Diffusion Imaging of Stroke at 21.1 by Spatiotemporal Encoding</b> Jens Rosenberg <sup>1</sup> Avigdor Leftin <sup>2</sup> , Eddy Salomon <sup>2</sup> , <sup>3</sup> Fabian Calixto Bejarano <sup>1</sup> , Lucio Frydman <sup>1</sup> , and Samuel Grant <sup>1</sup> <sup>1</sup> Florida State University, Tallahassee, FL, <sup>2</sup> Weizmann Institute of Science, Rovot Israel
11:30	50	<b>Scoliosis Analog Model for the Evaluation of Bracing Technology</b> Cloe Chung, and Denis DiAngelo, The University of Tennessee Health Science Center, Memphis, TN
11:45	51	<b>Multiple Path Particle Dosimetry Simulation of Respiratory Deposition of Nanoaerosol in the Mouse Lung</b> Mohammed Ali <sup>1</sup> , Bradford Gutting <sup>2</sup> , Victor Morozov <sup>3</sup> , and Monique van Hoek <sup>4</sup> , <sup>1</sup> Dept of Industrial Systems and Technology, Jackson State university, Jackson, MS, Naval Surface Warfare Center, Dahlgren VA, <sup>3</sup> Institute of Theoretical and Experimental Biophysics of the Russian Academy of Sciences, Pushchino, Moscow, <sup>4</sup> George Mason University, Manassas, VA
12:00	52	<b>Choice Of Statistical Techniques: Parametric Versus Non Parametric Methods</b> Elgenaid Hamadain, University of Mississippi Medical Center

<i>Saturday Morning</i>	Talk #	<b>Conference Room: Salon 5-6</b>
<b>Time</b>		<b>Session IX (Cancer)</b> <b>Session Chair: Dr. Pradip Biswas Co-Chair: Dr. Ibrahim Farah</b>
11:00	53	<b>Dietary Stilbenes and Epigenetic Regulation for Prostate Cancer Chemoprevention and Treatment</b> Levenson AS <sup>1,2*</sup> , Swati Dhar <sup>1</sup> , Avinash Kumar <sup>1</sup> , Agnes M. Rimando <sup>3</sup> , Janice M. Lage <sup>2</sup> , Jack R. Lewin <sup>2</sup> and Xu Zhang <sup>4</sup> <sup>1</sup> Cancer Institute and <sup>2</sup> Department of Pathology, <sup>4</sup> Center of Biostatistics and Bioinformatics, University of Mississippi Medical Center, Jackson, MS <sup>3</sup> United States Department of Agriculture, Agricultural Research Service, Natural Products Utilization Research Unit, University, MS

11:15	54	<b>Identifying Hormone Independent Targets &amp; Drug Designing For Breast And Prostate Cancers</b> Pradip K Biswas Laboratory of Computational Biophysics & Bioengineering, Department of Physics, Tougaloo College, Tougaloo, MS
11:30	55	<b>Theranostic Hybrid Graphene Materials With Label-Free Biosensing And Combined Therapy Capability</b> Paresh C Ray, Christine Tchounwou, Stacy Jones, Yongliang Shi, Aruna Vangara, Rajashekhar Kanchanapally, Bhanu Priya Viraka Nellore, Sudarson Sekhar Sinha, Avijit Pramanik, Suhash Reddy Chavva Department of Chemistry and Biochemistry, Jackson State University, Jackson, MS
11:45	56	<b>Novel Antibody Conjugated Hybrid Gold-Graphene Oxide Nanoparticles For The Treatment Of Cytomegalovirus Infection</b> Madeline A. Aylward <sup>1</sup> , Karen Stokes <sup>2</sup> , Sudarson S. Sinha <sup>3</sup> , Paresh C. Ray <sup>3</sup> and Ritesh Tandon <sup>1*</sup> <sup>1</sup> Department of Microbiology and Immunology, University of Mississippi Medical Center, 2500 North State Street, Jackson, MS, USA. <sup>2</sup> Department of Molecular and Cellular Physiology, Center for Cardiovascular Disease and Sciences, Center for Molecular and Tumor Virology, Louisiana State University Health Sciences Center, Shreveport, LA. <sup>3</sup> Department of Chemistry and Biochemistry, Jackson State University, Jackson, MS
12:00	57	<b>New Sites for Old Suspects: Environmental Allosteric Modifiers of Human Estrogen Receptors</b> Rajendram V Rajnarayanan University of Buffalo, Buffalo, NY
		<b>LUNCH</b>

**12:15-2:00 PM: Lunch & Keynote Speaker Followed by Student Award Presentation**  
**Keynote Speaker: Dr. Ham Benghuzzi,**

**Title: Advances in Ceramic Drug Delivery Systems**

**5:00 pm-9:00 Program Committee Meeting**

# ROBOTIZED METHOD FOR COMPARATIVE TESTING OF BACK SUPPORT DEVICES

Denis J. DiAngelo, John Simmons, Daniel Wido

BioRobotics Laboratory, Department of Orthopedic Surgery and Biomedical Engineering,  
The University of Tennessee Health Science Center, 956 Court Ave., Suite E226, Memphis, TN 38163

## ABSTRACT

**Introduction.** Many spinal diseases affect the mechanical integrity of the lower back causing instability and low back pain. Braces are often used as non-surgical treatment and serve to support the spine and alleviate the pain. More recently dynamic braces claiming to decompress the spine have been introduced. However no scientific data or testing methodology exists to determine how well back braces work. A mechanical analogue of the upper torso and lower spine was developed and integrated into a robotic testing platform to analyze spinal orthosis' mechanics.

**Methods.** Two orthoses were evaluated: a decompression stabilizing orthosis (DSO) and a new novel distractive mobility orthosis (DMO). Three loading conditions were simulated: upper torso loads up to 400N in upright stance, ii) initiation of flexion (5deg) and extension (3deg) from upright stance, and iii) extended ranges of flexion (28deg) and extension (10deg) from upright stance. Loads applied to the torso-orthosis assembly and transferred through the spine were used to determine the off-loading capacity of the orthoses and combined with the displacement changes to calculate the orthoses' rotational stiffness properties.

**Results and Discussion.** Both orthoses reduced spinal loading by 300N in upright stance. Initiation of flexion and extension required moments of 18Nm and 7.1Nm for the DSO and 9.4Nm and 5.5Nm for the DMO. The DMO reached 20Nm at 28deg flexion and 15Nm at 10deg extension. The DSO was too stiff for extended range testing.

**Conclusion.** The unique biomechanical test assembly was able to determine the biomechanical properties of two different back support devices.

**Keywords:** spinal orthosis, low back pain, biomechanical testing

## INTRODUCTION

Diseases of the spine presenting symptoms of lower back pain (LBP) are at epidemic proportions in the United States and elsewhere. LBP affects 60% to 80% of individuals during their lifetime [1] and has disabled more than 5 million Americans [2,3]. It is the most expensive cause of work-related disability in terms of worker's compensation and medical expenses [4,5,6]. The Spine Patient Outcomes Research Trial (SPORT) was created to improve clinical decision making for surgical treatment of low back pain problems [7sport]. SPORT represents the largest clinical investigation yet conducted of the three most common, disabling and costly low back disorders: intervertebral disc herniation (IDH), spinal stenosis (SpS), and degenerative spondylolisthesis (DS). These diseases are largely mechanical in nature and comprise more than 70% of the LBP population [6]. Although conservative and surgical options are available for treating many of these LBP conditions, little evidence documents the efficacy and cost-effectiveness between surgical therapy and non-operative management [7]. Conservative treatment options include medication, exercise strengthening, or any method that decompresses the lower spine, such as water therapy,

inversion therapy, or use of a spinal orthosis.

Numerous spinal orthoses are marketed for treating LBP that provide varying degrees of immobilization, support-stabilization and/or spinal decompression. However, with so many product choices and contributing disease factors, the process by which caregivers select an orthosis to treat patient-specific symptoms has been described as "random and empirical" and often resulting in abandonment of treatment [8,9]. Someone with early onset of disc degeneration may benefit from an orthosis that stabilizes and axially off-loads the lower spine whereas a person with spondylolisthesis would benefit from an orthosis that restricts anterior-posterior shear to alleviate or exacerbate spinal instability and cord compression. Between these two examples, the mechanical function required by the spinal orthosis varies between responding to an axial compressive force versus an orthogonally directed shear force. In some instances different combinations of force compensation may be required. Table 1 represents the first step towards establishing a relationship between the lost mechanical function of the spinal disorder and the structural engineering requirements of a spinal orthosis.

The objective of this research was to design a mechanical analogue of the upper torso and lower spine that was integrated into a robotic testing platform. The test assembly was programmed to simulated spinal loading mechanics of typical daily living activities [10] and used to

compare the structural properties of two different lumbar spinal orthoses.

Table 1: Relationship between clinical problem and Require Mechanical Function

Clinical Disorder	Require Mechanical Function	Equivalent Structural Properties	Engineering Model
Disc degeneration	Disc Decompression Stabilization	- Load sharing Capacity - Axial stiffness	- Axial force - Ratio of Axial force to Displacement
Spondylolisthesis	Cord Decompression Stenosis	- Shear Force Shielding - Stabilization	- Shear force - A-P stiffness - Ratio of Shear force to Displacement
Fusion surgery	Stabilization / Immobilization	- Stiffness	- Rotational Stiffness - Axial Stiffness
Muscle Weakness With Age	Posture Control Postural Protection	Mobility, Trunk Dynamization	- Rotational Stiffness - Axial Displacement - Axial force
Discomfort Wearing Orthosis	Reduce Pressure Sores Minimize Skin Breakdown	Contact Pressure	

## ROBOTIC TESTING PLATFORM

A multi-axis robotic testing platform (RTP) was used that provided four programmable degrees of freedom having a positional resolution of  $2\mu\text{m}$  in x,  $0.31\mu\text{m}$  in z, and  $0.0002^\circ$  about y (Figure 2) [11]. The RTP included six-axis load cells mounted to the upper gimbal assembly and to the lower base plate. The upper load cell (ULC), which measured applied forces and moments, had a maximum axial force of 445N and a resolution of 0.2N. The base load cell (BLC) has a maximum axial force of 4,445N and a resolution of 0.73N.

## MECHANICAL ANALOGUE OF HUMAN TORSO

An upper torso, biomimetic lumbar spine, and pelvic girdle assembly (referred to as the human mechanical analogue) were designed to emulate the structural properties of a human torso. The biomimetic lumbar spine, Figure 3, consisted of individual spinal components having shape and size comparable to the human lumbar motion segments. The L1-L5 vertebral bodies were cast in rubber molds made from harvested human spines. The individual discs were fabricated based on characteristics from the literature [12] and provided the anterior and posterior heights for each disc. The material for each disc was 30 Durometer urethane (74-30D Urethane from US

Composites, 6670 White Drive West Palm Beach, FL 33407). A first motion segment unit (MSU) was assembled with L1, the disc for L1-L2, and L2. After preliminary testing of the mechanical properties of this first MSU, additional segments were incrementally added. The full L1-L5 lumbar assembly was coated with 30 durometer urethane. The assembly was then tested for axial and rotational stiffness. Where more stiffness was required, based on human cadaver spine data[13], additional urethane was added with a brush. To emulate the simultaneously fibrous and flexible nature of ligaments, small loops of ordinary duct tape between segments were used to provide additional rotational stiffness. The final motion segmental unit (MSU) responses and rotational stiffness properties of the biomimetic spine are shown in Figures 3B) and 3C) and approximated the cadaveric test data.

A life size male mannequin was cut and substantially reinforced internally with carbon fiber and epoxy resin to provide an upper torso frame and separate pelvic girdle assembly for engaging a worn orthosis as it was tested. Multiple layers of a textured material (Kobalt Zerust drawer liner, Zerust Corrosion Products. Twinsburg, OH 44087) were placed around the external surface of the upper torso component that simulated the texture and orthosis-engagement properties of human

tissue. The material had a hardness of approximately 30 Durometers Shore A at its thickest section of weave pattern. Each layer was impregnated and externally coated with a thin coating of 30 Durometer Shore A urethane. The biomimetic spine was mounted superiorly to the upper torso frame and inferiorly to the BLC (Figure 2B). The BLC was surrounded by but not in contact with the pelvic girdle assembly. The pelvic girdle assembly, which is shown individually at the bottom of Figure 2B), was provided to mount to and engage the lower portion of an orthosis to be tested and was anchored to the base plate of the RTP.

#### TEST PROTOCOL AND FORCE ANALYSIS

The DSO was mounted on the human analogue for evaluation as shown in Figure 2C) for testing analyses.

Three test conditions were simulated: upper torso loads up to 400N in upright stance, ii) initiation of flexion (5deg) and extension (3deg) from upright stance, and iii) extended ranges of motion (ROM): flexion (28deg) and extension (10deg) from upright stance. A 400N value simulated the upper body (above the abdomen) weight of a person whose approximate total body weight is 225 pounds based on the upper body comprising approximately 40% of total body weight [14]. For flexion and extension tests, the robot was programmed to rotate the upper torso of the human analogue around the calculated axis of rotation of the whole lumbar spine and then applied the vertical torso weight loads.

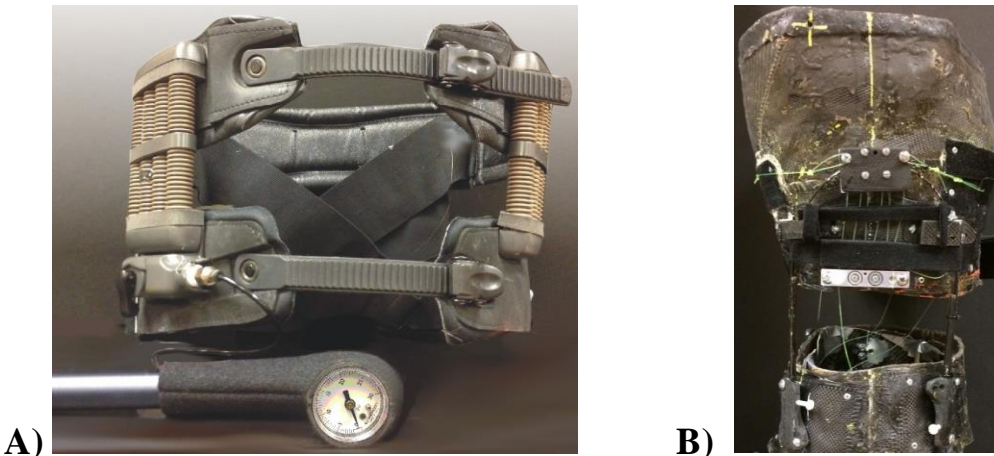


**Figure 1. Spinal Orthoses. A) The Orthotrac Pneumatic Vest is a dynamic stabilizing orthosis (DSO). B) Novel dynamic mobility orthosis (DMO).**

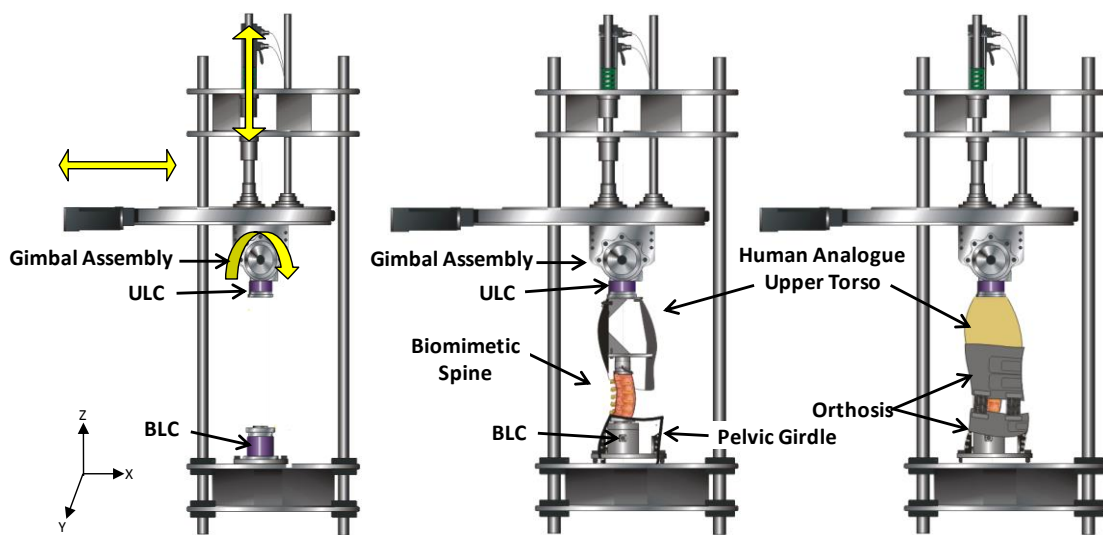


Figure 2. BioRobotic Testing Assembly. A) The multi-axis robotic platform applies and measures forces and moments through an upper load cell (ULC) and base load cell (BLC). Control axes are shown by yellow arrows. B) A human analogue is shown mounted in the multi-axis testing platform with the base of the biomimetic spine attached to the BLC. C) Schematic of an orthosis worn by the human analogue.

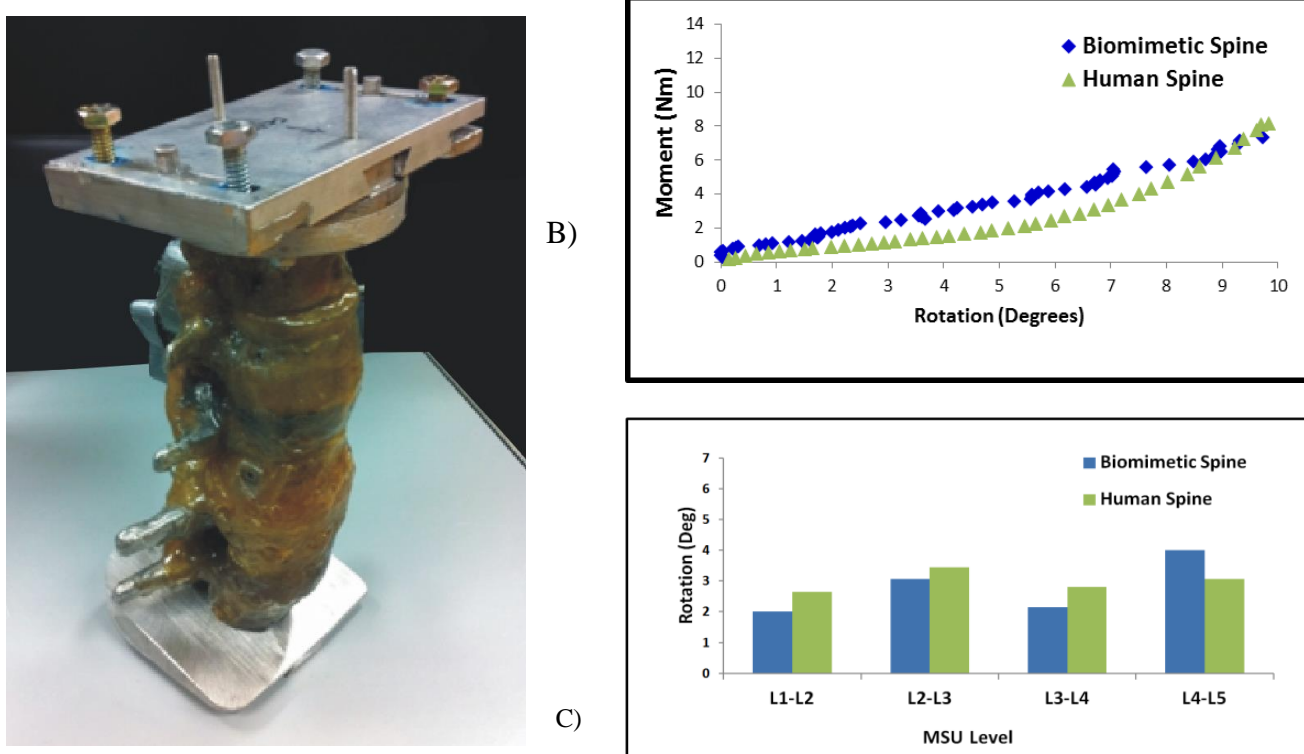


Figure 3. The biomimetic spine was compared to cadaveric data [14] for A) Rotational stiffness and B) individual motion segment rotation responsive to approximately 8Nm of bending moment.

Loads applied to the torso-orthosis assembly were measured at the ULC and the loads transferred through the lower spine were measured at the BLC. The ULC and BLC forces and bending moments (BM) were transformed to the sacral disc plane, SDP (Figure 4A), and compared. With a spinal orthosis mounted (Figure 4B), differences in the two load cell readings transformed to the SDP represented the portion of the applied forces and moments carried by the

orthosis. The axial stiffness of the orthosis was calculated as the difference of the ULC applied axial force and the BLC measured axial force divided by axial deformation of the biomimetic spine. The rotational stiffness of the orthosis was calculated as the difference of the applied moment and the BLC moment divided by degrees of rotation.

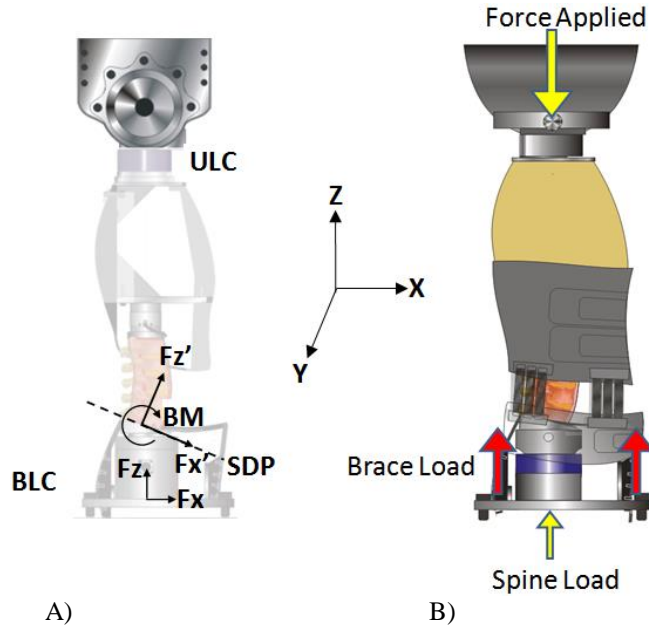


Figure 4. Force Analysis: A) The ULC and BLC forces and bending moments (BM) were transformed to the SDP and compared. B) With Orthosis (brace) Mounted: Brace load is the difference of ULC Force Applied and the BLC-measured Spine Load.

## RESULTS

### UPRIGHT VERTICAL STANCE

The load sharing capacity of the two orthoses tested in the upright orientation are shown in Table 2. For 400N applied load the DSO carried 271N. For applied vertical torso loads of 300N, the DSO carried 220N and the DMO carried 273N.

### INITIATION OF MOTION

The moment versus angular displacement response of the DSO and DMO devices are shown in Figure 5 for initiation of flexion and extension. The slope of the curves represents the rotational stiffness properties. The

flexion stiffness values were 1.25Nm/deg and 0.72Nm/deg for the DSO and DMO respectively and the extension stiffness values were 0.09Nm/deg and 1.01Nm/deg. At the end ranges of 3deg extension and 5deg flexion, only 18% and 63% of the applied load was carried by the DSO device while the DMO device carried 91% and 82% (see Table 3).

### EXTENDED ROM

The DSO was too stiff for extended range testing. For the DMO device, up to 10deg extension and 28deg flexion were reached. The rotational stiffness values of the DMO were 1.01Nm/deg in extension and 0.42Nm/deg on flexion (Figure 6) and end range moment-rotation values are provided in Table 4.

**Table 2: Applied and Brace Loads for Upright Stance Condition**

DSO		DMO	
Applied Load (N)	Brace Load (N)	Applied Load (N)	Brace Load (N)
400	271	-	-
300	220	300	273

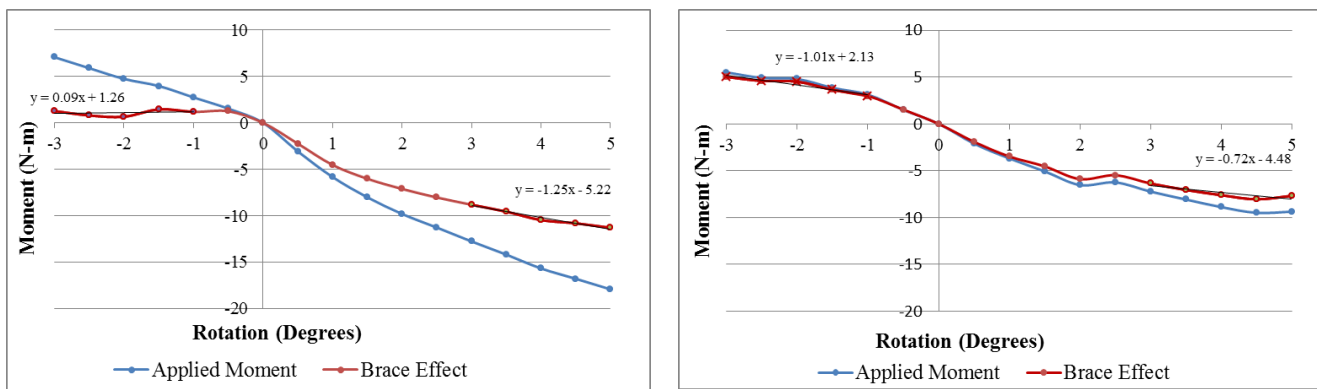


**Figure 5. Rotational Stiffness of DSO (left) and DMO (right). Positive degrees indicate flexion while negative degrees indicate extension.**

**Table 3. The Brace Effect on Applied Moment for 300N Applied Load**

Degrees of Rotation	DSO			DMO		
	Applied Moment (Nm)	Brace Effect (Nm)	Brace Effect as a Percentage of Applied Moment (%)	Applied Moment (Nm)	Brace Effect (Nm)	Brace Effect as a Percentage of Applied Moment (%)
At 3deg Extension	7.1	1.3	18%	5.5	5	91%
At 28deg Flexion	18	11.3	63%	9.4	7.7	82%

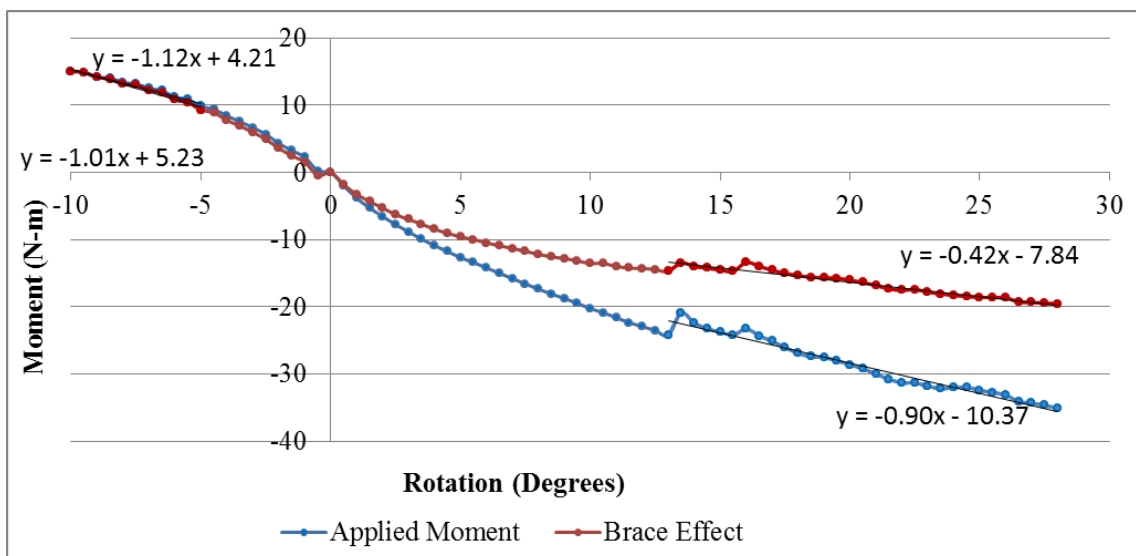


**Figure 6. Bending Moment Mechanics of DMO for Extended Ranges of Motion**

**Table 4. DMO Effect on Applied Moment for Extended Ranges of Motion**

Degrees of Rotation	DMO		
	Applied Moment (Nm)	Brace Effect (Nm)	Brace Effect as a Percentage of Applied Moment (%)
At 10deg Extension	15	15	100%
At 28deg Flexion	35	19.6	56%

## DISCUSSION

For all tests motion was confined to the sagittal plane and the spinal loading mechanics were analyzed at the L5-S1 disc plane. The biomimetic lumbar spine was validated under flexion and compression loading only. The testing protocol simulated the force components of the gravitational torso loading mechanics but not the corresponding *in vivo* spinal bending moment. The applied bending moment was a function of the biomimetic spine's structural properties as well as the brace.

Both orthoses reduced the loads transferred through the spine during vertical stance load simulations: 73% for the DSO device and 91% for the DMO device. The applied moments required to move through 3deg extension and 5deg flexion for the DMO were much lower than for the DSO highlighting the differences between a stabilization device a mobilizing one. The DSO provided minimal moment support in extension (18%) compared to 91% for the DMO. The DMO also carried a larger percentage of the applied flexion moment compared to the

DSO.

The DMO allowed ranges of motion comparable to many daily living activities within bending moment levels under 20Nm. The physical size of the testing platform limited the extended range of motion tests to 28deg flexion and 10deg extension. Initiation of flexion and extension required moments of 18Nm and 7.1Nm for the DSO and 9.4Nm and 5.5Nm for the DMO.

## CONCLUSIONS

The unique biomimetic human analogue and robotic testing platform were able to assess the beneficial and/or adverse biomechanical properties of two different spinal orthoses as well as predict the approximate loads that a given orthosis could support. In the future, this biomechanical testing assembly can function as a research tool and serving as a rapid development platform for designing new and improved orthoses. It can also serve as the first steps towards developing a classification process and set of standards for ranking spinal orthoses which would better enable caregivers to select and administer the

orthoses best suited to treat a specific LBP causative pathology.

## ACKNOWLEDGMENTS

Clay Hillyard for technical assistance with manuscript preparation.

## REFERENCES

- [1] J. M. Fritz and J.A. Cleland. (2008, Jul.). Physical therapy for acute low back pain: associations with subsequent healthcare costs. *Spine*. [Online]. 33(16), 1800-5.
- [2] D. Akay and M. D. Toksari. (2008, Nov.). Ant colony optimization approach for classification of occupational low back disorder risks. *Human Factors and Ergonomics in Manufacturing*. [Online]. 19(1), 1-14.
- [3] L. S. Brecher. (2001, Apr. 4). Editor's Message. *JAOA*. [Online]. 101(4). Available: [http://www.jaoa.osteopathic.org/content/101/4\\_s\\_uppl\\_2/1S.full.pdf](http://www.jaoa.osteopathic.org/content/101/4_s_uppl_2/1S.full.pdf)
- [4] P. Pensri and P. Janwantanakul. (2010, Dec.). Biopsychosocial factors and perceived disability in saleswomen with concurrent low back pain. *Saf Health Work*. [Online]. 1(2), 149-57.
- [5] Andersson, G.B.J. (1999, Aug.). Epidemiological features of chronic low-back pain. *Lancet*. [Online]. 354(9178), 581-5.
- [6] R. A. Deyo and J. N. Weinstein. (2001, Feb.). Low Back Pain. *N Engl J Med*. [Online]. 344(5), 363-70.
- [7] A. N. Tosteson, J. S. Skinner and T. D. Tosteson. (2008, Sept.). The cost effectiveness of surgical versus nonoperative treatment for lumbar disc herniation over two years: evidence from the Spine Patient Outcomes Research Trial (SPORT). *Spine*. [Online]. 33(19), 2108-15.
- [8] T. M. Gavin. (1993, Jan.). Preliminary Results of Orthotic Treatment for Chronic Low Back Pain. *J. of Prosthetics & Orthotics*. [Online]. 5(1), 5-9.
- [9] J. Hsu, J. Michael and J. Fisk, "Orthoses for Osteoporosis," in *AAOS Atlas of Orthoses and Assistive Devices*, 4th ed., 2008, Chapter 11, Page 1.
- [10] J. E. Bible. (2010, Apr.). Normal functional range of motion of the lumbar spine during 15 activities of daily living. *J Spinal Disord Tech*. [Online]. 23(2), 106-12.
- [11] B. P. Kelly and D. J. DiAngelo. (2013, Jul.). A Multiaxis Programmable Robot for the Study of Multibody Spine Biomechanics Using a Real-Time Trajectory Path Modification Force and Displacement Control Strategy. *J. Med Devices*. [Online]. 7(3). Available: <http://dx.doi.org/10.1115/1.4024645>
- [12] I. Gilad and M. Nissan. (1986, Mar.). A study of vertebrae and disc geometric relations of the human cervical and lumbar spine. *Spine*. [Online]. 11(2), 154-7.
- [13] J. R. Stubbs, "Use of a multi-axis robotic testing platform to investigate the sagittal mechanics of the multi-body lumbar spine," M.S. Thesis, Dept. of Orthopaedic Surgery and Biomedical Eng., Univ. of Tennessee Health Science Center, Memphis, TN, 2014.
- [14] D. A. Winter. *Biomechanics of Human Movement*. John Wiley & Sons Inc, 197.

# SCOLIOSIS ANALOG MODEL FOR THE EVALUATION OF BRACING TECHNOLOGY

Chloe L. Chung & Denis J. DiAngelo

BioRobotics Laboratory, Department of Orthopaedic Surgery and Biomedical Engineering, The University of Tennessee Health Science Center, 956 Court Ave., Suite E226, Memphis, TN 38163

## ABSTRACT

**INTRODUCTION:** Thoracolumbar braces are commonly used to treat Adolescent Idiopathic Scoliosis (AIS). Braces serve to reduce and prevent progression of the spinal curve by applying multidirectional corrective forces. These forces may cause translational (inward, upward) and derotational (twist) responses of the spine. The objective was to develop a testing assembly capable of quantifying brace structural stiffness properties by measuring the corrective force components.

**METHODS:** A novel mechanically-equivalent analog model of the AIS condition was designed and developed to simulate 40deg of spinal correction. A linkage-based model was used in conjunction with a biorobotic testing platform to quantify scoliosis brace structural stiffness properties. Measurements of the force components applied to the model and displacement of the linkage assembly were used to calculate the brace stiffness. The brace was tested in both a constrained (via Velcro straps) configuration and an unconstrained configuration.

**RESULTS:** Calculated stiffness was expressed as a resistive force relative to the angular change of the linkage system from 30deg to 70deg. For the unconstrained and constrained configurations, vertical forces ranged between 10 and 100N and mean stiffness values were 3.2 N/deg (axial) and 0.3 N/deg (radial), and 40 and 450N and 51.3 N/deg and 3.2 N/deg respectively.

**DISCUSSION:** Structural properties provide a means to compare bracing technology and better understand design features. For example, addition of Velcro straps increased stiffness of the native brace 10 fold. This test assembly could be used as a design tool and to develop a standard for classifying braces.

**Keywords:** scoliosis, brace, biomechanics, analog model, axial stiffness, radial stiffness

## INTRODUCTION

Scoliosis is a three dimensional (3D) skeletal deformity of the spine consisting of a combination of axial rotation and lateral curvature that measures 10deg or greater in the coronal plane [1]. Scoliosis curve types can be single or double in nature and can be present in any one or multiple areas of the spine. According to the National Scoliosis Foundation [2], scoliosis affects an estimated 6 million people in the United States alone, approximately 2-3% of the population. Idiopathic scoliosis with an onset after 10 years of age, called adolescent idiopathic scoliosis (AIS), is the most common spinal deformity treated by primary care physicians, pediatricians, and spinal surgeons (representing 85% of cases or 0.5-3.0% pediatric population). There is currently no cure that exists for this condition. It is estimated that out of the 600,000 patient

visits, only 30,000 are treated with an orthosis and 38,000 are treated with extreme, multi-level spinal fusion surgery.

The standard method for assessing the curvature quantitatively is measurement of the Cobb angle (**Fig. 1a**), which is the angle between two lines, drawn perpendicular to the upper endplate of the uppermost vertebra involved and the lower endplate of the lowest vertebra involved [3]. Advanced imaging techniques have simplified the assessment of the scoliosis deformity and the determination of treatment efficacy. The EOS Imaging System simultaneously captures biplanar posteroanterior and lateral radiographs. SterEOS software uses these images to create a patient-specific 3D model of the spine (**Fig. 1b**) and to report scoliosis parameters such as the Cobb angle, critical vertebrae (highlighted in blue and yellow of Fig. 1b), and vertebral rotation.

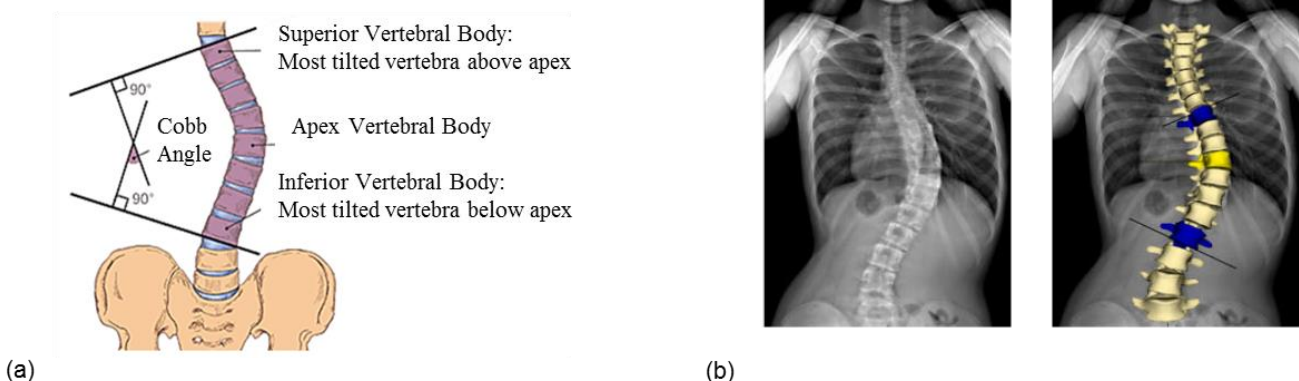


**Figure 1: Mid-Thoracic Three-point Single Curve Scoliotic Deformity. (a) Scoliosis Cobb Angle Measurement showing Critical Vertebral Anatomy [4] and (b) Radiographic and SterEOS 3D Model Reconstruction [5].**

Bracing is the standard of care for treating AIS curves between 25 and 45deg, and is used when the spine is assessed to be compliant or if the case is mild but there is a risk of progression before skeletal maturity is reached. Braces serve to reduce and prevent progression of the spinal curve by applying multidirectional corrective forces. The results at the end of the growth phase are a stable Cobb angle with up to 50% curve reduction and improved trunk, lower spine, and pelvic alignments [6]. Up until recently, bracing has been highly debatable. Weinstein et al. (2013) designed and conducted a 5 year follow-up study, the Bracing in Adolescent Idiopathic Scoliosis Trial (BRAIST) [7]. Findings from this study were reported in the Fall of 2013 and provided the first evidence that braces were effective (72% success rate) at treating scoliosis. The primary goal for bracing is to halt curve progression, though clinicians have occasionally been able to lessen the amount of spinal curvature [8]. Many braces use a three-point pressure principle as the method of correction, which involves fixation above, below, and at the apex of the curve. These forces may cause translational (inward, upward) and derotational (twist) responses of the spine, and are the result of careful brace design and fabrication.

Scoliosis braces can be rigid, flexible, or composite and can utilize passive or active correction mechanisms. An orthotist works with a manufacturer to fabricate the brace with custom contouring layers and padding. Typically an orthotist performs the final stages of custom fitting the brace on the patient. Extra pads can be used to improve the fit and comfort of the brace. However, there is no standard of application or common understanding of how changes to these fitting pads (size, placement, thickness) can affect the corrective capacity of brace. The process is largely subjective and follows best judgment and practice, yet these steps are critical and should affect the patient decision to wear the brace. In the

end, how well the brace works largely depends on the artisan experience-based fabrication methods of the orthotist. Imaging is used to measure the degree of spinal correction and determine brace efficacy. However, no force analysis is used during the brace design phase or evaluation process.

Most scoliosis braces lack supporting performance data. There is no validated scoliosis model or biomechanical testing environment known to exist, which has hindered experimental research of scoliosis bracing technology. Experimental research of scoliosis bracing mechanics has been limited to 2D and 3D imaging techniques [7] and computational models [9]. Imaging methods provide a measure of the angular deformity but no information of the brace mechanics or structural properties, such as axial and radial stiffness. The functional capacity of computational models is limited by the lack of validating *in vivo* and *in vitro* mechanics data. The objective of this research was to design and validate a novel mechanically-equivalent analog model of a mid-thoracic single curve scoliotic deformity. A scoliosis torso model was developed and integrated into a biomechanical testing platform to study the structural properties and loading mechanics of a scoliosis brace.

## METHODS

### MODEL DESIGN

A novel mechanically-equivalent analog model of the AIS condition was designed and developed to simulate 40deg of spinal correction. The Scoliosis Torso Model (STM) used a linkage-based system to simulate the kinematic behavior of a single-curve scoliotic spine. Anthropometric EOS data (**Fig. 2a**) of critical anatomical parameters served as the design parameters for the STM.

The spatial locations of the critical anatomy, including the superior, inferior, and apical vertebral bodies, correspond to the connection points of the main linkages of the STM (**Fig. 2b**). Each of the three critical vertebral bodies was represented in the STM by a linkage assembly. The linkage assembly consisted of a combination of linkages, connectors, arms, and shells (**Fig. 2c**). Each linkage component had a clevis joint and ball or pin joint at its ends held with a pin connector. The linkage lengths were defined by the patient's anthropometric measurements and

image data. The arm served to attach the shell to the linkages using pin connectors that were free to rotate. Each shell had a specific geometry that matched and interfaced with the internal contoured surface of the superior, apical, and inferior critical regions of the brace. The Cobb angle corresponded to the angular displacement of the linkages relative to the vertical axis. By using these critical anatomical parameters, the experimental STM replicated the clinical scoliosis deformity.

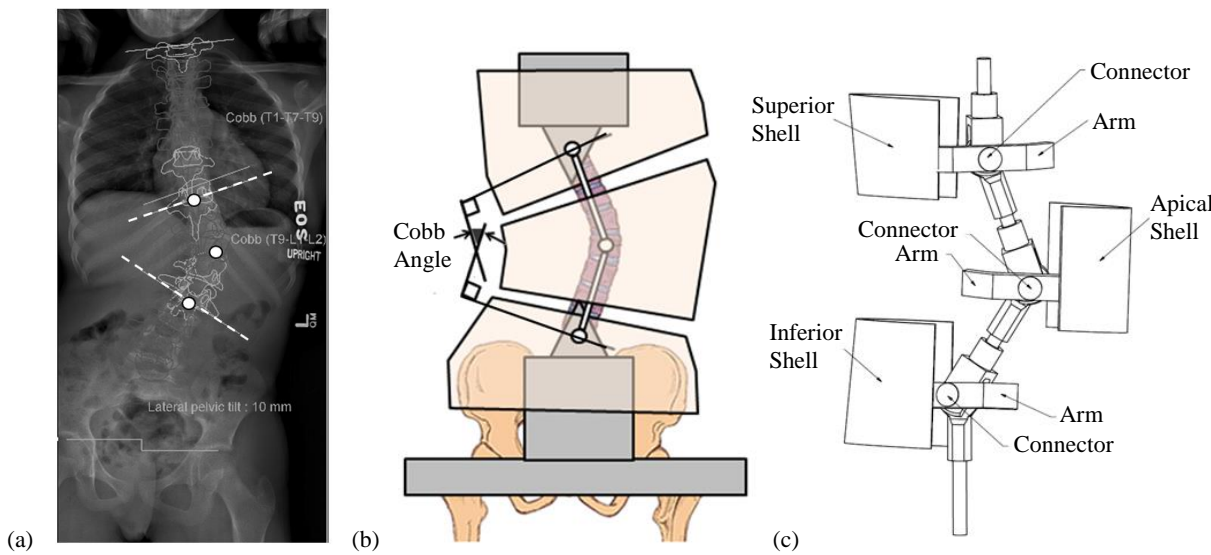


**Figure 2: Steps in Designing the Scoliosis Torso Model. (a) EOS Data, (b) Critical Anatomy Corresponding to STM Components, and (c) STM Components**

#### PROTOCOL

The upper and lower sections of the STM were attached to the moving actuation system and base of a robotic testing platform [10] as shown in **Fig. 3a**. The upper mounting plate of the STM was centered and fixed to the load cell that was attached to the actuator. The lower mounting plate of the STM was centered and fixed to a passive turn-table that prevented artifact frictional forces from building up in the linkages. The STM linkage assembly was tested first without a brace to ensure the links moved freely. Less than 2N of force occurred over 40deg of linkage rotation.

A single curve thoracolumbar Boston brace was mounted onto the STM assembly (**Fig. 3b**) and tested in two conditions: unconstrained (no straps) and constrained by straps. Velcro straps are often used by the orthotist to achieve proper fit and fixation of the brace on the user. The testing platform was programmed to displace along the

vertical axis a given distance and speed. Downward movement caused the STM to transition from the original state with an angular displacement of 30deg to the deformed state with an angular displacement of 70deg, thus simulating 40deg of spinal correction. Each brace condition was tested three times.

#### DATA MANAGEMENT

The net force components applied by the brace and the linkage assembly displacements were measured. Vertical force components and angular displacement of the linkage assembly were used to calculate the axial stiffness of the brace. Horizontal force components in the plane of motion and angular displacement of the linkage assembly were used to calculate the radial stiffness of the brace. A mean stiffness value was calculated for the three runs and compared between the two brace conditions. Reported angle and horizontal force measurements are doubled to represent the symmetry of the STM.

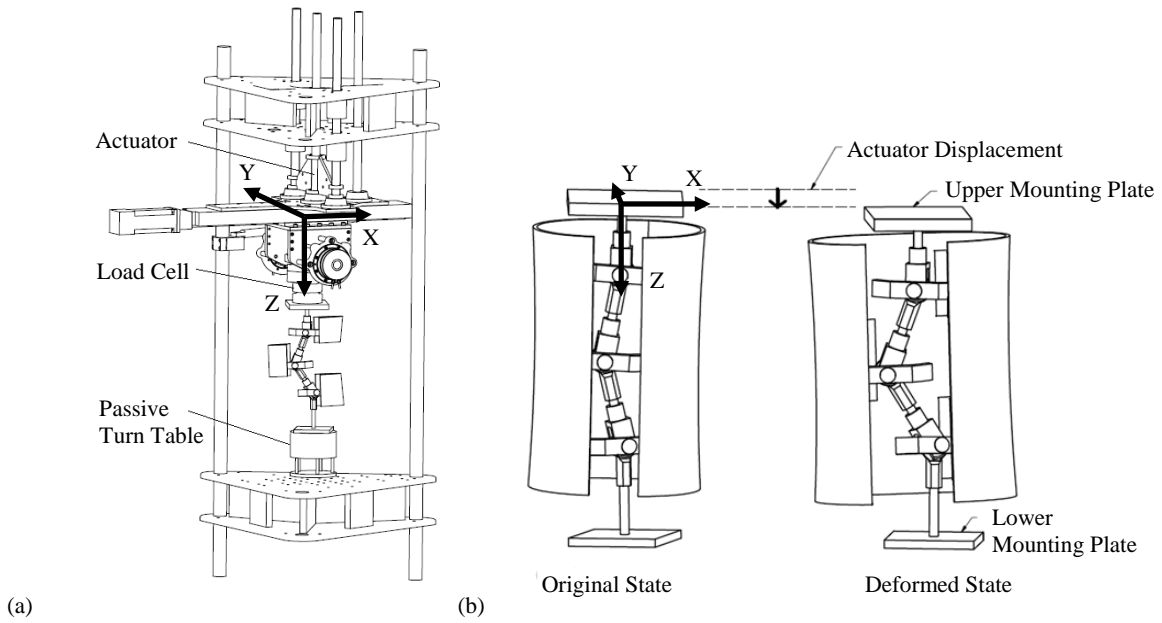


**Figure 3: STM Testing Protocol. (a) Robotic Testing Platform with STM assembly and (b) Methodology for Simulating a Changing Spinal Curve Using Linkage Components.**

## RESULTS

For the unconstrained and constrained brace configurations, the measured vertical forces ranged between 10 and 100N and 40 and 450N respectively and the measured horizontal forces ranged between 0 and 6N and 0 and 40N respectively. For both configurations, the vertical displacement ranged between 10 and 25mm and the total angular displacement was an average of 30deg (ranged between 20deg and 40deg). The axial and radial stiffness values for the unconstrained and constrained brace conditions are shown in **Fig. 4** and **Fig. 5**. Mean

stiffness values for the three runs were averaged over the linear region of the curves after brace engagement occurred. Stiffness was expressed as a resistive force relative to the angular change of the linkage system. This was preferred over the traditional linear stiffness measure so that the resultant stiffness was more easily relatable to the clinical Cobb angle measurement. For the unconstrained and constrained configurations, mean stiffness values were 3.2 N/deg along the Z direction (axial) and 0.3 N/deg along the Y direction (radial), and 51.3 N/deg and 3.2 N/deg respectively.

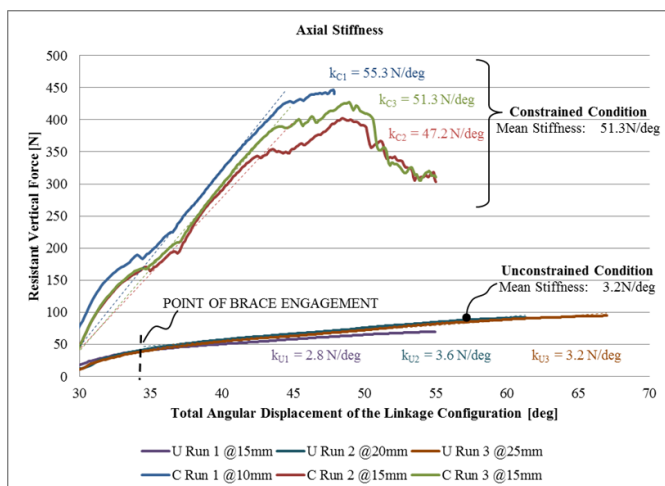


**Figure 4: Axial Stiffness of the Brace Configurations**

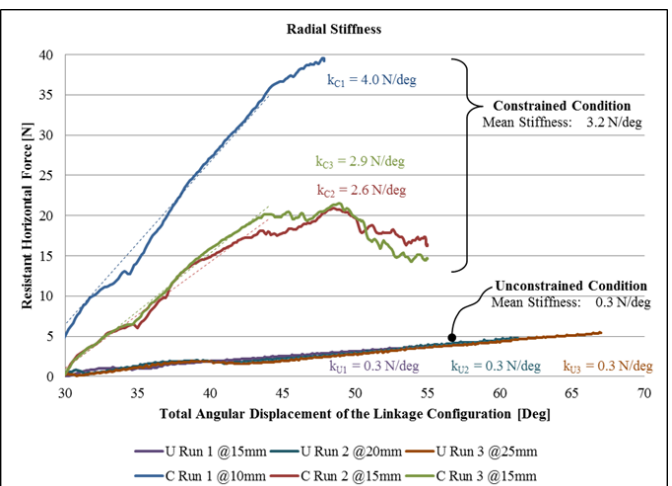


**Figure 5: Radial Stiffness of the Brace Configurations**

## DISCUSSION

### FINDINGS

Structural properties provide a means to compare bracing technology and better understand design features. The results show that the addition of Velcro straps increased the mean stiffness of the native brace 10 fold. Future testing using this model and methodology can be performed to analyze different design features of a brace that are used by the orthotist during brace fabrication. Some of these features include brace pads, pad placement, pad geometry, material selection, material cut-outs, rigid components, and other fitting elements. The orthotist may change brace structural stiffness with the methods listed above to achieve better patient fit or brace performance. For example, a patient with poor anatomical flexibility of the spine may require a stiffer brace to achieve the desired level of correction using a brace. In this case, the addition of Velcro straps could provide the increase in brace stiffness required for that patient.

Since this research model and testing methodology are novel, there is very little directly comparable data available. Van den Hout et al. [11] measured the magnitude of the direct compressive forces at the body-brace interface. The forces exerted by the internal lumbar and thoracic pads of a Boston brace were measured in 16 AIS patients using an electronic pressure measuring system. The mean forces measured at the lumbar brace pad was 214N (ranging from 0 to 727N) and at the thoracic brace pad was 66N (ranging from 4 to 209N). These force ranges are comparable to the magnitude of the forces measured by the STM in the constrained state.

As discussed earlier, the degree of correction achievable by a scoliosis brace largely depends on the

artisan experience-based fabrication methods of the orthotist. Braces serve to reduce and prevent progression of the spinal curve by applying multidirectional corrective forces. These forces may cause translational (inward, upward) responses of the spine (**Fig. 6a**). Up until now, there has been no evidence to prove an upward translational response of the spine. However, interpretation of the data has revealed that the brace pad engaged with the model in such a way to provide significant lift to the model. If a purely inward response occurred during the constrained brace condition tests, one would expect the measured net horizontal reaction force of 20N to be coupled with a net vertical reaction force of approximately 69N. However, under these conditions the measured data shows a net vertical reaction force of approximately 450N (**Fig. 6b**). These findings suggest that the brace reactant forces were not purely inward, but rather inward and upward.

### LIMITATIONS

General limitations that may affect the validity of these results include the oversimplification of the model versus *in vivo* biomechanics, the 2D analytical methods, the sample size of one brace, the lack of directly comparable validation data, and design approximations that were made during the development of this first scoliosis torso model prototype. Errors may have been introduced to the measurements by the variable kinematic behavior from one test to the next. To overcome this limitation, three runs were performed with different ranges of displacement. User error may have occurred when the Velcro straps were tightened between each constrained condition test, and this may have changed the reactant forces measured. The variation of the recorded horizontal forces of the constrained configuration can be attributed to this error. A way to overcome this error is to measure the strap tension between each test.

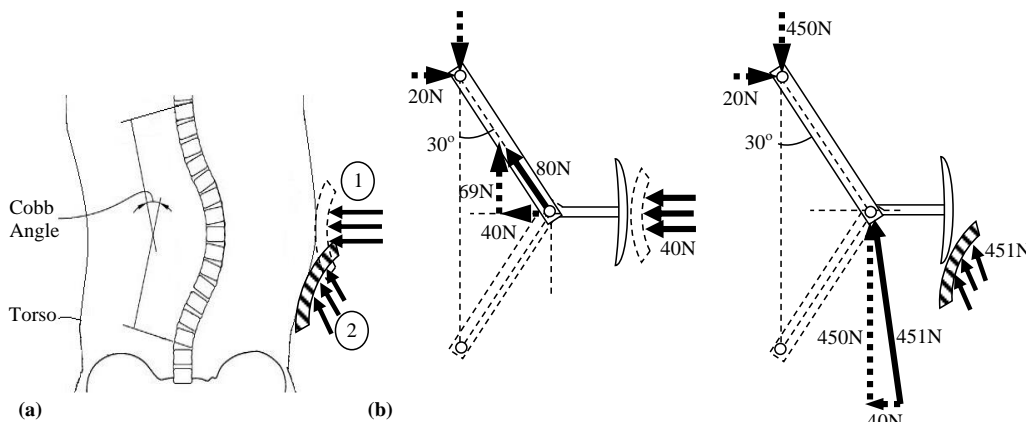


**Figure 6: Brace Pad Orientation and Force Response for 60 degree Cobb angle. (a) Translational Responses Case 1. Inward Only and Case 2. Inward and Upward (b) Free Body Diagram with Force Components Cases 1 and 2.**

Another limitation of this prototype model is the

assumption of symmetrical linkage geometry about the

apex. Also, the model is able to capture the force components, but does not consider the effective area of the applied forces. This could have been addressed by measuring the brace-model interface pressure and force distribution. The testing did not account for loss of brace stiffness over longer periods of wear. The elastic nature of the brace materials allowed for the brace to return to its original state after each test. An important design feature of the STM is that the "spine" is assumed to have negligible or zero stiffness. Thus all reactant forces measured can be attributed to the brace alone. Despite these limitations, this research has resulted in a novel model, methodology, and baseline data for future research.

## CONCLUSIONS

Through the development of this analog scoliosis torso model and testing methodology, we have enabled the study of bracing technologies. Measured force components provide the first evidence of force transmission by confirming an upward lifting effect. Future testing using this model and methodology can be performed to analyze different design features of a brace that are used by the orthotist during brace fabrication. Some of these features include brace pads, pad placement, pad geometry, material selection, material cut-outs, rigid components, and other fitting elements. This test assembly could also be used as a design tool and to develop a standard for classifying braces.

## ACKNOWLEDGMENTS

Usage of the EOS System at Le Bonheur Children's Hospital, Memphis, TN. Jack Steele, CO, LPO, FAAOP of the Center for Orthotics and Prosthetics, Inc., Memphis, TN.

## REFERENCES

- [1] F. Altaf, A. Gibson, Z. Dannawi, and H. Noordeen, "Adolescent idiopathic scoliosis," *BMJ*, vol. 346, pp. f2508, 2013.
- [2] National Scoliosis Foundation. (2015, February 26). *Information and Support* [Online]. Available: <http://www.scoliosis.org/info.php>.
- [3] I. Busscher, F. H. Wapstra, and A. G. Veldhuizen, "Predicting growth and curve progression in the individual patient with adolescent idiopathic scoliosis: design of a prospective longitudinal cohort study," *BMC Musculoskelet Disord*, vol. 11, pp. 93, 2010.
- [4] K. A. Greiner, "Adolescent idiopathic scoliosis: radiologic decision-making," *Am Fam Physician*, vol. 65, no. 9, pp. 1817-22, May 1, 2002.
- [5] T. Illes, M. Tunyogi-Csapo, and S. Somoskeoy, "Breakthrough in three-dimensional scoliosis diagnosis: significance of horizontal plane view and vertebra vectors," *Eur Spine J*, vol. 20, no. 1, pp. 135-43, Jan, 2011.
- [6] D. Gallo, "Control of Idiopathic Scoliosis Treatment in 147 Patients while using the RSC Brace," *JPO Journal of Prosthetics and Orthotics*, vol. 23, no. 2, pp. 69-77, 2011.
- [7] S. L. Weinstein, L. A. Dolan, J. G. Wright, and M. B. Dobbs, "Effects of bracing in adolescents with idiopathic scoliosis," *N Engl J Med*, vol. 369, no. 16, pp. 1512-21, Oct 17, 2013.
- [8] L. A. Rinsky, and J. G. Gamble, "Adolescent idiopathic scoliosis," *West J Med*, vol. 148, no. 2, pp. 182-91, Feb, 1988.
- [9] J. M. Mac-Thiong, Y. Petit, C. E. Aubin, S. Delorme, J. Dansereau, and H. Labelle, "Biomechanical evaluation of the Boston brace system for the treatment of adolescent idiopathic scoliosis: relationship between strap tension and brace interface forces," *Spine (Phila Pa 1976)*, vol. 29, no. 1, pp. 26-32, Jan 1, 2004.
- [10] B. P. Kelly, and D. J. DiAngelo, "A Multiaxis Programmable Robot for the Study of Multibody Spine Biomechanics Using a Real-Time Trajectory Path Modification Force and Displacement Control Strategy," *Journal of Medical Devices*, vol. 7, no. 3, pp. 034502-034502, 2013.
- [11] J. A. van den Hout, L. W. van Rhijn, R. J. van den Munckhof, and A. van Ooy, "Interface corrective force measurements in Boston brace treatment," *Eur Spine J*, vol. 11, no. 4, pp. 332-5, Aug, 2002.

# TOWARDS THE DESIGN OF A DISTRACTIVE AND MOBILITY-ENABLING BACK SUPPORT DEVICE

Denis J. DiAngelo and John C. Simmons

BioRobotics Laboratory, Department of Orthopedic Surgery and Biomedical Engineering,  
The University of Tennessee Health Science Center, 956 Court Ave., Suite E226, Memphis, TN 38163

## ABSTRACT

**Introduction.** Spinal orthoses have historically been designed to stabilize the spine and are used to treat low back pain (LBP). Recent bracing technologies claim to axially decompress the spine while restricting motion. However, no supportive experimental or clinical data exist. LBP patients also try therapeutic exercises, like water therapy, to distract and decompress the spine, but for short periods. The objective was to design a distractive mobility orthosis (DMO) that mimicked spinal traction and water therapy but did not restrict movement.

**Methods.** A mechanical analogue upper torso model and robotic testing platform were used to design features of the DMO: a distractive force component (DFC) and a mobility-enabling component (MEC). A cable pulley array system and flexible graphite rods provided distractive force capabilities. The MEC consisted of a rail and coaster system. Test conditions were 300N vertical torso load and extended ranges of flexion (28deg) and extension (10deg). Spinal off-loading capacity of the brace was measured and combined with displacement changes to calculate rotational stiffness.

**Results and Discussion.** The DMO reduced all spinal loading in upright stance and continued off-loading through 28deg flexion (125N) and 10deg extension (34N). During extended ranges of movement the brace was able to support 56% of the flexion moment and 100% of the extension moment. The rotational stiffness of the DMO during extended flexion (0.4Nm/deg) was comparable to the mechanical analogue spine (0.5Nm/deg).

**Conclusion.** Aspects of a novel back support device were designed that provided distractive forces across the spine during unconstrained flexion and extension.

Keywords: spinal orthosis, low back pain, biomechanical testing, dynamic back brace, load-sharing

## INTRODUCTION

Low back pain (PPB) affects 60% to 90% of individuals during their lifetime [1]-[3] and disables 5.4 million Americans per year [4,5]. It is the most expensive cause of work-related disability in terms of worker's compensation and medical expenses [6]-[8]. LBP disability is not confined to the aged. In fact, it is the most common cause of disability for those under the age of 45 years [9]. Current treatments range from surgery to rest. Approximately 200,000 lumbar laminectomies for back and/or leg pain are performed yearly in the United States [10]. Others suffering from LBP seek alternative treatments hoping to avoid surgery including medication, exercise strengthening, or any method that decompresses the lower spine, such as water therapy, inversion therapy, or use of a spinal orthosis.

Water therapy [11]-[13] usually involves some exercise while the buoyancy of the water reduces the spinal load. Clinical-related studies [11]-[13] have suggested that, with adequate frequency and duration of treatment, water therapy can be beneficial in the treatment of low back pain.

Spinal orthoses are widely used to facilitate post-surgical recovery where the role of the brace is to stabilize the spine during the fusion process. Back orthoses have also been used to treat other spinal diseases where the role of the brace is to replace the lost mechanical function brought on by the disease. Table 1 provides a list of several spinal diseases that exhibit an associated lost mechanical function along with some of the target populations that may be associated with them. Of those populations listed, the first three are currently being treated with stabilizing and shape correcting orthoses. More recently, for those suffering from pinched nerves or disc or spinal cord compression, dynamic back braces have been introduced that claim to axially decompress the spine while restricting motion. However, no supportive experimental or clinical data exist that supports these dynamic devices. *While many current orthoses serve a significant population, un-served populations may include those who require both a reduced spinal load and mobility for therapeutic exercise, independent living, and return to active work.* These unserved populations may include, for example, many who are suffering from disc degeneration, recovering from an injury, limited by weakness, and the elderly with several

degenerative conditions.

The objective was to design a distractive mobility orthosis

(DMO) that mimicked spinal traction and water therapy but did not restrict movement.

**Table 1: Current Capacities of Back Orthoses for Treating Spine Diseases**

Spinal Disease	Lost Mechanical Function	Some Populations	Target	Met/Unmet Needs
Fusion Surgery	Mobility	Injury Elderly	Treated with stabilizing braces.	
Spondylolisthesis / Spinal Stenosis	Translational Stability Axial Stability Axial Support Rotational Stability Positional Integrity	Elderly	Treated with stabilizing braces.	
Scoliosis	Positional Integrity Rotational Stability Axial Stability	Typically treating younger patients who are still growing		Treated with stabilizing and curvature correcting orthoses.
Pinched Nerve / Disc or Cord Compression	Axial stability	Young adult Elderly		Treat with decompression stabilizing orthosis
Weak Elderly	Translational Stability Axial Stability Axial Support Rotational Stability Positional Integrity	Older patients with chronic LBP		<b>UNMET NEEDS:</b> <b>Spinal Decompression</b> <b>Mobility (when mobility is indicated).</b>
Disc Degeneration	Axial Support Axial Stability Rotational Stability	Young often w/injury condition		<b>Spinal Decompression</b> <b>Mobility</b>

## Methods

### ROBOTIC TESTING PLATFORM

A multi-axis robotic testing platform (RTP) was used that provided four programmable degrees of freedom having a positional resolution of  $2\mu\text{m}$  in x,  $0.31\mu\text{m}$  in z, and  $0.0002^\circ$  about y (Figure 1) [14]. The RTP included six-axis load cells mounted to the upper gimbal assembly and to the lower base plate. The upper load cell (ULC), which measured applied forces and moments, had a maximum axial force of 445N and a resolution of 0.2N. The base load cell (BLC) has a maximum axial force of 4,445N and a resolution of 0.73N.

### MECHANICAL ANALOGUE OF HUMAN TORSO

An upper torso, biomimetic lumbar spine, and pelvic girdle assembly (referred to as the human mechanical analogue) were designed to emulate the structural properties of a human torso. The biomimetic lumbar spine consisted of individual spinal components having shape and size comparable to the human lumbar motion segments. The L1-L5 vertebral bodies were cast in rubber molds made from harvested human spines. The individual discs were fabricated based on characteristics from the literature [15] and provided the anterior and posterior heights for each disc. The material for each disc was 30 Durometer urethane (74-30D Urethane from US Composites, 6670 White Drive West Palm Beach, FL 33407). The full L1-L5 lumbar assembly was coated with 30 durometer urethane. The final flexural rotational stiffness over 10deg was 0.66Nm/deg which approximated

cadaveric test data [16].

A life size male mannequin was cut and substantially reinforced internally with carbon fiber and epoxy resin to provide an upper torso frame and separate pelvic girdle assembly for engaging a worn orthosis as it was tested. Multiple layers of a textured material (Kobalt Zerust drawer liner, Zerust Corrosion Products. Twinsburg, OH 44087) were placed around the external surface of the upper torso component that simulated the texture and orthosis-engagement properties of human tissue. The material had a hardness of approximately 30 Durometers Shore A at its thickest section of weave pattern. Each layer was impregnated and externally coated with a thin coating of 30 Durometer Shore A urethane. The biomimetic spine was mounted superiorly to the upper torso frame and inferiorly to the BLC (Figure 2). The BLC was surrounded by but not in contact with the pelvic girdle

assembly. The pelvic girdle assembly, which is shown individually at the bottom of Figure 2, was provided to mount to and engage the lower portion of an orthosis to be tested and was anchored to the base plate of the RTP.

#### ORTHOSIS

The DMO was placed on the mechanical analogue upper torso model that was mounted in the robotic testing platform and collectively used to design unique features of the device (Figure 3): a distractive force component (DFC) and a mobility-enabling component (MEC). The goal of the design features was to provide a distractive lifting force across the lumbar spine while enabling unconstrained flexion and extension motion. A cable pulley array system and flexible graphite rods provided distractive force capabilities (Figure 4A). The MEC consisted of a rail and coaster system (Figure 4B).

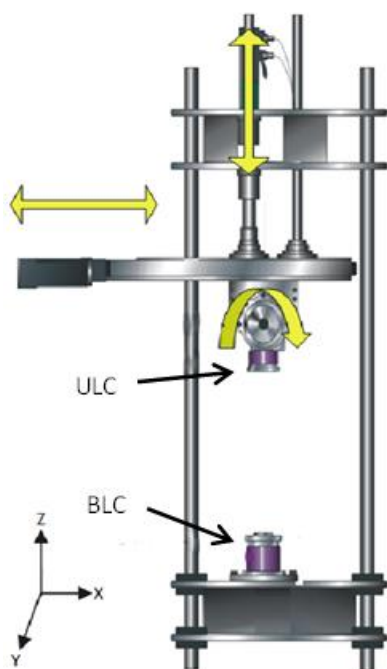


Figure 1: The programmable axes of the RTP.

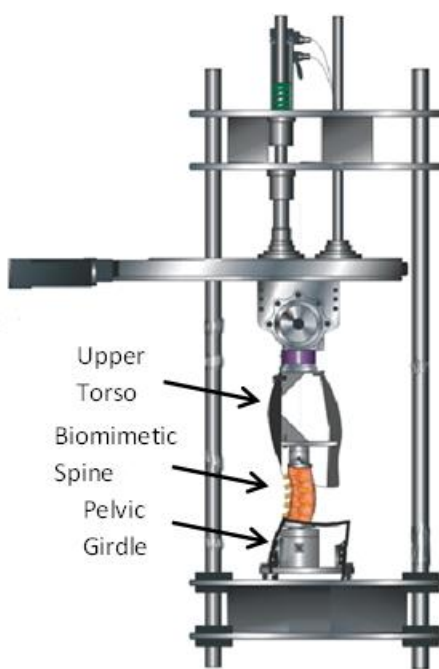


Figure 2. The torso analogue, biomimetic spine and pelvic girdle mounted in the testing platform.

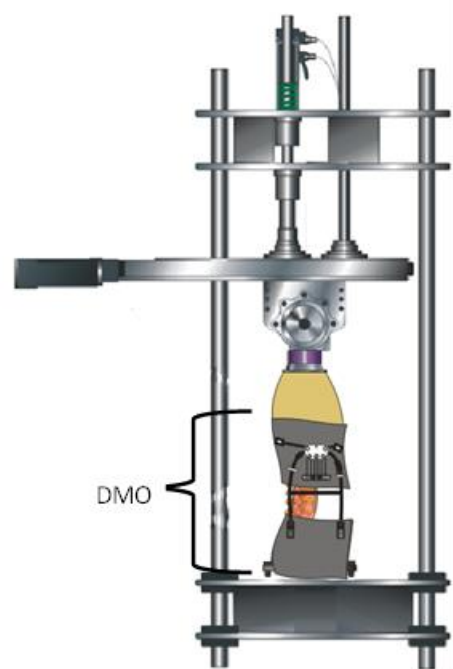


Figure 3. The DMO placed over the mechanical analogue mounted in the RTP.

DFC: The DFC consisted of a pulley cable system that attached to the lower part of the torso glove and a mobile coaster. The coaster was unconstrained and rolled along a rod anchored to the pelvic belt. Tension on the cable caused the cable assembly to pull the coaster against the

rod. As the rod deflected under the coaster's load, the base of the torso glove was pulled up to engage the torso. A band was added mid-level to support the rod and control its bending properties (like the mid supports for column buckling). MEC: The MEC consisted of coaster and rod.

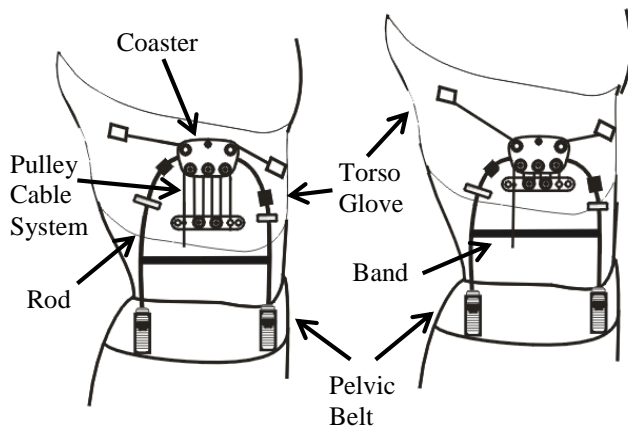
The coaster was unconstrained from the torso glove and rolled freely along the rod to permit flexion and extension.

#### TEST PROTOCOL AND FORCE ANALYSIS

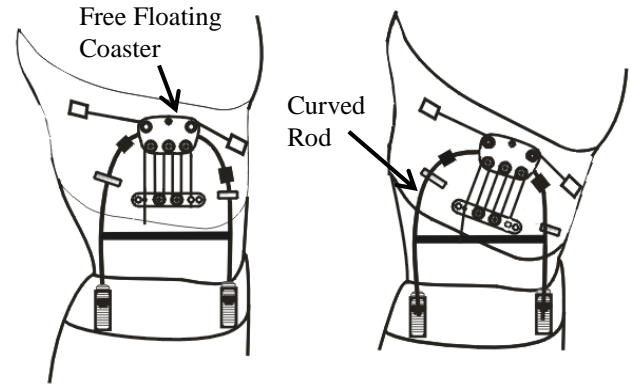
Two test conditions were simulated: upper torso loads up to 300N in upright stance and extended ranges of motion (ROM): flexion (28deg) and extension (10deg) from upright stance. A 300N value simulated the upper body (above the abdomen) weight of a person whose approximate total body weight is 170 pounds based on the upper body comprising approximately 40% of total body weight [17]. For flexion and extension tests, the robot was programmed to rotate the upper torso of the human

analogue around the calculated axis of rotation of the whole lumbar spine and then applied the vertical torso weight loads.

Loads applied to the torso-orthosis assembly were measured at the ULC and the loads transferred through the lower spine were measured at the BLC. The ULC and BLC forces and bending moments (BM) were transformed to the sacral disc plane, SDP (Figure 5A), and compared. With a spinal orthosis mounted (Figure 5B), differences in the two load cell readings transformed to the SDP represented the portion of the applied forces and moments carried by the orthosis. The rotational stiffness of the orthosis was equal to the slope of the brace effect moment – rotation curve.



A) Distributive Force Components (DFC)



B) Mobility-Enabling Components (MEC)

Figure 4. DMO Design Components. A) The DFC used the deformable properties of the rod and a cable pulley system to provide a load input to the torso glove. The rod input load was transferred to the two anchors on the pelvic belt. The pulley system lifted the upper torso at its attachment point on the torso glove. B) The MEC consisted of a free-floating coaster that was tethered to the glove such that it moved as the torso moved. The coaster's wheels rolled along the rod.

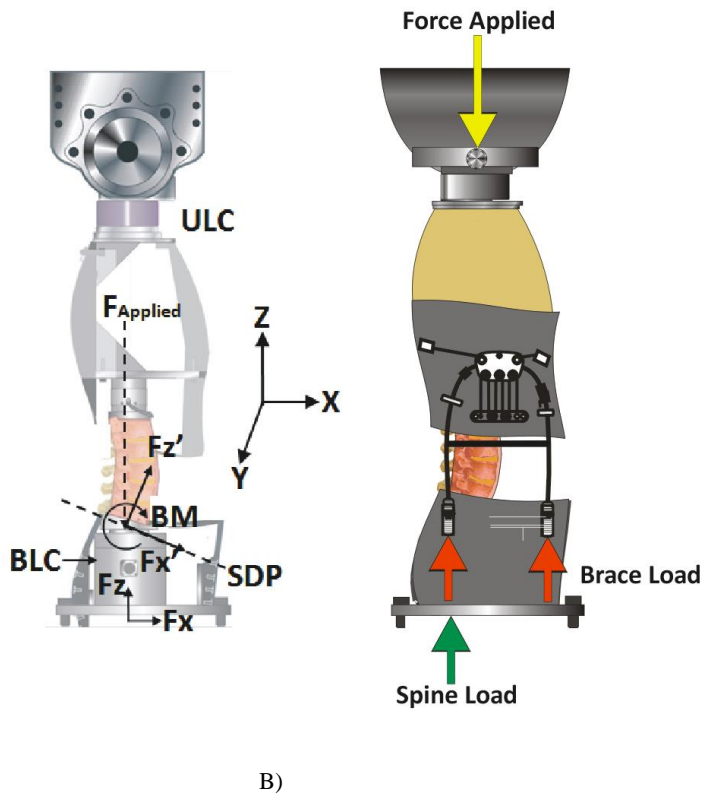


Figure 5. Force Analysis: A) The ULC and BLC forces and bending moments (BM) were transformed to the SDP and compared. B) With Orthosis (brace) Mounted: Brace load was the difference of ULC Force Applied and the BLC-measured Spine Load.

## RESULTS

### LOADING ANALYSIS

The load sharing capacity of the DMO are shown in Figure 6 for the upright orientation, 10deg extension and 28deg flexion. For the 300N applied load condition, the load values carried by the brace and transferred through the spine are listed in Table 2.

### STIFFNESS ANALYSIS

The moment versus angular displacement response of the DMO device is shown in Figure 7 for ranges of 28deg flexion through 10deg extension. The slope of the curves represents the rotational stiffness properties. The flexion brace stiffness value was 0.42Nm/deg and the extension brace stiffness value was 1.01Nm/deg (Figure 7). End range moment-rotation values are provided in Table 3. The flexion and extension moment capacities of DMO at the end range of motion carried 56% and 100% of the applied moment respectively.

Table 2. DMO Load Values During Extended Range-of-Motion Test Under a 300N Load.

Degrees of Rotation	Applied Load (N)	Brace Load (N)	Transferred Load (N)
At 10deg Extension	297	263	34
At 0deg	300	300	0
At 28deg Flexion	267	142	125

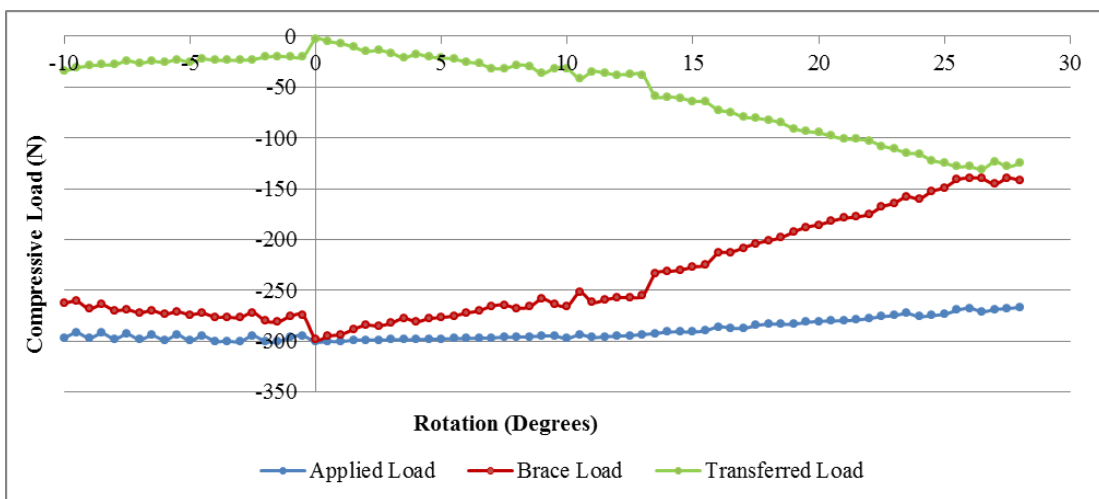


Figure 6. Compressive load versus rotation with the DMO. Positive degrees indicate flexion while negative degrees indicate extension

Table 3. DMO Moment Values During Extended Range-of-Motion Test Under a 300 N Load

Degrees of Rotation	Applied Moment (Nm)	Brace Effect (Nm)	Brace Effect as a Percentage of Applied Moment (%)	Transferred Moment (Nm)	Transferred Moment as a Percentage of Applied Moment (%)
At 10deg Extension	15	15	100 %	0	0 %
At 28deg Flexion	35	19.5	56 %	15.5	44 %

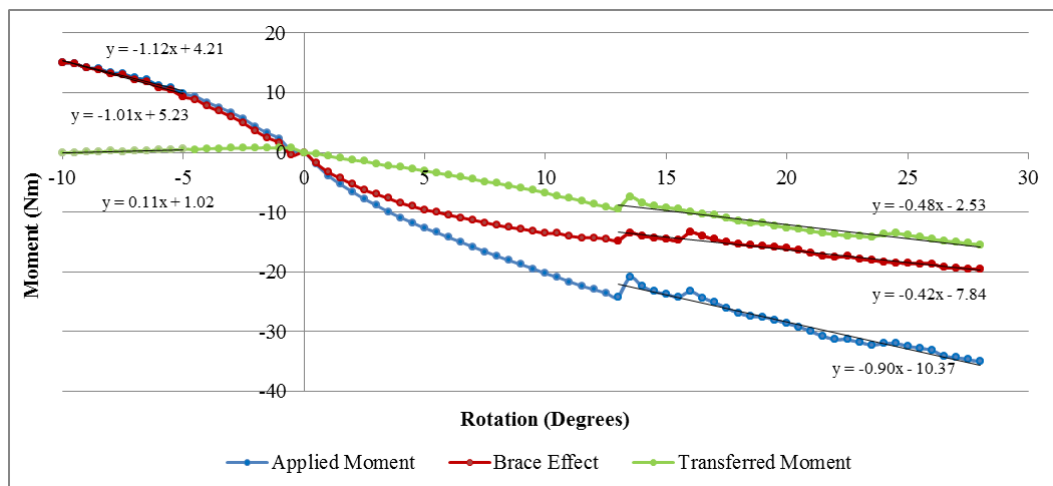


Figure 7. Bending Moment Mechanics of DMO for Extended Ranges of Motion.

## DISCUSSION

The ranges of motion simulated in this study were representative of many daily living activities associated with upright stance posture [18]. Future research plans are to expand the movements to include lateral bending and coupled axial rotation. The testing protocol simulated the force components of the gravitational torso loading mechanics but not the corresponding in vivo spinal bending moment. The resultant applied bending moment was a function of the biomimetic spine's structural properties which were designed to emulate a normal healthy person. Changes to the structural properties of the biomimetic spine are needed to better represent select disease conditions, e.g., lower Durometer material for injured/weaker disc.

The DMO reduced all spinal loading in upright stance and continued off-loading through the extended ranges of flexion and extension. These levels could be adjusted (higher or lower) by changing the rod's stiffness properties. The DMO allowed ranges of motion comparable to many daily living activities.

During extended ranges of movement the brace was able to support 56% of the flexion moment and 100% of the extension moment. These values could be modified by changing the stiffness properties of the control band as well as the material properties and diameter of the support rods. Further, by locating the rotational axis of the DMO coaster and rod assembly near the flexion/extension axis of the biomimetic spine, the applied torso load did not create any additional bending moment minimizing the effort required to move while wearing the DMO device. For flexion of 13.5 degrees and greater, the approximate magnitude of the rotational stiffness of the brace (0.4 Nm/deg) and the mechanical analogue spine (0.5 Nm/deg) were similar. The approximate magnitude of the rotational stiffness of the spine and brace together (labeled in Figure 7 as Applied Moment) was 0.9 Nm/deg. Hence, the brace and biomimetic spine are working effectively together.

## CONCLUSIONS

The combination of the mechanical analogue of a life-size human upper torso and advance testing protocol served as a design tool to create a novel back support orthosis that provided distractive forces across the spine during unconstrained flexion and extension. This testing assembly can also serve as the foundation for new testing methods needed to classify and rank spinal orthoses.

## ACKNOWLEDGMENTS

Maturation grant from the University of Tennessee Research Foundation (UTRF). Clay Hillyard for technical assistance with manuscript preparation. Daniel

Wido for assistance with programming the RTP.

## REFERENCES

- [1] J. M. Fritz and J. A. Cleland. (2008, Jul.). Physical therapy for acute low back pain: associations with subsequent healthcare costs. *Spine*. [Online]. 33(16), 1800-5.
- [2] G. B. Andersson. (2008, Dec.). Surgical Treatment of Spinal Stenosis with and without Degenerative Spondylolisthesis: Cost-Effectiveness after 2 Years. *Annals of Internal Medicine*. [Online]. 149(12), 845-53.
- [3] (2006, May 15). *Patient-Operated Spinal Unloading Devices* (2) [Online]. Available: [https://my.cigna.com/teamsite/health/provider/medical/procedural/coverage\\_positions/medical/mm\\_0346\\_coveragepositioncriteria\\_patient\\_operated\\_spinal\\_unloading\\_devices.pdf](https://my.cigna.com/teamsite/health/provider/medical/procedural/coverage_positions/medical/mm_0346_coveragepositioncriteria_patient_operated_spinal_unloading_devices.pdf)
- [4] D. Akay and M. D. Toksari. (2008, Nov.). Ant colony optimization approach for classification of occupational low back disorder risks. *Human Factors and Ergonomics in Manufacturing*. [Online]. 19(1), 1-14.
- [5] L. S. Brecher. (2001, Apr.4). Editor's Message. *JAOA*. [Online]. 101(4). Available: [http://www.jaoa.osteopathic.org/content/101/4\\_suppl\\_2/1S.full.pdf](http://www.jaoa.osteopathic.org/content/101/4_suppl_2/1S.full.pdf)
- [6] P. Pensri and P. Janwantanakul. (2010, Dec.). Biopsychosocial factors and perceived disability in saleswomen with concurrent low back pain. *Saf Health Work*. [Online]. 1(2), 149-57.
- [7] Andersson, G.B.J. (1999). Epidemiological features of chronic low-back pain. *Lancet*. [Online]. 354(9178), 581-5.
- [8] R. A. Deyo and J. N. Weinstein. (2001, Feb.). Low Back Pain. *N Engl J Med*. [Online]. 344(5), 363-70.
- [9] S. Bigos, Bowyer O, Braen G. Acute low back problems in adults. Clinical practice guideline Number 14. AHCPR Pub. No. 95-0642. Rockville: U.S. Department of Health and Human Services, Public Health Service, Agency for Health Care Policy and Research; 1994. Report No.:AHCPR Publication no. 95-0642.
- [10] L. D. Herron, J. A. Turner and L.A. Novell (1996, Apr.). Patient selection for lumbar laminectomy and discectomy with a revised objective rating system. *Clin Orthop Relat Res*. [Online]. (325), 148-55.
- [11] P. A. Baena-Beato and M. Arroyo-Morales. (2013, Jan.). Effects of different frequencies (2-3

- days/week) of aquatic therapy program in adults with chronic low back pain. A non-randomized comparison trial. *Pain Med.* [Online]. 14(1), 145-58.
- [12] A. I. Cuesta-Vargas, N. Adams and J. A. Salazar. (2012, Jul.). Deep water running and general practice in primary care for non-specific low back pain versus general practice alone: randomized controlled trial. *Clin Rheumatol.* [Online]. 31(7), 1073-8.
- [13] U. Dundar, O. Solak and D. Evcik. (2009, Jun.). Clinical effectiveness of aquatic exercise to treat chronic low back pain: a randomized controlled trial. *Spine.* [Online]. 34(14), 1436-40.
- [14] B. P. Kelly and D. J. DiAngelo. (2013, Jul.). A Multiaxis Programmable Robot for the Study of Multibody Spine Biomechanics Using a Real-Time Trajectory Path Modification Force and Displacement Control Strategy. *J. Med Devices.* [Online]. 7(3). Available: <http://dx.doi.org/10.1115/1.4024645>
- [15] I. Gilad and M. Nissan. (1986, Mar.). A study of vertebrae and disc geometric relations of the human cervical and lumbar spine. *Spine.* [Online]. 11(2), 154-7.
- [16] J. R. Stubbs, "Use of a multi-axis robotic testing platform to investigate the sagittal mechanics of the multi-body lumbar spine," M.S. Thesis, Dept. of Orthopaedic Surgery and Biomedical Eng., Univ. of Tennessee Health Science Center, Memphis, TN, 2014.
- [17] D. A. Winter. *Biomechanics of Human Movement.* John Wiley & Sons Inc, 1979.
- [18] J. E. Bible. (2010, Apr.). Normal functional range of motion of the lumbar spine during 15 activities of daily living. *J Spinal Disord Tech.* [Online]. 23(2), 106-12.

# DIFFERENTIAL DIAGNOSIS OF SLEEP DISORDERS BASED ON EEG ANALYSIS

**Sai Mohan Rudrashetty, Ashmit Pyakurel, Bharat Karumuri, Rui Liu, Ioannis Vlachos, Leonidas Iasemidis**

Biomedical Engineering,  
Louisiana Tech University, Ruston, LA

## ABSTRACT

In this study we test the hypothesis that four sleep disorders, the periodic limb movement behavioral disorder (PLMBD), rapid eye movement behavior disorder (REMBD), insomnia, and nocturnal frontal lobe epilepsy (NFLE), can be differentiated from one another and from the healthy condition through analysis of the sleep electroencephalogram (EEG). Frequency (median frequency and spectral entropy) and complexity (Higuchi fractal dimension) measures of the EEG signal were estimated over time and used to extract features related to the different sleep stages and the sleep-specific activity of the Cyclic Alternating Pattern (CAP) (EEG data from the Physionet database). Analysis of Variance (ANOVA) of the extracted features was used to compare the five groups: PLMBD (10 subjects), REMBD (22 subjects), NFLE (37 subjects), insomnia (9 subjects) and healthy (11 subjects). ANOVA revealed significant differences ( $\alpha=0.05$ ) between some but not all of the groups. Subsequent multivariate analysis of variance (MANOVA) revealed that all five groups could be differentiated ( $p<0.05$ ) with the use of the top 5 ranked features obtained from a feature selection procedure (mRMR). These results indicate that proper EEG-based analysis of sleep, even from a single EEG channel, may assist in the differential diagnosis of sleep disorders, and thus their treatment.

**Keywords:** EEG, sleep stages, CAP, differential diagnosis PLMBD, REMBD, NFLE, insomnia.

## INTRODUCTION

Sleep is a quotidian cycle of repeatable sequence of sleep stages over several hours [1, 2]. A healthy sleep cycle is associated with good performance of normal activities during the awake state, such as concentration, learning and memory recollection [3]. About 12.7% of the US population suffer from some form of chronic sleep disorder that may lead to adverse health conditions, such as rise in risk of hypertension and obesity, decrease in the efficacy of immune system, kidney disease, anemia, diabetes, Parkinson's and heart problems [4].

There are two basic states of sleep, non-rapid eye movement (NREM) and rapid-eye movement (REM) sleep, with NREM constituting approximately 75% and REM 25% of a healthy night's sleep. NREM sleep state is further divided into three stages with stage 1 corresponding to a state between wakefulness and sleep, stage 2 where awareness of the outside world begins to fade completely and stage 3 being deep sleep. During NREM stages a sleep specific activity called Cyclic Alternating Pattern (CAP) occurs. CAP is a quasi-periodic EEG activity characterized by cyclic sequences of cerebral activation (phase A; about 8-15 seconds) followed by periods of deactivation (phase B; about 15-20 seconds) [5-7]. Based on occurrence of high voltage slow waves (EEG synchrony) or low-amplitude fast rhythms (EEG desynchrony) [7], CAP-A phase is divided into three subtypes: A1, A2 and A3.

Common types of sleep disorders are parasomnias (periodic limb movement disorder-PLMD, rapid eye movement behavior disorder-REMBD), nocturnal frontal lobe epilepsy-NFLE, and insomnia. In PLMD, involuntarily movement of limbs is observed at periodic intervals of 20-40 seconds in duration [8]. In REMBD, abnormal behavior is observed during the REM stage of sleep, where movement of limbs (kicking, grabbing, or jumping etc.) occurs while the patient unconsciously acts out his dreams. In NFLE, epileptic seizures emanate from the frontal lobes of the brain during sleep, caused by tumors, head trauma or has a genetic base that causes abrasions in the frontal lobes [7]. Insomnia, also called sleeplessness, is when the patient is either unable to fall asleep or has difficulty in sleeping long enough [10].

These sleep disorders are diagnosed by physicians after visual inspection of the patients' sleep patterns from their recorded EEG. This requires an extensive amount of experience and observation time, and is thus a costly and lengthy process [11]. A quantitative and accurate evaluation of sleep EEG can play an important role in the fast and accurate diagnosis of sleep disorders and therefore help provide the necessary treatment with reduced time and cost.

## MATERIALS AND METHODS

### Data:

In this study, we used polysomnographic (PSG) recordings from the CAP sleep database – PhysioNet [5, 6] recorded at the Sleep Disorders Center of the Ospedale Maggiore of Parma, Italy. The database includes EEG, EMG, EOG, EKG and respiration waveforms from subjects with clinical history of various sleep disorders, as well as from healthy individuals. Recordings from 22 subjects with REMBD, 10 with PLMBD, 37 with NFLE, and 9 with insomnia were included in our analysis. Data from 15 healthy subjects were also included. The data are accompanied by a hypnogram, a temporal profile of the sleep stages scored by an expert neurologist every 30 seconds of recording. We analyzed sleep records based on extraction of features from: a) EEG activity during the different sleep stages, b) CAP activity and c) EEG during CAP activity.

### Feature Extraction:

Measures were estimated per nonoverlapping 30 second EEG data segments over the entirety of each subject's recording in order to correspond with the subject's hypnogram. Channel C4-A1 was selected for analysis in most of the subjects. For some subjects where C4-A1 channel was not present, C3-A2 channel was used instead. The EEG was down-sampled to a common sampling frequency of 100Hz. Advanced signal processing techniques were employed to extract quantitative biomarkers relevant to the different sleep stages and CAP phases. Measures used in the analysis of EEG were frequency (median frequency and spectral entropy) and signal complexity (Higuchi fractal dimension) dependent.

Median frequency [1] is defined as the frequency below which 50% of the total EEG spectral power is located and

is given by

$$mf_{50} = \min\{f \mid \sum_{i=0}^f P(i) > 0.5 * P_{50 \text{ Hz}}\} \quad (1)$$

where  $P_{50 \text{ Hz}}$  is the total power of the EEG signal within the frequency range of 0 to 50 Hz. From the median frequency values we estimated the median period  $mp = 1/mf_{50}$ .

Spectral entropy (SE) measures the irregularity of the EEG signal in the frequency domain. SE is estimated by Shannon's entropy [12] as

$$SE = \frac{\sum_{i=1}^N p_i \log(p_i)}{\log(N)} \quad (2)$$

where  $p_i$  are the normalized spectral magnitudes  $P(i)$  at frequencies  $i$  and  $N$  is the number of discrete frequencies in the spectrum.

Higuchi fractal dimension (HFD) measures the complexity and self-similarity of a signal [1, 12] in the time domain. A self-similar signal would have HFD equal to 2, while a simple signal with no self-similarity (e.g. a simple sinus wave) would have HFD equal to 1. Susmakova and Kravovska used the Higuchi fractal dimension to distinguish individual stages of sleep, specifically stage 3 sleep from other sleep stages [14].

**Figure 1** shows the characteristic trends of  $mp$ , SE and Higuchi fractal dimension (HFD) from the beginning to the end of a sleep record from a healthy subject along with his hypnogram.

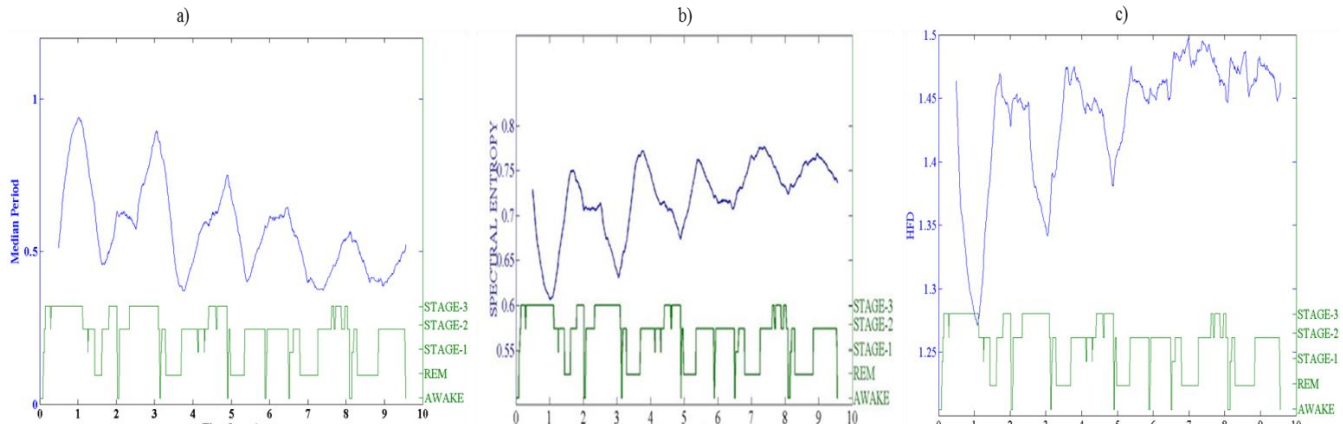


**Figure 1.** Sleep record from a healthy subject and the estimated EEG measures (blue lines) and hypnogram (green line). (a) Median Period, (b) Spectral Entropy and (c) Higuchi fractal dimension values against the corresponding hypnogram.

Sleep stage-based features were extracted using the values of the above measures. Normalization to compensate for across subject variability was performed as follows. The mean ( $\mu(\star)_{s_n}$ ) and standard deviation ( $\sigma(\star)_{s_n}$ ) of each measure ( $\star$ ) values were computed for each sleep stage  $s_n$  separately, where  $n = 0$  stands for the awake state,  $n = i$  for sleep stages ( $i = 1, 2, 3$  and  $n = 4$  for REM). The normalized features were then estimated as [12]

$$n \star_{s_n} = \frac{\text{abs}(\mu(\star)_{s_0} - \mu(\star)_{s_n})}{\sigma(\star)_{s_0} + \sigma(\star)_{s_n}}. \quad (3)$$

Thus, 12 features (candidate quantitative biomarkers), four from each of the three measures ( $nmp_{s_n}$ ,  $nSE_{s_n}$ ,  $nHFD_{s_n}$  with  $n = 1, 2, 3, 4$ ) were obtained.

In addition to the above 12 sleep stage-based features, features based on the cyclic alternating pattern (CAP) in the EEG were also extracted. These CAP-features were categorized according to the various CAP subtypes ( $CAP_{A(1)}$  to  $CAP_{A(3)}$ ), the total number of CAP cycles during sleep and time intervals related to CAP activity. The CAP features were defined as in [15]:  $CAP$  rate (the ratio of CAP time to NREM sleep time);  $CAP_{A(i)}/CAP$  (the percentage of  $CAP_{A(i)}$  subtype in the total CAP time, for  $i = 1, 2, 3$ );  $CAP_{A(i)}/TST$  (the percentage of  $CAP_{A(i)}$  in the total sleep time TST);  $CAP_{A(i)}/NREM$  (the percentage of  $CAP_{A(i)}$  in the total NREM time) and  $dCAP_{A(i)}$  (average duration of CAP subtypes, i.e. total duration of  $CAP_{A(i)}$  subtype divided by the number of  $CAP_{A(i)}$  cycles, for  $i = 1, 2, 3$ ). Similarly, for CAP A phases:  $CAP_{A/CAP}$  (the percentage of CAP A phase in the total CAP time);

$CAP_{A/TST}$  (the percentage of CAP A phase in the total sleep time);  $CAP_{A/NREM}$  (the percentage of CAP A phase in the total NREM time); and  $dCAP_A$  (average duration of CAP A phases). A total of 17 traditional CAP based features were thus obtained.

Finally, the median period, Higuchi fractal dimension and the spectral entropy were also estimated for the CAP phases. Each measure was estimated for each CAP A phase and its ensuing CAP B phase, the ratios of the measure values were then estimated and averaged across all CAP cycles. These are denoted as median period of CAP phase ( $CAP_{mp}$ ), Higuchi fractal dimension of CAP phase ( $CAP_{HFD}$ ) and spectral entropy of CAP phase ( $CAP_{SE}$ ). So a total of 32 features were estimated from the EEG recordings: sleep stage-based (12 features), CAP-based measures (17 features) and CAP/EEG based measures (3 features).

#### Statistical Analysis:

Statistical testing was performed using Analysis of Variance (ANOVA) [16] and Multivariate Analysis of Variance (MANOVA) to test for statistically significant difference between the 5 groups of subjects on the basis of combined features. In order to rank and combine features, feature selection was done to select the top ten best features with the minimum Redundancy Maximum Relevance (mRMR) procedure [17]. mRMR is a sequential process that gives the set of the most relevant features that can be used for differentiating between groups of subjects.

**Figure 2** shows the steps involved in our analysis, from data selection, feature extraction and statistical analysis to differentiating between groups.

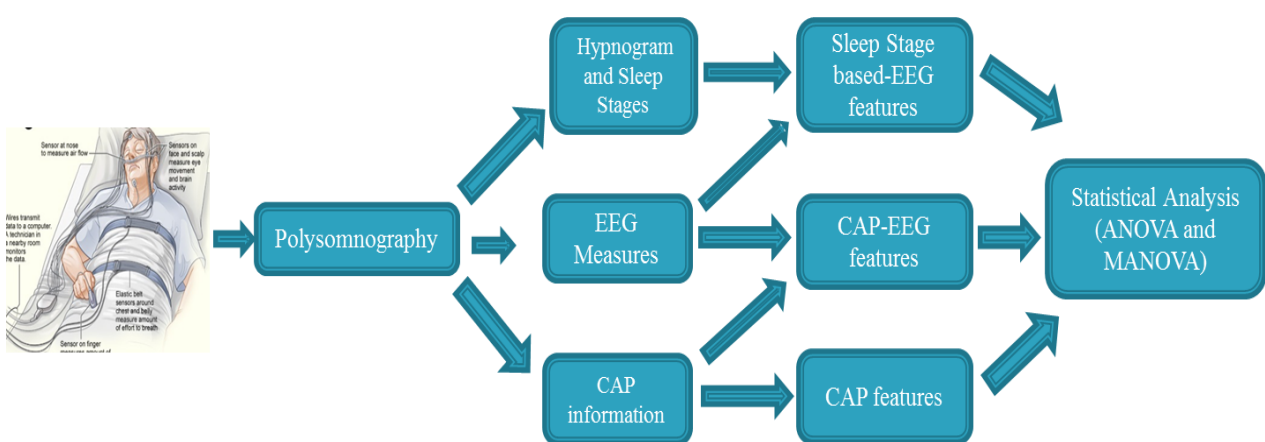


**Figure 2.** Flow chart depicting the steps of our analysis.

## RESULTS

With five subject groups, ten pairs of comparisons can be performed (e.g. normal vs PLMBD, normal vs. NFLE, etc). When ANOVA test was performed for the sleep stage-based and CAP-based features individually, we were able to find statistically significant differences in a maximum of six out of the ten group pairs (e.g.  $CAP_{A(3)}/CAP$  feature).

After performing the mRMR procedure we were able to rank the features with respect to different subject groups (see **Table 1**). When the highest ranked feature of Higuchi fractal dimension of total CAP cycle ( $CAP_{HFD}$  in Table 1) was used in ANOVA, we see from **Figure 3** that the insomnia group was statistically significant different

from all other groups (p-value < 0.001). Using this feature, four out of the ten pairs of groups are statistically significant.

When MANOVA test was performed with increasing number of features (i.e., using the first feature only, then the first and second, etc.), we were able to see statistically significant differences between all five groups (all ten out of the ten group pairs). As the number of features increases, we see that the performance is reduced, most probably due to the small sample size in some of the patient groups.

**Table 1.** Effect of increasing the number of features (up to top ten features) on the number of statistically significant different group pairs.

Number	Top 10 CAP and sleep stage-based features	MANOVA P values	No. of statistically significant different pairs
1.	$CAP_{HFD}$	$5.825 * 10^{-9}$	4
2.	$CAP \text{ rate}$	$1.74 * 10^{-11}$	6
3.	$CAP_{A(3)}/CAP$	$7.9 * 10^{-16}$	8
4.	$nHFD_{S_4}$	$2.0308 * 10^{-18}$	9
5.	$CAP_{A/CAP}$	$1.8 * 10^{-18}$	10
6.	$nHFD_{S_1}$	$2.13 * 10^{-17}$	10
7.	$CAP_{A/TST}$	$2.107 * 10^{-16}$	9
8.	$dCAP_{A(2)}$	$4.34 * 10^{-18}$	9
9.	$nSE_{S4}$	$4.79 * 10^{-17}$	9
10.	$CAP_{SE}$	$2.87 * 10^{-18}$	9

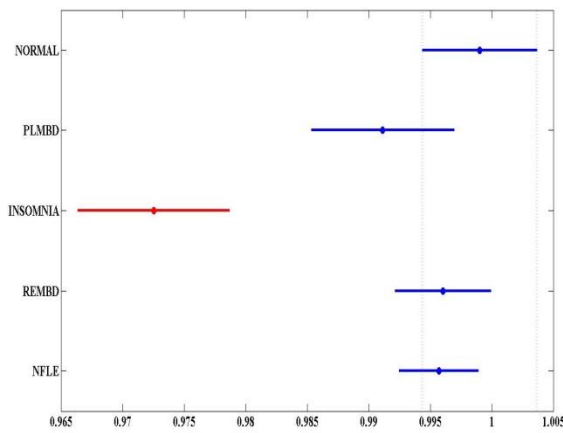


**Figure 3.** ANOVA for the five groups of subjects based on the CAP-EEG measure of Higuchi Fractal dimension- $CAP_{HFD}$ . Statistical significant difference was observed only between the Insomnia group and the other 4 groups. The p-value in this case was  $5.825 * 10^{-9}$ . The other 4 groups were not statistically significant different from each other.

Group scatter plots using the first two canonical variables obtained from Canonical Analysis for the combinations of first five features from Table 1 are shown in **Figure 4**. Five clusters with statistically distinct specific centers ( $p\text{-value} < 0.001$  – not fully visible in the 2D representation). The features set contained nonlinear features extracted from CAP activity of the EEG signal (i.e. Higuchi of total CAP cycle-  $CAP_{HFD}$ ) as well as non-linear features from the sleep-stages (i.e. Higuchi dimension of REM stage, and sleep stage 1 -  $nHFD_{S4}$  and  $nHFD_{S1}$ ) along with the more traditional CAP features (i.e.  $CAP$  rate and  $CAP_{A(3)}/CAP$ ).

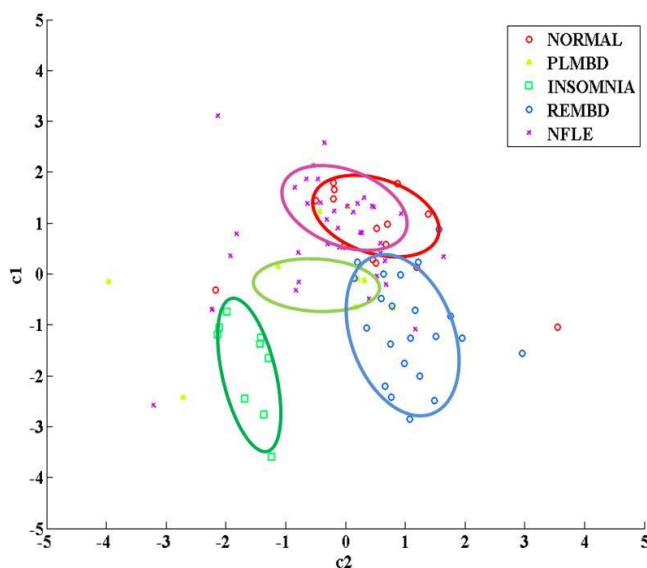


**Figure 4.** Group differentiation using the first two canonical vectors of features obtained from Canonical Analysis

(five best features from Table 1).

## DISCUSSION AND CONCLUSIONS

Our single EEG channel-based quantitative approach investigated the possibility to differentiate between four sleep disorders as well as against the healthy condition, based on features relevant to specific characteristics of the EEG, in particular frequency content (median frequency and spectral entropy) and signal complexity (Higuchi fractal dimension), and to specific sleep-related patterns (sleep stages, CAP). In total thirty-two features (candidate quantitative biomarkers) were obtained from PSG records of 93 subjects. To differentiate between the five groups of subjects, ANOVA and MANOVA tests were performed. Univariate analysis showed that only some of the groups were statistically significant different from the other groups. Multivariate analysis that included sleep and CAP-based biomarkers revealed that all five groups of subjects can be differentiated using the combination of five features, that is,  $CAP_{HFD}$ ,  $CAP$  rate,  $CAP_{A(3)}/CAP$ ,  $nHFD_4$  and  $CAP_{A/CAP}$ . In conclusion, combination of sleep stage and CAP features properly extracted from a single scalp EEG channel can be employed to construct novel quantitative and very effective biomarkers for non-invasive differential diagnosis of sleep disorders. Further analysis with incorporation of machine learning techniques could improve the classification of subjects to a specific sleep condition (disorder or healthy).

## REFERENCES

- [1] B. Koley, D. Dey, An ensemble system for automatic sleep stage classification using single channel EEG signal. *Computational Biology and Medicine*, **1**, 2012, 1186-95.

- [2] W.J. Randerath, B.M. Sanner, V.K. Somers, Sleep Apnea Current Diagnosis and Treatment. Rochester, MN, *Karger Science and medical Publishers*, **35**, 2006.
- [3] D.P. White, Sleep apnea, *Proceedings of the American Thoracic Society*, **3**, 2006, 124–128.
- [4] T. Young, P.E. Peppard, D.G. Gottlieb, Epidemiology of obstructive sleep apnea, a population health perspective, *American Journal Respiratory Critical Care Medicine*, **165**, 2002, 1217–1239.
- [5] M.G. Terzano, L. Parrino, A. Sherieri, R. Chervin, S. Chokroverty, C. Guilleminault, M. Hirshkowitz, M. Mahowald, H. Moldofsky, A. Rosa, R. Thomas, A. Walters. Atlas, rules, and recording techniques for the scoring of cyclic alternating pattern (CAP) in human sleep. *Sleep Medicine*, **2**, 2001, 537-553.
- [6] A.L. Goldberger, L.A.N. Amaral, L. Glass, J.M. Hausdorff, P.Ch. Ivanov, R.G. Mark, J.E. Mietus, G.B. Moody, C.K. Peng, H.E. Stanley. PhysioBank, PhysioToolkit, and PhysioNet: Components of a New Research Resource for Complex Physiologic Signals. *Circulation* **101**(23):e215-e220 [Circulation Electronic Pages; <http://circ.ahajournals.org/cgi/content/full/101/23/e215>; **13**, 2000.
- [7] L. Parrino, F.D. Paolis, G. Milioli,G. Gioi,A. Grassi,S. Riccardi,E. Colizzi, and M.G. Terzano, “Distinctive polysomnographic traits in nocturnal frontal lobe epilepsy,” *Epilepsia*, **53**, 2012, 1178–1184.
- [8] L. Parrino, M. Boselli, G. P. Buccino, M. C. Spaggiari, G. Di Giovanni, and M. G. Terzano, “The cyclic alternating pattern plays a gate-control on periodic limb movements during non-rapid eye movement sleep,” *Journal of Clinical Neurophysiology. Off. Publication American Electroencephalography Society*, **13**, 1996, 314–323.
- [9] B. F. Boeve, “REM sleep behavior disorder: Updated review of the core features, the REM sleep behavior disorder-neurodegenerative disease association, evolving concepts, controversies, and future directions,” *Annals of the New York Academy of Science*, **1184**, 2010, 15–54.
- [10] T. Roth. ["Insomnia: Definition, prevalence, etiology, and consequences"](#). *Journal of clinical sleep medicine: JCSM: official publication of the American Academy of Sleep Medicine*, **3**,2007, S7–10.
- [11] N. V. Thakor, “Quantitative EEG Analysis Methods and Clinical Applications”. *Artech House Publishers*-2009.
- [12] J. Fell, J. Roschke, K. Mann, C. Schaffner,” Discrimination of sleep stages: a comparison between spectral and nonlinear EEG measures,” *Electroencephalography and Clinical Neurophysiology*, **98**, 1996, 401–410.
- [13] C. Gómez, A. Mediavilla, R. Hornero, D. Abásolo, and A. Fernández, “Use of the Higuchi’s fractal dimension for the analysis of MEG recordings from Alzheimer’s disease patients,” *Medical Engineering and Physics*, **31**, 2009, 306–313.
- [14] K. Susmakova, A. Krakovska, “Discrimination ability of individual measures used in sleep stages classification,” *Artificial Intelligence in Medicine*, **44**, 2008, 261–277.
- [15] L. Parrino, F.D. Paolis, G. Milioli,G. Gioi,A. Grassi,S. Riccardi,E. Colizzi, and M.G. Terzano, “Distinctive polysomnographic traits in nocturnal frontal lobe epilepsy,” *Epilepsia*, **53**, 2012, 1178–1184
- [16] H. J. Keselman, Carl J. Huberty, Lisa M. Lix, Stephen Olejnik, Robert A. Cribbie, arbbara Donahue, Rhonda K. Kowalchuk, Laureen L. Lowman, Martha D. Petoskey, Joanne C. Keselman and Joel R. Levin, “Statistical Practices of Educational Researchers: An Analysis of Their ANOVA, MANOVA, and ANCOVA Analyses,” *Review Of Educational Research*, 1998, 350-386.
- [17] H.C. Peng, F. Long and C. Ding, "Feature selection based on mutual information: criteria of max-dependency, max-relevance, and min-redundancy". *IEEE Transactions on Pattern Analysis and Machine Intelligence*, **27**, 2005, 1226-1238. doi:10.1109/TPAMI.2005.159. PMID 16119262.

## SPATIOTEMPORAL DYNAMICS OF INTERICTAL SPIKES

**Balu Krishnan\***, **Ioannis Vlachos<sup>#</sup>**, **Aaron Faith<sup>^</sup>**, **Stephen Mullane<sup>+</sup>**, **Korwyn Williams<sup>~</sup>**,  
**Leonidas Iasemidis<sup>#</sup>**

Cleveland Clinic Foundation\*, Cleveland, OH; Louisiana Tech University<sup>#</sup>, Ruston, LA; Phoenix Children's Hospital~, Phoenix, AZ; Arizona State University<sup>^</sup>, Tempe, AZ; Biotronik<sup>+</sup>, Lake Oswego, OR.

### ABSTRACT

The relationship of epileptic spikes to seizures has been a matter of debate with researchers reporting higher or lower spike rates before and after seizures. To elucidate a possible role of spikes in ictogenesis (seizure generation) we developed a mathematical framework to investigate the spatiotemporal dynamics of spikes in the epileptic brain. Long-term (5-10 days) intracranial electroencephalograms (iEEGs) from 2 patients with temporal lobe epilepsy who underwent presurgical evaluation for localization of candidate epileptic foci were used in the study. First, spikes were detected using an in-house spike detection algorithm. To characterize the spatiotemporal changes in spikes a novel spatial synchronization measure (SSM) of spikes was developed. Application of SSM to iEEG revealed monotonically increasing long-term preictal synchronization between spike trains at brain sites that included the epileptogenic zone. The presence of preictal synchronization of spikes hours to minutes prior to the onset of seizures indicates a possible predictive value of spike synchronization for seizure occurrence. Furthermore, across seizures and patients, we observed that desynchronization of spikes at critical brain sites mostly occurred in postictal epochs. We characterized these observed changes between preictal and postictal spike synchronization by a measure of resetting based on the fraction of pairs that synchronize preictally and desynchronize postictally. On the basis of this resetting measure, we showed that resetting of spike synchronization occurs more commonly at seizures than interictally ( $p < 0.05$ ). These results are in agreement with our previously postulated hypothesis that seizures occur to reset a pathologically established preictal hypersynchrony of EEG dynamics among critical brain sites.

**Keywords:** Epilepsy, Spikes, Seizures, Spatiotemporal Analysis, Ictogenesis

### INTRODUCTION

Epilepsy is a widely prevalent neurological disorder affecting around 50 million people worldwide and has been classified as the third most common neurological disorder next to stroke and Alzheimer's. There are two distinct neuronal hallmarks that characterize epilepsy: epileptic seizures and epileptic spikes. Epileptic spikes are high amplitude ( $>50 \mu\text{V}$ ) fast electrographic activity, sometimes followed by a slow wave, and last for only a couple of hundreds of milliseconds when recorded at the brain surface (e.g. via scalp electroencephalography - scalp EEG). Although spikes have been recognized as a diagnostic tool for epilepsy, the cause of their occurrence is still unknown. Spiking may occur interictally, preictally (before seizures) and postictally (after seizures), and the neural networks generating seizures and spikes may be different from each other. A quantitative analysis of spiking in patients with temporal lobe epilepsy by Lieb et al [1] has revealed that the epileptogenic focus (the region of the brain that triggers a seizure) generates spikes at maximum mean spiking rate and minimum coefficient of variation, and minimum variance in inter-spike intervals. The study suggested that spikes can be used as biomarkers for identification of the epileptogenic focus. Also, spatiotemporal changes in preictal spike activity in human temporal lobe epilepsy [2] revealed that the degree of bilateral interdependence in medial temporal lobe spike activity increased prior to onset of a seizure, thus indicating

that spikes may herald the interictal to ictal transition. Contrary to the notion that epileptic spikes are precursors to seizures, postictal increase in spike rate in human focal epilepsy was reported independently by Gotman [3] and Katz et al. [4]. Most of the studies relating epileptic spikes and seizures have been quantitative in nature but limited to analysis of either spike rate or spike location. Herein we investigate the spatiotemporal evolution of epileptic spikes themselves and its predictive value for an impending seizure.

### METHODS

#### Spike Synchronization Measure (SSM)

SSM is a normalized measure of spike synchrony that is parameter-free, time-scale adaptive and sensitive to both spike rate and the number of coincident spikes [5]. The measure is computationally fast and relies on the differences between spike times in two spike trains under consideration and their interspike intervals. Consider two point process  $x$  and  $y$  containing  $M_x$  and  $M_y$  spikes respectively. Let  $t_i^x$  and  $t_j^y$  denote the occurrence times of spikes in process  $x$  and  $y$  respectively. Let  $t_x = \{t_1^x, t_2^x, \dots, t_{M_x}^x\}$  and  $t_y = \{t_1^y, t_2^y, \dots, t_{M_y}^y\}$  be the time series containing the spike times of  $x$  and  $y$  respectively. We define  $e^i(x|y)$  for spike  $i$  in process  $x$  as

$$e^i(x|y) = 0.5 \exp\left(-\frac{d_i^{x,\min}}{(t_{i+1}^x - t_i^x)}\right) \quad i \in [1, 2, \dots, M_x]$$

Where  $d_i^{x,\min} = \min(t_j^y - t_i^x)$  for  $j \in [1, 2, \dots, M_y]$ , that is, the difference in spike time  $t_i^x$  of process  $x$  from the time of the next occurring spike in process  $y$ . Similarly we estimate  $e^i(y|x)$  for spike  $i$  in process  $y$ . Now we combine  $e(x|y)$  and  $e(y|x)$  in one symmetric measure as

$$Q = \frac{\sum_{i=1}^{Mx-1} e^i(x|y) + \sum_{i=1}^{My-1} e^i(y|x)}{\sqrt{(M_x - 1)(M_y - 1)}}$$

The SSM measure  $Q$  takes values in  $[0, 1]$ , with 0 when spike trains are desynchronized and 1 when there is perfect coincidence of spikes. By using the interspike interval  $t_{i+1}^x - t_i^x$  of the point process under consideration in the exponential decay function, we normalize SSM with

respect to the firing rate of the process making it robust to dynamical changes of spike rate. (1)

## RESULTS

Long-term (days) continuous intracranial EEG recordings from two patients, who underwent presurgical evaluation for localization of their epileptogenic focus at the epilepsy monitoring unit (EMU) of Shands Hospital in Gainesville, Florida, were analyzed (see **Table 1**). Informed consent for participation in this study was obtained from the patients. The EEG was recorded by a Nicolet BMSI 4000 EEG machine at sampling rate of 200 Hz and with an average common reference and band-pass analog filter settings of 0.1 Hz -70 Hz. Depth electrodes were placed in the right and left hippocampi, two subdural strips were placed at right and left orbitofrontal lobes, and two subdural strips were placed at right and left subtemporal lobes.

**Table 1:** Patient and EEG Data Characteristics

Patient ID	# of electrodes	Recording Duration	# of Seizures		Focus (clinical assessment)
			Sub-clinical	Clinical	
P1	28	143.4 Hrs	10	9	Right Anterior Mesial Temporal
P2	28	322.8 Hrs	7	10	Right Temporal

Per electrode site, epileptic spikes were detected for the entire duration of the EEG recordings using improved morphological filtering with adaptive structure elements as described in [5]. The SSM measure of spike synchronization was estimated for each patient from successive EEG segments of 30.72 seconds duration and overlapped by 10.24 seconds per pair of electrodes for the whole EEG recording. **Figure 1** shows the average

synchronization profile across all pairs of electrodes and across all seizures for the two patients. For both patients, increased synchronization in the preictal and desynchronization in the postictal periods can be observed. These results are similar to our previous synchronization studies where we observed preictal synchronization and postictal desynchronization between pairs of electrodes in terms of their Lyapunov exponents [6-7].

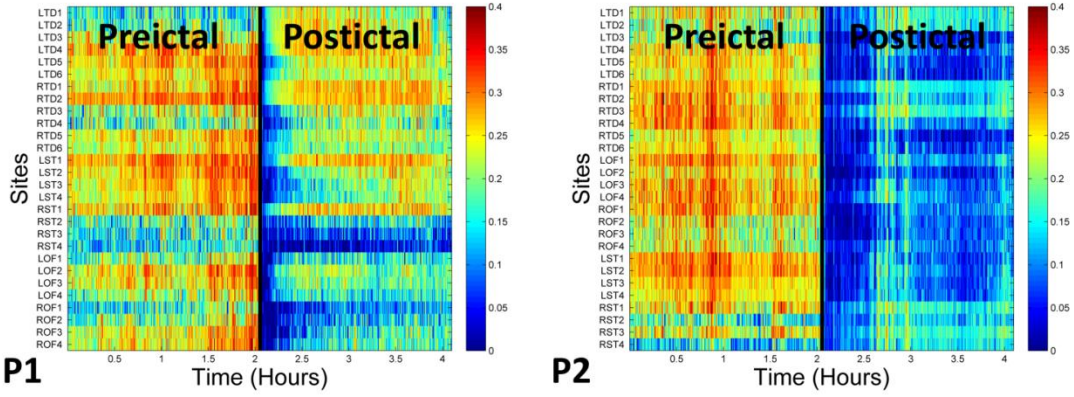


**Figure 1:** Spike synchronization profiles in 4 hours of continuous EEG recording around seizures from: (a) patient 1 (P1) and (b) patient 2 (P2). The black vertical line denotes the seizures' duration (about 3.5 minutes). We can observe increased (yellow/red color) preictal synchronization and postictal desynchronization (blue color).

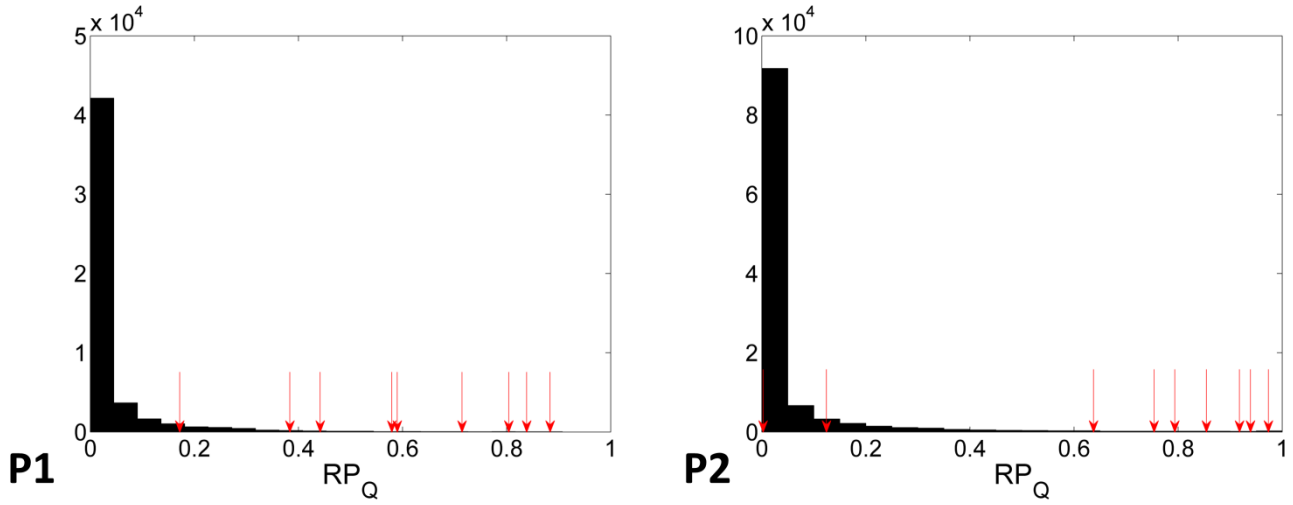


Figure 2: Histogram of resetting power  $RP_Q$  estimated from every 10.24 seconds over the entire EEG recordings for the two patients. The red arrows denote the high resetting power  $RP_Q$  values at seizure points and are mostly into the tail of the histogram being infrequent events.

Finally, to quantify the dynamical changes around seizures, we developed a measure of resetting similar to the method discussed in [8]. Given the set of profiles and for a time point  $t$ , for each pair of sites  $(i,j)$  we define as  $Q_{ij}^{pre}(t)$  the vector that has components the spike synchronization values within a preictal window  $w_{pre}(t) = \{t - 60 * 10.24, \dots, t\}$ , and  $Q_{ij}^{post}(t)$  the vector of spike synchronization values in the postictal window  $w_{post}(t) = \{t + d_{sz}, \dots, t + d_{sz} + 60 * 10.24\}$ , where  $d_{sz} = 5 \text{ min}$  is taken as the maximum duration of a seizure. Mann-Whitney's U test is employed to compare the distribution of  $Q_{ij}^{pre}(t)$  and  $Q_{ij}^{post}(t)$ . Since Mann-Whitney's U test can only suggest that the distributions are

different, we performed a Z-test to test whether the mean of one distribution is larger than the other. We define the resetting power ( $RP_Q(t)$ ) at time  $t$  as

$$RP_Q(t) = \frac{2}{N_e(N_e-1)} \sum_{i=1}^{N_e-1} \sum_{j=i+1}^{N_e} [\Theta(Q_{ij}^{pre}(t) \neq Q_{ij}^{post}(t)) \cdot \Theta(Z_{ij}(t) > Z_{thr})] \quad (3)$$

where  $\Theta(A)$  is the Heaviside step function and is equal to 1 when  $A$  is true and is equal to 0 when it is false, and  $Q_{ij}^{pre}(t) \neq Q_{ij}^{post}(t)$  denotes the result of the U-test.  $Z_{thr}$ , the statistical threshold for the Z-score, was set to 4 (corresponding to a significance level of  $p < 0.001$ ), and  $N_e$  is the number of available electrode sites. By using a high Z-score threshold we ascertained that only pairs of

sites that have significant change in  $Q_{ij}$  were selected. The distribution of  $RP_Q$  at interictal and during seizures for the two patients is shown in **Figure 2**.

To statistically validate the significance of resetting at seizures compared to interictal, we defined the resetting score ( $SRP_Q(t_0)$ ) at time  $t_0$  as

$$SRP_Q(t_0) = \frac{1}{N_{rec}} \sum_{t=1}^{N_{rec}} \Theta(RP_Q(t) \geq RP_Q(t_0))$$

where  $N_{rec}$  is the recording length of the EEG. The resetting score quantifies how unlikely it is to observe large resetting power at random times  $t$  anywhere in the entire EEG recording compared to those at time  $t_0$  (seizure times). Since  $SRP_Q$  is an independent measure of overall resetting power, we can compare the values of  $SRP_Q$  across patients. Each  $SRP_Q$  can be perceived as the  $p$  value of testing if “resetting at time  $t_0$  is significantly different than any time in the interictal period”. Finally we estimated the *combined p value* for each patient by using Fischer’s method for combining  $p$ . The method has been previously described [8]. For the two patients, these combined  $p$  values were found to be less than 0.001 and hence we can state that statistically significant resetting occurs mostly at epileptic seizures than at any random point in the interictal periods.

## DISCUSSION AND CONCLUSIONS

Previous studies on prediction of epileptic seizures have revealed the existence of a preictal period where the dynamics of different brain sites become entrained (synchronized). The existence of a preictal period provides us with a time window for intervention to prevent seizure occurrence [9-11]. However, the physiological substrate of the observed entrainment of dynamics has not been established yet. In this study we investigated whether preictal synchronization of epileptic spikes could constitute such a physiological substrate. We observed that synchronization of epileptic spikes occurs in the preictal periods and dynamical desynchronization in the postictal periods. Also, the presence of preictal synchronization hours to minutes prior to the onset of the ictal state indicates a possible predictive value of interictal spikes. Further, these observations suggest that epileptic seizures might have an antagonist effect on spiking, reflecting a physiological mechanism for resetting of the spiking by seizures (e.g., ictal activity may severely deplete critical neurotransmitters and deactivate critical neuroreceptors for generation and propagation of spike activity). The relationship between spikes and seizures depends on the applied spatiotemporal meta-analysis and could partially

explain the inconclusive and at times conflicting results in the literature about epileptic seizures and spikes. Therefore, appropriate analysis of the EEG could lead to further elucidation of the mechanisms of ictogenesis and epileptogenesis. Extension of this study to more subjects and into the role of epileptogenic focus in the generation of epileptic spikes and ictogenesis is currently underway.

## REFERENCES

- [1] J. P. Lieb, S. C. Woods, A. Siccardi, P. H. Crandall, D. O. Walter & B. Leake, "Quantitative analysis of depth spiking in relation to seizure foci in patients with temporal lobe epilepsy," *Electroencephalogr. Clin. Neurophysiol.*, vol. 44, pp.641-663 1978.
- [2] H. H. Lange, J. P. Lieb, J. Engel Jr. & P. H. Crandall, "Temporo-spatial patterns of preictal spike activity in human temporal lobe epilepsy," *Electroencephalogr. Clin. Neurophysiol.*, vol. 56, pp. 543-555, 12, 1983.
- [3] J. Gotman, "Relationships between interictal spiking and seizures - Human and Experimental evidence," *Canadian Journal of Neurological Sciences*, vol. 18, pp. 573-576, 1991.
- [4] A. Katz, D. Marks, G. McCarthy and S. Spencer, "Does interictal spiking change prior to seizures?" *Electroencephalogr. Clin. Neurophysiol.*, vol. 79, pp. 153-156, 1991.
- [5] B. Krishnan, I. Vlachos, A. Faith, S. Mullane, K. Williams, A. Alexopoulos, & L. Iasemidis. "A Novel spatiotemporal analysis of peri-ictal spiking to probe the relation of spikes and seizures in epilepsy," *Annals of Biomedical Engineering*, 42(8), 1606-1617, 2014.
- [6] L.D. Iasemidis, J.C. Principe & J.C. Sackellares, "Measurement and quantification of spatiotemporal dynamics of human epileptic seizures", In: *Nonlinear biomedical signal processing*, ed. M. Akay, IEEE Press, vol. II, pp. 294-318, 2000.
- [7] L.D. Iasemidis, D. S. Shiau, J. Sackellares, P. Pardalos and A. Prasad, "Dynamical resetting of the human brain at epileptic seizures: application of nonlinear dynamics and global optimization techniques," *IEEE Transactions on Biomedical Engineering*, vol. 51, pp. 493-506, 2004.
- [8] B. Krishnan, A. Faith, I. Vlachos, A. Roth, K. Williams, K. Noe, J. Drazkowski, L. Tapsell, J. Sirven and L. Iasemidis, "Resetting of brain dynamics: epileptic versus psychogenic nonepileptic seizures," *Epilepsy & Behavior*, vol. 22, pp. S74-S81, 2011.
- [9] N. Chakravarthy, K. Tsakalis, S. Sabesan & L.D. Iasemidis, "Homeostasis of brain dynamics in epilepsy: a feedback control systems perspective of seizures," *Annals of Biomedical Engineering*, vol. 37, pp. 565-585, 2009.
- [10] L. Good, S. Sabesan, S. Marsh, K. Tsakalis, D. Treiman & L.D. Iasemidis, "Control of synchronization of brain dynamics leads to control of epileptic seizures in rodents," *Int. J. Neural Systems*, vol. 19, pp. 173-196, 2009.
- [11] L.D. Iasemidis, "Seizure prediction and its applications," *Neurosurg. Clin. N. Am.*, vol. 22, pp. 489-506, 2011.

# ROLE OF PDE4 ISOFORMS IN REGULATING cAMP COMPARTMENTALIZATION AND PULMONARY MICROVASCULAR ENDOTHELIAL CELL (PMVEC) BARRIER PERMEABILITY

Naga S Annamdevula<sup>1,2</sup>, Andrea Britain<sup>2</sup>, Thomas C Rich<sup>2,3</sup>, Silas J Leavesley<sup>1,2,3</sup>

<sup>1</sup>Department of Chemical and Biomolecular Engineering, <sup>2</sup>Department of Pharmacology, <sup>3</sup>Center for Lung Biology, University of South Alabama, Mobile, AL

## ABSTRACT

An emerging concept in the field of signal transduction is cAMP signal compartmentalization and localization in discrete locations of the cell and spatial localization dictating signaling specificity. In the pulmonary microvasculature, cAMP produced by membrane-bound adenylyl cyclase (AC) has been shown to be barrier protective, while cAMP produced by soluble AC is membrane disruptive. Several studies suggest that phosphodiesterases (PDEs) play a key role in regulating the spatial spread of cAMP signaling. PDE4 is primarily responsible for cAMP and PDE activity in pulmonary microvascular endothelial cells (PMVECs). However, the distribution of PDE4 isoforms in PMVECS and their contribution to cAMP compartmentalization is not well understood.

We have begun utilizing hyperspectral FRET imaging and analysis techniques to determine the subcellular localization of cAMP signals in PMVECs. Wild-type and PDE4B knockout PMVECs were infected using a soluble Epac FRET probe (CFP-EPAC-YFP). We labeled nuclei (Hoechst), mitochondria (Mitotracker Red) and the plasma membrane (WGA-Tritc) for subcellular cAMP measurements. Time-lapse hyperspectral image data were acquired using an A1 spectral confocal microscope. A library containing the pure spectra of endmembers (CFP, YFP, Hoechst, Mitotracker red, Tritc) was used to determine the abundance of respective fluorophores/labels in the hyperspectral images. We then utilized automated and unbiased analysis techniques (Cell Profiler software), to measure the FRET efficiency in the subcellular compartments. We will assess cAMP levels using FRET efficiency that was measured in different subcellular compartments within the cell or across different cell types. In the future, we plan to assess the spatial distribution of PDE4 isoforms using isoform-specific antibodies and their role in maintaining endothelial permeability.

The ability to measure cAMP levels in discrete subcellular compartments will also allow us to determine the role of different PDE4 isoforms in regulating compartmentalized cAMP signaling and thus in maintaining the endothelial barrier permeability. In addition to PDE4B KO cells, we will also use PDE4A and PDE4D KO cells to determine the role of each isoform in maintaining the endothelial permeability.

**Keywords:** Hyperspectral Microscopy, FRET spectral Microscopy, Image Cytometry, Phosphodiesterases, cyclic AMP, and Subcellular second messenger signaling.

## INTRODUCTION

An emerging concept in the field of signal transduction is that cAMP signals are compartmentalized and localized to discrete locations in the cell and that spatial localization dictates signaling specificity[1-5]. For example, in pulmonary endothelium, cAMP produced by plasma membrane-localized adenylyl cyclase is endothelial barrier protective; whereas, cAMP produced by both endogenous and heterologously-expressed AC is barrier disruptive[6,7]. However, the mechanism of how these compartmentalized cAMP signals are regulated is not clearly understood. The possible mechanisms of how these cAMP signals are regulated includes cAMP synthesis AC [4], or cAMP diffusion in the cell, or the cAMP degradation by PDEs. Previous work strongly suggests that PDEs are key molecules in regulating the compartmentalized nature of cAMP signals[8-12].

However, the mechanisms underlying compartmentalization and the roles of specific PDEs in regulating cAMP compartmentalization are not well understood. This lack of knowledge is due to the difficulty of quantitatively assessing subcellular cAMP concentrations.

Recently, Förster resonance energy transfer (FRET) probes have been developed for measuring intracellular cAMP levels. The FRET probe that we are currently using to measure subcellular cAMP signaling events in PMVECs is H188-2. H188-2 utilizes a catalytically inactive Epac (Exchange protein activated by cAMP) fused with Turquoise (donor fluorophore) and Venus (an acceptor fluorophore) as shown in **Error! Reference source not found.**. At basal or low cAMP conditions, donor and acceptor are in close proximity and energy is transferred from donor to acceptor, and thus

maximum FRET occurs. Maximum energy transfer or the maximum FRET is dependent on the distance between the donor and the acceptor fluorophore (closer the probes = maximum energy transfer = Maximum FRET). When cAMP binds to EPAC, there is a conformational change in donor and acceptor where the distance between the two fluorophores increases. Due to this conformational change, energy is not transferred from CFP to YFP and there is a

minimal FRET response. However, FRET signals are difficult to interpret due to the weak signal strength and limited dynamic range of current FRET analysis techniques currently in use. To address these limitations, we will use hyperspectral imaging approaches that will provide FRET quantification with increased sensitivity and accuracy.

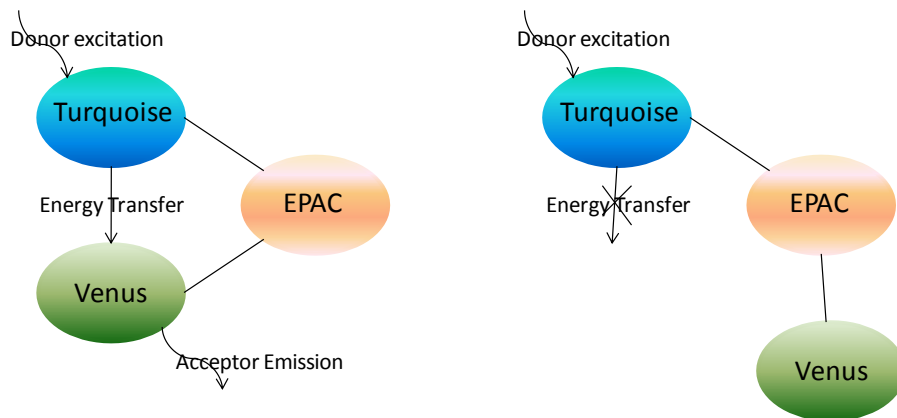


Figure 1: EPAC-based cAMP sensors. These sensors utilize a catalytically-inactive cAMP binding protein, EPAC, sandwiched between the fluorescent donor (Turquoise) and fluorescent acceptor (Venus).

Hyperspectral imaging utilizes spectral filtering to scan the fluorescence emission and produce a contiguous spectrum. Sampling many wavelength bands results in increased spectral discrimination and decreased FRET variance[13-14]. In addition, traditional image analysis uses manually-selected regions of interest (ROIs) to interpret signaling kinetics. However, selecting ROIs manually is time consuming, often leading to only 1 or 2 regions selected for a field of view. In addition, manual ROI selection may inadvertently bias data interpretation. We, and others, have utilized automatic image analysis and cell segmentation approaches to overcome this limitation[15]. Automated image analysis (image cytometry) permits the ability to accurately define and quantify the subcellular cAMP signals without operator bias. This approach allowed sampling of a much higher number of cells than sampling with manual ROI-based analysis. Furthermore, this unbiased technique yields more accurate statistical measures. In our present studies, we utilized automated cell segmentation approaches (using Cell Profiler software and custom developed MATLAB algorithms) and feature quantification to extract data describing the subcellular localization of cAMP signals in cells.

In this work, we have utilized hyperspectral FRET microscopy and image cytometry analysis to measure cAMP signaling events in subcellular locations such as cytoplasm, para-nuclear, peri-plasma membrane, and mitochondrial regions. Delineation of these regions permitted comparison of signaling events that are measured in different subcellular locations in a cell. In addition, we compared the signaling events that are measured in wildtype to PDE4 isoform specific KO cells to determine the role of each PDE4 isoform in regulating localized cAMP signals in cells.

## METHODS

**Cell Culture and Transfection:** Rat pulmonary microvascular endothelial cells (PMVECs) were seeded on 35mm round coverslips in 6-well dish plates and incubated for 24 hours (cells attained 70-80% confluence). After incubation, the cells were transfected with 1:3 ratio of cDNA encoding FRET probe (Turquoise – catalytically inactive EPAC – Venus): Transit – X2 (transfection reagent from Mirusbio). The transfected cells were incubated for 48 hours. The cells were labeled with 0.1 $\mu$ g/ml Hoechst 33342, 100nM Mitotracker red and 1mg/ml wheat germ agglutinin conjugated to TRITC (WGA – TRITC) to

visualize nuclei, mitochondria, and plasma membrane respectively. Coverslips were placed in Tyrodes buffer prior to imaging.

**Hyperspectral Microscopy:** A Nikon A1R hyperspectral confocal microscope was used to acquire the hyperspectral images. We maintained the settings of the imaging parameters to be uniform throughout each experiment. Briefly, laser excitations of 405 nm and 561 nm, a constant photomultiplier tube gain, pinhole diameter of 2.9AD units, scan area of 1024 x 1024 pixels, scan speed of 0.5, and averaging of 4 were used to acquire all the hyperspectral images. Time-lapse hyperspectral images were acquired for 25 minutes. During acquisition, 50 $\mu$ M Forskolin (adenylate cyclase activator) is added at 5 minutes of time and 10 $\mu$ M Rolipram+ 500 $\mu$ M IBMX (phosphodiesterase inhibitors) were added at time point of

15 minutes. These reagents increase the accumulation of cAMP levels in the cell.

**Spectral Library:** A spectral library containing the pure spectra (endmembers) of Turquoise, Venus, Hoechst, Mitotracker red, and WGA-TRITC was obtained using transfected - Turquoise, transfected - Venus, and single labeled (Hoechst or Mitotracker red or WGA) non-transfected PMVECs, respectively (Figure 2). The spectral library was used to unmix the hyperspectral images into their individual endmembers using linear unmixing algorithms ([Error! Reference source not found.](#)). Linear unmixing was performed using MATLAB software. The unmixed donor (Turquoise) and acceptor (Venus) images were summed to produce total fluorescent protein signals (donor+acceptor signal) and FRET image. The unmixed, summed and FRET images were then used to measure FRET efficiency using image cytometry.

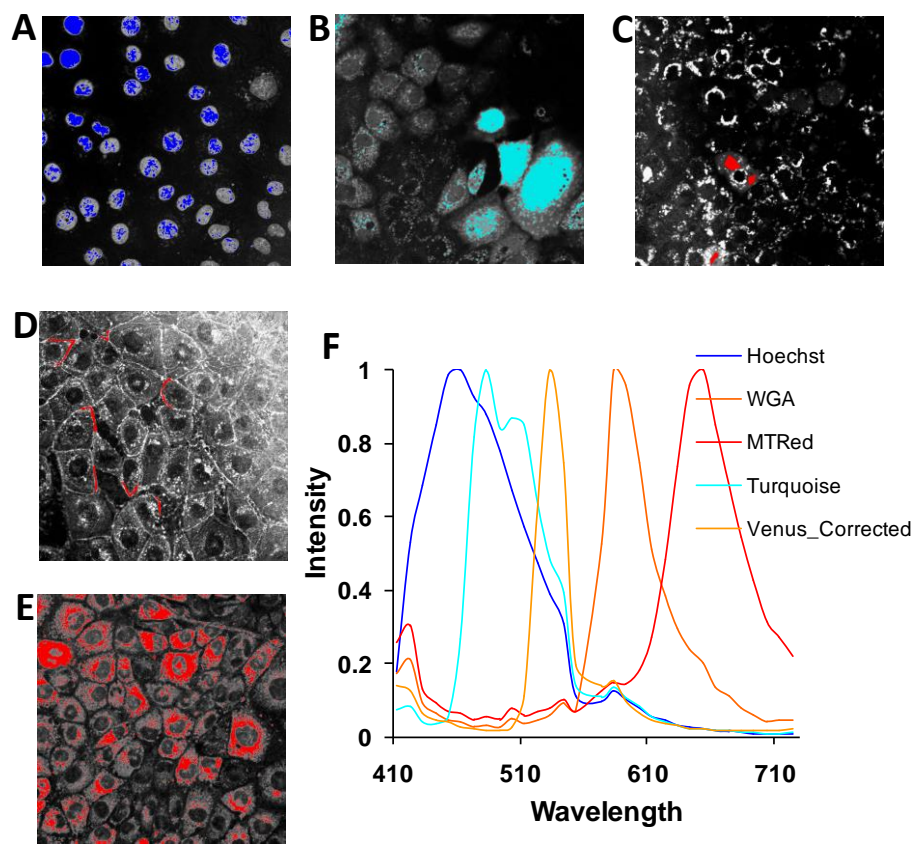


Figure 1: Spectral library (F) containing pure spectra of individual endmembers was obtained by selecting either band thresholded or manually drawn region of interest (ROI) in Hoechst (A), Turquoise (B), Venus (C), WGA-Trito(D), and Mitotracker Red (E) hyperspectral images

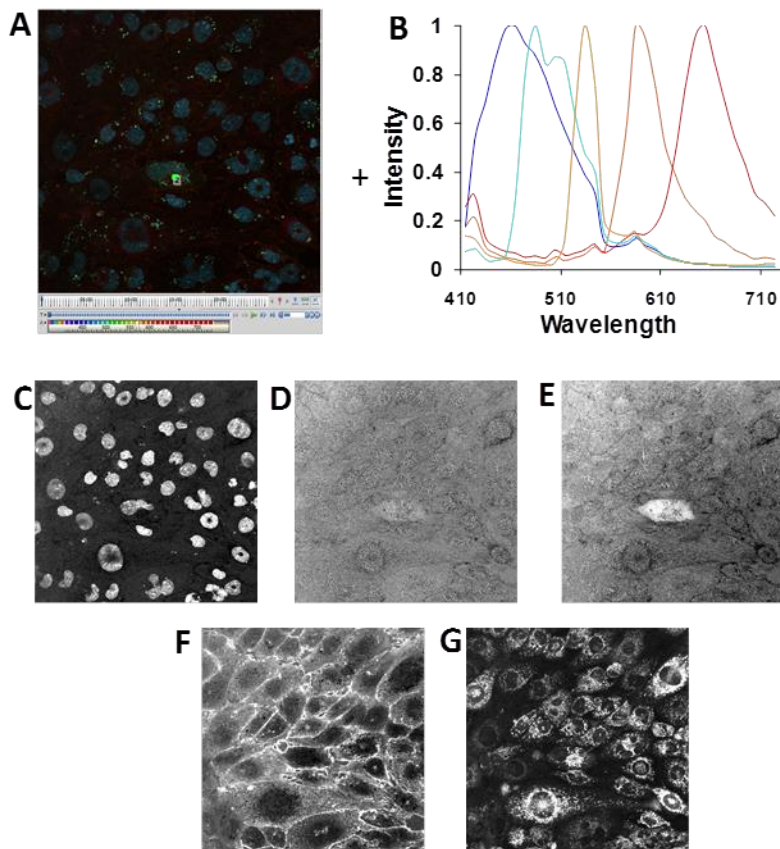


Figure 3: Spectral library (B) was used to unmix hyperspectral image (A) to their individual endmembers: Hoechst (C), Turquoise (D), Venus (E), WGA (F), and Mitotracker red (G).

**Image Cytometry:** Cell Profiler was used to perform unbiased image cytometry and to measure FRET efficiency in subcellular locations of the cells. The schematic representation of steps involved in measurement of FRET efficiency is shown in Figure 4. Briefly, nuclei were identified in the unmixed Hoechst (Figure 4C) and positively-expressing regions were identified in the donor+acceptor image (Figure 4F). Nuclei within expressing cells (Figure 4I) were then masked and subsequently propagated to estimate the borders of expressing cells (Figure 4J). Expressing cell cytoplasm (Figure 4K) was then identified by subtracting nuclear areas from expressing cell areas and the pixel-averaged FRET efficiency was measured within the cytoplasm for

each time point in time-lapse hyperspectral images. Similarly, we identified the para-nuclear and peri-plasma membrane regions as the area surrounding each nuclei in Hoechst unmixed image and each cell membrane in WGA-TRITC unmixed image. These regions were masked with the expressing cells image to extract the expressing peri-nuclear and peri-plasma membrane regions. FRET efficiency was measured in these peri-nuclear and peri-plasma membrane regions. Similarly, we will measure FRET efficiency in mitochondrial subcellular regions using unmixed Mitotracker Red. As expected, the treated samples showed increase in cAMP levels corresponding to decreased FRET efficiency. Whereas, there is no change in FRET efficiency in control sample cells.

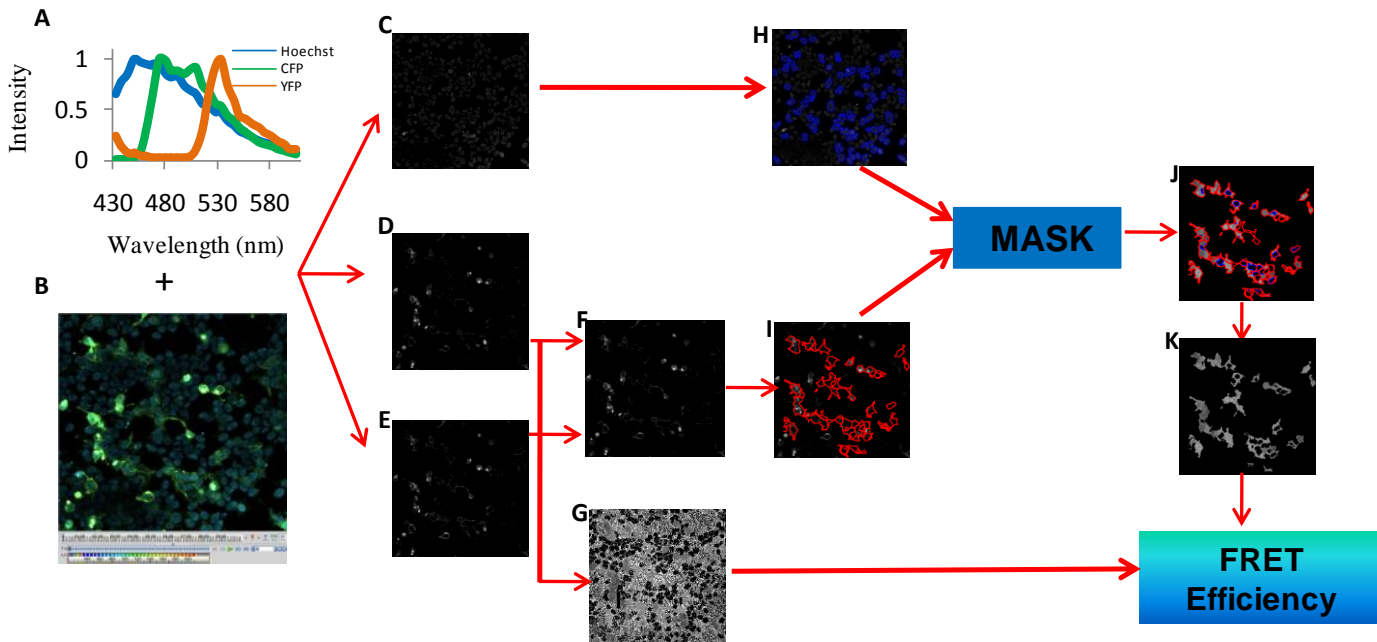


Figure 2: Schematic representation showing the steps involved in measuring the FRET efficiency using cell profiler analysis

**FRET Efficiency:** We measured the FRET efficiency in extracted cell cytoplasm. With the addition of Forskolin, the FRET efficiency decreased, corresponding to increased cAMP levels. We observed a further decrease in FRET efficiency with the addition of rolipram and IBMX. As shown in Figure 5, the vehicle control treated cells did not show any changes in FRET response. We used  $n=1$  (one coverslip containing around 5-6 expressing cells). We will do at least  $n=8$ , to compare subcellular FRET in cells or in between cell types (WT and PDE4 isoform specific KO cells).

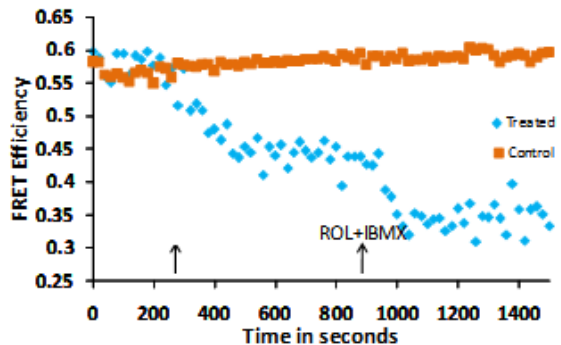


Figure 3: FRET Efficiency measured in bulk cytosol. FRET efficiency decreased with addition of forskolin, and further decreased with rolipram and IBMX treatments corresponding to

#### FUTURE WORK

We will measure cAMP signals in subcellular locations. We will then compare the localized FRET signals (cAMP signals) within the cell or among different cell types including wild-type and PDE4 isoform-specific knock out cells. This will allow us to determine the role of PDE4 isoforms in maintaining the cAMP compartmentalization in cells.

## CONCLUSIONS

The combination of spectral imaging and image cytometry provided FRET traces with greatly reduced noise, allowing analysis of small subcellular regions. Assessment of near-membrane and para-nuclear regions indicated varying cAMP response rates, likely due to diffusional and compartmentation effects.

These measurements will allow us to define the roles of different PDE4 isoforms in regulating cAMP compartmentalization and their role in maintain the endothelial barrier permeability. These data show great promise for validating new models for compartmentalized second messenger signaling.

## REFERENCES

- [1] W. P. Feinstein, B. Zhu, S. J. Leavesley, S. L. Sayner, and T. C. Rich, "Assessment of cellular mechanisms contributing to cAMP compartmentalization in pulmonary microvascular endothelial cells," *Am. J. Physiol. - Cell Physiol.*, vol. 302, no. 6, pp. C839–C852, Mar. 2012.
- [2] T. C. Rich, K. A. Fagan, T. E. Tse, J. Schaack, D. M. F. Cooper, and J. W. Karpen, "A uniform extracellular stimulus triggers distinct cAMP signals in different compartments of a simple cell," *Proc. Natl. Acad. Sci.*, vol. 98, no. 23, pp. 13049–13054, Nov. 2001.
- [3] T. C. Rich, K. J. Webb, and S. J. Leavesley, "Can we decipher the information content contained within cyclic nucleotide signals?," *J. Gen. Physiol.*, vol. 143, no. 1, pp. 17–27, Jan. 2014.
- [4] T. C. Rich, K. A. Fagan, H. Nakata, J. Schaack, D. M. F. Cooper, and J. W. Karpen, "Cyclic Nucleotide-Gated Channels Colocalize with Adenylyl Cyclase in Regions of Restricted Camp Diffusion," *J. Gen. Physiol.*, vol. 116, no. 2, pp. 147–162, Aug. 2000.
- [5] J. A. Beavo and L. L. Brunton, "Cyclic nucleotide research — still expanding after half a century," *Nat. Rev. Mol. Cell Biol.*, vol. 3, no. 9, pp. 710–718, Sep. 2002.
- [6] S. L. Sayner, D. W. Frank, J. King, H. Chen, J. Vandewaa, and T. Stevens, "Paradoxical cAMP-Induced Lung Endothelial Hyperpermeability Revealed by *Pseudomonas aeruginosa* ExoY," *Circ. Res.*, vol. 95, no. 2, pp. 196–203, Jul. 2004.
- [7] Sarah L. Sayner, M. Alexeyev, C. W. Dessauer, and T. Stevens, "Soluble Adenylyl Cyclase Reveals the Significance of cAMP Compartmentation on Pulmonary Microvascular Endothelial Cell Barrier," *Circ. Res.*, vol. 98, no. 5, pp. 675–681, Mar. 2006.
- [8] G. S. Baillie, "Compartmentalized signalling: spatial regulation of cAMP by the action of compartmentalized phosphodiesterases," *FEBS J.*, vol. 276, no. 7, pp. 1790–1799, Apr. 2009.
- [9] R. Fischmeister, L. R. V. Castro, A. Abi-Gerges, F. Rochais, J. Jurevičius, J. Leroy, and G. Vandecasteele, "Compartmentation of Cyclic Nucleotide Signaling in the Heart The Role of Cyclic Nucleotide Phosphodiesterases," *Circ. Res.*, vol. 99, no. 8, pp. 816–828, Oct. 2006.
- [10] R. F. Oliveira, A. Terrin, G. Di Benedetto, R. C. Cannon, W. Koh, M. Kim, M. Zaccolo, and K. T. Blackwell, "The Role of Type 4 Phosphodiesterases in Generating Microdomains of cAMP: Large Scale Stochastic Simulations," *PLoS ONE*, vol. 5, no. 7, p. e11725, Jul. 2010.
- [11] B. E. Blackman, K. Horner, J. Heidmann, D. Wang, W. Richter, T. C. Rich, and M. Conti, "PDE4D and PDE4B Function in Distinct Subcellular Compartments in Mouse Embryonic Fibroblasts," *J. Biol. Chem.*, vol. 286, no. 14, pp. 12590–12601, Apr. 2011.
- [12] M. D. Houslay and D. R. Adams, "PDE4 cAMP phosphodiesterases: modular enzymes that orchestrate signalling cross-talk, desensitization and compartmentalization," *Biochem. J.*, vol. 370, no. 1, p. 1, Feb. 2003.
- [13] N. S. Annamdevula, B. Sweat, P. Favreau, A. S. Lindsey, D. F. Alvarez, T. C. Rich, and S. J. Leavesley, "An Approach for Characterizing and Comparing Hyperspectral Microscopy Systems," *Sensors*, vol. 13, no. 7, pp. 9267–9293, Jul. 2013.
- [14] S. J. Leavesley, N. Annamdevula, J. Boni, S. Stocker, K. Grant, B. Troyanovsky, T. C. Rich, and D. F. Alvarez, "Hyperspectral imaging microscopy for identification and quantitative analysis of fluorescently-labeled cells in highly autofluorescent tissue," *J. Biophotonics*, vol. 5, no. 1, pp. 67–84, Jan. 2012.
- [15] S. J. Leavesley, A. L. Britain, L. K. Cichon, V. O. Nikolaev, and T. C. Rich, "Assessing FRET using spectral techniques," *Cytometry A*, vol. 83, no. 10, pp. 898–912, Oct. 2013.

# IMPULSE OSCILLOMETRY REFERENCE VALUES IN ANGLO AND HISPANIC CHILDREN

Roya Edalatpour <sup>1</sup>, Karla Montano <sup>1</sup>, Erika Meraz <sup>2</sup>, Carlos Rodriguez <sup>1</sup>, Christopher Aguilar <sup>1</sup>, Homer Nazeran <sup>1</sup>

<sup>1</sup> Department of Electrical and Computer Engineering, The University of Texas at El Paso, El Paso, Texas, USA

<sup>2</sup> Universidad Autónoma de Ciudad Juárez, Cd. Juárez, Chihuahua, México

## ABSTRACT

Lung function testing performed by the Impulse Oscillometry System (IOS) has been proven effective in the accurate diagnosis of small airway impairments in patients by measuring respiratory impedance ( $Z$ ) in terms of resistance ( $R$ ) and reactance ( $X$ ) at 5 – 25 Hz. Research conducted by our group provides reference values for IOS in Anglo and Hispanic children living in the border region of El Paso, TX, using different IOS parameters. Our previous studies have shown that IOS parameters AX (the “Goldman Triangle”) and the extended Resistor-Inductor-Capacitor (eRIC) model-derived parameter  $C_p$  (representing small airway compliance) are the most reliable parameters for tracking lung function. The predictive equations using the following parameters were determined from 112 Anglo and Hispanic asthmatic and non-asthmatic children: Resistance of the respiratory system at 5 Hz [R5], Resistance at 5Hz-20Hz [R5-R20] also called frequency-dependence of resistance (fdR), Reactance Area/“the Goldman Triangle” (AX), Resonant Frequency (Fres), and Peripheral (small airway) Compliance (eRIC  $C_p$ ). Linear prediction equations were developed by regression analysis with measuring (R5, R5-R20, AX, Fres, eRIC\_Cp) as dependent variables regressed against height (H).

The prediction equations for R5 and AX are as follows:

$$R5: 1.4280 - 0.0063 \times \text{height}$$

$$AX: 1.2128 - 0.0052 \times \text{height}$$

Our results therefore provide an original frame of reference for different IOS model parameters in the Anglo and Hispanic adolescent population between the ages of 5-17, obtained from a standardized forced oscillation technique.

**Keywords:** Impulse Oscillometry, Asthma, Children, Diagnosis, Treatment, Reference Values, Pediatric Pulmonology

## INTRODUCTION

Asthma is one of the most chronic respiratory conditions that is prevalent in and currently affects approximately 550,000 Texas children [1]. Detection of lung function within the early developmental stages of the pulmonary system is extremely critical in the intervention and treatment of asthmatic children [2,3]. Conventional detection methods of airway impairments are conducted using a pulmonary function test known as Spirometry, which requires strenuous breathing maneuvers [4]. This makes measuring lung function in the pediatric population a challenge. In addition, multiple studies have shown that Spirometry lacks the sensitivity to diagnose patients with asthma [5,6].

Impulse Oscillometry (IOS) provides an alternative patient-friendly lung function test that only

requires passive patient cooperation [7-9]. The impulse oscillometric method is a Forced Oscillation Technique (FOT) that is capable of measuring respiratory impedance in terms of the Resistance ( $R$ ) and Reactance ( $X$ ) of the lungs at frequencies between 5 Hz – 25 Hz [10].

As previous research conducted by our group has indicated, parameters of the equivalent electrical circuit models of the human respiratory system along with those of the IOS measurements have proven to be valuable in the diagnosis of patients with central and peripheral airway obstruction [11-13]. The purpose of this study was to develop predictive IOS equations for 112 asthmatic and non-asthmatic Anglo and Hispanic children in order to provide an original frame of reference for different IOS model parameters within this population.

## METHODS

Impulse Oscillometry data were collected in 2006-2008 at Western Sky Medical Research Clinic from 112 Anglo and Hispanic asthmatic and non-asthmatic children residing in the El Paso, Texas area. To avoid airflow leak, all subjects were asked to breathe normally while wearing a nose clip through a mouthpiece. Three to five repeat IOS measurements were recorded for each child to ensure accuracy in data collection. The data were then quality assured by our expert clinician and pulmonologist, and categorized into 4 classes as follows: Normal (N), Possible Small Airway Impairment (PSAI), Small Airway Impairment (SAI), or Asthmatic (A).

The average values of the following parameters were used for data analysis: Resistance of the respiratory system at 5 Hz [R5], Resistance at 5Hz-20Hz [R5-R20] or frequency-dependence of resistance, Reactance Area/“the Goldman Triangle” (AX), Resonant Frequency (Fres), and

Peripheral (small airway) Compliance (eRIC\_Cp). To identify any correlations, we employed statistical analyses of the IOS parameters. Linear prediction equations were developed by regression analysis with measuring (R5, R5-R20, AX, Fres, eRIC\_CP) as dependent variables regressed against height (H).

## RESULTS

The predictive equations of the following parameters, R5, R5-R20, AX, and eRIC Cp were calculated. These are shown in Table 1. Previous studies conducted by our research group established correlations between the IOS parameters and height to correctly diagnose patients as Normal (N), PSAI, and SAI, and Asthmatic (A), and we conducted these calculations using algorithms that we developed in our research lab [14]. The results obtained by this study and other similar studies show that AX is considered a relevant indicator in the proper diagnosis of asthma in children.

**Table 1: IOS Reference Equations for Pre-Bronchodilator Subjects**

IOS Reference Equations						
	Normal			PSAI		
	Reference Equations	SEE <sup>†</sup>	r <sup>2</sup> <sup>‡</sup>	Reference Equations	SEE	r <sup>2</sup>
R5	1.4280 - 0.0063 × height	0.057	0.645	1.2493 - 0.0049 × height	0.069	0.646
R5-R20	0.3635 - 0.0018 × height	0.027	0.432	0.5299 - 0.0025 × height	0.049	0.487
AX	1.2128 - 0.0052 × height	0.110	0.245	4.4259 - 0.0232 × height	0.272	0.725
eRIC_Cp	-0.3268 + 0.0031 × height	0.058	0.301	-0.1412 + 0.0016 × height	0.024	0.628
	SAI			Asthma		
	Reference Equations	SEE	r <sup>2</sup>	Reference Equations	SEE	r <sup>2</sup>
R5	1.3280 - 0.0049 × height	0.110	0.432	1.6843 - 0.0067 × height	0.112	0.559
R5-R20	0.7039 - 0.0033 × height	0.063	0.511	1.0039 - 0.0049 × height	0.074	0.610
AX	5.9360 - 0.0295 × height	0.481	0.592	8.7637 - 0.0448 × height	0.528	0.720
eRIC_Cp	-0.0763 + 0.0010 × height	0.019	0.506	-0.0348 + 5.8503e-04 × height	0.008	0.675

<sup>†</sup>SEE = Standard Error of the Estimate

<sup>‡</sup>r<sup>2</sup> = Coefficient of Determination

## CONCLUSIONS

Impulse Oscillometry is a patient-friendly test that has been proven to be more sensitive than Spirometry in clinical settings. It has also been proven to be of valuable and clinical significant due to the fact that it can track pulmonary function over a period of time [12, 13, 15]. Here we were able to successfully develop predictive IOS equations for 112 asthmatic and non-asthmatic Anglo and Hispanic children in order to provide an original frame of reference for different IOS model parameters within this population. This study and our previous work showed that the AX parameter is a relevant indicator in the proper diagnosis of asthmatic children. As such, Impulse Oscillometry may serve as a viable candidate for consideration for integration into clinical settings where a child-friendly approach to the reliable treatment of children with asthma is of paramount interest.

## ACKNOWLEDGEMENTS

The data collection for this research was supported by NIH grant #1 S11 ES013339-01A1: UTEP-UNM HSC ARCH Program on Border Asthma.

## REFERENCES

- [1] Texas Department of State Health Services (2014, December). 2012 Child Asthma Fact Sheet—Texas [Online] Available: <https://www.dshs.state.tx.us/WorkArea/linkit.aspx?LinkIdentifier=id&ItemID=8589994054>.
- [2] Martinez FD, Morgan WJ, Wright AL, Holberg CJ, Taussig LM. Diminished lung function as a predisposing factor for wheezing respiratory illness in infants. *N Engl J Med* 1988; 319: 1112-1117.
- [3] Young S, Sherrill DL, Arnott J, Diepeveen D, LeSouef PN, Landau LI. Parental factors affecting respiratory function during the first year of life. *Pediatr Pulmonol* 2000; 29:331-340.
- [4] Rodriguez, L.; Nazeran, H.; Meraz, E.; Estrada, E.; Rodriguez, C.; Edalatpour, R., "Discriminative Capacity of Impulse Oscillometry in Diagnosis and Treatment of Asthmatic Children," Biomedical Engineering Conference (SBEC), 2013 29th Southern , vol., no., pp.13,14, 3-5 May 2013.
- [5] Centers for Disease Control and Prevention (2012, Mar. 6). Asthma [Online]. Available: <http://www.cdc.gov/asthma/faqs.htm>.
- [6] E. A. Antonova, L. A. Zhelenina, L. M. Ladinskaia, G. A. Bochkova and T. M. Ivashikina, "Sensitivity impulse oscillometry and spirometry for assessment degree of severity of bronchial asthma in preschool children" 2009.
- [7] G. V. M. Vink, H. G. M. M. Arets, van der Laag, J. and van der Ent, C.K., "Impulse Oscillometry: A measure for Airway Obstruction," *Pediatr Pulmonol*, vol. 35, pp. 214-219, 2003.
- [8] U. Frey, "Forced Oscillation Technique in infants and young children," *Paediatric Respiratory*, vol. 6, pp. 246-254, 2006.
- [9] M. Goldman, E. Meraz, B. Diong and H. Nazeran, "Airflow perturbation analyses using simplified models can assess upper airway shunt during resting breathing Biomedical Engineering: Recent Developments, Washington, DC, Apr 2007
- [10] Dencker M, Malmberg LP, Valind S, Thorsson O, Karlssonmk, Pelkonen A. Reference values for respiratory system impedance by using impulse oscillometry in children aged 2-11 years. *Clin Physiol funct imaging* 2006; 26(4):247-50.
- [11] Diong, B., H. Nazeran, P. Nava, and M. Goldman. "Modeling Human Respiratory Impedance." *IEEE Engineering in Medicine and Biology Magazine* 26.1 (2007): 48-55.
- [12] Meraz et al.: Analysis of impulse oscillometric measures of lung function and respiratory system model parameters in small airway-impaired and healthy children over a 2-year period. *BioMedical Engineering OnLine* 2011 10:21.
- [13] Meraz E, Nazeran H, Goldman M, Diong B: Respiratory System Model Parameters Track Changes in Lung Function after Bronchodilation. In proceedings of the 25th Southern Biomedical Engineering Conference, Miami, Florida. ; 2009:319-322.
- [14] E.G. Meraz "" Ph.D. dissertation, Dept. Elect. Eng., Univ. of TX at El Paso, El Paso, TX, 2011
- [15] H. D. Komarow, J. Skinner, M. Young, D. Gaskins, C. Nelson, P. J. Gergen and D. D. Metcalfe, "A Study of the Use of Impulse Oscillometry in the Evaluation of Children with Asthma: Analysis of Lung Parameters, Order Effect, and Utility Compared with Spirometry," *Pediatric Pulmonology*, 2011.

# HOTSPOT ANALYSIS FOR EXAMINING THE ASSOCIATION BETWEEN SPATIAL AIR POLLUTANTS AND ASTHMA IN NEW YORK STATE, USA USING KERNEL DENSITY ESTIMATION (KDE)

Francis Tuluri<sup>1</sup> and A. K. Gorai<sup>2</sup>

<sup>1</sup>Department of Technology, Jackson State University, Jackson, MS 39217, USA,

email: francis.tuluri@jsums.edu

<sup>2</sup>Department of Mining Engineering, National Institute of Technology, Rourkela, Odisha -769008, India.

email: amit\_gorai@yahoo.co.uk

## ABSTRACT

Air pollutants play a predominant role in effecting human health. Identifying hot spots of air pollutants in a location will facilitate in taking measures to improve human health and hence protecting the local people from health disorders. The present study examines the use of spatial analysis of air pollutants in New York State, U.S.A. Based on the availability of data in the study region, three air pollutants ( $PM_{2.5}$ ,  $SO_2$ , and  $O_3$ ) were considered for the hot spot analysis to identify zones with higher pollutant concentration levels for the period of 2005 to 2007. The corresponding asthma discharge rates were then determined for understanding the effect of exposure of high air pollutants to asthma discharge rate. In the present investigation, kernel density estimation (KDE) technique was used for hotspot analysis of air pollution from annual average air pollutants concentrations. Using KDE technique, air pollution hotspots and polluted sampling densities are clearly defined based on point data of air pollutants. In the study area, multiple hotspots were observed for these three air pollutants, and they are significantly correlated to the locations of asthma discharge rate. The spatial patterns of hazard probability reveal hotspots of  $PM_{2.5}$  are situated in the counties of Rockland, Westchester, Bronx, Queen, Brooklyn and Nassau. The hotspots of  $O_3$  coincide with that of  $PM_{2.5}$ , and  $SO_2$  but many other hotspots areas were observed for  $O_3$ . The major hotspots for asthma discharge rate are observed in the same counties as that of  $PM_{2.5}$ ,  $SO_2$ , and  $O_3$ . KDE technique enables capturing hot spots without requiring exhaustive sampling to identify risk prone areas.

**Keywords:** kernel density estimation (KDE); air pollution; asthma

## INTRODUCTION

Air pollution may be described as contamination of the atmosphere by gaseous, liquid or solid substances that can endanger human health and welfare of plants and animals, attack materials, reduce visibility, or produce undesirable odors. Airborne pollutants may influence the symptoms of asthma patients [1, 2]. Asthma is not only related to genetic and environmental factors, but also it is believed to be affected by air pollutants. Asthma is a chronic disease linked with considerable morbidity, mortality, and health care use. An estimated 300 million people worldwide suffer from asthma, with 250,000 annual deaths attributed to the disease [3].

The available literature on asthma studies shows a large geographic variation from local/community level all the way to country level. The studies on asthma and other epidemics have raised some important questions as what factors contribute to the emergence of asthma outbreak. Many epidemiologic studies demonstrated positive associations between air pollution and mortality [4 – 8].

Hotspot mapping has become a valuable technique for visualizing the geographic incidence of air pollution and asthma. One of the most widely used techniques for generating hotspot maps as smooth continuous surfaces is kernel density estimation (KDE). Hotspot mapping can be used for identifying the locations where hazardous level of air pollution exists. KDE has been widely used for hotspot analysis and detection. KDE is one of the methods for analyzing the first order properties of a point event distribution [9 – 11], in part because it is easy to understand and implement. Schnabel and Tietje [12] applied the KDE method to spatially distributed heavy metal soil data and compared it with ordinary kriging. The objective of KDE is to produce a smooth density surface of point events over space by computing event intensity as density estimation [11 – 13].

The primary objective of the present work was to investigate the association between geographical incidence of air pollutants and asthma cases. For this study, an alternative approaches was proposed in searching the hotspots locations of air pollutants and asthma incidences.

First, KDE identify the hotspots of air pollution and asthma incidence based on the monitored/survey data.

## METHODS

Kernel density estimation (KDE) is used to identify the location, spatial extent and intensity of air pollution and asthma cases hotspots. Moreover, the spatial patterns of hazardous probability for three air pollutants ( $PM_{2.5}$ ,  $SO_2$ , and  $O_3$ ) and asthma incidence are estimated for examining the association between these two. The KDE method is used for visualization of hotspots of air pollutions and asthma incidence in the case study. Study area and data sources of air pollutants and asthma cases are discussed in the following sections.

### Study Area

In the present work, New York State is selected as the area of study for the analysis and estimation. New York is a state in the Northeastern region of the United States. The longitude and latitude of the state are  $71^{\circ} 47' 25''$  W to  $79^{\circ} 45' 54''$  W and  $40^{\circ} 29' 40''$  N to  $45^{\circ} 0' 42''$  N respectively. It is the third most populous (19,378,102), and the seventh most densely populated (415.3 inhabitants per square mile) state of the 50 United States. New York covers 54,556 square miles and ranks as the 27th largest state by size. In general, New York has a humid continental climate.

### Air Pollution Data

Air quality data collected by U.S. EPA's Air Quality System (AQS) at the various monitoring stations located in different counties of New York State for the three years from 2005 to 2007 were used for the study. The air pollution data used in this study was taken from the United States Environmental Protection Agency (U.S. EPA) air quality system data mart (**Source:** [http://www.epa.gov/airdata/ad\\_rep\\_mon.html/](http://www.epa.gov/airdata/ad_rep_mon.html/)) [14]. Three criteria air pollutant parameters ( $SO_2$ ,  $PM_{2.5}$ , and  $O_3$ ) were selected for the proposed study. The pollution concentrations of these three criteria air pollutant parameters in various monitoring stations located in different counties were retrieved for a three-year period from 2005 to 2007. Air pollution concentrations of  $SO_2$ ,  $PM_{2.5}$ , and  $O_3$  were collected from twenty two, twenty five, and twenty five monitoring stations, respectively. The characteristics of the these three pollutants retrieved from the website are daily average (24 hrs.) concentrations of  $PM_{2.5}$ , daily maximum 8 hours average concentrations of  $O_3$ , and daily maximum 1 hour average concentrations of  $SO_2$ . The daily data for each monitoring station were used for determination of annual average concentrations.

### Asthma data

County- wise asthma hospital discharge data for

the period 2005 through 2007 were obtained from Department of Health, New York State's Asthma Surveillance Summary Report, 2009 (Source:[https://www.health.ny.gov/statistics/ny\\_asthma/pdf/2009\\_asthma\\_surveillance\\_summary\\_report.pdf](https://www.health.ny.gov/statistics/ny_asthma/pdf/2009_asthma_surveillance_summary_report.pdf)) [15]. The International Classification of Disease, Ninth Revision, Clinical Modification (ICD-9-CM) diagnosis code 493 was used to identify asthma hospitalization discharge diagnosis [16].

Asthma hospital discharge rate (ADR) indicates the number of asthma-related hospital discharges per 10,000 populations for a specified period of time. ADR for 2005, 2006, and 2007 were calculated by dividing the number of asthma hospital discharges by the estimated population for that time period in a particular zone and then multiplying by 10,000. The estimated rates represent crude rate on the basis of estimated population of the county. The county wise population estimates for the year 2005, 2006 and 2007 were obtained from the United States' Census Bureau (Source: <http://www.census.gov/popest/data/intercensal/county/tables/CO-EST00INT-01/CO-EST00INT-01-36.csv45>) [17,18].

### Kernel Density Estimation (KDE)

Kernel density estimation was used to visualize the spatial distribution of cumulative incidence. Kernel density estimation is a technique for calculating the weighted density of an event over a gridded surface within a kernel, or spatial filter [19]. Kernel density estimation was performed with the Spatial Analyst Extension for ArcGIS 10. The general form of a kernel density estimator (KDE) in a 2-D space [11] is given by

$$\lambda(x) = \sum_{i=1}^n \frac{1}{nh} K\left(\frac{x-x_i}{h}\right) \quad (\text{eq.1})$$

where  $\lambda(x)$  is the density at location  $x$ ,  $h$  is the bandwidth of the KDE,  $n$  is the number of sampling points,  $x-X_i$  is the distance to each point  $x$  to location  $X_i$ ,  $K$  is the weight of a point  $i$  at distance  $x-X_i$  to location  $x$ .  $K$  is usually modelled as a kernel function of the ratio between  $x-X_i$  and  $h$ . In this study, a quadratic kernel function [10] is used for estimation. This is given by

$$K\left(\frac{x-x_i}{h}\right) = \begin{cases} 3/4(1-x^2) & \text{if } |x| \leq 1 \\ 0, & x > 1 \end{cases} \quad (\text{eq.2})$$

This function was employed to estimate air pollutants and asthma densities using cumulative incidence as the weight. The resulting outputs are map surfaces representing the cumulative risk for air pollution episodes and asthma incidences across the New York State.

## RESULTS

Table 1 summarizes the descriptive statistics of the investigated three pollutants ( $PM_{2.5}$ ,  $SO_2$  and  $O_3$ ) and asthma discharge rate (ADR) from the monitored data. In United State of America, the pollution control standards (maximum allowable concentrations) for the investigated pollutants are as:  $PM_{2.5}$ -12  $\mu g/m^3$  (annual average) and 35

$\mu g/m^3$  (24 hours average),  $SO_2$ - 75 ppb (maximum 1 hr. average), and  $O_3$ - 75 ppb (maximum 8 hrs. average). Moreover, the high variability of the pollutant concentrations at various air pollutants requires a detailed evaluation and interpretation. The application of KDE method is an efficient tool in achieving better understanding of the hazardous level of the air pollution and asthma incidence.

**Table 1: Descriptive statistics of data**

	Minimum	Maximum	Mean	Standard Deviation
<b>2005</b>				
Asthma Rate	37.77	94.05	53.04	8.39
Ozone	29.56	44.48	40.21	1.17
$PM_{2.5}$	7.15	16.15	11.39	1.15
$SO_2$	2.58	18.65	8.46	2.88
<b>2006</b>				
Asthma Rate	37.34	98.30	52.46	9.77
Ozone	30.49	41.92	37.42	1.21
$PM_{2.5}$	5.68	13.30	8.73	1.05
$SO_2$	2.14	18.69	6.91	2.31
<b>2007</b>				
Asthma Rate	36.56	94.87	50.96	10.43
Ozone	31.75	42.69	39.08	1.76
$PM_{2.5}$	5.73	15.91	9.49	1.08
$SO_2$	2.81	13.79	7.18	2.38

The minimum annual average concentrations of  $PM_{2.5}$  for 2005, 2006, and 2007 were 6.7  $\mu g/m^3$ , 5.5  $\mu g/m^3$ , and 5.6  $\mu g/m^3$ , respectively. The maximum average concentrations of  $PM_{2.5}$  for 2005, 2006 and 2007 were 17  $\mu g/m^3$ , 14.4  $\mu g/m^3$ , and 16.1  $\mu g/m^3$ , respectively. The maximum values of annual average of maximum 8 hours daily average concentration of  $O_3$  in 2005, 2006, and 2007 were found to be 46.38 ppb, 45.03 ppb, and 47.93 ppb respectively. The minimum values of annual average of maximum 8 hours daily average concentrations of  $O_3$  in 2005, 2006, and 2007 were found to be 26.84 ppb, 26.41

ppb, and 16.78 ppb respectively.

The hotspot patterns of  $PM_{2.5}$ ,  $SO_2$ ,  $O_3$ , and ADR on the kernel density map are shown in Figure 1, Figure 2, Figure 3, and Figure 4, respectively. KDE transforms a dot pattern into a continuous surface, providing a more useful representation of pollution and asthma cases distributions, allowing for easier detection of possible pollution hotspots and its association with asthma cases. Results show that the asthma cases hotspots associated with the three air pollutants in the study area.

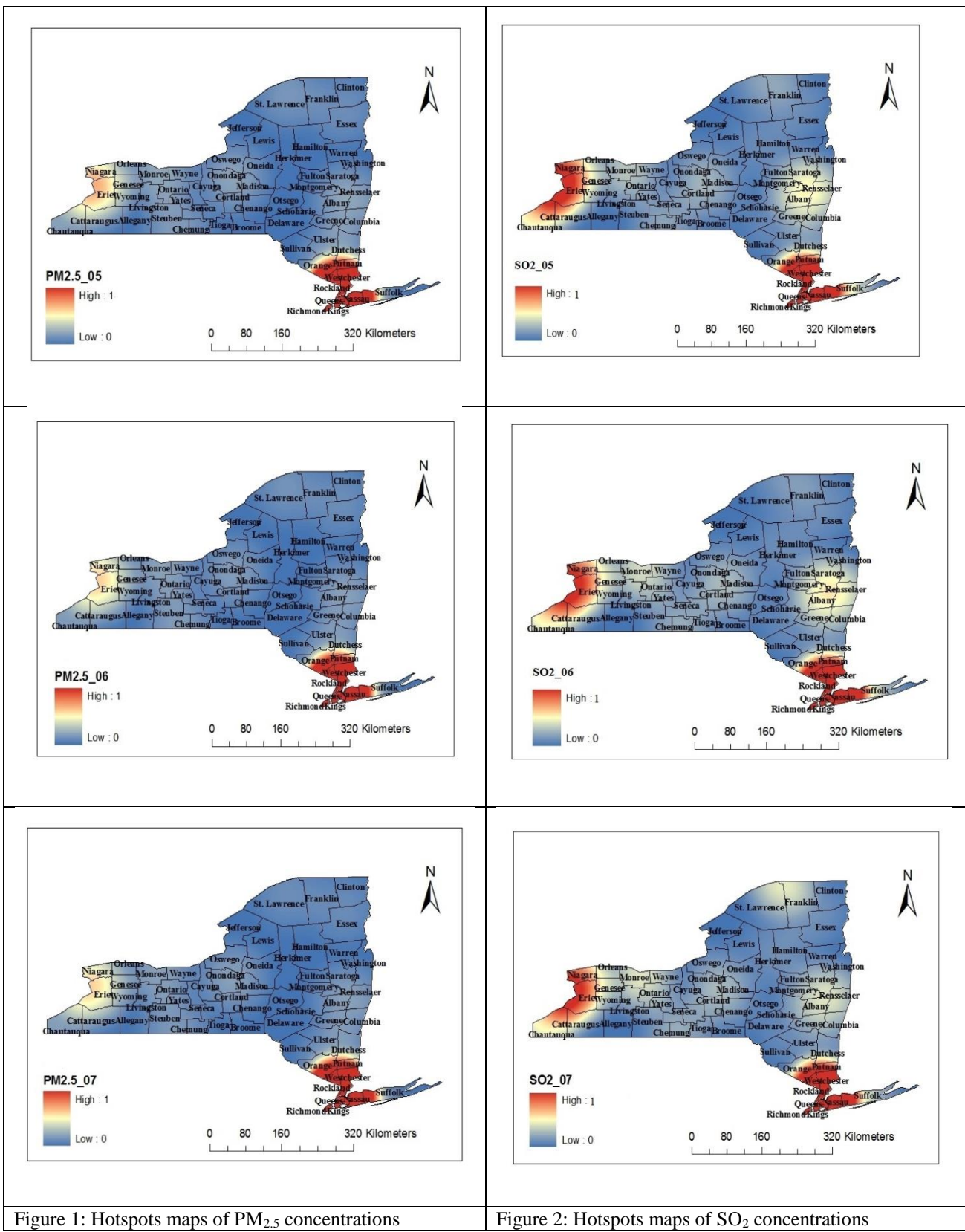


Figure 1: Hotspots maps of PM<sub>2.5</sub> concentrations

Figure 2: Hotspots maps of SO<sub>2</sub> concentrations

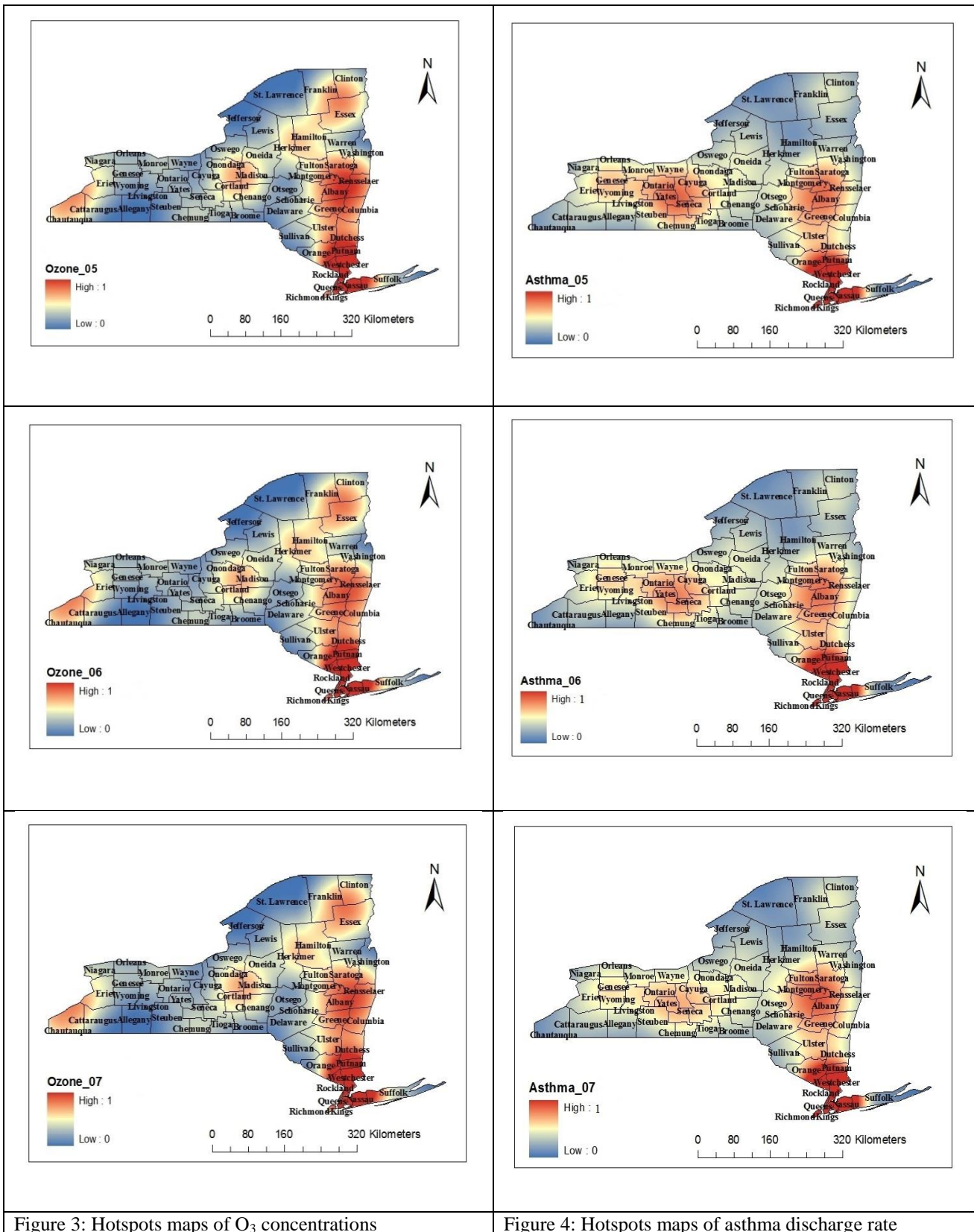


Figure 3: Hotspots maps of O<sub>3</sub> concentrations

Figure 4: Hotspots maps of asthma discharge rate

The maximum values of annual average of maximum 1 hour daily average concentration of SO<sub>2</sub> in 2005, 2006, and 2007 were found to be 22.99 ppb, 19.86 ppb, and 23.16 ppb respectively. The minimum values of annual average of maximum 1 hr. daily average concentrations of SO<sub>2</sub> in 2005, 2006, and 2007 was found to be 1.9 ppb, 1.79 ppb, and 1.93 ppb respectively.

## DISCUSSION

The results demonstrate that the hotspots of hazard probability for PM2.5 and SO<sub>2</sub> are similar. The spatial patterns of hazard probability also reveal hotspots of PM2.5 are situated in the counties of Rockland, Westchester, Bronx, Queen, Brooklyn and Nassau. All these counties are situated in the coastal part of south-east side of the state. Two other counties (Erie and Niagara) also show hotspots. The same trend is observed in each of the three years (2005 to 2007). Similar spatial trends are observed for SO<sub>2</sub> in each of the three year. The hotspots of O<sub>3</sub> are revealing those spatial trends are similar in each year (2005 to 2007). The hotspots of O<sub>3</sub> coincide with that of PM2.5, and SO<sub>2</sub> but many other hotspots areas were observed for O<sub>3</sub>.

The hotspots for ADR are represented in Fig. 4, clearly indicates that the major hotspots for ADR are observed in the same counties as that of PM2.5, SO<sub>2</sub>, and O<sub>3</sub>. But, the distribution patterns are more similar to O<sub>3</sub> episode. Furthermore, the hotspots are observed in the same counties in three years (2005 to 2007). Hotspot analyses clearly indicate that there are multiple hotspots of hazard probability and these are identified in same location in each year.

## CONCLUSIONS

An important component of human health protection due to poor air quality is identification hotspots in respect to poor air quality in the area. Three air pollutants (PM2.5, SO<sub>2</sub>, and O<sub>3</sub>) and asthma discharge rate (ADR) were considered for the hot spot analyses to examine the association of air pollution and asthma in New York State, U.S.A. Higher concentrations zone were identified and the ADR in those areas were determined for understanding the effect of exposure of high air pollutants to asthma discharge rate (ADR). Kernel density estimation (KDE) technique was used for hotspot analyses. Results show that there are multiple hotspots for these three air pollutants and they are significantly correlated to the locations of ADR in the study area. Air pollution hotspots are clearly defined using the KDE approach based on point data of air pollutants. Furthermore, the risk prone areas are explored by this technique (KDE) and the hotspot areas are captured without requiring exhaustive sampling.

## ACKNOWLEDGMENTS

This research work was carried out in part of the corresponding author's Raman Postdoctoral Fellowship-2013 awarded by UGC, New Delhi, India. Authors are also thankful to U.S. EPA for making air pollution data available on the website for public use. The support from the DST, New Delhi Grant No. SR/FTP/ES-17/2012 is also acknowledged. The authors are thankful to Dr. Paul Tchounwou, Associate Dean and Professor of College of Science and Technology, Jackson State University for his interest and encouragement in the work.

## REFERENCES

- [1] Delfino, R.J.; Coate, B.D.; Zeiger, R.S.; Seltzer, J.M.; Street, D.H.; Koutrakis, P. Daily asthma severity in relation to personal ozone exposures and outdoor fungal spores. *Amer. J. Respir. Crit. Care Med.* 1996, 154, 633–641.
- [2] Delfino, R.J.; Zeiger, R.S.; Seltzer, J.M.; Street, D.H.; Matteucci, R.M.; Anderson, P.R.; Koutrakis, P. The effect of outdoor fungal spore concentrations on daily asthma severity. *Environ. Health Perspect.* 1997, 105, 622–635.
- [3] World Health Organization. Global surveillance, prevention and control of chronic respiratory diseases: a comprehensive approach, 2007.
- [4] Levy, J.I.; Hammitt, J.K.; Spengler, J.D. Estimating the mortality impacts of particulate matter: What can be learned from between-study variability? *Environ. Health Perspect.* 2000, 108, 109–117.
- [5] Pope, C.A., III; Burnett, R.T.; Thurston, G.D.; Thun, M.J.; Calle, E.E.; Krewski, D.; Godleski, J.J. Cardiovascular mortality and long-term exposure to particulate air pollution: Epidemiological evidence of general pathophysiological pathways of disease. *Circulation* 2004, 109, 71–77.
- [6] Goodman, P.G.; Dockery, D.W.; Clancy, L. Cause-specific mortality and the extended effects of particulate pollution and temperature exposure. *Environ. Health Perspect.* 2004, 112, 179–185.
- [7] Schwartz, J. The effects of particulate air pollution on daily deaths: A multi-city case-crossover analysis. *Occup. Environ. Med.* 2004, 61, 956–961.
- [8] Analitis, A.; Katsouyanni, K.; Dimakopoulou, K.; Samoli, E.; Nikoloulopoulos, A.K.; Petasaki, Y.; Touloumi, G.; Schwartz, J.; Anderson, H.R.; Cambra, K.; et al. Short-term effects of ambient particles on cardiovascular and respiratory mortality. *Epidemiology* 2006, 17, 230–233.
- [9] Bailey, T.C.; Gatrell, A.C. *Interactive Spatial Data Analysis*; Longman: Essex, UK, 1995.
- [10] Silverman, B. W. *Density Estimation for Statistics and Data Analysis*. New York: Chapman and Hall, 1986.
- [11] Xie, Z.X.; Yan, J. Kernel Density Estimation of traffic accidents in a network space. *Comput. Environ. Urban*

- 2008, 32, 396-406.
- [12] Schnabel, U; Tietje, O. Explorative data analysis of heavy metal contaminated soil using multidimensional spatial regression. *Envir. Geol.* 2003, 44, 893-904.
- [13] Serra-Sogas, N.; O'Hara, P.D.; Canessa, R.; Keller, P.; Pelot, R. Visualization of spatial patterns and temporal trends for aerial surveillance of illegal oil discharges in western Canadian marine waters. *Mar. Pollut. Bull.* 2008, 56, 825-833.
- [14] US Environmental Protection Agency, Technology Transfer Network (TTN) Air Quality System (AQS) Data Mart. Available online: [http://www.epa.gov/airdata/ad\\_rep\\_mon.html/](http://www.epa.gov/airdata/ad_rep_mon.html/) (accessed on 15 December 2013).
- [15] New York State Department of Health, Public Health Information Group, National Asthma Survey—New York State Summary Report. Available online: [https://www.health.ny.gov/statistics/ny\\_asthma/pdf/2009\\_asthma\\_surveillance\\_summary\\_report.pdf](https://www.health.ny.gov/statistics/ny_asthma/pdf/2009_asthma_surveillance_summary_report.pdf) (accessed on 13 December 2013).
- [16] International Classification of Diseases (Ninth Revision, Clinical Modification); Department of Health and Human Services, Public Health Service, U.S.: Washington, DC, USA, 1988.
- [17] U.S.A Census Bureau. Intercensal Estimates of the Resident Population for Counties and States: 1 April 2000 to 1 July 2010, New York State. Available online: <http://www.census.gov/popest/data/intercensal/county/tabc/CO-EST00INT-01/CO-EST00INT-01-36.csv> (accessed on 13 December 2013).
- [18] U.S.A Census Bureau. Resident Population Data—2010 Census. Available online: <http://www.census.gov/2010census/> (accessed on 13 December 2013).
- [19] Fotheringham, S., Brunsdon, C. and Charlton, M. (2000). Quantitative Geography: Perspectives on Spatial Data, SAGE Publications Ltd.. London

# **IMPACT OF COMMON ORGANICS ON CELLULAR GLYCOLYSIS AND THE DIFFERENTIAL SURVIVAL OF LUNG FIBROBLAST AND LUNG CARCINOMA CELL LINES**

**Ibrahim O. Farah**

Department of Biology, Jackson State University, Jackson, MS 39217

## **ABSTRACT**

Tumor growth and abnormal cell survival were shown to be associated with a number of cellular metabolic abnormalities revealed by impaired oral glucose tolerance, depressed lipoprotein lipase activity leading to hypertriglyceridemia, and changes in amino acid profile as evidenced by increased plasma free tryptophan levels in patients with breast, lung, colon, stomach, and other cancers from various origins. The above findings seem to relate to or indicate a shift to non-oxidative metabolic pathways in cancer. In contrast to normal cells, cancer cells may lose the ability to utilize aerobic respiration due to either defective mitochondria or hypoxia within the tumor microenvironments. Glucose was shown to be the major energy source in cancer cells where it utilizes aerobic /anaerobic glycolysis with the resultant lactic acid formation. The role of energetic modulations and use of glycolytic inhibitors on cancer/normal cell survival is not clearly established in the literature. We hypothesize that natural intermediates of glycolysis and the citric acid cycle will differentially and negatively impact the cancer phenotype in contrast to their no effects on the normal cell phenotype. Therefore, the purpose of this study was to evaluate six potential glycolytic modulators namely, Pyruvic acid, oxalic acid, Zn acetate, sodium citrate, fructose diphosphate (FDP) and sodium bicarbonate at  $\mu\text{M}$  concentrations on growing A549 (lung cancer) and MRC-5 (normal; human lung fibroblast) cell lines with the objective of determining their influence on visual impact, cell metabolic activity, cell viability and end-point cell survival. Exposed and non-exposed cells were tested with phase-contrast micro-scanning, survival/death and metabolic activity trends through MTT-assays, as well as death end-point determinations by testing re-growth on complete media and T4 cellometer counts. Results showed that oxalic acid and Zn acetate both influenced the pH of the medium and resulted in differential massive cell debris within the exposure period. Pyruvic acid, sodium citrate, sodium bicarbonate and FDP did not cause pH changes; however, they caused detectable cell disfigurement and loss of metabolic activity, viability and survival/ death end points with the resultant death of the A549 cell line. The MRC-5 cell line was differentially unaffected by exposure to pyruvic acid, sodium citrate, sodium bicarbonate, FDP and Zn acetate, underwent complete recovery and remained both attached and healthy for 6 weeks upon subculture when transferred to a new complete medium. Oxalic acid did not show differential modulation with the consequent loss of survival and death of the MRC-5 cell line. Phase contrast, metabolic activity, cell counts as well as death end-point findings confirmed our hypothesis. These studies show the potential possibly for exploiting cellular metabolic differences in cancer control.

**Keywords:** Energetics, MRC-5, A549, Cancer, survival, modulation, glycolytic inhibitors, mitochondria

## **INTRODUCTION**

The need for chemo and /or radiotherapy in addition to medical and surgical treatment for cancer has been rising side by side with the human life expectancy. This need was concurrent with increases in the number of cancer afflictions where one in every four victims is suffering terminal consequences [1, 2]. Most chemotherapeutic agents have negative toxic side effects on healthy normal cellular survival manifested by nausea, vomiting, diarrhea, chronic anemia, hair and weight losses that limit their efficacy and application. There is an ongoing war with this epidemic, and modern technology predominantly indulges in invasive treatments such as chemotherapy and surgery. Unfortunately, these treatments often have serious side effects with a higher probability for recurrences [3]. Noninvasive treatments like chemoprevention, natural products, and cryotherapy were being implemented in medical practices in recent

years [4].

Many studies showed that tumor growth and abnormal cell survival was associated with a number of metabolic abnormalities [5, 6, and 7]. Glucose metabolism, for example, is known to be deranged as frequently revealed, by an impaired oral glucose tolerance due to the extensive reliance of cancer cell on glycolysis as their mode of energy generation with lactic acid as the final product. Protein metabolism was also found to be deranged in cancer patients as revealed by changes in plasma amino acid profile and evidenced by an increased plasma free tryptophan levels in cancer patients. Plasma free tryptophan concentrations were found to be significantly elevated in patients with breast, lung, colon, stomach, and cancers from various origins [8, 9, 10, 11 and 12].

Studies have also shown the existence of

metabolic differences between normal and diseased cells including cancer. Based on these studies, energy metabolism was differentially targeted in brain cancer as based on glycolytic dependency in cancer cells and their great sensitivity to extreme shifts in physiological environment. They showed that cancer cells were unable to adapt to ketone bodies as a fuel for their survival and hence they were eliminated through this differential metabolic environment [4]. Warburg [6, 7], was the first to observe that tumor cells exhibit increases in their glycolytic metabolism and are largely dependent on this pathway for their ATP generation. This phenomenon was attributed to mitochondrial injury, hence the above cellular behavior seems to relate to or pose as a consequence of a shift to non-oxidative metabolic pathway. The role of glucose as the sole source of energy in cancer cells and the influence of glycolysis on tumor survival was not clearly established in the literature, however, we suspected a problem with glucose transport and degradation mechanisms including lactic acid as an end product due to the up-regulation of the lactic dehydrogenase enzyme in tumor cells. Both situations are tumor-specific and could be well controlled specifically in hypoxic tumors [13-26].

The role of energy modulation and the use of glycolytic inhibitors on cancer cell survival are, however, not clearly established in the literature. Therefore, the purpose of this study was to evaluate six potential glycolytic modulators namely, pyruvic acid, oxalic acid, Zn acetate, sodium citrate, fructose diphosphate (FDP) and sodium bicarbonate on actively growing A549 (cancer) and MRC-5 (normal) cell lines. We hypothesize that exposing A549 cells to pyruvic acid, oxalic acid, fructose diphosphate (FDP), sodium citrate and Zn acetate should negatively influence their survival by modulating central energetics, while MRC-5 will not be adversely influenced by such treatment.

## METHODS

**Reagents:** F-12K, Dulbecco's Modified Eagle's Medium (DMEM) culture media, Phosphate- buffered saline (PBS), Trypsin EDTA, Fetal bovine serum (FBS), Penicillin-Streptomycin, A549 human lung cancer cell line, and MRC-5 human normal lung cells line were each purchased from American Type Culture Collection (ATCC) located in Manassas, VA, USA. The analytical grade chemical reagents are pyruvic acid, oxalic acid, sodium citrate; oxaloacetate, sodium bicarbonate, and FDP were purchased from Sigma-Aldrich, Inc. in St. Louis, MO, USA. **Cell Culture:** A549 are adherent

epithelial cell line derived from a human lung carcinoma with an epithelial-like morphology. MRC-5 is human lung fibroblast cells that are often used as "normal" cells. These cells have a fibroblast-like morphology. Both cell types were obtained from the American Type Culture Collection (ATCC; Manassas, VA, USA)

**Cell morphology assay:** Cell morphology and evaluation of cell damage/ death were performed using a Nikon Phase-contrast microscope and images were captured digitally and transferred to a computer for image analysis. **Death End Points Studies:** were performed by transferring cells after exposure to the inhibitors (sodium bicarbonate, pyruvic acid, sodium citrate, FDP, Zn acetate and oxalic acid to new complete media and observation for growth regeneration for a 6 week period. **Cell Metabolic Activity by MTT Assays:** Media used were F12 and DMEM (Dulbecco's Modified Eagle's Minimal Essential Medium; both from ATCC). Complete medium was supplemented with 10% fetal bovine serum (FBS) and 1% streptomycin and penicillin (ATCC). Vials containing the A549 and MRC-5 cells (cryosafe preserved) were thawed by gentle agitation for 2 minutes in a water bath at 37°C. Preparation of cell cultures followed standard inoculation and incubation protocols. On reaching about 90% confluence, both cells were washed with phosphate buffered saline (PBS), trypsinized with 5 mL of 0.25% (w/v) trypsin-0.03% (w/v) EDTA, diluted with fresh medium, counted, and seeded ( $2.5-5 \times 10^5$  cells/ml) in two sets of 96-well microtiter tissue culture plates for cell viability/metabolic activity determination. Aliquots of chemical modulators (200  $\mu$ l of each concentration (0-2000  $\mu$ g/ml were added to growing confluent cells column wise to each of the 96-well plates). The plates (three replicate and two repeats) were incubated for 48 hours. The medium in each well was removed, wells were washed with 200  $\mu$ l of cold PBS, and then 50- $\mu$ l MTT [3-(4,5-dimethylthiazol-2-yl)-2,5-diphenyltetrazolium bromide], working solution in PBS, ATCC) was added column wise to each well and incubated for 2 h and were read with a plate reader. The values obtained per concentration were analyzed using the Excel software and were eventually converted to percentage cell metabolic activity / viability tables to illustrate the metabolic activity/ death trends of the two cell types. . **T4 Cell Analyzer:** Cell Analysis by High Content Cell Analyzer (HCCA), (Nexcelom, Bioscience in Lawrence, MA, USA). The culture begun with 4ml of the F-12k media and 1 ml of A-549 cells in a 5ml flask and also 4 ml of DMEM media and 1 ml of MRC-5 cells in a 5ml flask (Corning). Both flasks were maintained at 37°C and 5% CO<sub>2</sub> and when the cells were confluent they were harvested by trypsinization and suspended in fresh DMEM and F-12k

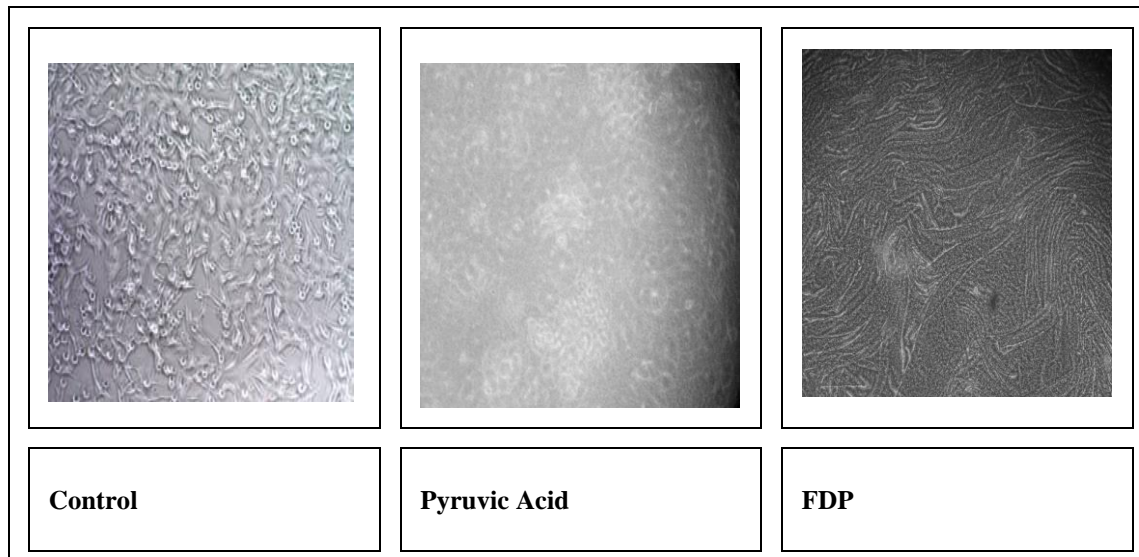
media of 12 different 5ml flasks for each cell line. Once the cells became confluent, cells were exposed to each organic chemical mixture at 2,000 µg/mL concentration for 48 hours in an incubator at 37°C and 5% CO<sub>2</sub>. Afterwards, the cells were trypsinized, centrifuged, and suspended in fresh media (2 mLs) and 20µL of the cell-containing media and 20 µL of trypan blue were mixed and injected into a slide and read by the high content cell analyzer. Chemically exposed cells were compared to control cells in at least duplicate samples/chemical exposure. **Statistical Analysis:** The death and viability parameters of both the A549 and MRC-5 were determined by using ANOVA and the Students' T-test to determine differences that are statistically significant in value. These tests were used to determine the p-value of treated A549 compared to MRC-5 cell line and their respective control. Data was also normalized through the use of percentage, tested for statistical significance as based on means, standard deviation, and p-values.

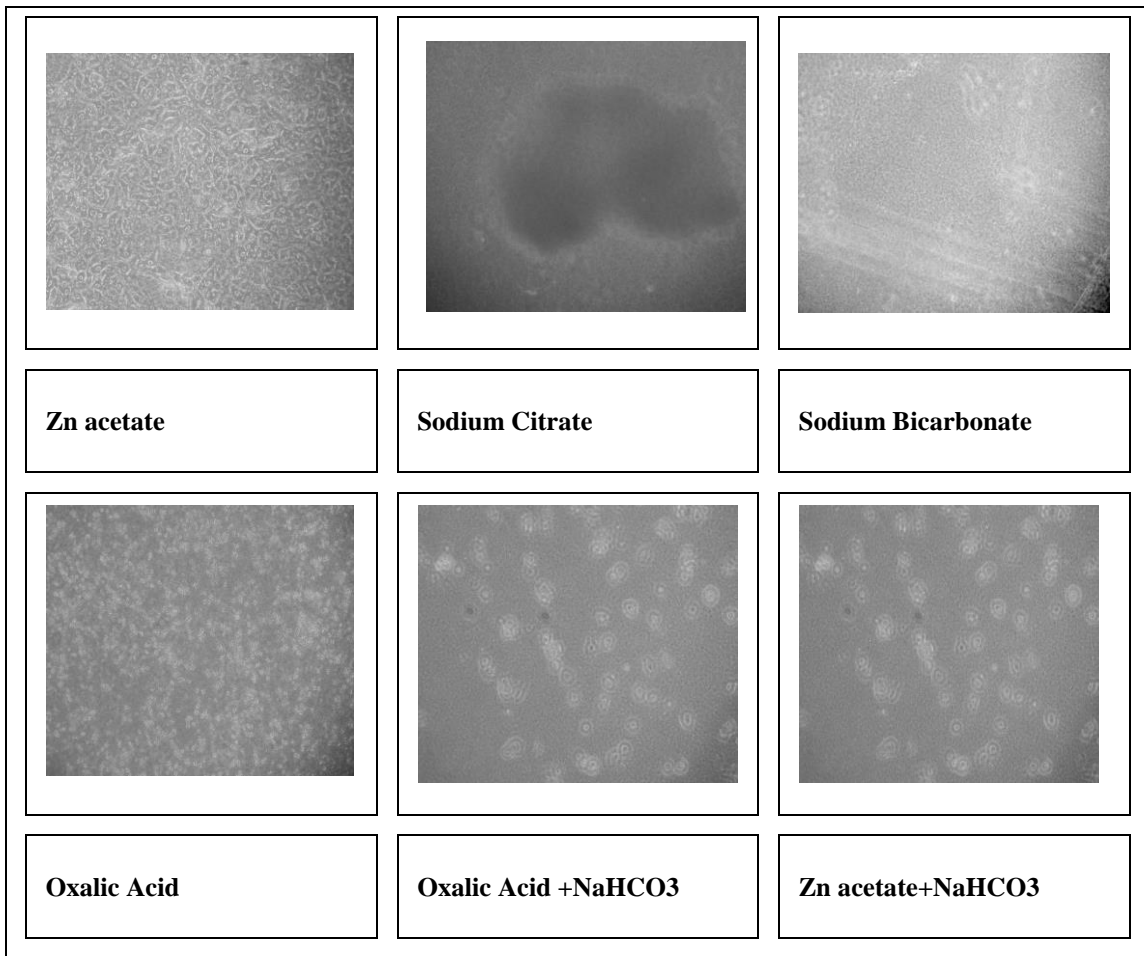
## RESULTS AND DISCUSSION

This study analyzed the in-vitro responses of the A549 and MRC-5 cell lines upon their exposure to pyruvic acid, Sodium Citrate, Sodium Bicarbonate, FDP, Zn

acetate, and Oxalic acid. Results on cell morphology by phase contrast analysis was presented Figures 1A and 1B. As can be seen all of the organics had a negative impact on the cell morphology on the A549 cell line; effects ranged from cell disfigurement, changes in size and morphology, abundance of cell debris and patches of cell damage. In contrast, their effects on the MRC-5 cell line were milder and these cells kept their morphology except for the oxalic acid where the cells showed extensive damage in response to their exposure.

Data on the MTT assay are presented in Figures 2A and 2B. As can be seen, all organics reduced the metabolic activity of both cell lines to a range of 20-60% for the A549 and 20-70% for the MRC-5 (normalized data). Data on tables 1 and 2 confirms this lag in metabolic activity in both cell lines as compared to the controls (untreated). These effects ranged from metabolic injury to metabolic boost depending on the type of organic and the cell line involved. Data presented in table 3 shows the actual cell counts using the T4 cellometer. As can be seen, cell viability ranged between 63.5% to 73.5% for A549 and 88.9% to 99.5% for the MRC-5 cell line showing a differential contrast between their responses to this group of organics.





Figure

1A: Morphological Responses of A549 Cells in response to glycolytic inhibitors

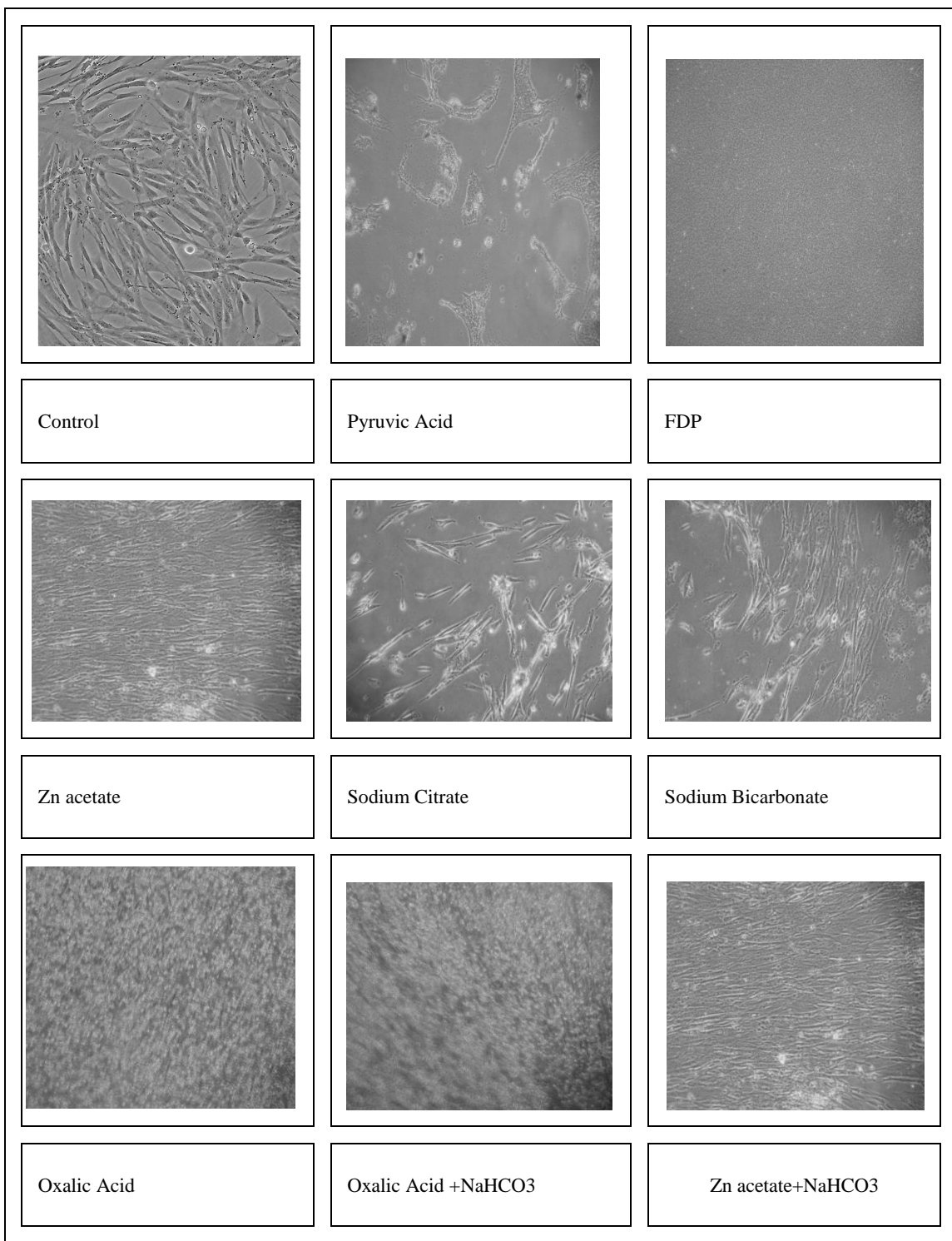


Figure1B: Morphological Responses of MRC-5 Cells in response to glycolytic inhibitors

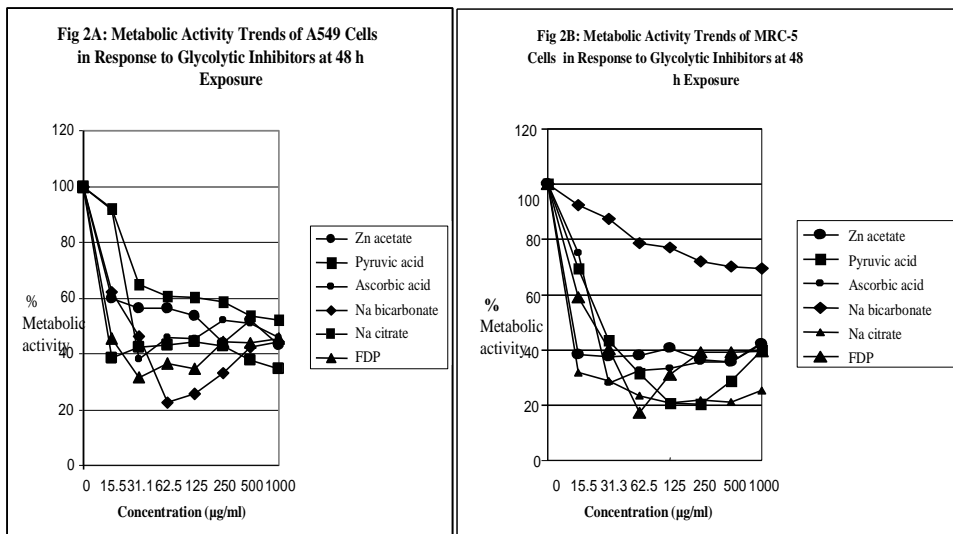


Table 1: ANOVA Mean Comparisons, Statistical Significance, and P-values of A549 cell line using MTT assay data for 2,000 µg/ml of chemical at 48 h of incubation

Chemical	Mean ±SD Control	Mean ±SD Chemical	P- Value	Level of Statistical Significance
Pyruvic acid	<b>1.05±0.48</b>	<b>2.34±0.93</b>	<b>0.011*</b>	Statistically Significant metabolic boost
Sodium Citrate	<b>0.84±0.37</b>	<b>0.35±0.29</b>	<b>0.025*</b>	Statistically significant metabolic injury
NaHCO <sub>3</sub>	<b>0.96±.62</b>	<b>1.84±0.42</b>	<b>0.034*</b>	Statistically Significant metabolic boost
FDP	<b>0.89±0.95</b>	<b>0.27±0.81</b>	<b>0.0139</b>	Statistically Significant metabolic injury
Zn acetate	<b>1.0±0.37</b>	<b>0.35±0.56</b>	<b>0.0009</b>	Highly Statistically Significant metabolic injury
Oxalic acid	<b>0.98±0.91</b>	<b>0.19±0.01</b>	<b>0.0001</b>	Highly Statistically Significant metabolic injury

Table 2: ANOVA Mean Comparisons, Statistical Significance, and -values of MRC-5 cell line using the MTT normalized data.

Chemical	Mean ±SD A549	Mean ±SD MRC5	P- Value	Level of Statistically Significance
Pyruvic acid	<b>155.95±11.59</b>	<b>140.72±23.27</b>	<b>0.714</b>	Not Statistically Significant Metabolic boost in both
Sodium Citrate	<b>110.84±24.43</b>	<b>157.64±19.07</b>	<b>0.022*</b>	Statistically Significant Metabolic boost in MRC-5
NaHCO <sub>3</sub>	<b>115.50±15.48</b>	<b>57.81±8.78</b>	<b>0.027*</b>	Statistically Significant Metabolic injury
FDP	<b>76.20±9.70</b>	<b>49.90±5.40</b>	<b>0.0001*</b>	Statistically Significant metabolic injury
Zn acetate	<b>72.00±3.72</b>	<b>149.00±6.30</b>	<b>0.0027*</b>	Statistically significant metabolic boost
Oxalic acid	<b>22.20±17.10</b>	<b>30.40±3.80</b>	<b>0.5953</b>	Not Statistically Significant metabolic injury

Table 3: T4 Cellometer % Viability Data and T-test Statistical Analysis on the Exposure of A549

Chemicals	Control A549 Cells	Treated A549 Cells	P- Value	Control MRC-5 Cells	Treated MRC-5 Cells	P-Value	Treated A549 Cells	Treated MRC-5 Cells	P-Value
Pyruvic Acid	100%	64.7%	0.049*	100%	99.40%	0.500	64.70%	99.4%	0.003*
Sodium Citrate	100%	63.50%	0.043*	100%	99.15%	0.037	63.50%	99.15%	0.007*
Sodium Bicarbonate	100%	73.50%	0.115	100%	88.90%	0.500	73.50%	88.90%	0.305
FDP	100%	66.25%	0.0042	100%	97.9%	0.5000	66.25%	97.9%	0.0128
Zn acetate	100%	70.2%	0.0036 *	100%	99.5%	0.5000	70.2%	99.5%	0.0081*
Oxalic Acid	100%	66.42%	0.0459	100%	98.60%	0.1344	66.42%	98.60%	0.0002

Data on table 4 shows the actual death endpoint responses of these two cell lines to six organics. As can be seen, there is a clear differential distinction in the response of the MRC-5 in comparison to the A 549 cell line in that, all organics have killed the A549 and that the MRC- 5 cell line was not affected except for the Oxalic acid (even after PH neutralization ). The combination of Zn acetate and NaHCO<sub>3</sub> also showed the same trend as to their effects on the two cell lines.

To this end, collectively the data have shown a clear differential in the response of the two cell lines to six different organics in regards to cell morphology, cellular metabolic activities, cell viability and cell death endpoints;

perhaps due to differences in the cancer cell phenotype metabolism that relies on glycolysis as compared to the oxidative metabolism in the normal cells. Another finding from this study is that morphology, metabolic activity analysis and cell viability by T4 analysis does not reflect the true status of cell death or cell sterility as was seen in this study.

Table 4: Death endpoints of A549 and MRC-5 Cells in Response to Glycolytic Inhibitors (2,000 µg/ml)

Time	A549 Cells			MRC-5 Cells		
	24 h	48 h	72 h	24 h	48 h	72 h
Control	+++**	+++**	+++**	+++**	+++**	+++**
Sodium bicarbonate	+++**	+++**	-*	+++**	+++**	+++**
Pyruvic acid	+++**	-*	-*	+++**	+++**	+++**
Sodium Citrate	+++**	-*	-*	+++**	+++**	+++**
FDP	+++**	-*	-*	+++**	+++**	+++**
Oxaloacetic acid	+++**	-*	-*	+++**	+++**	+++**
Zn acetate + Sodium bicarbonate	+++**	-*	-*	+++**	+++**	+++**
Oxalic acid	+++**	-*	-*	-*	-*	-*
Oxalic acid + Sodium bicarbonate	+++**	-*	-*	-*	-*	-*

+++ denotes the presence of intact attached cells \*\* denotes control continued to be attached and intact for 6 weeks in new media. -\* denotes effects after transfer of cells to new medium and following up growth and attachment for 6 weeks and the result being negative.

The assessments performed in this study proved that pyruvic acid is effective in the treatment of lung cancer due to its ability to destroy the lung cancer cell line A549 without effects on the MRC-5 normal lung fibroblast cell line. From the research of others, it was shown that pyruvic acid might actually contribute to the proliferation of cancer cells; in contrast to our findings [17, 18, and 19]. In 1997, Biswas and others with the Indian Institute of Chemical Biology in Calcutta concluded that methylglyoxal (an aldehyde form of pyruvic acid) could hinder glycolysis and mitochondrial respiration due to its ability to inhibit glucose utilization and glucose 6-phosphate (G6P) and L-lactate formation in the whole EAC cells [20].

The assessments used during this study also supported sodium citrate are an effective candidate for lung cancer therapy due to its ability to aid in the differential destruction of A549 cells. In 2007, Bucay from the Hospital Angeles Lomas in Mexico evaluated the mitochondria as a cause of cancer and suggested the inhibition of glycolysis with citrate as a cancer treatment option. He proved that citric acid inhibits the basic enzymes that participate in mitochondrial metabolism, which could contribute to eliminating cancerous cells [3]. This study showed that sodium bicarbonate was an effective candidate for killing lung cancer cells due to its ability to induced decline of A549 cells; perhaps due to its inhibition to the lactate dehydrogenase enzyme that is very essential in the generation of ATP for the cancer phenotype. In 2007, Mark Sircus with the International Medical Veritas Association completed news commentaries concluding that sodium bicarbonate produces an extreme amount of alkalinity, which allows more oxygen into the cancer cells than they can tolerate [29].

The assessments performed in this research showed that FDP has a potential in the treatment of lung cancer due to ability to aid in the differential decline of cell viability of A549 cells in comparison to its positive effects on the viability of the MRC-5 cell line. In 2011, Diaz-Ruiz and colleagues conducted research on the Crabtree effect and it was concluded that fructose 1,6 biphosphate acts as a regulator of oxidative phosphorylation and contributes to the development of Crabtree effect in explanation for the assay findings with regards to the A549 cell lines [30].

Our assessments in this study supports that zinc acetate is an effective agent for lung cancer treatment, which corresponds to earlier research by others showing that zinc acetate is an effective anti-proliferation agent in the

treatment of prostate cancer [31]. The assessments that are used during this research also showed that oxalic acid is an effective anti-proliferative agent in lung cancer which corresponds to earlier research by Buc et al. showing that oxalic acid inhibits glycolysis at the pyruvate kinase step with an increase of phosphoenolpyruvate, a decrease in lactate and pyruvate production and a reduction of glycolytic flux that will explain its differential efficacy on the A549 cell line [5]. These potential effective roles of organics in the differential destruction of lung cancer warrants further investigations including dosage, exposure time and the possibility of combining them to synergize the destruction of lung cancer cells.

## CONCLUSIONS

Glucose is the major energy source in cancer cells where it utilizes both aerobic and anaerobic glycolysis with the resultant lactic acid formation. Therefore, cancer cells in contrast to normal cells were unable to utilize aerobic respiration due to either defective mitochondria or hypoxia within the tumor microenvironments. Oxalic acid influenced the pH of the medium and resulted in massive cell debris within the exposure period. Pyruvic acid, sodium citrate, FDP, and sodium bicarbonate, and Zn acetate did not cause pH changes or massive cell debris. However, they caused detectable cell disfigurement with the resultant permanent death of the A549 cell line. The MRC-5 cell line, on the other hand, were generally unaffected by exposure to pyruvic acid, FDP, sodium bicarbonate, Zn acetate, and sodium citrate were able to recover upon subculture and remained attached and healthy. Our data also showed that neither cell morphology and MTT assay, nor the T4 cell counts were sufficient to predict correctly the fate of these exposures as it relates to the death endpoints for these cell lines. We conclude that the A549 cell line showed differential metabolic trends and responses to the organic glycolytic inhibitors as compared to the MRC-5 cell line. This study supports the plausibility of the use of glycolytic inhibitors for the differential destruction of cancer cells *in vitro* and expresses the potential for exploiting cellular metabolic differences in cancer control.

## ACKNOWLEDGEMENTS

This research is supported by NIH/NCRR RCMI grant # G12-MD007581.

## REFERENCES

1. ACS, NCHS\_CDC. Cancer Statistics. Cancer Facts and Figures for 2014. P 4,
2. Warburg, Otto. (1956). "On the Origin of Cancer Cells." *Science*. <http://www.sciencemag.org>., 2007.
3. Bucay, H. "The biological significance of cancer: Mitochondria as a cause of cancer and the inhibition of glycolysis with citrate as a cancer treatment" *Medical Hypotheses*, Volume 69, Issue 4, Pages 826-828A, 1989.
4. Seyfried, TN. and Mukherjee, P. Targetting energy metabolism in brain cancer. *Nutrition and Metabolism* 2:30-51, 2005.
5. Buc, S. Demaugre, M. Moncion and N. Leroux "Metabolic consequences of pyruvate kinase inhibition by oxalate in intact hepatocytes". *Biochemie*. 63(7): 595-602, 1981.
6. National Cancer Institute "Understaning Cancer Series: Cancer". [www.cancer.gov](http://www.cancer.gov).2006.
7. Za XI, and Guppy, M. Cancer Metabolism facts; fantasy and fiction. *Biochem Biophys.Res..* 313:459-465, 2004.
8. Carew JS. And Huang, P. Mitochondrial defects in cancer. *Mol. Cancer*: 1-9, 2002.
9. Galluzzi L, Larochette N, Zamzami N, Kroemer G "Mitochondria as therapeutic targets for cancer chemotherapy." *Oncogene*. 25(34):4812-30, 2006.
10. Hardie DG. Metabolic control: an new solution to an old problem. *Curr. Biol.* 10:R757-759, 2000.
11. Geschwind, JF.,Giorriades, CS., Ko, YH., and {Pederson, PI. Recently elucidated energy catabolism pathways provide novel treatments in hepatocellular carcinoma. *Expert Rev. Anticancer Ther.* 4: 449-457, 2004.
12. Maher, JC., Kristian, A., and Lampidis, T. Greater cell cycle inhibition and cytotoxicity induced by 2-deoxyglucose in tumor cells treated under hypoxic vs. aerobic conditions. *Cancer Chemother. Pharmacol.* 53:116-122, 2004.
13. Xu, RH., Pelicano, H., Zhou, Y., Carew, JS.,Feng, LI, and Bhalla, KN. Inhibition of glycolysis in cancer cells: A novel strategy to overcome drug resistance associated with mitochondrial respiratory defect and hypoxia. *Cancer Res.* 65: (2): 613-519, 2005.
14. Cuevza, JM, Ostronoff, LK, Ricart, J, Lopez de Heredia, M,De Liegro, CM, and Izquierdo, JM. Mitochondrial biogenesis in liver during development and oncogenesis. *J. Bioenerg. Biomembr.* 29(4): 365-377, 1997.
15. Brand, MD. The effeciency and plasticity of mitochondrial energy transduction. *Biochemical Society Trasactions*. Vol.33, part 5: 897-404, 2005.
16. Pederson, P. Energy blocker kills big tumors in rats. John Hopkins Medicine, Office of Communications; 2004.
17. St. John, T. "With Every Breath: A Lung Cancer Guidebook." [www.lungcancerguidebook.org](http://www.lungcancerguidebook.org)., 2003.
18. Marceline, T., et al. Fructose-1,6 biphosphate preserves adenosine triphosphate but not intracellular pH during hypoxia in respiring neonatal rat brain slices. *Anesthesiology*. 88(2):461-472, 1898.
19. Liu, H., Savaraj, N., Priebe W, and T.J. Lampidis "Hypoxia increases tumor cell sensitivity to glycolytic inhibitors: a strategy for solid tumor therapy (Model C)." *Biochem. Pharmacol.* 64(12): 1745-51, 2002.
20. Wu, M, Neilson A, Swift A, Moran R, Tamagnine , Parslow D, Armistead S, Lemire K, Orrell J, Teich J, Chomicz S,
21. Ferrick D. "Multiparameter Metabolic Analysis Reveals a Close Link between Attenuated Mitochondrial Bioenergetics and Enhanced Glycolysis Dependency in Human Tumor Cells." *Am J Physiol.* 2006.
22. Chesney J. "6-phosphofructo-2-kinase/fructose-2,6-biphosphate and tumor cell glycolysis." *Curr Opin Clin Nutr Metab. Care.* (5):535-9, 2006..
23. Galliano H, Martin DS, Xu RH, Huang P. "Glycolysis inhibition for anticancer treatment." *Oncogene*. 25(34):4633-46, 2006.
24. Kroemer G. "Mitochondria in cancer." *Oncogene*25 (34):4630-2, 2006.
25. Nociari, M., Shalev, A., Benias, P. , and Russo, C. "A novel one-step, highly sensitive fluorometric assay to evaluate cell-mediated cytotoxicity." *J Immunol Methods*. Vol.78, 221-27, 1998.
26. LideD.R. "Handbook of Data on Organic Compounds, 3<sup>rd</sup> ed; CRC Press: Boca Raton, FL. p.4386, 1994.
27. Roudier, Bachelet, and Perrin "Pyruvate reduces DNA damage during hypoxia and after reoxygenation in hepatocellular carcinoma cells." Vol. 274 Issue 19 pp. 5188-98, 2007.
28. Roudier, B., and Perrin, A. "Pyruvate reduces DNA damage during hypoxia and after reoxygenation in hepatocellular carcinoma cells." Vol. 274 Issue 19 pp. 5188-98, 2007.
29. Biswas, S., Ray, M., Misra, S., Dutta, D.P., and Ray, S.: Selective inhibition of mitochondrial respiration and glycolysis in human leukaemic leucocytes by methylglyoxal. *Biochem J.* 323(Pt 2): 343-348. 1997PMCID: PMC2128325.
30. Sircus, M. The Changing Landscape of Cancer. Natural Allopathic Approach to Treating Cancer. E-Book, 208, 2007.
31. Diaz-Ruiz,R., Rigoulet, M., and Devin, A. The Warburg and Crabtree effects: On the origin of cancer cell energy metabolism and of yeast glucose repression. *Biochem. Biophys. Acta* 2011.
32. Sliwinski, T., Czechowska, A., Kolodziejczak, M., Jajte, J., et. al. Zinc salts differentially modulate DNA damage in normal and cancer cells. *Cell Biology International* 33 (2009) 542e547.

# A HYBRID SEQUENCE-SPECIFIC OLIGONUCLEOTIDE-ELISA METHOD FOR RAPID DETECTION OF BACTEREMIA

D. Olga McDaniel<sup>1,2</sup>, Jason Guillot<sup>2</sup>, Larry S. McDaniel<sup>2,3</sup>, William W. Turner<sup>1,2</sup>, Ross Fremin<sup>1</sup>, Gita Subramony<sup>1</sup>, Mark Williams<sup>1,2</sup>

<sup>1</sup>Department of Surgery, <sup>2</sup>School of Medicine, <sup>3</sup>Department of Microbiology  
University of Mississippi Medical Center, Jackson, Mississippi

## ABSTRACT

The rapid diagnosis of bacteremia is essential to the efficient and appropriate antimicrobial management of the patients with sepsis. We tested the practical application and sensitivity of PCR technology in a hybrid assay using sequence-specific oligonucleotide (SSO) probes and an enzyme linked immuno-assay (ELISA) technique for the detection of bacteremia. Strains of bacteria frequently identified in surgical intensive care unit patients were tested. In the SSO-ELISA technique, species specific probes for detection of 2 staphylococci (*S. aureus* and *S. epidermidis*), 4 streptococci (group G, group C, *S. agalactiae*, and *S. pneumoniae*) and *Enterococcus faecalis* were immobilized onto streptavidin treated polystyrene 96-well plates. Then biotin labeled PCR amplified DNA was captured by the immobilized probes. Streptavidin-alkaline phosphatase enzyme conjugate (SA-AP) was used to bind to the biotinylated targets. Positive signals were detected based on the intensity of color interpreted by a programmed ELISA reader. Our assay format currently allows simultaneous analysis of 12 test samples and the detection of seven common gram-positive clinical isolates in less than 5-6 hours. This is a highly versatile technique for detection of other bacteria and microorganisms. It could provide a rapid, sensitive and cost effective diagnostic method for identification of microorganisms causing bacteremia. In addition, the technique is simple and suitable for the clinical laboratory settings with the potential for automation, and integration into the laboratory electronic data-information system.

**KEY WORDS:** Bacteremia, Diagnosis, DNA, ELISA, Rapid-detection, SSO-PCR

## INTRODUCTION

Rapid detection of blood stream infections (BSIs) and appropriate antimicrobial treatment may facilitate more efficient management of patients with bacteremia and/or sepsis. Mortality rates related to sepsis remain high in spite of advances in pharmacologic agents, improvement in infection control and clinical management of patients (1). Inadequate antimicrobial therapy during first 24 hours of patient's admission results in a significant decline in survival (2, 3). Standard diagnosis of bacteremia mainly relies on culture-based testing, which requires at least 48 to 72 hours for completion. Although molecular methods based on nucleic acid testing (NATs) demonstrated more rapid diagnoses and are highly sensitive, blood cultures are still considered the gold standard for diagnosis of bacteremia. However, the NATs are routinely used to identify many microbial pathogens, and have provided a significant technological advantage for rapid identification of various microorganisms (4-6). Nonetheless, technically, some are complex and can be cumbersome in a clinical laboratory setting. This study describes a simple procedure allowing rapid identification of species specific bacterium from a mixed amplified sample, using patient's blood. The procedure consists of a hybrid assay based on PCR and ELISA format. Currently, this technique allows detection and identification of selected gram-positive bacteria in less than 5-6 hours and may provide a rapid, sensitive and cost effective detection method for identification of microorganisms commonly cultured from patient's blood diagnosed with bacteremia or sepsis.

## MATERIALS AND METHODS

### Bacterial strains and DNA isolation

The bacterial strains used in this study were obtained from hospital clinical laboratory at the University of Mississippi Medical Center. Bacteria were obtained in the form of isolated cultures on agar plates. Prior to DNA extraction, each sample was streaked on blood agar and was examined by Gram staining to confirm purity and Gram reaction. Overnight cultures were washed with chilled STE (100mM NaCl, 10mM Tris, 1mM EDTA) and quantified by spectrophotometer. Then the DNA was extracted using the instruction provided by the manufacturer (DNeasy kit; Qiagen, Valencia, CA). The extraction of DNA from blood was performed using a modification of the *Purescript Capture Column* method (Gentra Systems, Minneapolis, MN). Briefly, 400 µl aliquot of whole blood was subjected to red blood cell lysis-buffer. Nucleated cells were recovered by centrifugation for 3 minutes at 10,000 rpm. The cell pellet was resuspended in 200 µl of lysis buffer (TE containing 50-100 µg/ml of lysostaphin), then was applied to a capture column. The DNA extraction was performed according to the manufacturer's instruction.

### Estimation of sensitivity

The sensitivity of bacterial detection by PCR in the blood samples was initially tested with *S. aureus*. *S. aureus* was grown in Todd-Hewitt medium to approximately  $2.8 \times 10^6$  colony forming units (CFU)/ml. Tenfold serial dilutions of the bacterial culture was prepared, and 50 µl of each dilution was inoculated into 400 µl of healthy donor blood. Then 50 µl of each blood

sample was plated on blood agar plates to estimate the bacterial CFU in the blood. The sensitivity of bacterial detection by PCR in the blood samples was initially tested with *S. aureus*.

#### Bacterial cell counts via PCR

DNA was extracted from blood samples as described above. Prior to PCR analysis, reagents (buffer, nucleotides and primers) were filtered through a Centricon-100 centrifugal filter device (Millipore, Millipore Corporation), to reduce the amount of endogenous contaminating DNA. For PCR analysis, two primers (DG74 and 143SA) corresponding to a region within the 16S ribosomal RNA gene were used to amplify gram positive bacterial DNA (7). The same PCR protocol was utilized for both bacterial DNA extracted from cultures and from blood samples.

#### Evaluation of probe specificity

Probe specificity was tested by sequence specific oligonucleotide (SSO) hybridization (8). For detection of selected gram-positive bacteria, the DNA was amplified with group specific primers (Table 1) and hybridized to the SSO probes. The hybridization blot was prepared using 2 µl each of the amplified products, blotted onto Nytran membranes using a 96-well manifold (8). The blots were hybridized with  $^{32}\text{P}$ -labeled SSO-probes (9). Six sequence-specific probes (listed in Table 1) were used for identification of *S. aureus*; *S. capitis*; *S. epidermidis*; *S. gp G*; *S. agalactiae*; *S. pneumoniae*; *S. gp C* and *E. faecalis*. In addition, a positive control (*S. pneumoniae*) and a negative control were subjected to the same SSO hybridization analysis.

#### SSO-ELISA Assay

Maxisorb 96-well flat bottom plates (Nunc, Nalge Nunc International Corporation, USA. [www.nuncbrand.com](http://www.nuncbrand.com)) were used to develop this assay. The plates were coated with 100 µl of Streptavidin (5 µg/ml) per plate. To optimize probe concentration as well as to determine the sensitivity of probe sequence, two-fold decreasing serial dilutions of each probe (500-1 pmol), was immobilized in a 96-well flat bottom plate, wells (1-10), and wells 11-12 were blanks. The biotin incorporated PCR product of bacterial DNA (total 50 µl) was tested in the plate according to the manufacturer instruction provided in the ELISA kit (Invitrogen-BRL-Gibco), as previously described (10). Positive signals were detected based on the absorbance at 405 nm interpreted by a programmed ELISA reader (Dynex Technologies Inc. Chantilly, VA).

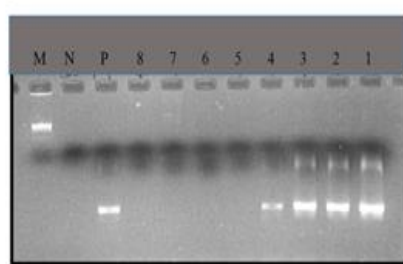


Figure 1. Amplification pattern of *S. aureus* initiated at ten fold decreasing concentrations of DNA from blood sample. M: Standard Marker; N: Negative control; P: Positive control. 1-4: Positive amplification; 5-8: No amplification was detected

Table 1. Amplification Primers and SSO-probes

ID	Specificity	Sequences
DG74	Universal	5'-agg-agg-tga-tcc-aac-cgc-a-3'
143SA	Universal	5'-gan-gac-gtc-aar-tcn-tca-tgc-3'
P1	<i>S. epidermidis</i>	5'-ccg-gtg-gag-taa-cca-ttt-gga-gct-3'
P2	<i>S. aureus</i>	5'-ccg-gtg-gag-taa-cct-ttt-agg-agc-3'
P3	<i>S. gp G</i>	5'-cgg-tga-ggt-aac-cta-tta-gga-gcc-3'
P4	<i>S. agalactiae</i>	5'-cgg-tga-ggt-aac-ctt-tta-gga-gcc-3'
P5	<i>S. gp C</i>	5'-cgg-tga-ggt-aac-cgt-aag-gag-cc-3'
P6	<i>S. pneumoniae</i>	5'-aac-tga-gac-tgg-ctt-taa-gag-att-a-
P7	<i>E. faecalis</i>	5'-cgg-tga-ggt-aac-cct-ttt-gga-gcc-3'

## RESULTS

The sensitivity of detection of bacterial DNA in blood samples was examined using the generic amplification primers DG74 and 143SA. The amplification pattern of the *S. aureus* DNA extracted from blood is shown in Figure 1. At 45 cycles, we observed amplification bands with decreasing density (samples 1-4), in ethidium bromide-stained agarose gel, with maximum detection at a dilution ( $1.38 \times 10^2$ ) corresponding to 1-2 CFU/µl. Incorporating the dilution factors, it was evident that the 1 µl of DNA sample that was utilized for tubes 5-9 in PCR assay contained no bacterial DNA (Figure 1). The SSO hybridization pattern is shown in Figure 2.

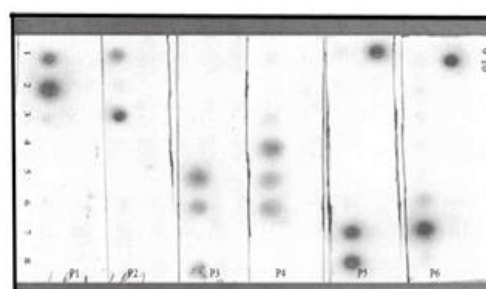


Figure 2. SSO-dot blot hybridization patterns. 1. *S. capitis*, 2. *S. epidermidis*, 3. *S. aureus*, 4. *S. agalactiae*, 5. *S. gp G*, 6. *E. faecalis*, 7. *S. pneumoniae*, 8. *S. gp C*, 9. *S. pneumoniae*, 10. Negative control. P1-P6 are SSO probes.

Although probes such as *S. epidermidis*, *S. aureus*, and *S. pneumoniae* were very specific, *S. capitis*, *S. gpG*, *S. gpC* and *S. agalactiae* were slightly cross-reactive within the species specificity. The *S. gp C* was as equally as *S. pneumoniae* reactive with *S. pneumoniae* probe, whereas, *S. pneumoniae* was not reactive with *S. gp C* probe. The probe sensitivity was evaluated within an OD reading range of 1.3-4.5, of which less than 1.3 was indicative of a weak signal and 4.5 was a strong signal as compared to reactivity of the negative control (Figure 3). *S. epidermidis*, *S. pneumoniae* and *S. gp C* were most sensitive and

were detectable at minimum SSO-probe concentration of about 15.63 pmol (well #6, OD of 1.45 and 1.68 respectively). *S. agalactiae*, *S. gpG* and *E. faecalis* (well #4, OD of 1.35 each) and *S. aureus* (well #3, OD of 1.9) were detectable at a level of 31.25 pmol and 125 pmol respectively. A summary of test result and orientation of the SSO-probes in the plate is given in Table 2. There was cross-reactivity between *S. gp G*, *E. faecalis* and *S. agalactiae*, however, intensity of color development was less within their respective detection threshold. *S. gp C* was cross-reactive with *S. pneumoniae* but *S. pneumoniae* was very specific

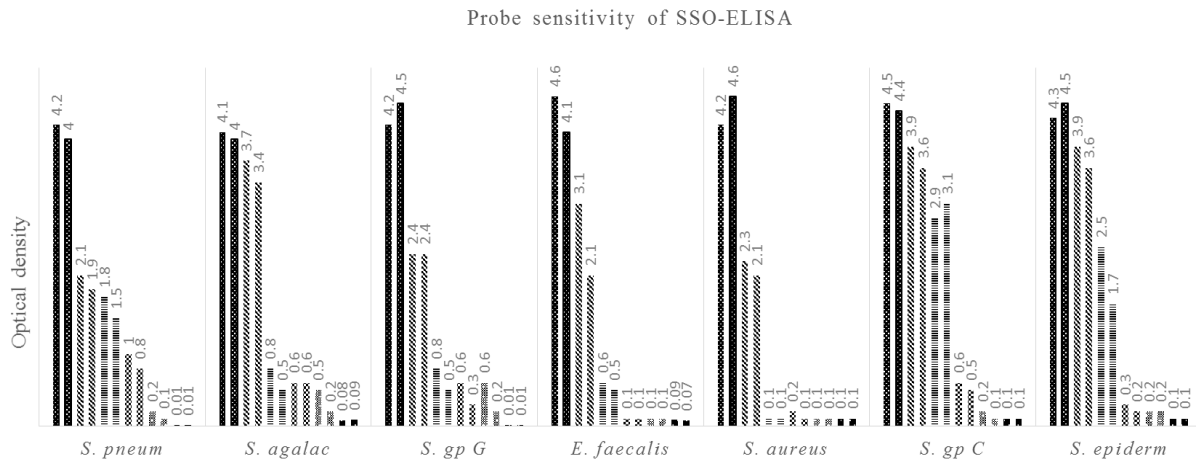


Table 2. Microtiter plate orientation and sample identification

Probes	<i>S. epi</i>	<i>S. aur</i>	<i>S. gp G</i>	<i>S. agal</i>	<i>S. gp C</i>	<i>S. pneum</i>
Control	+	+	+	+	+	+
<i>S. epidermididis</i>	+	-	-	-	-	-
<i>S. aureus</i>	-	+	-	-	-	-
<i>S. agalactiae</i>	-	-	-	+	-	-
<i>S. gp G</i>	-	-	+	+	-	-
<i>E. faecalis</i>	-	-	+	+	-	-
<i>S. pneumoniae</i>	-	-	-	-	+	+
<i>S. gp C</i>	-	-	-	-	+	-

## DISCUSSION

A hybrid SSO-ELISA technique described here was designed to detect and identify species specific gram-positive bacteria. This is a simple technique with the potential of detecting bacteria in clinical specimens including blood and body fluids and is highly suitable in the clinical laboratory setting. Current techniques for detection of bacteria in clinical specimens, although highly sensitive and rapid, require careful planning of amplification procedures as well as sophisticated instrumentation (6, 11). The limitation of this technique is the shelf life of the Streptavidin coated SSO probes, which is estimated to be about 3 months, as well as sensitivity of the SSO-probes that specifically

captures virtually all strains of different species. Several laboratories reported the use of PCR-ELISA-based techniques for diagnosis of microorganisms, however, these techniques were developed for the identification of a single microorganism (12, 13). Our technique was adapted, based on the principles, introduced by NUNC, Nalge International, 2000. However, it has been utilized in the field of molecular biology and immunology. In fact, the Gen Trak Inc. adapted such a technique for identification of the HLA class II (DR and DQ) genotypes.

## CONCLUSIONS

We have described a rapid, relatively, easy and highly sensitive method for detection and identification of clinically relevant gram-positive bacteria. This method allows species specific identification and with further development of probes, it could allow unlimited numbers of organisms to be identified by this technique. In addition, the technique is simple and suitable in a clinical laboratory setting with the potential for automation, and integration into the laboratory electronic data-information system.

## ACKNOWLEDGMENTS

This work was supported in part by a fund from the Department of Surgery at the University of Mississippi Medical Center. Additional support was also provided by the National Institutes of Health grant #AI4365.

## REFERENCES

1. Angus DC, van der Poll T. Severe sepsis and septic shock. *New Engl J Med* 2013; 369: 840-851.
2. Harbarth S, Garbino J, Pugin J, Romand J, Lew D, Pittet D. Inappropriate initial antimicrobial therapy and its effect on survival in a clinical trial of immunomodulating therapy for severe sepsis. *Am J Med* 2003; 115:529-535.
3. Kumar A, Ellis P, Arabi Y, et al: Cooperative antimicrobial therapy of septic shock database research group: Initiation of inappropriate antimicrobial therapy results in a fivefold reduction of survival in human septic shock. *Chest* 2009; 136:1237-1248.
4. Reno, W.L., McDaniel, D.O., Turner, W.W., Williams, M.D. Polymerase chain reaction for the detection of bacteremia. *The American Surgeon* 2001; 67:1-5.
5. Barghouthi SA. A universal method for the identification of bacteria based on general PCR primers. *Indian J Microbiol* 2011; 51:430-444.
6. Afshari A, Schrenzel J, Leven M, Harbarth S. Bench-to-bedside review: Rapid molecular diagnostics for bloodstream infection –a new frontier? *Critical Care* 2012; 16:222-233.
7. Greisen, K., Loeffelholz, M., Purohit, A., Leong, D. PCR primers and probes for the 16S rRNA gene of most species of pathogenic bacteria, including bacteria found in cerebrospinal fluid. *J Clin Microbiol* 1994; 32:335-351.
8. Rajalingam R, Mehra NK, Jain RC, Myneedu VP. Polymerase chain reaction-based sequence-specific oligonucleotide hybridization analysis of HLA Class II antigens in pulmonary tuberculosis: Relevance to chemotherapy and disease severity. *J Infectious Dis* 1996; 173:669-676.
9. McDaniel DO, Naftilan J, Barber WH. Limiting detection of an amplification signal for HLA-D region and VNTR genes by 32P-PCR. *Biotechniques*. 1993; 15:140-145.
10. Dave S, Carmicle S, Hammerschmidt S, Pangburn MK, McDaniel LS. Dual Roles of PspC, a surface protein of *Streptococcus pneumoniae*, in binding human secretory IgA and Factor H. *J Immunol* 2004; 173:471-477.
11. Liesenfeld O, Lehman L, Hunfeld K-P, Kost G. Molecular diagnosis of sepsis: New aspects and recent developments *European J Microbiol Immunol* 2014; 4: 1-25. DOI:10.1556/EuJMI.4.2014.1.1
12. Morata, P., Queipo-Ortufil, M., Reguera, J., Garcia-Ordoñez, M., Cardenas, A., Colmenero, J. Development and Evaluation of a PCR-Enzyme-Linked Immunosorbent Assay for Diagnosis of Human Brucellosis. *J Clin Microbiol* 2003; 144-148
13. Gillespie, BE, MatheGw, AG, Draughon, FA, Jayarao, BM, Oliveri, SP. Detection of *Salmonella enterica* somatic groups C1 and E1 by PCR-enzyme-linked immunosorbent assay. *J Food Prot* 2003; 66(12): 2367-2370

# THE SYNERGISTIC EFFECT OF THYMOQUINONE AND EPIGALLOCATECHIN-3-GALLATE ON THE FUNCTIONAL CAPACITY OF CAOV-3 OVARIAN CANCER LIKE CELL LINE

Jennifer L. Harpole, Michelle Tucci, and Hamed Benguzzi

Clinical Health Sciences, University of Mississippi Medical Center, Jackson, MS 39216

## ABSTRACT

Ovarian cancer is the leading cause of mortality among gynecologic cancers. Recent studies have indicated that antioxidant exposure may slow the progression in major neoplastic diseases. The objective of this study was to investigate the synergistic effect of antioxidants Thymoquinone (TQ) and Epigallocatechin-3-gallate (EGCG) using Caov-3 cell line as a model. A total of 144 wells were plated with  $10^5$  Caov-3 ovarian cancer cells. The wells were divided into groups of 72 wells for conventional and sustained delivery, respectively. Each group was subdivided into 4 groups of 6 wells. Group 1 served as control and groups 2, 3, and 4 were treated with TQ (16  $\mu$ M), EGCG (3  $\mu$ g/ml), and TQ + EGCG, respectively. Biomarker evaluations were performed following standard lab techniques. The results of the study revealed: (1) there were no differences in cellular protein concentrations between TQ, EGCG, and control in conventional and sustained delivery for 24 and 48 phases; conversely at 72 hours, protein concentration of TQ was significantly increased in conventional and unchanged in sustained delivery ( $p<0.05$ ) and (2) an increase in nitric oxide following administration of EGCG and combination therapy at 24 and 72 hours regardless of route of administration. Overall conclusion: the results of this study provided the literature with more insights regarding manipulation of ovarian cancer behavior through potent antioxidants such as TQ and EGCG. The results also indicated the use of sustained delivery of TQ + EGCG inhibited the metabolic activities of Caov-3 ovarian cancer cell line in culture.

**Keywords:** Caov -3 ovarian cancer cells, Thymoquinone, EGCG, Conventional Drug Delivery

## INTRODUCTION

According to Schildkraut *et al.*, 2010, ovarian cancer is the leading cause of mortality among the gynecologic cancers [1]. Unfortunately after being treated for ovarian cancer, a high percentage of patients experience relapse of their disease, and the treatment for recurrent disease has not achieved convincing success rates. Therefore, scientific efforts have focused on improving the current treatments [2]. The cause of ovarian cancer is unknown. Approximately 90% of the cancer is sporadic, and the remaining 10% are hereditary [3]. Different reproductive and hormonal factors have been studied to clarify their influence on ovarian carcinogenesis [4]. Ovarian adenocarcinoma can have distant metastasis, but these are most often to the liver or lung [5]. It has been established that the formation and growth of new blood vessels is a critical part for tumor survival, growth, and expansion. Thus, efforts to reduce the growth and spread of ovarian cancer have recently focused on angiogenesis because they are dependent in part on the formation of adequate vascular support [6]. The improvement of drug administration has brought forth the agents that are responsible for eliminating the disabling nausea associated with chemotherapy for ovarian cancer [7]. Caov-3 is an invasive human ovarian papillary carcinoma cell line [8]. It is from an ovarian adenocarcinoma that was harvested from a 54 year old female [9]. Past and current research of antioxidants continues to provide hopeful findings concerning the success of deterring certain disease processes such as cancers [10]. Food items most strongly related to decreased risk for ovarian cancer were raw carrots and tomato sauce. Consumption of fruits, vegetables and food items high in carotene and lycopene may reduce the risk of ovarian cancer [11]. TQ has antioxidant effects and has been shown to protect against heart, liver, and kidney damage in animal studies, as well as having possible anti-cancer effects. It also has analgesic and anticonvulsant effects in animal models [12]. The study of Yi *et al.* (2008) showed TQ effectively inhibited human umbilical vein endothelial cell

migration, invasion, and tube formation [13]. The anti-proliferative effects of EGCG have been demonstrated in many cancer cell lines. It has also demonstrated anti-carcinogenic activities in human and animal models, including cancer of the breast, prostate, stomach, esophagus, colon, pancreas, skin, and lung [14]. EGCG has been shown to block biochemical pathways involved in ovarian tumor growth [15]. Most of the current anticancer drugs are derived from plant sources, which act through different pathways converging ultimately into activation of apoptosis in cancer cells leading to cell cytotoxicity [16].

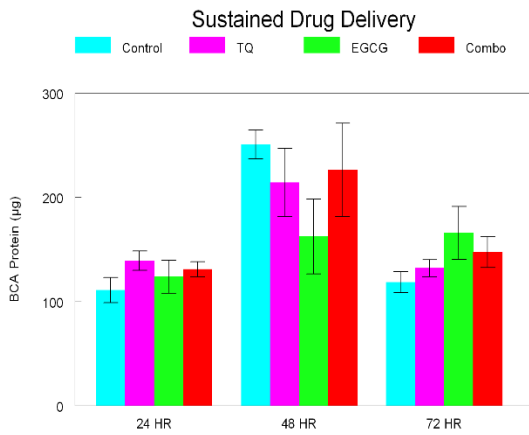
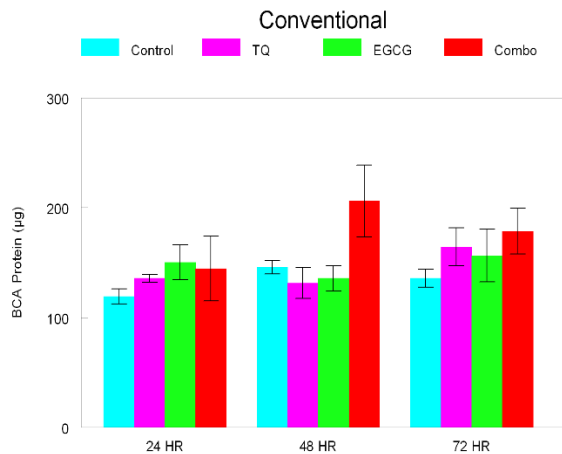
## METHODS

There were 4 groups. Group 1 served as control and groups 2, 3, and 4 were treated with TQ (16  $\mu$ M), EGCG (3  $\mu$ g/ml), and TQ + EGCG, respectively. Each group was terminated at 24, 48, and 72 hours. A total of 144 wells were plated with  $10^5$  Caov -3 ovarian cancer cells, respectively. The wells were divided into groups of 72 wells. Each group was subdivided into 4 groups of 6 wells. The antioxidants were administered using conventional and sustained delivery. The BCA assay is a biochemical assay for determining the total concentration of protein in a solution and was used to measure the metabolic activity of the cells. Nitric oxide can be assayed spectrophotometrically by measuring the accumulation of its stable degradation products, nitrate and nitrite. The nitric oxide assay measured cellular function. The glutathione assay measured the glutathione peroxidase that is used to evaluate cell injury.

## RESULTS

**Cellular Protein:** Conventional (bolus) dosing of TQ, EGCG, or a combination treatment of TQ and EGCG administered to Caov-3 cells did not cellular protein levels above control cells which were maintained in media alone. Cellular proteins were similar between all groups at 24, 48, and 72 hours following bolus dosing

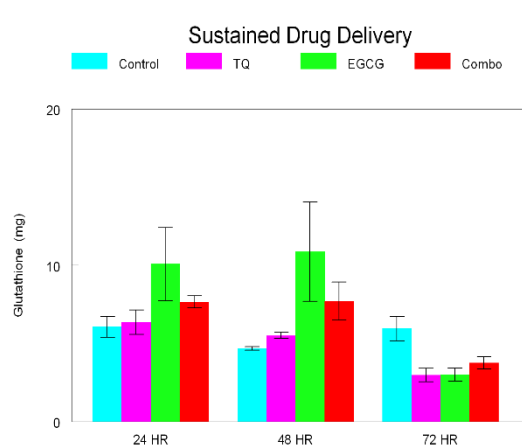
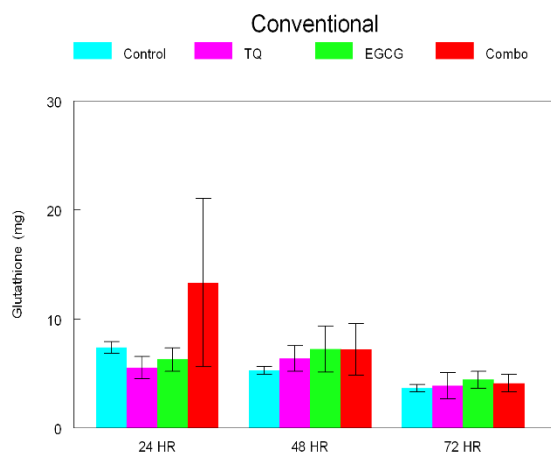
(Figure 1a). Sustained delivery of the antioxidants alone and in combination also showed no differences in cellular protein levels



Figures 1a and 1b. Cellular protein levels were determined following Conventional (a) or sustained delivery (b) of TQ, EGCG or a combination of EGCG and TQ at 24, 48, and 72 hours. The data are expressed as  $\mu\text{g}$  protein  $\pm$  SD.

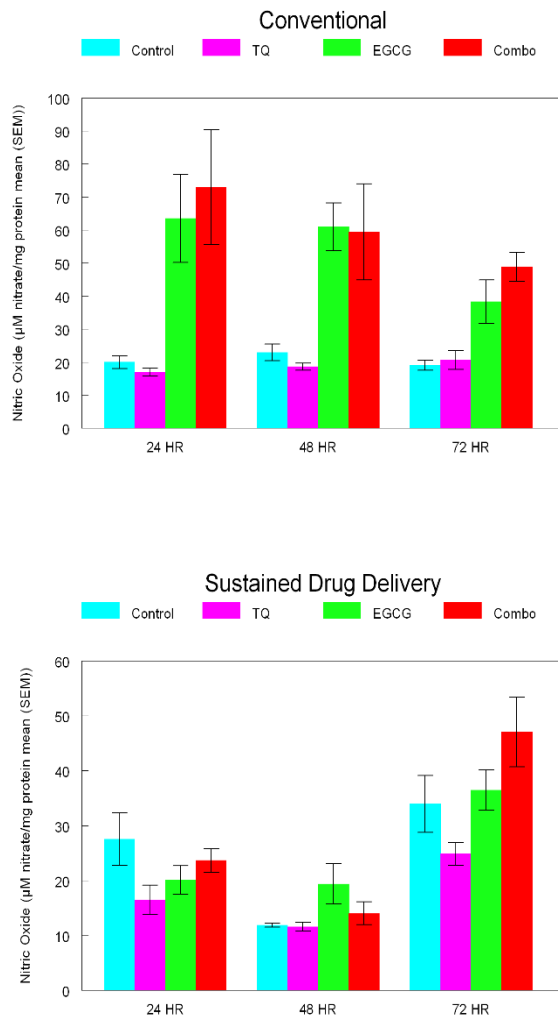
**Intracellular Glutathione Content:** Glutathione levels were increased slightly following bolus dosing of EGCG at 24 hours. This elevation was no longer evident at the 48 and 72 hour time points. No differences in cellular glutathione were detected following treatment with TQ or a combination of EGCG and TQ for the duration of the study when compared to control untreated cells (Figure 2a). Sustained delivery of TQ, EGCG, or combination of the antioxidants did not change intracellular glutathione levels in this cell line for the duration of the experiment (Figure 2b).

when compared to control untreated cells (Figure 1b).



Figures 2a and 2b. Intracellular reduced glutathione levels were determined following Conventional (a) or sustained delivery (b) of TQ, EGCG or a combination of EGCG and TQ at 24, 48, and 72 hours. The data are expressed as  $\mu\text{M}$  reduced glutathione per mg protein  $\pm$  SD.

**Nitric Oxide:** Nitric oxide levels were increased after 24 hours following bolus dosing of EGCG and a combination of EGCG and TQ. The levels in these two treatment groups were still elevated at the 48 hour time period, before returning toward control values by 72 hours (Figure 3a). Nitric oxide was elevated in Caov-3 cells following sustained delivery of EGCG and EGCG+TQ after 48 hours and was maintained over the duration of the study (Figure 3b).



Figures 3a and 3b. Nitric oxide levels were determined following Conventional (a) or sustained delivery (b) of TQ, EGCG or a combination of EGCG and TQ at 24, 48, and 72 hours. The data are expressed as  $\mu\text{M}$  nitrate per mg protein  $\pm$  SD.

## DISCUSSION

Ovarian cancer is the fifth most frequent cause of cancer death in women. Ovarian epithelial cancer accounts for 90% of all ovarian cancers and is the leading cause of death from gynecological cancers in North America. Current chemotherapies for ovarian cancer often lead to resistance or relapse, making it necessary for identification of novel treatments and therapeutic targets. Our study indicates that EGCG alone and in combination with TQ is an effective inducer of nitric oxide in this particular cancer cell. Nitric oxide is a highly reactive molecule within biological systems, reacting with other free radicals, molecular oxygen and heavy metals. It has been suggested that the biological effects of NO can be mediated by

the products of different NO metabolites. Nitric oxide is produced by three isoforms of nitric oxide synthase (NOS). Several studies have shown that all three isoforms of NOS, (iNOS, eNOS and nNOS), have been detected in tumor cells; however, the role of NO in tumor cells is not clearly defined. In human ovarian cancer, iNOS activity has been localized in tumor cells and not found in normal tissue [16]. Several papers suggest that NO may play dual roles in tumor cells. One possible role is to promote angiogenesis a play a role in tumor survival. A second possible suggestion is that NO rapidly reacts intracellularly to form nitrite and nitrate, S-nitroso-thiols or peroxynitrate, and these metabolites are believed to play key roles in mediating many of the NO-associated genotoxic effects. Damage to the DNA may lead to upregulation of tumor suppressor genes; namely, p53.

EGCG has been shown in numerous investigations to upregulate p53, but the mechanism has not been fully elucidated. Our findings suggests that EGCG induces nitric oxide which may be the essential mediator that triggers upregulation of p53 leading to cellular apoptosis.

If there is a correlation between NO and p53 following EGCG administration, then this may be a therapeutic target for treating Ovarian cancer or in cancer cells that express NOS. In addition, our findings show that sustained release is capable of sustaining the nitric oxide response in the Caov-3 cells.

## CONCLUSIONS

The use of antioxidants has proven to offer promising effects as chemo-preventive agents of ovarian cancer. The data of this study suggest that combination therapy with antioxidants is an effective means of generating physiological responses, such as cell suppression, decrease in protein levels, and cell cycle disruption. Future studies are needed to further investigate the possibilities of antioxidant treatment and prevention of ovarian cancer.

These results have indicated new findings which are considered novel. According to the literature, no studies have been conducted following the same treatment protocols. Further investigation of frequent dosing has to be elicited to confirm such outcomes with related research.

## REFERENCES

- [1] Schildkraut, Joellen M., Edwin S. Iversen, Melanie A. Wilson, Merlise A. Clyde, Patricia G. Moorman, Rachel T. Palmieri, Rex C. Bentley, Jeffrey R. Marks, and Andrew Berchuck. "Association between DNA Damage Response and Repair Genes and Risk of Invasive Serous Ovarian Cancer." *Plos ONE*. 5.4 (2010): Print.
- [2] Steffensen, Karina Dahl, Marianne Waldstrom, Rikke Kolby Christensen, Annette Bartels, Nils Brunner, and Anders Jakobsen. "Lack of relationship between TIMP-tumour cell immunoreactivity, treatment efficacy and prognosis in patients with advanced epithelial ovarian cancer." *BioMed Central Cancer Journal*. 10.185 (2010): Print.

- [3] Okuda, Tsuyoshi, Akihiko Sekizawa, Yuditiya Purwosunu, Masaaki Nagatsuka, Miki Morioka, Masaki Hayashi, and Takashi Okai. "Genetics of Endometrial Cancers." *Obstetrics and Gynecology International*. (2010): Print.
- [4] Braem, M. G. M., N. C. Onland-Moret, P. A. van den Brandt, R. A. Goldbohm, P. H. M. Peeters, R. F. P. M. Kruitwagen, and L. J. Schouten. "Reproductive and Hormonal Factors in Association with Ovarian Cancer in the Netherlands Cohort Study." *American Journal of Epidemiology*. 172:10 (2010): Print.
- [5] Sparks, Dorothy A., Daniel M. Chase, Mark Forsyth, Gregg Bogen, and Jon Arnott. "Late presentation of a mucinous ovarian adenocarcinoma which was initially diagnosed as a primary pancreatic carcinoma: a case report and review of the literature." *Journal of Medical Case Reports*. 4:90 (2010): Print.
- [6] Zhu, Pengfei, Yanxia Ning, Liangqing Yao, Mo Chen, and Congjia Xu. "The proliferation, apoptosis, invasion of endothelial-like epithelial ovarian cancer cells induced by hypoxia." *Journal of Experimental and Clinical Cancer Research*. 29:124 (2010): Print.
- [7] Robinson, William R. and Julie Beyer. "Impact of Shifting from Office-to Hospital-Based Treatment Facilities on the Administration of Intraperitoneal Chemotherapy for Ovarian Cancer." *Journal of Oncology Practice*. 6:5 (2010): Print.
- [8] Johnson, Erica L, Rajesh Singh, Shailesh Singh, Crystal M. Johnson-Holiday, William E. Grizzle, Edward E. Partridge, and James W. Lillard, Jr. "CCL25-CCR9 interaction modulates ovarian cancer cell ligation, metalloproteinase expression, and invasion." *World Journal of Surgical Oncology*. (2010): Print.
- [9] "Caov-3." ATCC, 1976. <http://www.atcc.org/ATCCAdvancedCatalogSearch/ProductDetails/tbid/452/Default.aspx?ATCCNum=HTB-75&Template=cellBiology>
- [10] Norwood, Anne A., Michelle Tucci, and Hamed Benghuzzi. "A Comparison of 5-Fluorouracil and Natural Therapeutic Agents, EGCG and Thymoquinone, Delivered by Sustained Drug Delivery on Colon Cancer Cells." *Biomedical Sciences Instrumentation*. (2007): Print.
- [11] Cramer, DW, H Kuper, BL Harlow, and L Titus-Ernstoff. "Carotenoids, antioxidants and ovarian cancer risk in pre- and postmenopausal women." *International Journal of Cancer* 94.1 (2001): 128-34. Web. 14 Jul 2010. <http://www.ncbi.nlm.nih.gov/pubmed/11668487>
- [12] "Thymoquinone." Wikipedia. 2010. Web. <http://en.wikipedia.org/wiki/Thymoquinone>
- [13] Yi, Tingfang, Sung-Gook Cho, Zhengfang Yi, Xiufeng Pang, Melissa Rodriguez, Ying Wang, Gautam Sethi, Bharat B. Aggarwal, and Mingyao Liu. "Thymoquinone inhibits tumor angiogenesis and tumor growth through suppressing AKT and extracellular signal-regulated kinase signalling pathways." *Molecular Cancer Therapy*. 7.7 (2008): 1789-96. Print.
- [14] Kim, Yong Wook, Su Mi Bae, Joon Mo Lee, Sung Eun Namkoong, Sei Jun Han, Byoung Rai Lee, Insu P. Lee, Sang Hee Kim, Young Joo Lee, Chong Kook Kim, Yong-Wan Kim, and Woong Shick Ahn. "Activity of Green Tea Polyphenol Epigallocatechin-3-gallate Against Ovarian Carcinoma Cell Lines." *Cancer Research and Treatment*. 36.5 (2004): Print.
- [15] Spinella, Francesca, Laura Rosano, Valeriana Di Castro, Samatha Decandia, Adriana Albini, Maria Rita Nicotra, Pier Giorgio Natali, and Anna Bagnato. "Antitumor Effect of Green Tea Polyphenol Epigallocatechin-3-Gallate in Ovarian Carcinoma Cells: Evidence for the Endothelin-1 as a Potential Target." *Society for Experimental Biology and Medicine*. (2005): Print.
- [16] Mishra, Tulika, Madhu Khullar, and Aruna Bhatia. "Anticancer Potential of Aqueous Ethanol Seed Extract of *Ziziphus mauritiana* against Cancer Cell Lines and Ehrlich Ascites Carcinoma." *Evidence-Based Complementary and Alternative Medicine*. (2011): Print.
- [17] "Cell Proliferation Assay." KK Biomed Corporation. Retrieved (2010, December 20) <http://www.kkbimed.com/prod0211.htm>

# Frequency Dependence of Focus Localization using Directional Information Measures from the EEG

Joshua Adkinson, Ioannis Vlachos, Leonidas Iasemidis

Biomedical Engineering  
Louisiana Tech University, Ruston, LA

## ABSTRACT

For patients with focal epilepsy, a promising treatment to resolve recurrent seizure activity is resection of the brain tissue responsible for seizure generation (epileptogenic focus). Because of the associated risks with this invasive procedure of removing eloquent tissue, correct localization of the focus is of paramount importance. Computational analysis of recorded intracranial electroencephalographic (iEEG) signals from multiple brain regions can be effective in identifying the epileptogenic focus. Such multi-channel signals ideally require multivariate analysis, in the time or frequency domain, that can also help us understand how different brain regions interact with the focus. We employed the measure of Generalized Partial Directed Coherence (GPDC) in the frequency domain to measure the strength of directional interactions between brain sites from long-term iEEG recordings in 4 patients with focal temporal lobe epilepsy. In 3 out of 4 patients, the maximum directed interactions into brain sites (inflow of information) was found to be statistically significant more frequent ( $p < 0.01$ ) at the epileptogenic focus than other brain sites, and for frequencies greater than 10Hz. In the fourth patient, interactions in the same frequency range generated similar results at the location of the focus, with the exception that these results were not statistical significant at the  $\alpha = 0.01$  level. These preliminary findings indicate that optimal localization of the epileptogenic focus from the EEG by measures of directional information flow requires the employment of higher than lower frequency bands in the respective mathematical analysis.

**Keywords:** GPDC, frequency analysis, focus localization, focal epilepsy

## INTRODUCTION

Epilepsy afflicts approximately 1% of the global population, making it one of the most common neurological disorders [1]. Epilepsy is characterized by intermittent abnormal events (seizures), which result from a sudden onset of synchronous firing of neurons that disrupts the normal operation of the brain. Electrodes positioned on the surface of the head (scalp EEG) or inside the brain (intracranial EEG) can be used to study the various epilepsy hallmarks, such as seizures and interictal (between seizures) epileptiform discharges (spikes or spike-and-wave complexes). Seizure onset is observed as a synchronous neural firing in a well-confined brain region (focal/partial seizures) or globally in both cerebral hemispheres (generalized seizures).

Approximately 60% of all patients with epilepsy experience focal (partial) epilepsy. Seizures emanating from a pathological region (focus) usually propagate across the brain through the connections of the focus with other (non-pathological) brain sites [2]. Once epilepsy is diagnosed in a patient, one of the first treatment methods is to place the patient on a regimen of antiepileptic drugs. Unfortunately, about 30% of all patients with epilepsy are resistant to drug therapy, so, depending on the severity, type of epilepsy and location of the focus, surgical removal of the brain tissue where seizures originate can be employed as a treatment method. To utilize surgery as treatment, accurate detection of the epileptogenic focus is of utmost importance. In clinical practice, in order to determine the focus, iEEG recordings are obtained from the patient for prolonged periods (days) in a properly suited iEEG recording environment, the epilepsy monitoring unit (EMU), until a number of the patient's typical seizures are captured in scalp EEG (phase I) or iEEG (phase II) recordings. Physicians determine the focus by visual inspection of the EEG (typically in 10 sec segments) seeking focal epilepsy characteristics such as interictal

epileptiform discharges and seizure origination brain sites. This procedure is time consuming and requires the scanning of data sets of days in duration. Furthermore, visual inspection of the EEG may fail to detect electrophysiological changes occurring over long periods of time or across a large number of communicating brain sites [3]. Properly developed techniques employing computational analysis of the data could be very efficient and effective in capturing abnormal waveforms associated with epilepsy.

Measuring the functional connectivity using frequency domain-based measures such as Coherence [4], Directed Transfer Function (DTF) [5] and Partial Directed Coherence (PDC) [6] is a growing field of brain research. Coherence measures the synchrony between brain signals but is unable to determine the direction of the involved interactions. PDC and DTF on the other hand allow for estimation of directional interactions, but generally are ill-defined for determination of synchrony. We have used the measure of Generalized Partial Directed Coherence (GPDC) [7], an improvement of PDC, to devise a focus localization algorithm based on the direction of interactions [8]. Herein we expand on that research by investigating if certain frequencies from the iEEG data are better suited to determining the location of the focus.

## METHODS

The data used in this study were recordings from 4 patients with focal temporal lobe epilepsy. The patients underwent surgery so that electrodes could be placed within the brain. Patients 1 and 2 underwent stereotactic placement of bilateral depth electrodes in the hippocampi (RTD1 to RTD6 along the right hippocampus and LTD1 to LTD6 along the left hippocampus, with LTD1 adjacent to the left amygdala and RTD1 adjacent to the right)

amygdala), subdural strip electrodes bilaterally on the orbitofrontal cortex (electrodes LOF1 to LOF4 and ROF1 to ROF4, with ROF1 and ROF1 being most mesial and LOF4 and ROF4 most lateral), and subtemporal strips bilaterally on the temporal cortex (LST1 to LST4 and RST1 to RST4, with LST1 and RST1 being most mesial and LST4 and RST4 most lateral). With this electrode montage, iEEG was recorded from a total of 28 brain sites in these patients. The iEEG from patients 3 and 4 was recorded with a similar electrode montage: stereotactic placement of depth electrodes along the hippocampi with 8-contact flexible depth electrodes with bilaterally symmetric

positioning, in amygdala (LA, RA), mid hippocampus (LH, RH), orbitofrontal areas (LO, RO), and in frontal cortex from superior sagittal region near the supplementary motor area and cingulate (higher electrode numbers were more posterior). This montage provided recording from a total of 40 brain sites. **Figure 1** shows the electrode montages used. Total recording time for each patient ranged between 34 and 156 hours, and all EEG data were either recorded with 200Hz sampling rate or downsampled to 200Hz for estimation of GPDC. Supplementary clinical information on the patients is provided in **Table 1**

**TABLE 1.** Patient clinical data

Patient	Duration of iEEG (hours)	Gender	Clinically assessed focus/foci
1	49	M	Right Hippocampus (RTD)
2	156	M	Left and Right Hippocampus (LTD/RTD)
3	47	F	Left amygdala (LA)
4	34	F	Right amygdala and Right Hippocampus (RA/RH)

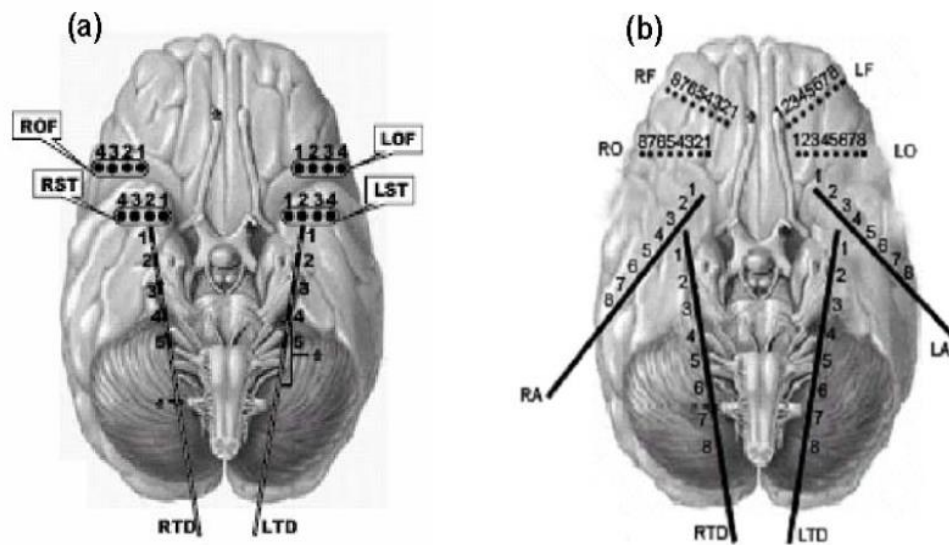


**Figure 1.** Intracranial EEG montages. (a) Electrode montage for patients 1 and 2. (b) Electrode montage for patients 3 and 4.

The directed coupling between EEG signals from different brain sites was estimated by GPDC. If  $X(t) = (X_1(t), \dots, X_n(t))'$  is the  $n$ -dimensional time series created from the recorded EEG signals at  $n$  brain sites, each vector component  $X_i(t)$  denotes the EEG signal recorded at the  $i^{th}$  recording brain site. A vector autoregressive linear model VAR( $p$ ) of order  $p$  can then be constructed for  $X$  as:

$$X(t) = \sum_{\tau=1}^p \gamma(\tau)X(t-\tau) + \epsilon(t) \quad (1)$$

where  $\gamma(\tau)$  are the  $n \times n$  coefficient matrices of the model. The residuals  $\epsilon(t)$  follow a multivariate Gaussian white noise process if the model reliably models the processes. Then, GPDC measures the direct effect of signal  $j$  to  $i$  at frequency  $f$  as:

$$GPDC_{j \rightarrow i}(f) = \frac{|B_{ij}(f)|/\sigma_{ii}}{\sqrt{\sum_{k=1}^n |B_{kj}(f)|^2 / \sigma_{kk}^2}} \quad (2)$$

where  $\sigma_{ii}$  are obtained from the covariance matrix  $S = [\sigma_{ij}]_{i,j=1,\dots,n}$  of the noise process  $\epsilon(t)$ ,  $B_{ij}(f)$  is the  $(i,j)^{th}$  element of the matrix  $B(f) = I - \sum_{\tau=1}^p \gamma(\tau)e^{-i2\pi f\tau}$  and  $I$  is the  $n \times n$  identity matrix.

Because GPDC measures the linear dependence of  $X_i$  on  $X_j$  at a given frequency  $f$ , the set of GPDC values estimated from all brain sites can be considered a weighted, directed network in which the directed coupling into brain site  $i$  from site  $j$  at a given frequency  $f$  is reflected by the value of  $GPDC_{j \rightarrow i}(f)$ .

**Figure 2** shows examples of the dependency of GPDC values on frequency, estimated from a 10 second EEG segment from patient 2. In panel A we see a strong bidirectional interaction between sites LD3 and LD5 over the majority of frequencies. As frequency increases we see that the interaction from LD5 to LD3 increases in strength up to 20Hz and decreases thereafter, whereas in the opposite direction the strength of interaction remains relatively constant over frequencies. In panel B we see that the strength of interaction from site LD5 to LD1 increases as frequency increases up to 30Hz; it remains consistently low in the opposite direction. Panel C shows that, between channels LD3 and LD11, there are very weak (or nonexistent) interactions in both directions over the full available frequency band.

## RESULTS

We applied our focus localization methodology on successive 10 sec non-overlapping epochs from long-term interical iEEG recordings from 4 patients with temporal lobe epilepsy, spanning the full available frequency band (0-50Hz) with a step of 1 Hz. In the estimation of GPDC values, we used a VAR model of order  $p = 7$  as in our previous work [8]. For

Grubb's test, a statistical significance level of  $\alpha = 0.01$  was selected.

The results of our study are presented in **Figure 3**. For patient 1 (first row, left panel), we see an increase in the occurrences of maximum inflow beginning at 5Hz at the clinically determined focus (RTD). This increase in the occurrences of maximum inflow continues at higher than 5Hz frequencies. Gradual increase of occurrence of maximum inflow with frequency also occurs at one site of the contralateral hippocampus (LTD), peaks at around 35Hz and then decreases. Statistically (first row, right panel) we see significantly higher occurrence of maximum inflows first detected at 10Hz at the focus. Detection of statistically significant outliers is found intermittently as frequency increases. Gaps in significance occur when multiple brain sites show frequent maximum inflow.

For patient 2 (second row, left panel), high occurrence of maximum inflow values were found in LTD and RTD. However, statistically (second row, right panel), these were not deemed outliers, implying inability of the algorithm to localize to one focal region at confidence level  $\alpha = 0.01$  (due to the fact that LTD and RTD are both highly active). This is consistent with the fact that patient 2 was the only patient with clinically determined foci in two different hemispheres (LTD, RTD).

Patient 3 (third row, left panel) shows increase in occurrence of maximum inflows beginning at 5Hz at the focus (left amygdala - LA) that continually increases in prevalence as frequency increases beyond 5Hz. This is also observed in the left hippocampus (LH) beyond 25Hz. Statistically (third row, right panel), significant occurrence of maximum inflows to LA begins at 10Hz with a gap between 17Hz and 23Hz. Significant occurrence of maximum inflow is observed in the left hippocampus (LH) at 32-33Hz.

Patient 4 clinical foci were in the right amygdala (RA) and right hippocampus (RH) (Table 1) and did show increased occurrence of maximum inflow (forth row, left panel): in the right amygdala at low frequencies up to 20Hz and the right hippocampus beyond 20Hz. Statistically (forth row, right panel) significant occurrence of maximum inflows occurs in the right amygdala for frequencies up to 18Hz and in the right hippocampus for frequencies greater than 28Hz.

In summary, in all patients, increased occurrence of maximum inflow was observed at the clinically assessed foci at frequencies greater than 10Hz. For 3 of 4 patients, significant occurrence of maximum inflows was also found at the clinically assessed foci at frequencies greater than 10Hz.

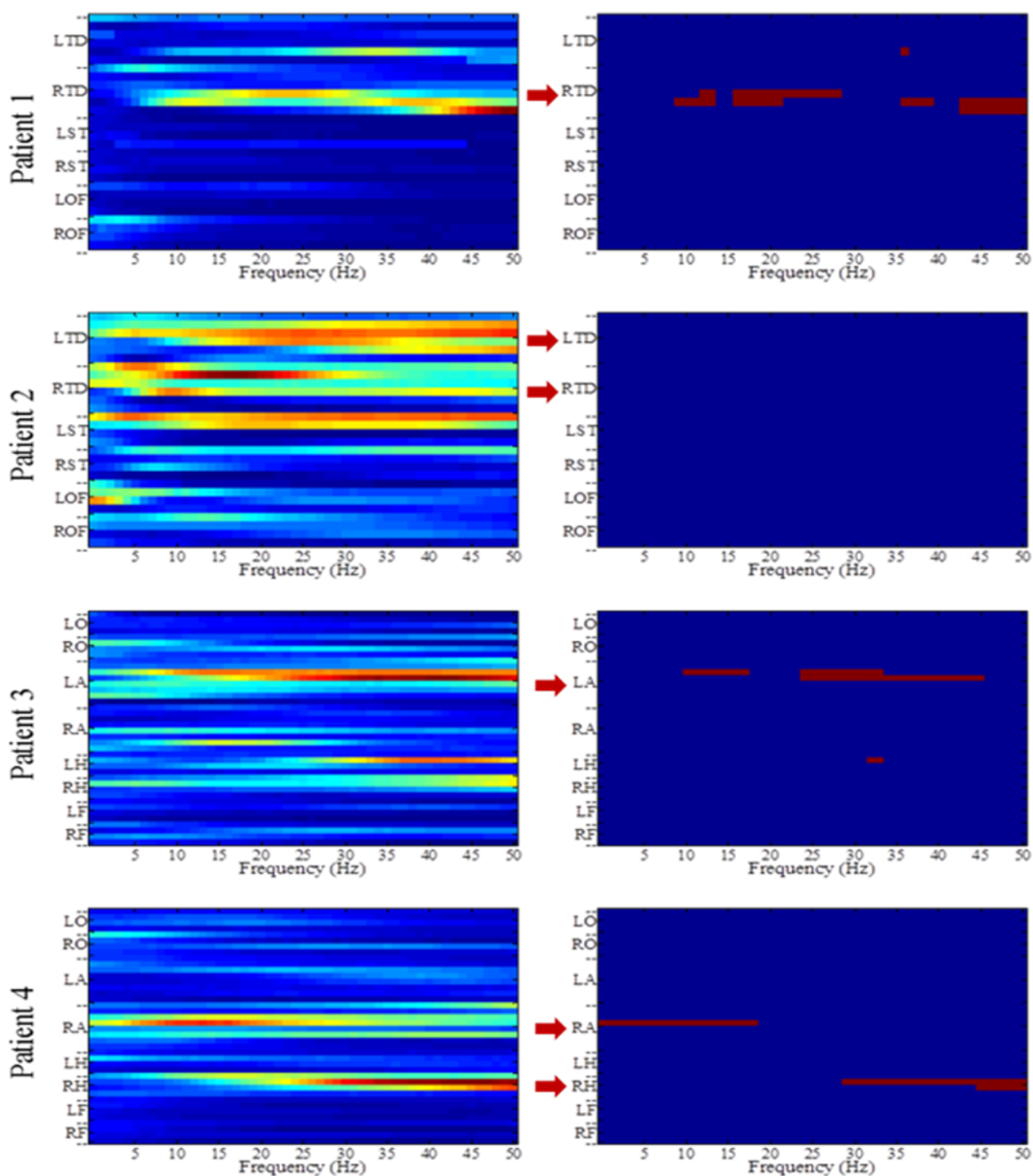


Figure 3. Left panels: Percentage of time over the duration of the whole EEG recording ( $HIF_i(f)$  values – see text) that each brain site  $i$  exhibits maximum information inflow from the rest of brain sites as a function of EEG frequencies  $f$ . Blue color denotes infrequent and red color most frequent maximum inflow. Right panels: Illustration with red color of only the sites with statistically significant percentages of time with maximum inflow ( $HIF_i(f)$ ) as a function of EEG frequencies  $f$ . Red arrows in right panels denote the clinically determined focus (foci) for each patient.

## DISCUSSION AND CONCLUSIONS

The frequency dependence of the interictal localization of the epileptogenic focus by a promising method of EEG analysis that we developed in the past was investigated. The method was applied to the entire EEG datasets (days) recorded from patients with temporal lobe epilepsy. The preliminary results from this analysis show that statistically significant localization of the epileptogenic focus at the  $\alpha = 0.01$  level is best achieved by estimating the directional flows of information in the brain for frequencies higher than 10Hz. This new knowledge should help improve the clinical assessment of epileptic foci from EEG recordings and may lead to new insights in the communication of different brain sites at different frequency bands. It should be noted that the patients were weaned off their antiepileptic drugs (AEDs) during the recording period to increase the probability of seizure occurrence, as necessary for the traditional assessment of epileptogenic focus localization. Since AEDs do affect the EEG spectrum, an indirect effect on the reported results due to AEDs change during the EEG recordings from our patients is possible and remains to be further investigated.

## REFERENCES

- [1] A. K. Ngugi, C. Bottomley, I. Kleinschmidt, J. W. Sander and C. R. Newton, "Estimation of the burden of active and life-time epilepsy: a meta-analytic approach.", *Epilepsia*, vol. 51, no. 5, pp. 883–90, May 2010.
- [2] W. A. Hauser, J. F. Annegers and W. A. Rocca, "Descriptive Epidemiology of Epilepsy: Contributions of Population-Based Studies From Rochester, Minnesota," *Mayo Clinic Proc.*, vol. 71, no. 6, pp. 576-586, Jun. 1996.
- [3] A. Fingelkurts, A. Fingelkurts and A. Kaplan, "Interictal EEG as a physiological adaptation. Part I. Composition of brain oscillations in interictal EEG," *Clinical Neurophysiology*, vol. 117, no. 1, pp. 208-222, 2006.
- [4] M. Kamiński, K. Blinowska and W. Szelenberger, "Topographic analysis of coherence and propagation of EEG activity during sleep and wakefulness," *Electroencephalography and Clinical Neurophysiology*, vol. 102, no. 3, pp. 216-227, 1997.
- [5] A. Korzeniewska, M. Mańczak, M. Kamiński, K. Blinowska and S. Kasicki, "Determination of information flow direction among brain structures by a modified directed transfer function (dDTF) method," *Journal of Neuroscience Methods*, vol. 125, no. 1-2, pp. 195-207, 2003.
- [6] L. Baccalá and K. Sameshima, "Partial directed coherence: a new concept in neural structure determination," *Biol Cybern*, vol. 84, no. 6, pp. 463-474, 2001.
- [7] L. A. Baccala, K. Sameshima and D. Y. Takahashi, "Generalized Partial Directed Coherence," *Proc. of the 2007 15th Int'l. Conf. on Digital Signal Processing*, pp.163-166, Jul. 2007.
- [8] I. Vlachos, B. Krishnan, J. Sirven, K. Noe, J. Drazkowski and L. Iasemidis, "Frequency-based Connectivity Analysis of Interictal iEEG to Localize the Epileptogenic Focus," *Proc. of the 29<sup>th</sup> Southern Biomedical Engr. Conf.*, May 2013.
- [9] F. Grubbs, "Sample Criteria for Testing Outlying Observations," *Ann. Math. Statist.*, vol. 21, no. 1, pp. 27-58, 1950.

# INFLAMMATORY MOLECULES RELEASED DURING ISCHEMIA/REPERFUSION IN A RAT MODEL OF CARDIAC LAD OCCLUSION

D. Olga McDaniel<sup>1,2</sup>, Lance Majors<sup>1,2</sup>, Larry S. McDaniel<sup>2,3</sup>, Danielle A. Redd<sup>1,3</sup>, Taolin Fang<sup>1</sup>, Alan A. Simeone<sup>1,2</sup>

<sup>1</sup>Department of Surgery, <sup>2</sup>School of Medicine, <sup>3</sup>Department of Microbiology  
University of Mississippi Medical Center, Jackson, Mississippi

## ABSTRACT

Ischemia/reperfusion (IR) during organ procurement contributes significantly to tissue injury and may cause early organ dysfunction after transplantation. The molecular markers associated with innate immunity are prime activators of early inflammatory responses to an allograft that lead to host-induced inflammation and organ rejection. This study was undertaken to investigate the possible release of molecular markers during cardiac IR in a rat model of the left anterior descending artery (LAD) occlusion. Adult Sprague-Dawley rats randomly assigned to five groups of control; 30 min LAD occlusion; 60 min LAD occlusion; 30 min LAD occlusion/10 min reperfusion and 30 min LAD occlusion/60 min reperfusion. The LAD was occluded to generate ischemia in left ventricle (LV) of the heart. Blood and cardiac tissues were tested for the presence of Toll-like receptor 2 and -4 (TLR-2 and TLR-4) at different time intervals. TLR mRNA transcripts were significantly increased in a time dependent- manner after IR. These markers were upregulated as early as 10 minutes after reperfusion and further they were increased several-fold after 60 minutes of reperfusion in tissue and peripheral blood cells as compared to the control group. The TLR-2 levels were greater in blood samples, whereas, the TLR-4 levels were greater in cardiac LV after 30 min LADI/60 min reperfusion. The method was an effective approach to generate a localized cardiac IR in the rat, which allowed examination of the molecular markers associated with IR in peripheral blood and cardiac tissues.

**Key words:** Cardiac, innate immunity, ischemia, LAD, myocardium, rat, reperfusion, toll-like receptors.

## INTRODUCTION

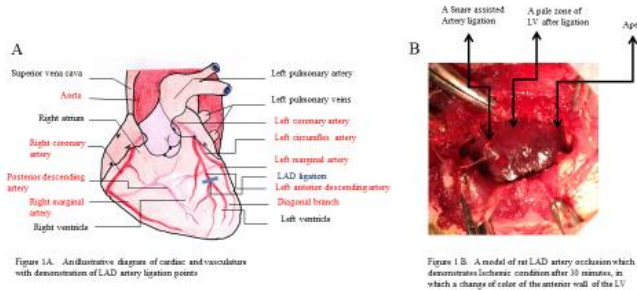
Ischemia reperfusion (IR) during cardiac procurement is associated with a distinct form of myocardial injury which may cause organ dysfunction after transplantation. The injury is often recognized as an inflammatory cause of damaged-tissue debris or molecular factors associated with unusual activation of the innate immune response, independent of host immunologic background (1). The impact of IR induced inflammation in the heart has been reported in association with left ventricular (LV) dysfunction (2, 3). Therefore we proposed a rat model of the left anterior descending (LAD) artery ligation to induce coronary artery occlusion which causes ischemic LV, followed by reperfusion of the blood to generate an experimental cardiac IR injury (IRI). Earlier studies reported that cardiac tissue represent an intact immune system that becomes activated in response to myocardial IRI (4, 5). There is evidence that the leukocytes migrating through the returning blood during reperfusion release a host of inflammatory factors in response to the tissue damage (6, 7), which may play a significant role in the initial activation of the host-inflammatory response to the donor organ.

A broad range of non-pathogenic motifs could trigger the induction of an inflammatory episodes in the myocardium. We have recently reported increased levels of allograft inflammatory factor-1 (AIF-1) in an *in vitro* model of IR, as well as in an *in vivo* experimental model of LAD artery occlusion (8, 9). In addition, in the *in vitro* model of IR, the Toll-like receptors (TLRs) were differentially expressed at various time intervals in association with IR (8). TLRs initially, identified as a family of pattern-recognition receptors (PRR) that allow mammalian cells to recognize pathogen associated molecular patterns (PAMPs) causing activation of the immune system and inflammation (10, 11). However, increasing evidence indicated that the TLRs can also be stimulated by non-infectious endogenous molecules generated by disease or IR, known as DAMPs (1, 12-14). Direct evidence identifying presence of TLRs in cardiomyocytes after IR has not been established. In this study we investigated the presence of TLR-2 and -4 in an experimental rat model of IRI in cardiac tissues and peripheral blood.

## MATERIALS AND METHODS

### Surgical Preparation and Procedure

Male Sprague-Dawley rats aged 2-3 months; 300-350 grams were tested in this study. The study was conducted according to the guidelines required by Institutional Animal Care and Use Committee (IACUC) for the use of live rodents at UMMC. Rats were anesthetized in an anesthesia chamber and isoflurane delivery system. Surgical procedure for myocardial IR was previously described (9). Briefly a left intercostal thoracotomy was performed. Before the ribs were cut, the 3rd-5th ribs were clamped off to prevent bleeding. The LAD artery, about 2-3 mm below the anterior-inferior edge of the left atrium was ligated with a tapered point needle and a 5-0 silk ligature (Figure 1A). A local ischemic condition was achieved when a change in color to paleness of the anterior wall of the LV of myocardium observed (Figure 1B).



### Experimental Protocol

Twenty five rats, assigned to five groups (5 in each group) summarized in Table 1 were studied. In all rats a left thoracotomy was performed, but in the control group no further procedure was applied. In groups 2-4, and 5 the LAD artery was ligated using a small tube as described earlier for reversible LAD artery occlusion (9). In group 2 and 3 at the end of 30 minutes or 60 minutes completion of ischemia, blood was directly drawn from left ventricle for testing of the levels of TLR-2 and TLR-4 expression. In group 4 and 5, the LAD artery was ligated for 30 minutes followed by 10 minutes or 60 minutes reperfusion respectively. Blood was drawn at the completion of reperfusion for TLR-2 and TLR-4 mRNA testing. The heart was then excised and stored either at -20°C for pathologic studies or at -80°C to be used for RNA preparation.

Table 1. Study protocol for determination of TLR-2 and TLR-4 expression during ischemia vs. reperfusion

Groups	Incision	Ischemia	Reperfusion
1. Control	yes	No	No
2. 30 minutes Ischemia	Yes	Yes	No
3. 60 minutes Ischemia	Yes	Yes	No
4. 30 minutes Ischemia	Yes	Yes	10 minutes reperfusion
5. 30 minutes Ischemia	Yes	Yes	60 minutes reperfusion

### Measurement of TLR-2 and TLR-4 expression

RNA was isolated from rat peripheral blood cells (PBMCs and PMNCs) and cardiac tissue specimen as described previously (9). The cell pellets were immediately homogenized in TRIzol and were stored at -80°C for subsequent RNA extraction. RNA from PBMCs and PMNCs were extracted using "Pure Link" RNA kit (Life Technologies, Carlsbad, CA, USA), and was reversely transcribed using ImProm-II Reverse Transcriptase (Promega, Madison, WI). All samples were tested by 25 cycles of semi-quantitative RT-PCR and the values were calculated as described previously (9). The primer sequences are given in Table 2. The group differences for mRNA transcript levels between experiments were determined by one-way analysis of variance. The level of significance was set at  $p<0.05$  for comparison between the groups.

Table 2. Rat primer sequences (5'-3') for Reverse Transcriptase -PCR

Genes	Sequences
TLR-2-L	5'-gaa-aga-tgc-gct-tcc-tga-ac-3'
TLR-2-R	5'-cgc-cta-aga-gca-gga-tca-ac-3'
TLR-4-L	5'-gtg-ggt-caa-gga-cca-gaa-aa-3'
TLR-4-R	5'-gaa-act-gcc-atg-tct-gag-ca-3'
GAPDH forward primer	5'-cag-gga-aga-tgg-tga-gca-tt-3'
GAPDH reverse primer	5'-ctg-ctc-ctc-tgt-cat-ttc-ag-3'

### Immunohistochemistry (IHC)

The formalin fixed paraffin embedded (FFPE) rat cardiac tissue sections were prepared for IHC stain (15). After antigen retrieval, sections were incubated with primary antibodies corresponding with each TLR-2 and TLR-4 for 1 hour at room temperature followed by the IHC staining procedure previously described (16).

## RESULTS

The procedure was performed under an operating microscope. In the groups with IR some rats demonstrated a minimal ventricular fibrillation (VF), or ventricular tachycardia (VT), during the early period of both ischemia and reperfusion, which did not have impact on the course of the study. The LAD artery occlusion is shown in Figure 1A and B, where myocardial color-changes are visible on the LV wall during ischemic conditions.

The levels of TLR-2 and TLR-4 expression were slightly increased after 30 minutes and 60 minutes of ischemia as compared with control group in both PBMCs and PMNCs. However, the data was not statistically significant. The levels of TLR-2 and TLR-4 expression were significantly increased in the groups with 30 min

ischemia followed by 10 min or 60 min reperfusion in both PBMCs and PMNCs. The TLR-2 mean  $\pm$  SEM were increased 2.6-fold in PBMCs and 5.5-folds in PMNCs ( $p<0.05$  and  $p<0.03$  respectively) after 30 M LADI/10 MR; 10.6-folds in PBMCs and 11.8-folds in PMNCs ( $p<0.01$  and  $p<0.001$  respectively) after 30 M LADI/60 MR as compared to the control groups (Figure 2A). The TLR-4 mean  $\pm$  SEM were increased 2.1-fold in PBMCs and 3.6-folds in PMNCs ( $p<0.05$  and  $p<0.05$  respectively) after 30 M LADI/10 MR; 9.7-folds in PBMCs and 5.2-folds in PMNCs ( $p<0.001$  and  $p<0.01$  respectively) after 30 M LADI/60 M R as compared to the control groups (Figure 2B).

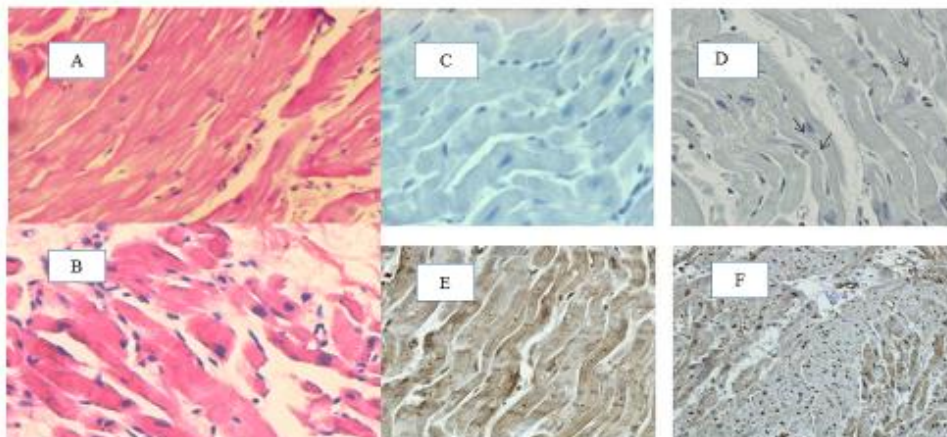


Figure 4. Cross-sections of cardiac LV IR. A-B, represent HE staining from control and post IR respectively. C-D, IHC stain of cardiac tissues stained with TLR-2 antibody. E-F, IHC stain of cardiac tissues stained with TLR-4 antibody. Positive stain indicated by brown color are observed in both nucleus of myocytes and in interstitial cells.

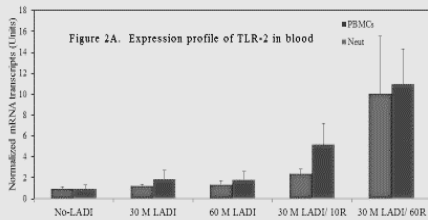


Figure 2A. TLR-2 mRNA transcripts at different time intervals are shown in PBMCs and Neutrophils. TLR-2 expression was significantly increased after 30 or 60 minutes of reperfusion observed in PBMCs and Neutrophils. For 30 minutes of ischemia (LADI/10 minutes of reperfusion), control the  $p$  values were (PBMCs,  $p=0.05$ ; Neutrophils,  $p=0.03$ ). For 30 minutes of ischemia (LADI/60 minutes of reperfusion), control the  $p$  values were (PBMCs,  $p=0.01$ ; Neutrophils,  $p=0.01$ ).

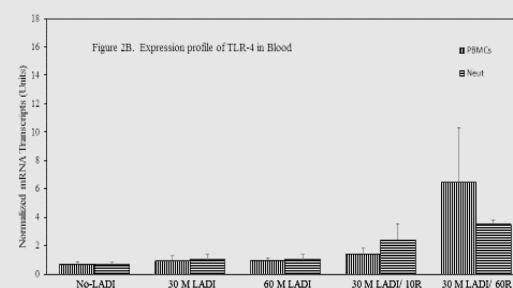


Figure 2B. TLR-4 mRNA transcripts at different time intervals are shown in PBMCs and Neutrophils. TLR-4 expression was significantly increased after 30 or 60 minutes of reperfusion observed in PBMCs and Neutrophils. For 30 minutes of ischemia (LADI/10 minutes of reperfusion vs control the  $p$  values were (PBMCs,  $p=0.05$ ; Neutrophils,  $p=0.03$ ). For 30 minutes of ischemia (LADI/60 minutes of reperfusion vs control the  $p$  values were (PBMCs,  $p=0.001$  and Neutrophils,  $p=0.01$ ).

As shown in Figure 3A and 3B, there were no significant changes in the mRNA expression levels between groups 1-3 in cardiac tissues. However, in group 4 (30 min LADI, followed by 10 min reperfusion) the TLR-2 levels in LV tissues were 1.9-fold greater than the levels in tissues from group 1, and 2.7-fold greater than RV tissues ( $p<0.04$ ), but the TLR-4 expression levels were not changed. In group 5 (30 min LADI, followed by 60 min reperfusion), the mean  $\pm$  SEM TLR-2 levels were increased 4.2-fold in LV tissues as compared to the tissues from RV ( $P<0.001$ ). The TLR-4 expression levels were 8.2-fold greater than the levels in RV tissues ( $P<0.0001$ ).

To localize the presence of TLR-2 and -4 after IR, rat LV tissues were tested by histology and immune-

staining. Figure 4, panel A and B show a representative hematoxylin and eosin (H & E) staining of LV tissues from control and post IR groups. In the control group, no pathological changes were observed. In the post IR group, degenerative changes in myocardial fibers and inflammatory cells were seen in the perimeter of myocytes, which are an indication of myocyte injury (Figure 4B). Immunohistochemistry staining for TLR-2 and TLR-4 are shown in Figure 4, panels C-F. Anti-TLR-2 and TLR-4 stain as present in both the nucleus of myocytes and in interstitial cells. TLR-4 positive cells were significantly higher than the TLR-2 after reperfusion.

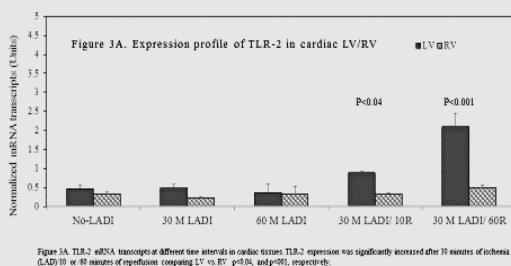


Figure 3A. TLR-2 mRNA transcripts at different time intervals in cardiac tissues. TLR-2 expression was significantly increased after 30 minutes of ischemia (LAD) 10 or 60 minutes of reperfusion, comparing LV vs. RV,  $p<0.04$ , and  $p<0.001$ , respectively.

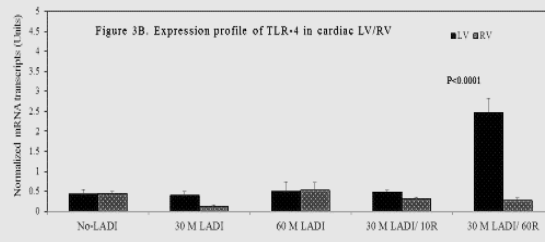


Figure 3B. TLR-4 mRNA transcripts at different time intervals are shown in cardiac tissues. The TLR-4 expression was slightly increased in LV vs. RV after 30 minutes ischemia but was not significant; however, after 60 minutes of ischemia (LAD) 60 minutes of reperfusion it was increased significantly in LV vs. RV ( $p<0.0001$ ).

## DISCUSSION

The practical value of this study was the findings that the TLR-2 and -4 were variably expressed in the blood and cardiac tissues after IR. The elevated levels of the TLRs during IR may cause the organ to become susceptible to early inflammatory attacks. In organ transplantation settings, such a paradigm may support the relationship between the initial tissue injury and systemic inflammatory response to the organ and allograft dysfunction. Furthermore, recent studies reported that the blockage of TLR-2 during early reperfusion reduces the risk of cardiac tissue damage and preserve cardiac function (17). Regulation of the TLR-2 and/or -4 expressions within the heart is not known. However, it is speculated that they are engaged in regulation of the inflammatory processes in cardiomyocytes during IR (18). The advantage of rat model of LAD has at least 4-points: cardiac size; the relative ease to access coronary vasculature; the relative ease of collecting blood from femoral vein; and physiologic density of blood, comparable with human. Additionally, rat

heart provided the relative ease during the LAD artery ligation and the achievement of successful ischemic condition which was observed by a rapid color change in the anterior wall of the LV.

## CONCLUSIONS

The method was an effective approach to generate a localized cardiac IR in the rat that allowed examination of the molecular markers in peripheral blood and cardiac tissues after IR. Such studies may help to improve transplantation outcomes.

## ACKNOWLEDGEMENTS

The authors thank the Microsurgery Laboratory in the Department of Surgery at University of Mississippi Medical Center (UMMC) for providing the facility; Dr. Richard J. Roman, Professor and Chair of Pharmacology and Toxicology at UMMC providing small rodent ventilator. This work was supported in part by Funds from Mississippi INBRE funded under grant number P20GM103476 and by the Transplantation

Immunogenetics Laboratory (PI: D.O.M) in the Department of Surgery at UMMC.

## REFERENCES

1. Land WG. Emerging role of innate immunity in organ transplantation part II: Potential of damage-associated molecular patterns to generate immune-stimulatory dendritic cells. *Transplantation Reviews* 2012; 26:73-87.
2. Sakata Y, Dong J-W, Vallejo JG, et al. Toll-like receptor 2 modulates left ventricular function following ischemia-reperfusion injury. *Am J Physiol Heart Circ Physiol* 2007; 292:H503-H509.
3. McEvoy MD, Sabagh MJ, Taylor AG, et al. Aprotinin modifies LV contractility and cytokine release following ischemia-reperfusion in a dose-dependent manner in a murine model. *Anesth Analg* 2009; 108(2):399-406.
4. Mann DL. Tumor necrosis factor and viral myocarditis: the fine line between innate and inappropriate immune response in the heart. *Circulation* 2001; 103: 626-629.
5. Knuefermann P, Vallejo V, Mann DL. The role of innate immune responses in the heart in health and disease. *Trends Cardiovasc Med* 2004; 14:1-7.
6. Francischetti I, Moreno JB, Scholz M, Yoshida WB. Leukocyte and inflammatory response in ischemia-reperfusion injury. *Rev Bras Cir Cardiovasc* 2010; 25(4):575-584.
7. Zuidema MY, Zhang C. Ischemia/reperfusion injury: The role of immune cells. *World J Cardiol* 2010; 2(10): 325-332.
8. McDaniel DO, Zhou X, Rigney DA, et al. Allograft inflammatory factor-1 in cardiac ischemia reperfusion injury: release of molecular markers in an in vitro setting. *OJOTS* 2013; 3:5-12.
9. McDaniel DO, Majors L, Fang T, Zhang F, McDaniel LS. Allograft inflammatory factor-1 induction during ischemia reperfusion injury: A rat model of LAD occlusion. *Int J Clinical Cardiol* 2014; 1:1-6.
10. Beutler B. Inferences, questions and possibilities in Toll-like receptors signaling. *Nature* 2004; 430:257-263.
11. Takeda K, Akira S. Toll-like receptors in innate immunity. *International Immunol* 2005; 17(1): 1-14.
12. Yu L, Wang L, Chen S. Endogenous Toll-like receptor ligands and their biological significance. *J Cell Mol Med* 2010; 14:2592-2603.
13. Zhang P, Cox CJ, Alvarez KM, et al. Cutting edge: cardiac myosin activates innate immune responses through TLRs. *J Immunol* 2009; 183:27-31.
14. Vilahur G, Badimon L. Ischemia/reperfusion activates myocardial innate immune response: the key role of the toll-like receptor. *Front Physiol* 2014; doi: 10.3389/fphys.2014.00496.
15. Zhou X, He Z, Henegar J, Allen B, Bigler S. Expression of allograft inflammatory factor-1 (AIF-1) in acute cellular rejection of cardiac allografts. *Cardiovasc Pathol* 2011; 20: e177-e184.
16. Barker AK, McDaniel DO, Zhou X, et al. Combined analysis of allograft inflammatory factor-1, interleukin-18 and Toll-like receptor expression and association with allograft rejection and coronary vasculopathy. *Am Surg* 2010; 76: 872-878.
17. Favre J, Musette P, Douin-Echinard V, et al. Toll-like receptors 2 deficient mice are protected against postischemic coronary endothelial dysfunction. *Arterioscler Thromb Vasc Biol* 2007; 27: 064-1071
18. Arslan F, Smeets MB, O'Neill LAJ, et al. Myocardial ischemia/reperfusion injury is mediated by leukocytic toll-like receptor-2 and reduced by systemic administration of a novel anti-toll-like receptor-2 antibody. *Circulation* 2010; 121:80-90.

# OSTEOCHONDRAL XENOGRAFT DEVELOPMENT FOR ARTICULAR CARTILAGE REPAIR

A. Garza<sup>1</sup>, C. Young<sup>2</sup>, S. Moore<sup>2</sup>, S. Elder<sup>2</sup>

Department of Biochemistry, Molecular Biology, Entomology, and Plant Pathology, Mississippi State University<sup>1</sup>

Department of Agricultural and Biological Engineering, Mississippi State University<sup>2</sup>

## ABSTRACT

Fresh osteochondral allografts are an effective treatment for large articular cartilage lesions, but their shelf life and supply are limited. We aim to develop decellularized osteochondral xenografts with mechanical properties similar to those of human cartilage. This study characterizes the effect of antigen removal and genipin crosslinking on the biochemistry, biomechanics, and biocompatibility of porcine osteochondral tissue. The ninhydrin assay was used to assess the degree of crosslinking, which was found to exceed 90% if the tissue was incubated in 0.1% genipin for 24 hours. Decellularization for 48 hours in a solution which included 2% SDS and 0.5 mg/ml DNase I removed over 80% of DNA and also removed approximately 50% of the glycosaminoglycan. However, it did not affect collagen content. Native, decellularized (no crosslinking), and crosslinked osteochondral samples were subjected to mechanical testing to determine the shear stiffness of the cartilage-subchondral bone interface. Decellularization did not significantly reduce the shear stiffness and strength compared to native tissue, and genipin fixation had little effect compared to decellularization alone. Regarding biocompatibility, genipin-fixed cartilage was shown to support 100% chondrocyte viability 5 days after cell seeding. These data demonstrate that our antigen removal protocol is effective and preserves collagen but not GAG. Decellularization does not seem to substantially weaken the cartilage-bone interface, and genipin fixation does not appear to reinforce it. Furthermore, this study confirms the low cytotoxicity of genipin. This study adds to a growing body of evidence that antigen removal from porcine osteochondral tissue, followed by genipin fixation, can produce a strong, durable extracellular matrix scaffold with low immunogenicity.

Keywords: xenografts, crosslinking, genipin, cartilage, mechanical properties

like Sodium dodecyl sulfate (SDS) [1].

## INTRODUCTION

Multiple studies have been conducted with the objective of repairing articular cartilage lesions in symptomatic patients. Some of this research indicates that osteochondral xenografts may be able to restore the same biomechanical properties that these individuals once possessed [1]. Fresh allogenic transplants are very effective, but their supply and shelf life are limited. They also carry risks of immune rejection and disease transmission. Xenografts have the potential advantages of abundant supply, low cost, longer shelf life, product uniformity, and low risk of disease transmission. Biological tissue transplantation provides a huge advantage in that it could match normal mechanical properties compared to traditional arthroscopic surgeries such as microfracture. However, before an osteochondral xenograft can be used to treat patients it has to overcome biological hurdles such as preventing host rejection from immunologic responses. Immunologic responses can range from biomechanical failure of the xenograft to host death due to antigens present on the graft [2]. By removing antigens through decellularization, the resulting xenograft articular cartilage becomes much less immunogenic scaffold which is more compatible for host acceptance and may even provide the opportunity for host cell migration [3,4,5,6]. Decellularization techniques include, but are not limited to, enzymatic digestion like DNase and detergents

The problem with decellularization of osteochondral xenografts is that it typically disrupts the structure of the extracellular matrix and degrades its biomechanical properties [3]. This study specifically focuses on the use of genipin to restore the tissue's biomechanical properties after decellularization. Glycosaminoglycan (GAG), which makes an important contribution to the biomechanical strength and structural integrity of the xenografts, is extracted when tissue is decellularized with high detergent concentration and with lengthy intervals of time [5,7]. However, we have previously demonstrated that crosslinking the collagen of a xenograft with genipin, from gardenia jasminoides Ellis fruit, increases compressive stiffness and inhibits enzymatic degradation. It also protects against immunogenic responses by masking antigens [1,8]. Moreover, genipin is a chemical crosslinker with low cytotoxicity; in comparison to glutaraldehyde it is reportedly 5,000 to 10,000 times less toxic [9]. The purposes of this study were to characterize the effect of decellularization on the biochemistry of porcine articular cartilage, determine the effect of genipin concentration on the degree of crosslinking, quantify the effect of genipin crosslinking on the stiffness of the cartilage-bone interface, and evaluate the effect of genipin-fixed cartilage on the viability of primary autologous chondrocytes. Overall we hypothesized that the degree of crosslinking would be

proportional to genipin concentration, that genipin fixation would reinforce the cartilage-bone interface, and that genipin-fixed cartilage would support attachment and survival of autologous chondrocytes.

## METHODS

**Decellularization and degree of crosslinking.** The decellularization solution was 10 mM Tris-HCl (pH 8), 2% SDS, 0.5 mg/ml DNase, 1 mM EDTA, 5 mM MgCl<sub>2</sub>, 0.5 mM CaCl<sub>2</sub>, 0.1 mM PMSF, and 1% antibiotic-antimycotic mixture. Full-thickness discs of porcine articular cartilage were decellularized for 48 hours at 37 °C with gentle agitation. Following decellularization, some samples were incubated in various concentrations of genipin in PBS ranging from 0.0008% to 0.1%. Incubation was for 24 hours at 37 °C with gentle agitation. The degree of crosslinking was determined using the ninhydrin assay as previously described [10].

**DNA, GAG, and collagen contents.** Native and decellularized porcine articular cartilage was freeze dried and digested in 100 mM sodium phosphate buffer/10 mM Na<sub>2</sub>EDTA/10 mM L-cysteine/0.125 mg/mL papain overnight at 60 °C. The Hoechst assay for DNA was performed by adding 50 µl of digestate to 2 ml of 10 mM Tris-HCl/1 mM EDTA/100 mM NaCl/0.2 µg/ml Hoechst 33258 and reading the raw fluorescence. Calf thymus DNA was used as a standard. The Blyscan Assay Kit for

GAG was used according the manufacturer's instructions. The chloramine-T assay for hydroxyproline was used to determine collagen content by assuming 12.5% of the collagen is hydroxyproline [11].

**Cartilage-bone shear test.** Cylindrical osteochondral plugs where extracted from porcine stifle joints (5 mm diameter × ~ 9 mm) were immediately washed with phosphate buffered saline. Some of the osteochondral samples were then decellularized or decellularized and crosslinked as above. The cartilage was cut sharply along the diameter and half the cartilage removed by cutting as close to the bone as possible. This exposed a rectangular shelf of cartilage, 5 mm × cartilage thickness (Fig. 1). Samples were then placed into polyurethane molds keeping the osteochondral interface exposed. Once the osteochondral plugs were firmly set, all the samples, including native osteochondral plugs, were subjected to a shear test in an Instron 1011 Universal Testing machine. The embedded bone and the cartilage shelf were aligned perpendicular to the axis of the Instron. A broad, flat ram attached to the actuator was positioned approximately 1 mm above the shelf of cartilage so that it just touched the exposed bone/calcified cartilage. The ram was then advanced at 5 mm/min until failure. Shear stiffness was calculated as the slope of the linear region of the force vs. displacement curve.

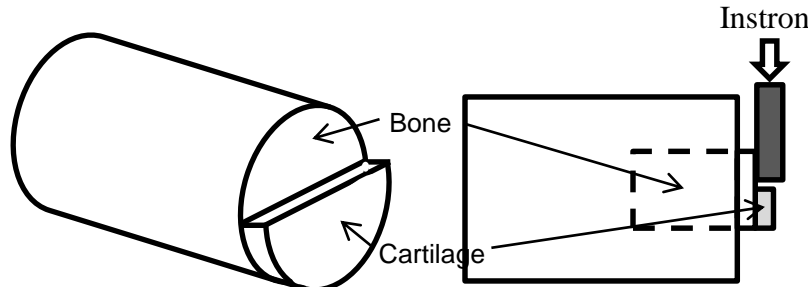


**Figure 1.** Preparation of osteochondral sample for testing strength of the cartilage-bone interface.

**Biocompatibility.** Porcine articular cartilage disks were decellularized as above. Residual decellularization solution was removed by several washes with PBS. Disks were sterilized by incubating for 3 hours 1% peracetic acid at room temperature followed by extensive washing in PBS until the pH of the rinsate had neutralized. Two control discs were further incubated in PBS. Two experimental discs were fixed in 0.1% sterile aqueous genipin as above. Residual genipin was removed by extensive washing with PBS. Decellularized controls and genipin-fixed discs were placed into separate wells of a 24-well plate and equilibrated in complete culture medium (DMEM, 10%

fetal bovine serum, 1% antibiotic-antimycotic mixture) by overnight incubation at 37 °C. They were then air dried in a biosafety cabinet for 90 min. Fresh porcine cartilage from the same joint was digested in collagase to liberate the cells, which were seeded into a T-175 flask with complete culture medium. Twenty-five microliters of a 5×10<sup>6</sup> cells/ml suspension was pipetted onto the surface of each disc. Additional culture medium was added after allowing 2 hours for cell attachment. Five days after seeding, cell viability was assessed using a fluorometric Live/Dead Cell Staining Kit (Promokine). Images were captured using a Leica DFC 420C camera attached to a

Leica DM2500 microscope.

## RESULTS

Table 1 displays the biochemical components of the articular cartilage disk and effects of decellularization and genipin fixation on biomechanics. Figure 2 exhibits

degree of articular cartilage crosslinking with the concentration of aqueous genipin. As the figure demonstrates, the degree of articular cartilage cross linking is directly proportional to the concentration of aqueous genipin present in the solution.

**Table 1** Biochemical and biomechanical properties of decellularized and genipin crosslinked cartilage.

	Native	Decellularized	Decellularized + Genipin
<b>DNA (ng DNA/mg dry wt)</b>	335.5±25.0	63.3±16.2*	N/A
<b>GAG (μg GAG/mg dry wt)</b>	242.6±21.8	150.5±17.3*	N/A
<b>Collagen (μg collagen/mg dry wt)</b>	151.7±37.9	191.9±37.1	N/A
<b>Shear stiffness (N/mm)</b>	13.1±2.8 (n=4)	11.3±2.4 (n=6)	12.3±1.7 (n=7)
<b>Shear strength (N)</b>	15.6±4.1 (n=4)	13.8±3.0 (n=4)	13.6±3.1 (n=4)

\*signifies ( $p < .05$ ) independent t-test

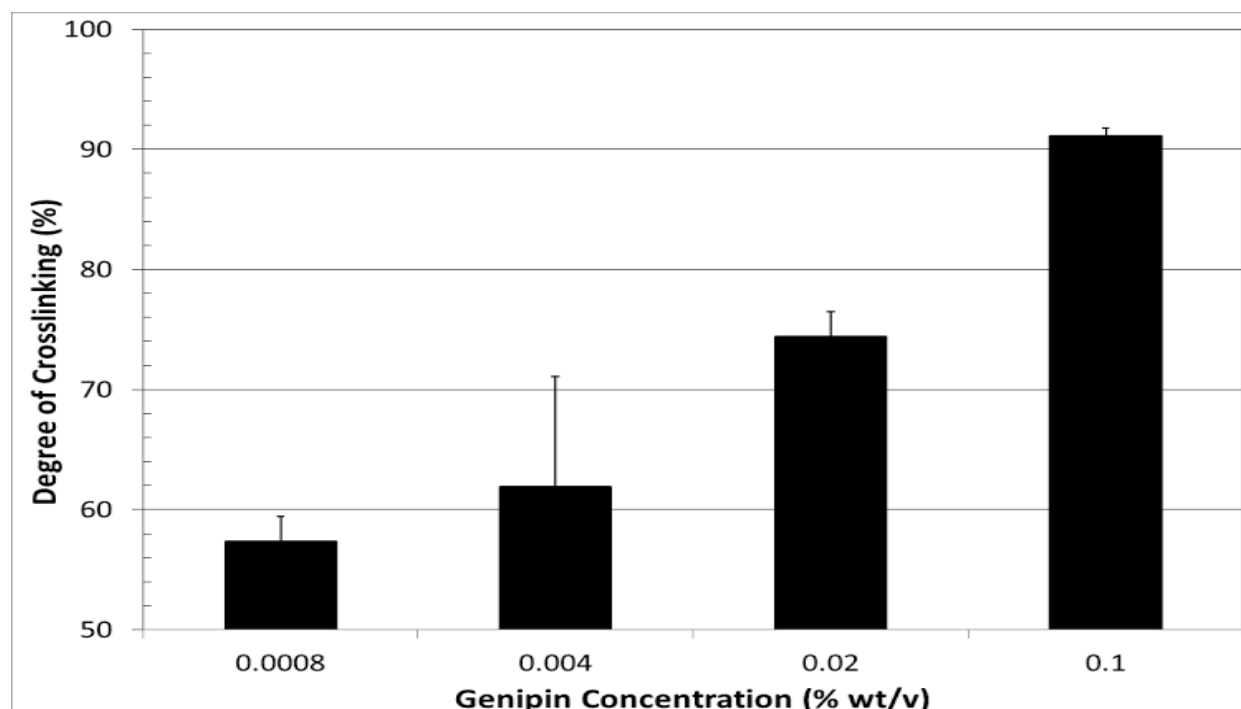


**Figure 2.** The degree of genipin crosslinking using ninhydrin assay

Figure 3 illustrates a sample of the mechanical shearing of cartilage from bone. Data collected for shear strength only includes samples that had articular cartilage completely shear off the cartilage/bone interface. The shear stiffness was determined and recorded by analyzing their corresponding curves like the example in figure 3. There

was no statistical difference among the groups with respect to shear stiffness and shear strength by one-way analysis of variance ( $\alpha = .05$ ). After decellularization of native articular cartilage (figure 4D), the tissue was then subjected to chemical crosslinking to genipin (figure 4C). It is important to note that in figure 4C the red is brighter from

the genipin itself. Moreover, it is observed from figure 4 cells were successful in being biocompatible with genipin fixation. By comparing the images between figures 4A and figure 4B it can be interpreted that there were no dead cells present on the genipin fixed samples.

## DISCUSSION

The data collected from processing ECM content exemplifies the effect of decellularization of osteochondral porcine tissue. In the process of removing antigens, approximately 80% of the DNA was removed from native porcine cartilage. However the high detergent effects of using SDS with decellularization degrades glycosaminoglycan content (GAG). GAG reduction after decellularization was roughly 50%. Conversely, there was

no significant effects on collagen content after decellularization. These findings indicate that immunogenic responses may be lowered and could prevent host rejection [2]. Furthermore, crosslinking with genipin, depending on the degree of crosslinking, may mask further antigens present on the articular cartilage and provide structural integrity. In regards to scaffold integrity and masking of antigens, higher degree of genipin fixation would be the most viable option.

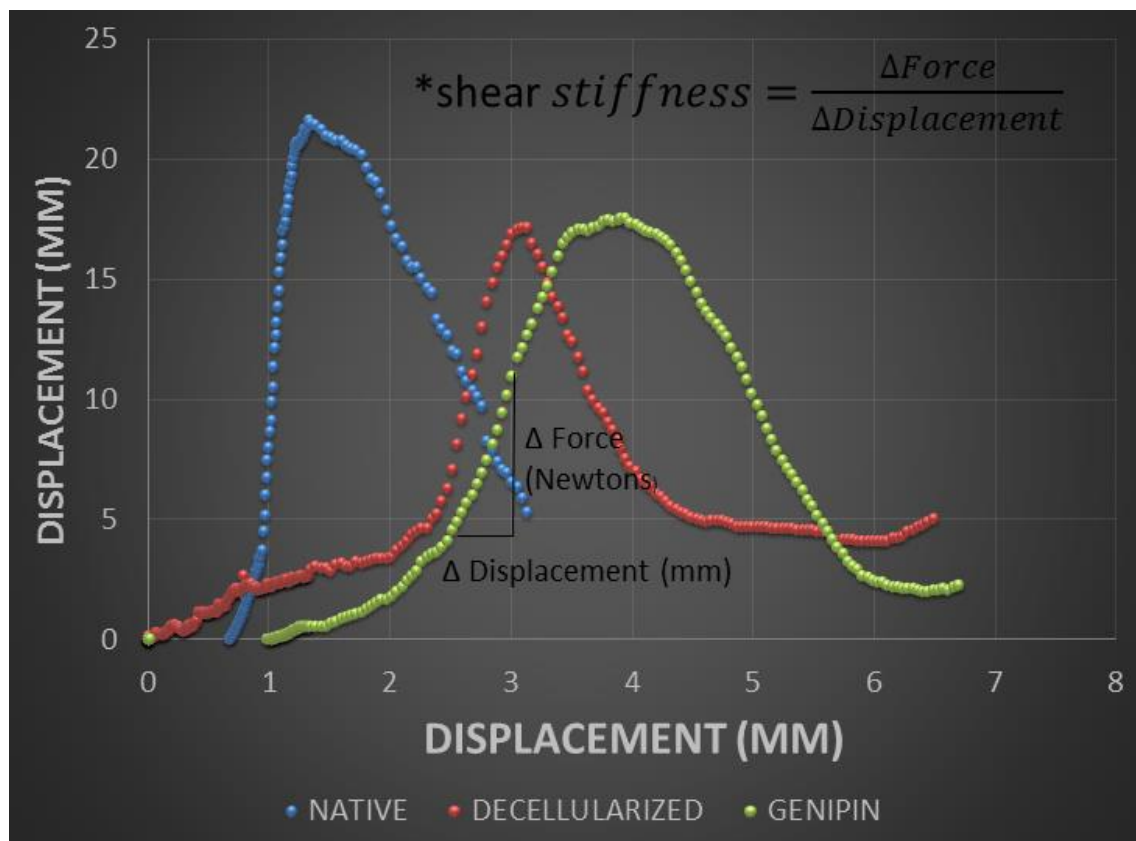


**Figure 3.** Representative force vs. displacement curves for the shearing of articular cartilage from the underlying bone.

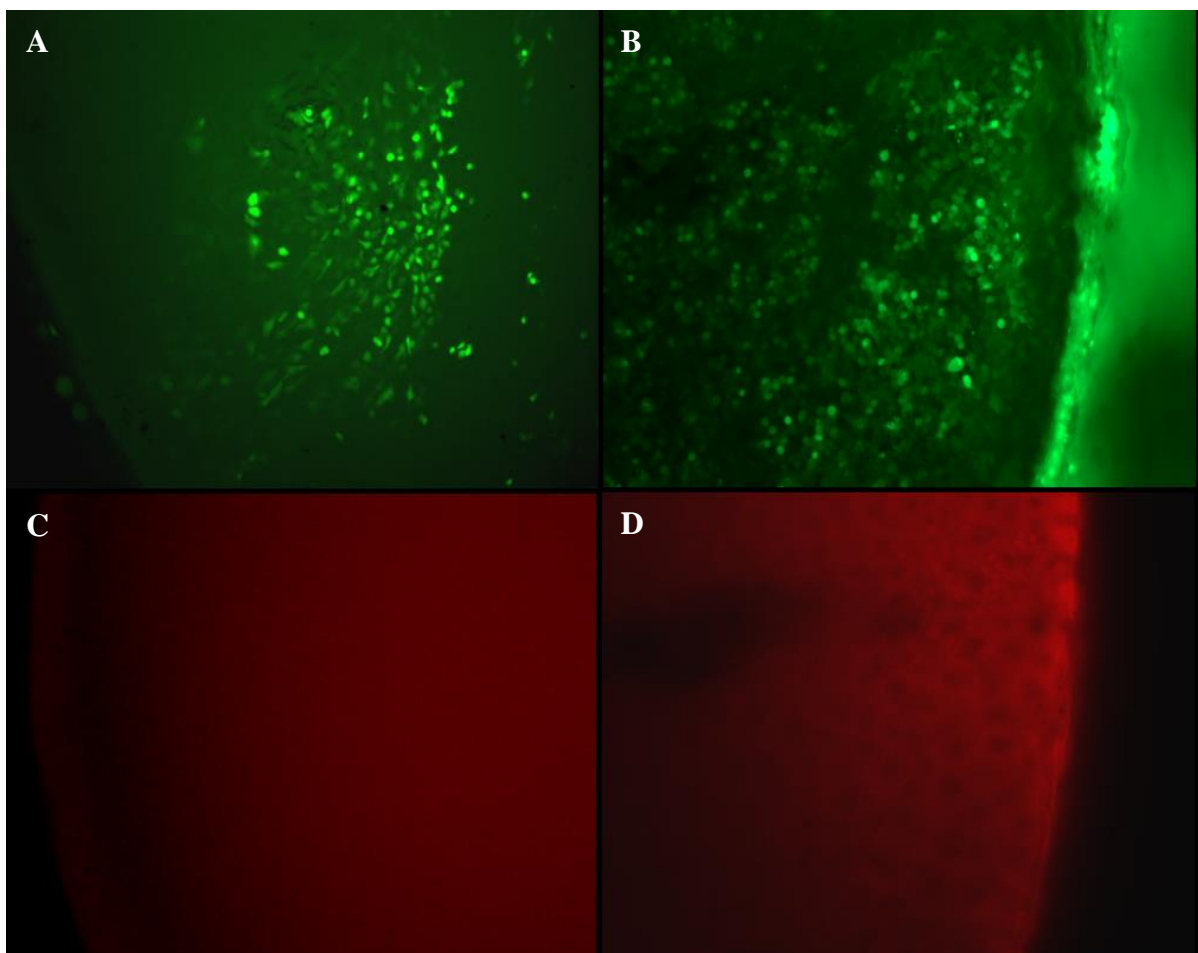


**Figure 4.** Photomicrographs of fluorescent live/dead staining of primary articular chondrocytes on PBS-fixed (control, A-C) and genipin-fixed cartilage (B-D). Live cells fluoresce green (A-B). Dead cells fluoresce red (C-D).

## DISCUSSION

The data collected from processing ECM content exemplifies the effect of decellularization of osteochondral porcine tissue. In the process of removing antigens, approximately 80% of the DNA was removed from native porcine cartilage. However the high detergent effects of using SDS with decellularization degrades glycosaminoglycan content (GAG). GAG reduction after decellularization was roughly 50%. Conversely, there was no significant effects on collagen content after decellularization. These findings indicate that immunogenic responses may be lowered and could prevent host rejection [2]. Furthermore, crosslinking with genipin, depending on the degree of crosslinking, may mask further antigens present on the articular cartilage and provide structural integrity. In regards to scaffold integrity and

masking of antigens, higher degree of genipin fixation would be the most viable option.

Neither decellularization nor genipin crosslinking significantly affected shear stiffness and strength. However, there is a trend toward decreasing mechanical properties with decellularization and a modest recovery after genipin crosslinking. The detergent minimally affected collagen content of the articular cartilage disk which contributes to the overall shear stiffness and strength. Due to the small sample size our data concerning the interfacial strength are not conclusive. However, they demonstrate that any differences are likely to be minor and clinically insignificant.

Due to genipin's properties of being a natural cross linker, it allows cells to adhere and grow to the osteochondral samples (Figure 4). Compared to other

crosslinkers, like glutaraldehyde, this growth is possible because of genipins low toxicity levels to cells. Furthermore, after thorough washing of any residual detergents, genipin's crosslinking makes the ECM stronger and it makes cell growth easier of the decellularized cartilage for chondrocytes. Our study confirmed genipin's low toxicity and specifically shows that it supports chondrocyte attachment and survival.

## CONCLUSIONS

In general, chemically crosslinking decellularized samples with .1% aqueous genipin may allow the development of osteochondral xenografts from porcine tissue. It is possible that immunogenic responses from the host organism will be significantly reduced or non-existent, however this cannot be determined until *in vivo* studies are conducted [1,8]. Additionally if host cells are able to migrate to the osteochondral xenograft, like in this study, it may be possible to regenerate additional mechanical properties. These findings also indicated that the mechanical data for decellularized and genipin-fixed cartilage did not significantly change in regards to native cartilage. Therefore, genipin-fixed xenografts may be able to withstand physiological pressures.

## ACKNOWLEDGEMENTS

This research was supported through the College of Agriculture and Life Sciences Undergraduate Research Scholars Program (URSP) at Mississippi State University and Mississippi State University's Bagley College of Engineering.

## REFERENCES

- [1] Revell, Christopher M., and Kyriacos A. Athanasiou, "Success Rates and Immunologic Responses of Autogenic, Allogenic, and Xenogenic Treatments to Repair Articular Cartilage Defects," *Tissue Engineering. Part B. Reviews*, vol. 15, no. 1, pp. 1-15, 2009.
- [2] Cissell DD, Hu JC, Griffiths LG, Athanasiou KA, "Antigen removal for the production of biomechanically functional, xenogeneic tissue grafts," *Journal Biomechanics*, vol. 47, no. 9, pp. 1987-1996, 2014.
- [3] Holger Koch, Cora Graneist, Frank Emmrich, et al., "Xenogenic Esophagus Scaffolds Fixed with Several Agents: Comparative In Vivo Study of Rejection and Inflammation," *Journal of Biomedicine and Biotechnology*, vol. 2012, pp.1-11, 2012.
- [4] Tavassoli, A., Mahdavi-Shahri, N., Matin, M., Fereidoni, M., & Shahabipour, F, "Bovine articular cartilage decellularized matrix as a scaffold for use in cartilage tissue engineering," *The Iranian Journal of Veterinary Science and Technology*, vol 4, no. 1, pp. 1-8, 2012.
- [5] Elder, Benjamin D., Sriram V. Eleswarapu, and Kyriacos A. Athanasiou, "Extraction Techniques for the Decellularization of Tissue Engineered Articular Cartilage Constructs," *Biomaterials*, vol. 30, no.12, pp. 3749-3756, 2009.
- [6] Schwarz, S., Elsaesser, A. F., Koerber, L., Goldberg-Bockhorn, E., Seitz, A. M., Bermueller, C., Dürselen, L., Ignatius, A., Breiter, R. and Rotter, "Processed xenogenic cartilage as innovative biomatrix for cartilage tissue engineering: effects on chondrocyte differentiation and function," *Journal of Tissue Engineering and Regenerative Medicine*, vol. Published online in Wiley Online Library, no. DOI: 10.1002/term.1650, 2012.
- [7] Zhang X, Chen X, Yang T, et al, "The effects of different crossing-linking conditions of genipin on type I collagen scaffolds: an in vitro evaluation," *Cell & Tissue Bank*, vol. 15, no. 4, pp. 531-541, 2014.
- [8] Hiraishi N, Sono R, Sofiqul I, et al, "In vitro evaluation of plant-derived agents to preserve dentin collagen," *Dental Materials*, vol. 29, no. 10, pp. 1048-54, 2013.
- [9] Cheng N-C, Estes BT, Young T-H, Guilak F, "Genipin-Crosslinked Cartilage-Derived Matrix as a Scaffold for Human Adipose-Derived Stem Cell Chondrogenesis," *Tissue Engineering. Part A*, vol. 19. No. 3-4, pp. 484-496, 2013.
- [10] Cui L, Jia J, Guo Y, Liu Y, Zhu P, "Preparation and characterization of IPN hydrogels composed of chitosan and gelatin cross-linked by genipin," *Carbohydrate Polymers*, Vol. 99, pp. 31-38, 2014.
- [11] Reddy GK, Enwemeka CS, "A simplified method for the analysis of hydroxyproline in biological tissues," *Clinical Biochemistry*, vol. 29, no. 3, pp. 225-229, 1996.

# THE EFFECTS OF INSULIN AND EGCG ON PANC-1 CELL SURVIVAL

Victoria Hodges, Michelle Tucci, and Hamed Benghuzzi

University of Mississippi Medical Center, Jackson, MS 39216

## ABSTRACT

There is less than a thirty percent survival rate for patients with a localized pancreatic tumor, and less than a ten percent survival rate for patients with metastases. There are diverse findings on the chemotherapeutic properties of insulin. Epigallocatechin (EGCG) is a polyphenolic antioxidant that has been shown to increase the AMPK pathway that increases cellular apoptosis. The objective of this study was to investigate the effectiveness of EGCG with a clinical dose of insulin ( $10\mu M$ ) in reducing the survival of a pancreatic like cell line in culture. PANC-1 cells were plated onto three 24 well plates at a density of  $1 \times 10^6$  cells per well. The experimental design consisted of four equal groups: Group 1 served as the control and groups 2-4 were treated with insulin, (EGCG) or insulin and EGCG, respectively. Biochemical and morphological evaluations were conducted following standard lab protocols. Results of this study show  $10\mu M$  of insulin was unable to reduce cell growth or proliferation, however, after a 72 hour period cells treated with insulin increased compared to control untreated cells. Meanwhile,  $50\mu M$  of EGCG alone or in combination with insulin were capable of reducing cell density and cellular protein levels at 24, 48 and 72 hours following treatment. The results show EGCG induced changes in cellular morphology which are characteristic of apoptosis. Overall, additional studies are needed to determine the effects of EGCG on AMPK and ATM pathways that are responsible in normal cellular apoptotic processes.

**Keywords:** Insulin, PANC-1, Antioxidants, Apoptosis, EGCG

## INTRODUCTION

Insulin is a protein produced in the islets of Langerhans by the beta cells in the pancreas of non-diabetics. Insulin acts by first binding to a target receptor in the cell [16]. These insulin-sensitive tissues are then able to breakdown and dispose of glucose. When cells are not able to utilize insulin properly or there is a defect in the mechanism of action of insulin, the body can develop glucose intolerance and type 2 diabetes mellitus [13]. Studies strongly support the idea that glucose intolerance is a risk factor for pancreatic cancer (McCarty, 2001). Other studies suggest that insulin promotes the growth of pancreatic tumors [6,4,3,11]. This suggestion is consistent with findings that human pancreatic adenocarcinomas express insulin receptors and these receptors stimulate mitosis [4]. In a study conducted on insulin receptor status of six human pancreatic cancer cell lines the authors found the presence of receptors in all six pancreatic cancer cell lines. In addition, cancer cells treated with insulin were found to have from 15-120% more cells than the control cells [3].

There is substantial literature on the effect of Epigallocatechin-3-Gallate (EGCG) on cancer cells. Polyphenols such as, Epigallocatechin-3-Gallate (EGCG), also activate AMPK. AMPK is mediated by enzymes such as LKB1, a tumor suppressor, and when AMPK is activated it inhibits anabolic processes and activates

catabolic process [5]. In addition to activation of AMPK, EGCG can also improve insulin uptake into cells and has both antioxidant and chemotherapeutic potential [17]. Antioxidants like EGCG are able to interact with free radicals and prevent them from initiating a chain reaction with important molecules such as DNA [2]. The chemotherapeutic effects of this polyphenol has been shown to reduce cell proliferation and/or viability in previous studies conducted on tumor cells [9, 19]. EGCG is able to arrest cell growth by inhibiting angiogenesis [8]. Angiogenesis is necessary for tumors to transition from non-cancerous to cancerous [12]. Another suggested mechanism in which EGCG is capable of inducing cell apoptosis is by altering the expression of cell cycle regulatory proteins, activating killer caspases, and suppressing NF $\kappa$ B activation [7]. This antioxidant is also capable of blocking carcinogenesis by modulating the signal transduction pathways that are necessary for the development of cancer [1]. This study investigated the ability of insulin and EGCG to act synergistically to reduce cancer cell viability. By combining insulin's ability to lower blood glucose level and the various EGCG mechanisms to induce apoptosis of cancerous cells, perhaps there will be a greater effect on antiproliferation of a fast growing pancreatic cancer cell line. The effects were measured by observing the change in cellular protein concentration, intracellular glutathione concentration, and morphological evaluation.

## METHODS

PANC-1 Cell line: A human pancreatic adenocarcinoma cell line (PANC-1) was obtained from American Type Culture Collection (ATCC, Rockville, MD). The PANC-1 pancreatic cells were grown in a Dulbecco's Modified Eagles' Medium (DMEM) containing 10% fetal bovine serum; and sub cultured by dissolution of the cells with trypsin and plating into new culture flasks every 3-4 days.

Experimental Design: A total of four groups were utilized in this study. PANC-1 cells were plated in a 24 well plate at a density of  $1 \times 10^6$  cells per well. Cells in Group I were maintained in media and served as the control group, while

cells in groups II-IV were exposed to the clinical bioavailable dose of insulin ( $10\mu\text{M}$ ), EGCG ( $50\mu\text{M}$ ), and a combination of insulin and EGCG, respectively. At the end of 24, 48, and 72 hours post treatment a total of ten wells per group were terminated by collecting the supernatant in a  $1.5\text{mL}$  centrifuge tube and storing in the freezer for future biochemical analysis. Cells were also harvested and collected in 1 ml PBS and stored in the freezer for cellular protein and glutathione analysis. In addition, cells were plated onto cover slips and harvested at corresponding time points and stained with Hematoxylin and Eosin for morphological evaluation. The experimental procedure was repeated twice.

Table 1: The experimental design investigates the effect of the antioxidant EGCG alone and in combination with metformin on the PANC-1 cell line.

	Groups	Duration (hrs.)	N	Dose ( $\mu\text{L}$ )
<b>1</b>	Control	24, 48, 72	10	0
<b>2</b>	Insulin	24, 48, 72	10	10
<b>4</b>	EGCG	24, 48, 72	10	10.5
<b>6</b>	Insulin + EGCG	24, 48, 72	10	10 + 10.5

### Biochemical Determinations:

The BCA Protein Assay was used to test for total protein concentration. Cells treated with insulin, EGCG, or insulin and EGCG were collected from harvesting at 24, 48, or 72 hours. A 96 well plate was used and  $25\mu\text{L}$  of each sample was added to the plate in duplicates along with an eight-fold dilution of standards. BCA working reagent was prepared immediately before use and  $200\mu\text{L}$  was added to all wells containing samples or standards. The plate was incubated at  $37^\circ\text{C}$  for 30 minutes. Immediately following incubation, the plate was read on the Sunrise plate reader at  $540\text{ nm}$  and data analyzed using Magellan software.

B. The glutathione assay was used to test for glutathione peroxidase to determine the amount of cellular injury. Cells were treated with insulin, EGCG, or insulin and EGCG and collected from harvesting at either 24, 48, or 72 hours. A 96 well plate was used and  $50\mu\text{L}$  of each sample was added to the plate in duplicates along with an eight-fold dilution of standards. A reagent to measure glutathione was prepared immediately before use and  $100\mu\text{L}$  was added to all wells containing samples or standards. An initial reading was taken using the Sunrise plate reader at  $490\text{ nm}$ . The plate was then incubated for

$37^\circ\text{C}$  for 10 minutes, and the plate was read on the Sunrise plate reader at  $490\text{ nm}$  and data analyzed using Magellan software.

Morphological Evaluation: Cover slips were stained immediately following harvesting at each time point (24, 48, 72 hr.) with blue hematoxylin and eosin. The cover slips were then fixed to a slide. After the cover slips dried they were observed under a high-powered microscope to assess the cell morphology. Cell properties observed under the slide included; cell shape, size, nucleus, nucleus size, cytoplasm, and cytoplasmic response.

Data Analysis: Data was exported from the Magellan software to an excel file. This data was then analyzed in Sigma Plot by performing descriptive statistics as well as One Way ANOVA. The experiments were conducted in duplicates and the number per group was determined to produce significant difference at  $P<0.05$  (Statistical Power indicated 10 samples per groups were needed for reliability and validity). This is represented by the mean data. SLIDEWRITE, graphing application was used to generate a graphical representation of the data.

## Results

**Cellular Protein:** Cells were treated once with a clinical dose of insulin ( $10\mu\text{M}$ ),  $50\mu\text{M}$  of EGCG (a dose that was determined to reduce cell numbers by approximately 50% in our previous studies) or insulin in combination with EGCG and followed for 24, 48, and 72 hours. Cellular protein levels following insulin administration was not statistically different from control untreated cells (Figure 1). EGCG administered to PANC-1 cells was able to reduce the cell numbers by 50% after 24 hours, 48 hours and 72 hours of culture ( $p<0.05$ ) (Figure 1). Combining EGCG with a clinical dose of insulin

resulted in a similar 50% reduction in cellular protein as EGCG given alone after 24, 48 and 72 hours

**Intracellular Glutathione:** Intracellular glutathione levels were increased by 20% to 30% in the EGCG alone and EGCG in combination with insulin treatment groups after 24, 48, and 72 hours when compared with untreated PANC-1 control cells. The difference was significant for EGCG alone at 24 and 72 hours and insulin in combination with EGCG after 24, 48 and 72 hours ( $p<.05$ ). Intracellular glutathione levels for the insulin treatment group were similar to control values at all time points.

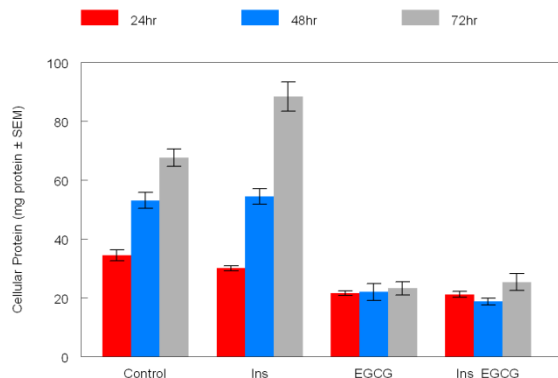


Figure 1. Cellular protein at 24, 48, and 72 hours following treatment with  $10\mu\text{M}$  insulin,  $50\mu\text{M}$  of EGCG or a combination of insulin and EGCG. The data are expressed as  $\mu\text{g Protein} \pm \text{SEM}$ . The results are representative of two separate experiments with  $n= 10$  per group. Differences are reported when  $p<0.05$ .

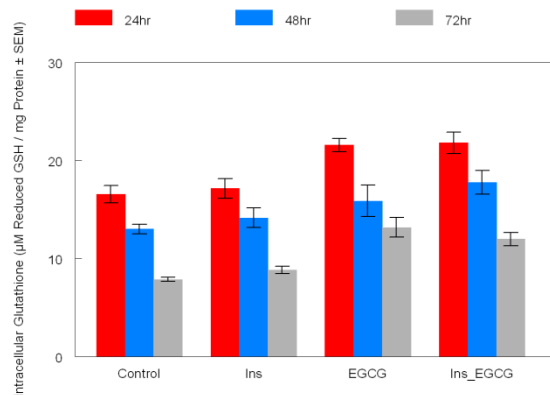
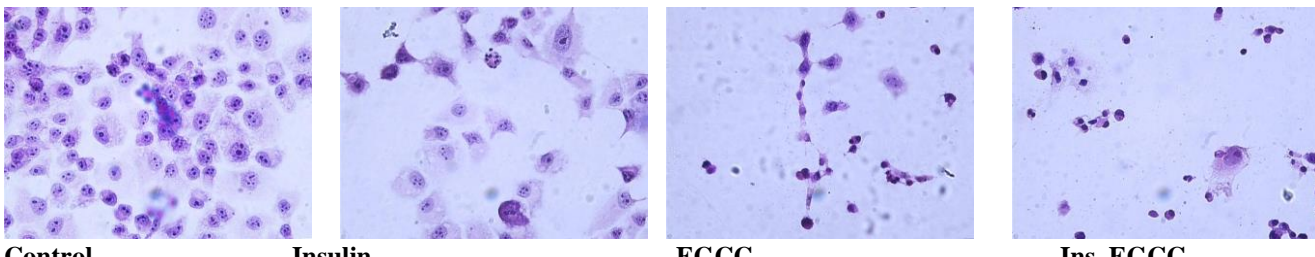


Figure 2. Intracellular glutathione at 24, 48, and 72 hours following treatment with  $10\mu\text{M}$  insulin,  $50\mu\text{M}$  of EGCG or a combination of insulin and EGCG. The data are expressed as  $\mu\text{M Reduced GSH}/\text{mg Protein} \pm \text{SEM}$ . The results are representative of two separate experiments with  $n= 10$  per group. Differences are reported when  $p<0.05$ .

**Cellular Morphological Evaluation:** Cells plated on cover slips were harvested and evaluated following treatment for cell density, shape, and signs of cytoplasmic and nuclear degradation (Figures 3a, 3b, and 3c). After 24 hours of treatment, cells treated with insulin showed signs of hydroptic swelling, which is an acute adaptive reaction of the cells. Cells treated with EGCG and the combination treatment resulted in changes in cell size with a larger portion of cells with hyper chromatic staining of the nucleus. After 48 hours of treatment, insulin treated cells were similar in size and density to control untreated PANC-1 cells, and after 72 hours of treatment insulin cells surpassed control untreated cells in density. Treatment

with EGCG and combination treatment resulted in a decrease in cell density consistent with the decline in cellular protein (Figure 1). In addition, EGCG and combination treatment caused a reduction in cell size and an increase in cells with a larger nuclear to cytoplasmic ratio as indicated by a larger percentage of cells with condensation of the nuclear chromatin and reduction in cytoplasm compared to the control untreated cells. The changes in cell morphology are consistent with features of apoptotic cells.



**Figure 3a** Representative photomicrographs of cells after 24 hours of treatment with 10 $\mu$ M insulin, 50 $\mu$ M EGCG or a combination of insulin and EGCG.

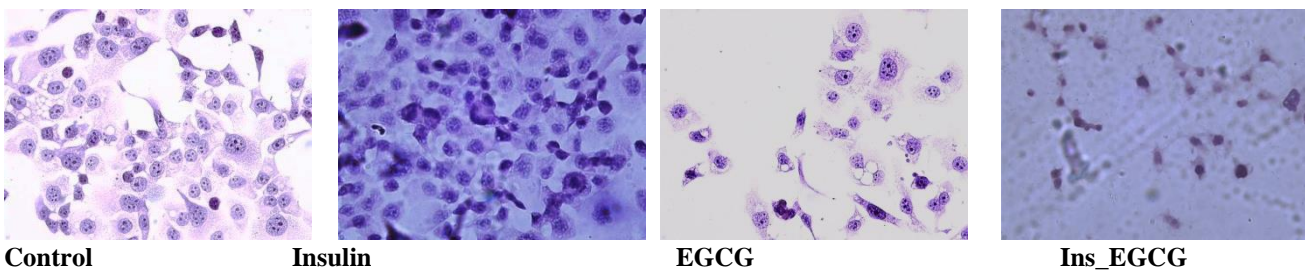


**Figure 3b** Representative photomicrographs of cells after 48 hours of treatment with 10 $\mu$ M insulin, 50 $\mu$ M EGCG or a combination of insulin and EGCG.

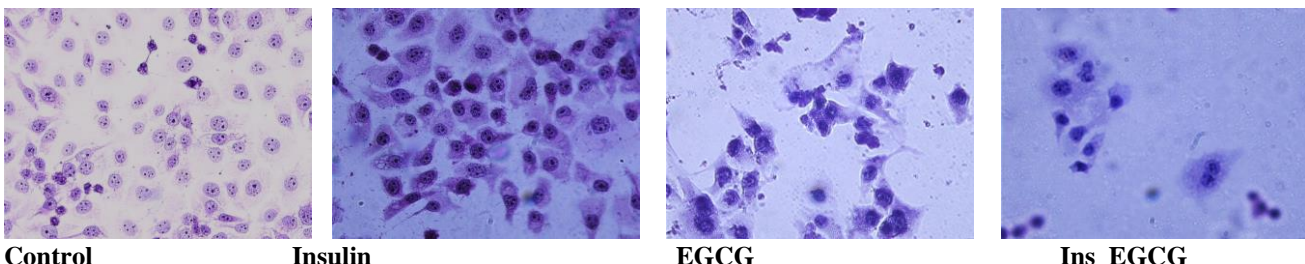


**Figure 3c** Representative photomicrographs of cells after 72 hours of treatment with 10 $\mu$ M insulin, 50 $\mu$ M EGCG or a combination of insulin and EGCG.

## DISCUSSION

While pancreatic cancer survival rates have been improving from decade to decade, the disease is still considered largely incurable. Pancreatic is one of the most aggressive cancers and the 5 year survival rate for a localized tumor is 26% and less than 5% for patients with metastasis [18]. Over the last few decades, numerous chemotherapy drugs have been tested alone and in various combinations in patients with pancreatic cancer, almost always with little or no impact on disease progression or survival. The newest four drug regime of 5-fluorouracil, leucovorin, irinotecan, and oxaliplatin has shown to increase survival rate by four months when compared with the standard drug, gemcitabine. Patients with pancreatic

cancer also show signs of glucose intolerance or type II diabetes so the use of antidiabetic drugs is a component of their treatment regime. Studies on the chemo-preventive properties of insulin vary depending on the host and cancer cell type. In our study using a concentration that represents the bioavailable therapeutic concentration, we did not see a significant reduction in cancer cell load or alteration in cellular morphology for the duration of the study. However, the use of 50  $\mu$ M EGCG alone and in combination with insulin resulted in a reduction in cellular protein and cellular density at 24, 48, and 72 hours in the PANC-1 cell line. Our findings are consistent with the findings of Tan [20], using the PANC-1 cell line. Other studies support the notion that EGCG is efficient at reducing cancer culture cells [9, 15]. The morphological

assessment of the cells indicates evidence of apoptotic cells after 24, 48 and 72 hours following treatment with EGCG or EGCG in combination with insulin. This aspect is important since cancer cells have defective apoptotic processes whereas an insufficient amount results in uncontrolled cell proliferation. Our results are consistent with previous studies on EGCG that suggest that the antioxidant is able to initiate or reestablish the apoptosis of cancer cells [14]. Our results did not show a synergistic or additive effect of using a combination of EGCG and insulin; however, it did indicate that EGCG at 50 $\mu$ M is capable of reducing cancer cell load after all time points even though insulin appeared to have a growth promoting effect after 72 hours.

## CONCLUSIONS

This study suggests that therapeutic doses of insulin will not reduce PANC-1 cancer cells. Furthermore, it may have growth promoting effect on PANC-1 cells. EGCG administered alone or in combination with a therapeutic dose of insulin can alter the survival of the PANC-1 cell line by enhancing apoptosis. Additional studies are needed to determine signaling mechanisms involved to increase cellular apoptosis. Investigation of the AMPK signaling targets may provide crucial information for the concentration of EGCG that is effective in re-establishing apoptosis and up-regulating tumor suppressor genes to provide a more natural effective way to reduce cancer cell load, which is safer than the standard chemotherapeutic drugs that induce cellular toxicity and death. In addition, more research is needed into the insulin signaling pathways and receptors that may stimulate cancer cell growth.

## ACKNOWLEDGMENTS

The authors would like to acknowledge Ms. Gerri Wilson and Ms. Lisa McCammon for their support in the preparation of the manuscript.

## REFERENCES

- [1] Ahmed S, Wang N, Lalonde M, Goldberg VM, Haqqi TM. Green tea polyphenol epigallocatechin-3-gallate (EGCG) differentially inhibits interleukin-1 beta-induced expression of matrix metalloproteinase-1 and -13 in human chondrocytes. *J Pharmacol Exp Ther.* 2004; 308:767–73.
- [2] Ali, B., Blunden, G. Pharmacological and toxicological properties of Nigella Sativa. *Phytotherapy research* 2003, 17: 299305.
- [3] Fisher, WE., Boros, LG., Schirmer, WJ. Reversal of enhanced pancreatic cancer growth in diabetes by insulin. *Surgery* 1995, 2: 453-457.
- [4] McCarty, MF. Insulin secretion as a determinant of pancreatic cancer risk. *Medical Hypotheses* 2001, 57:146-150.
- [5] Del Barco, S., Vasques-Martin, A., Cufi, S. Metformin: Multi-faceted protection against cancer. *Oncotarget* 2011, 2: 896-917.
- [6] Fisher, WE., Boros, LG., Schirmer, WJ. Insulin Promotes Pancreatic Cancer: Evidence for Endocrine Influence on Exocrine Pancreatic Tumors. *J of Surgical Research* 1996, 63: 310-313.
- [7] Gupta, S., Hussain, T., & Mukhtar, H. Molecular pathway for (-)-epigallocatechin-3-gallate-induced cell cycle arrest and apoptosis of human prostate carcinoma cells. *Archives Biochemical Biophysiology* 2003, 410: 177-185.
- [8] Jung, Y., Kim, M., & Shin, B. EGCG, a major component of green tea, inhibits tumor growth by inhibiting VEGF induction in human colon carcinoma cells. *British Journal Cancer* 2001, 84:844-850.
- [9] Kavanagh, K., Hafer, L., Kim, D., Mann, K., Sherr, D., Rogers, A., et al.: Greentea extracts decrease carcinogen-induced mammary tumor burden in rats and rate of breast cancer cell proliferation in culture. *Journal Cellular Biochemistry* 2001, 82:387-398.
- [10] Lorenz M, Urban J. Green and Black Tea are Equally Potent Stimuli of NOProduction and Vasodilatation: New Insights into Tea Ingredients Involved. *Basic Research in Cardiology* 2009, 104: 100–110.
- [11] Fisher, WE., Muscarella, P., Boros, LG., Schirmer, WJ. Variable effect of streptozotocin-diabetes on the growth of hamster pancreatic cancer (H2T) in the Syrian hamster and nude mouse. *Surgery* 1998, 123: 315–320.
- [12] Penn, J. *Retinal and Choroidal Angiogenesis*. Springer, 2008.
- [13] Dube, S., Errazuriz, I., Cobelli, C., et al.: Assessment of Insulin action on carbohydrate metabolism: physiological and non-physiological methods. *Diabetic Medicine* 2013, 30: 664-670.
- [14] Roy, M., Chakrabarty, S., Sinha, D., Bhattacharya, R., & Siddiqi, M. Anticlastogenic, antigenotoxic and apoptotic activity of epigallocatechin gallate: a green tea polyphenol. *Mutat. Res.* 2003, 523-524:33-41.
- [15] Sato, D., & Matsushima, M. Preventive effects of urinary bladder tumors induced by N-butyl-N-(4-

- hydroxybutyl)-nitrosamine in rat by green tea leaves. *International Journal Urology* 2003, 10:160-166.
- [16] Prager R., Schernthaner, G. Insulin Receptor Binding to Monocytes, Insulin secretion, and Glucose Tolerance Following Metformin Treatment. *Diabetes* 1983, 32: 1083-1086.
- [17] Singh, B., Shankar, S., Srivastava, R. Green tea catechin, epigallocatechin-3-gallate (EGCG): mechanisms, perspectives and clinical applications. *Biochem Pharmacol* 2011, 82: 1807-1821.
- [18] National Cancer Institute. (2015) Available: <http://seer.cancer.gov/statfacts/html/pancreas.html>
- [19] Takada, M., Nakamura, Y., Koizumi, T., Toyama, H., Kamigaki, T., Suzuki, Y., et al.:Suppression of human pancreatic carcinoma cell growth and invasion by epigallocatechin-3-gallate. *Pancreas* 2002, 25: 45-48
- [20] Tan, M., Norwood, A., May, M., et al.: Effects of (-) epigallocatechin gallate andthymoquinone on proliferation of a PANC-1 cell line in culture. *Biomedical Science Instrumentation* 2006, 42: 363-371.

# THE EFFECT OF MINOXIDIL ON SALT OVERLOAD AND BLOOD PRESSURE IN BOTH NORMOTENSIVE AND DOCA-SALT HYPERTENSIVE RATS

Min Huang<sup>1</sup>, Hamed Benghuzzi<sup>2</sup>, Michelle Tucci<sup>3</sup>, and Robert L. Hester<sup>4</sup>

Departments of Physical Therapy<sup>1</sup>, Diagnostics and Clinical Health Sciences<sup>2</sup>, Orthopedics<sup>3</sup>, and Physiology<sup>4</sup>: University of Mississippi Medical Center, Jackson, Mississippi 39216-4505

## ABSTRACT

It has been well documented that sodium overload is often an important factor in the pathogenesis of various forms of experimental and clinical hypertension. In this investigation we hypothesized that chronic-salt loading pressure-natriuresis curve determines the level of arterial blood pressure in both normotensive and DOCA-salt hypertensive rats during chronic minoxidil exposure. The specific aim of this study was to determine if minoxidil treatment resulted in a decrease in arterial blood pressure in DOCA-salt hypertensive rats, without affecting the renal function curve. A total of 58 adult SD-tats were randomly divided into 8 groups (control, minoxidil (3 mg/day; Route: Oral), salt, salt-minoxidil, DOCA, DOCA-minoxidil, DOCA-salt (75 mg; Route: pellets), and DOCA-salt minoxidil). The rats in the salt groups drank saline while the rats in the non-salt groups drank tap water. Sodium intake was measured every 24 hours. Mean arterial blood pressure was measured at the end of 6 weeks post treatment. The results revealed that there were no significant differences in salt intake among any of the non-salt groups. Minoxidil treatment did not significantly change salt intake in any of the tap water or saline animals ( $p < 0.05$ ). Arterial pressures measured were  $119 \pm 4$  mmHg (control),  $117 \pm 4$  mmHg (minoxidil),  $111 \pm 3$  mmHg (salt),  $111 \pm 3$  mmHg (salt minoxidil),  $139 \pm 8$  (DOCA),  $133 \pm 4$  (DOCA minoxidil),  $160 \pm 5$  (DOCA-salt), and  $146 \pm 9$  (DOCA-salt minoxidil). There was a significant effect of DOCA and an interaction was observed between DOCA and salt treatment. Furthermore, this resulted in a significant increase in MAP. However, neither saline nor minoxidil treatment alone had a significant effect on MAP. Chronic minoxidil treatment did not shift the chronic salt-loading pressure-natriuresis curve in either normotensive or hypertensive rats. These results indicate that chronic salt-loading pressure natriuresis curve plays a central role in long term control of arterial blood pressure and the development of DOCA-salt hypertension.

**Keywords:** Hypertensive Rats, Salt Intake, Minoxidil, Natriuresis, Sodium intake, Salt overload

## INTRODUCTION

We have previously demonstrated that a decrease in total peripheral resistance (TPR) caused by opening an A-V fistula or chronic administration of minoxidil, a potent peripheral vasodilator, does not decrease mean arterial blood pressure in normotensive rats. Additionally, DOCA-salt hypertension can still develop in the presence of a low TPR, suggesting that changes in TPR are not the primary mechanism by which mean arterial blood pressure is achieved. There is also no correlation between total peripheral resistance and mean arterial blood pressure (1-6). Numerous previous studies (1, 7-11) have shown that the long-term level of arterial blood pressure occurs where the sodium intake and chronic salt-loading pressure natriuresis curves intersect (equilibrium point). The long-term arterial blood pressure can be changed only by changing one or both of these two factors. If minoxidil treatment results in a decrease in MAP then there must be some change in the chronic salt-loading pressure natriuresis curve.

It has been demonstrated that sodium overload is often an important factor in the pathogenesis of various forms of experimental and clinical hypertension, including essential hypertension (12-15). For instance, a decrease in renal mass (a decrease in number of nephrons) to one-half or one third of normal does not usually change the long-term level of mean arterial blood pressure as long as the ratio of glomerular filtration rate and renal tubular reabsorption are constant. Animals with reduced kidney mass became hypertensive when high salt was administered (13, 14, 16-21). Another typical example of sodium dependent hypertension is mineralocorticoid hypertension. A nephrectomized animals that receives mineralocorticoid alone would have only a small increase in blood pressure, but a combination of both mineralocorticoid and high salt results in severe hypertension (13, 22, 23, 24), suggesting that the DOCA-salt hypertensive rats may be particularly sensitive to the overload of salt.

Both experimental and clinical studies have shown that a large change in salt intake (1/10-10 times) in animals or human beings with normal renal function can

change the arterial blood pressure no more than 10-20 mmHg. On the other hand, an excessive sodium load can cause a sustained hypertension when sodium excretion by the kidney is somehow compromised. Thus, the role of salt in the pathogenesis of hypertension is determined not only by salt intake but also by the ability of the kidneys to eliminate salt from body (1, 9, 13, 16, 18-21). Therefore, the main objective of the present study was to determine if minoxidil treatment resulted in a decrease in arterial blood pressure in DOCA-salt hypertensive rats, without affecting the renal function curve. We tested the hypothesis that there is a difference between sodium intake and mean arterial blood pressure in both normotensive and DOCA-salt hypertensive rats treated with or without minoxidil.

## METHODS

### Animal preparations

All experiments were conducted in male Sprague Dawley rats weighing 200-225 grams. The rats were divided into 8 groups: control (n=6), minoxidil (n=7), salt (n=8), salt-minoxidil (n=8), DOCA (n=8), DOCA-minoxidil (n=6), DOCA-salt (n=8), and DOCA-salt minoxidil (n=7). In the beginning of the experiments, all of the rats underwent a right nephrectomy during anesthesia with sodium pentobarbital (50 mg/kg i.p.). DOCA pellets (75 mg, Innovative Research of America, Toledo, Ohio, USA) were subcutaneously implanted into the rats in groups of DOCA, DOCA-minoxidil, DOCA-salt and DOCA-salt minoxidil. Minoxidil (Sigma) at a dose of 3 mg/day was given orally to the rats in the salt-minoxidil, DOCA-minoxidil, and DOCA-salt minoxidil groups throughout the experiments (duration:6 weeks). The rats in the salt, salt-minoxidil, DOCA-salt, and DOCA-salt minoxidil groups were given saline ad libitum. All animals were maintained on standard commercial rat diet. The rats were housed individually in animal cages in animal facilities where the temperature and humidity were constant, and they had a 12 hour light cycle from 6 A.M. to 6 P.M..

At the end of the 6 week experimental period, the rats were anesthetized with sodium pentobarbital (50 mg/kg). The carotid artery was cannulated with a polyethylene tubing (Clay-Adams no. 7411, 0.5 mm i.d., 0.97 mm o.d., Parsippany, NJ, USA) for the measurement of mean arterial blood pressure (MAP). The catheter was pre-filled with heparinized saline (1,000 u/ml). MAP was measured for 30 minutes using a Statham pressure transducer (P23ID, Oxnard, CA, USA). Following the MAP measurements, the rats were killed by pentobarbital overdose. Heart and kidneys were removed and weighed.

### Renal function curve

In a steady state condition, renal function curve

can be depicted by the relationship between the sodium intake and mean arterial blood pressure. Mean arterial pressure was measured at the end of 6 weeks. Sodium intake was measured every 24 hours throughout the experiments. Based on the previous study as well as the time course of sodium intake observed in the present study, sodium intake and arterial blood pressure in the DOCA-salt hypertensive rats reached to plateau after 4 weeks. Therefore, the data for sodium intake from the last week used for the renal function curve. The renal function curve was determined by two points: one point was the intersection between blood pressure and normal salt intake (tap water) in all groups, the other point was the intersection between blood pressure and high salt (saline) intake in all groups.

### Statistics

To determine if there was an interaction between any of the three treatments (salt intake, DOCA, or minoxidil) a  $2^3$  factorial analysis in a completely randomized design was performed. A statistically significant difference was accepted when  $p<0.05$ . Where statistical significance was determined the means grouped according to treatment are presented.

## RESULTS

### Sodium intake and mean arterial blood pressure

The time course of changes in sodium intake in both normotensive and DOCA-salt hypertensive rats is shown in Figure 1. The data reveal the total of all sources of sodium (0.4% in food, 3.9% in saline) and each data point represents the average value calculated on a weekly basis. The bottom four curves represent the daily sodium intake for the rats in the control, minoxidil, DOCA and DOCA-minoxidil groups (all of these rats drank tap water). The top four curves represent the sodium intake for the rats in the control-salt, control-salt minoxidil, DOCA-salt and DOCA-salt minoxidil groups (all of these rats drank saline).

Sodium intake during the 6<sup>th</sup> week induced a significant effect of DOCA on the level of salt intake ( $p<0.01$ ). Additionally, there was an interaction between DOCA and salt to affect salt intake ( $p<0.01$ ), such that the DOCA-salt animals had a significantly higher salt intake than the DOCA tap animals.

The MAP measured at the end of 6 weeks for the rats in the control group averaged  $119\pm4$  mmHg. MAPs for the rats in the minoxidil, salt and salt-minoxidil groups were  $117\pm4$  mmHg,  $111\pm3$  mmHg,  $111\pm3$  mmHg, respectively. The rats that received DOCA with tap water had a MAP of  $139\pm8$  mmHg (no minoxidil) and  $133\pm4$  mmHg (minoxidil). The MAP in the DOCA-salt animals

averaged  $160 \pm 5$  mmHg (no minoxidil) and  $146 \pm 9$  mmHg (minoxidil). DOCA treatment alone had a significant effect to increase pressure ( $p < 0.01$ ), and there was a significant interaction between DOCA and salt to increase blood pressure ( $p < 0.01$ ). Minoxidil treatment had no effect on blood pressure ( $p > 0.05$ ). The average data for the treatment groups is presented in Figure 2. The average MAP for all of the tap water no DOCA animals (with and without

minoxidil) averaged  $117 \pm 3$  mmHg ( $n=13$ ). The average MAP for the tap water, DOCA animals (with and without minoxidil) averaged  $136 \pm 5$  mmHg ( $n=14$ ). The average MAP for the saline animals, no DOCA treatment animals (with and without minoxidil) averaged  $111 \pm 2$  mmHg ( $n=16$ ). The average MAP for the saline-DOCA animals (with and without minoxidil) averaged  $154 \pm 5$  mmHg ( $n=15$ ).

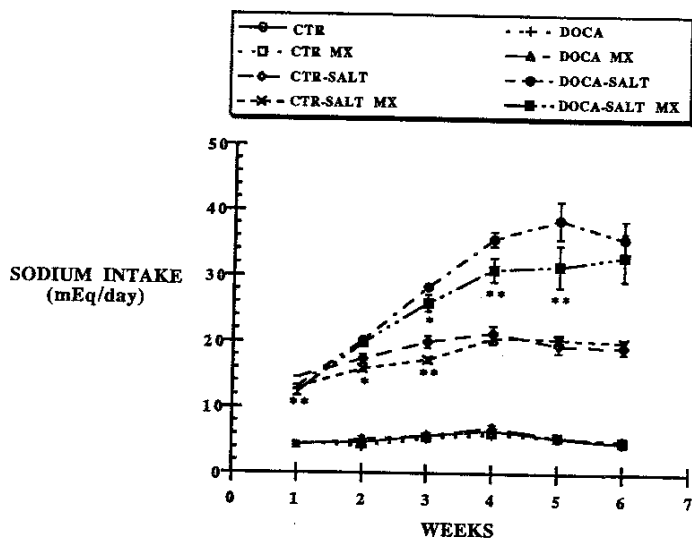


Figure 1: Daily values for sodium intake in both the normal and DOCA-salt hypertensive rats. The bottom four curves represent the sodium intake for the rats in the control, minoxidil, DOCA, and DOCA minoxidil groups (all the rats in these four groups drank tap water). There were no significant differences in sodium intake among any of these groups ( $p > 0.05$ ). Top four curves control-salt, control-salt minoxidil, DOCA-salt and DOCA-salt minoxidil groups. The data are presented as mean  $\pm$  SE.

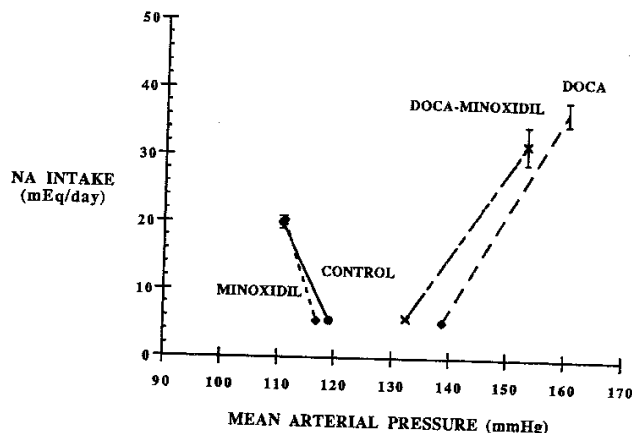


Figure 2: Effect of changes in saline intake and DOCA treatment on mean arterial pressure. DOCA treatment significantly increased mean arterial pressure, and there was an interaction between DOCA and salt to significantly increase mean arterial pressure.

### heart weight and kidney weight

The changes in heart weight (HWT), normalized to body weight, are shown in Figure 3. All of the treatments, salt intake, DOCA, and minoxidil, had a significant effect on heart weight, and there were significant interactions between all of the treatment groups. The changes in kidney weight (HWT), normalized to body

weight are shown in Figure 4. Both saline and DOCA treatment independently had a significant effect to increase kidney weight ( $p < 0.01$ ). There was also a significant interaction between DOCA and saline treatments to increase kidney weight ( $p < 0.01$ ). Minoxidil treatment had no effect on kidney weight with any of the treatments ( $p > 0.05$ ).

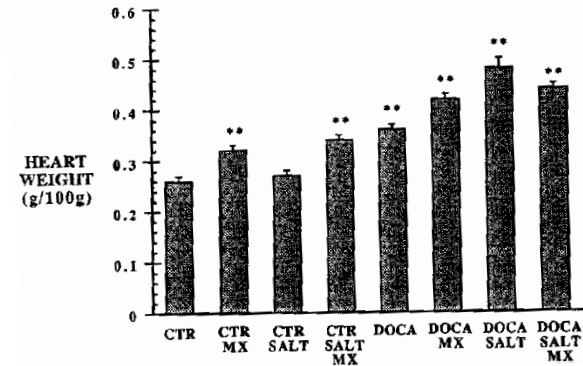


Figure 3: Effect of changes in saline intake, DOCA and minoxidil treatment on heart weight. All three treatments caused a significant effect on heart weight.

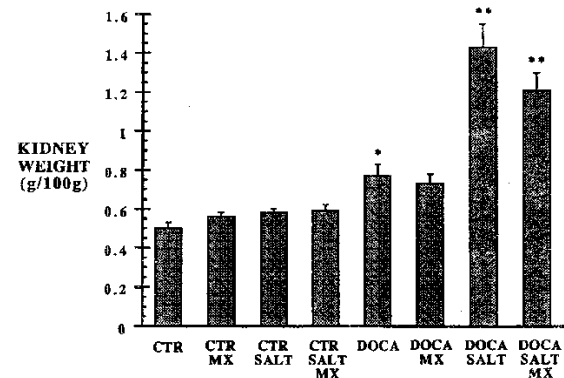


Figure 4: Effect of changes in saline intake and DOCA treatment on kidney weight. DOCA treatment significantly increased kidney weight, and there was an interaction between DOCA and salt to significantly increase kidney weight. Minoxidil treatment had no effect on kidney weight.

## DISCUSSION

The findings of the present study provide additional evidence that the DOCA treated rats are particularly sensitive to an increased salt intake, resulting in development of hypertension (13, 25, 26). When sodium intake increased from normal salt (tap water) to high salt (0.9% saline) in both control and minoxidil treated normotensive rats, mean arterial blood pressure was not significantly changed. DOCA treatment had a significant effect to increase blood pressure and the addition of saline intake in the DOCA treated animals resulted in a significant interaction, resulting in a larger increase in blood pressure. Additionally, minoxidil treatment had no effect on salt intake or mean arterial pressure in support of our hypothesis that the development of hypertension is not affected by total peripheral resistance. This study shows

that sodium intake plays an important role in the determination of the magnitude of rise in mean arterial blood pressure in DOCA-salt hypertensive rats.

Both experimental and clinical studies have shown that a large change of salt intake (1/10-10 times) in animals or human beings with normal renal function can change the arterial blood pressure no more than 10-20 mmHg. On the other hand, an excessive sodium load can cause a sustained hypertension when sodium excretion by the kidney is somehow compromised. Thus, the role of salt in the pathogenesis of hypertension is determined not only by salt intake but also by the ability of the kidneys to eliminate salt from body (2, 8, 13). Therefore, it was the second aim in the present study to determine the renal function curve in both the normal and DOCA-salt hypertensive rats treated with or without minoxidil. The

role of renal function in the long-term arterial blood pressure control can be graphically described by a chronic salt-loading pressure natriuresis curve. In the steady state condition, sodium intake is equal to sodium output. Therefore, renal function in the present study was plotted as the relationship between sodium intake and arterial blood pressure (Figure 3).

Several studies have demonstrated that the slope of the normal chronic salt-loading pressure natriuresis curve is very steep. Conversely, the slope of the chronic salt-loading pressure natriuresis curve is depressed when renal mass is reduced. On the other hand, infusion of aldosterone and angiotensin in animals results in a rightward shift of chronic salt-loading pressure natriuresis curve and a suppression of the slope (7, 8, 18). Gross et al (23) reported that DOCA-salt increased blood pressure and rightward shifted pressure natriuresis curve in salt sensitive Sabra rats. But there have been no studies showing the effect of DOCA-salt on the chronic salt-loading pressure natriuresis curve in Sprague Dawley rats during minoxidil treatment. The data presented in the present study have shown that the chronic administration of DOCA-salt in uninephrectomized rats resulted in a shift of pressure and sodium intake relationship to a higher pressure level and a suppression of the slope of this curve as compared to that seen in uninephrectomized control rats (see Figure 3). The possible mechanism responsible for the rightward shift of the chronic salt-loading pressure natriuresis curve in the uninephrectomized DOCA-salt hypertensive rats could be attributed to the increase in sodium reabsorption from renal tubules, or to the increase in renal vascular resistance.

Although increases in renal vascular resistance in DOCA-salt hypertensive rats were observed in our previous studies (3, 4), the precise portion of the renal vessels responsible for the increases in renal vascular resistance are still unknown. Evidence from the micropuncture studies of Dworkin et al. (16) has shown that afferent arteriolar vascular resistance is increased and efferent arteriolar resistance is decreased in DOCA-salt hypertensive rats. Also, Tojo et al. (27) has measured renal arteriolar diameter using a vascular cast technique and have found that the afferent arterioles were constricted while the efferent arterioles were dilated in DOCA-salt hypertensive rats. This pattern of the resistance changes in the DOCA-salt hypertension may be a regulatory mechanism to protect the glomeruli from hypertensive damage.

It has been demonstrated that a shift of the chronic salt-loading pressure natriuresis curve to a higher pressure level is a common feature of all forms of established hypertension. On the other hand, the shift of the chronic salt-loading pressure natriuresis curve toward normal is always the result of effective antihypertensive therapy.

Furthermore, antihypertensive drugs that do not affect chronic salt-loading pressure natriuresis curve will not cause a long-term decrease in arterial blood pressure. The results of the present study provide additional support for the contention that the chronic salt-loading pressure natriuresis curve is the most important determinant in the long-term control of arterial blood pressure and the pathogenesis of hypertension. As shown in Figure 3, the treatment of both normotensive and hypertensive rats with minoxidil did not shift the chronic salt-loading pressure natriuresis curve. This is the effect that would be expected since minoxidil had a preferential effect on peripheral arterioles, and not renal arterioles, as evidenced by a marked decrease in total peripheral resistance but no significant changes in renal vascular resistance (4, 6, 14, 22, 28).

All three treatments had a significant effect to increase heart weight and kidney weight, consistent with reports in the literature. The effect of DOCA and minoxidil on heart weight would be expected as DOCA resulted in an increase in mean arterial pressure and minoxidil treatment resulted in an increase in cardiac output (4). Vaskonen et al. (29) showed, in SHRs, that high salt intake resulted in cardiac and renal hypertrophy independent of any increase in blood pressure. Gu et al. (30) has shown, in cultured myoblasts, that elevated sodium concentration increases cell diameter, volume, and protein content. However for Gu's study it is unclear if the concentrations used *in vitro* are ever seen *in vivo*. DOCA has been shown to increase kidney weight in SHRs (31). However, in our studies, we are not sure if the increase in wet kidney weight was due to cellular hypertrophy or an increase in the amount of tubular fluid.

In summary, DOCA treatment alone increases blood pressure and the addition of a high salt diet results in a further increase in blood pressure. Chronic administration of the vasodilator minoxidil does not change long-term control of arterial blood pressure in either normotensive rats or hypertensive rats. The correlation between arterial blood pressure and chronic salt loading pressure natriuresis is the primary determinant in the long-term control of arterial blood pressure and the pathogenesis of hypertension.

## REFERENCES

1. Guyton, A. C. Arterial pressure and hypertension. Saunders, Philadelphia, 1980.
2. Guyton, A. C. The relationship of cardiac output and arterial pressure control. Circulation 64: 1078-1088, 1981.
3. Huang, M., R. L. Hester, and A. C. Guyton. Hemodynamic changes in rats after opening an arteriovenous fistula. Am. J. Physiol. 262 (Heart Circ. Physiol. 31): H846-H851, 1992.
4. Huang, M, and R. A. Norman, Jr. Hemodynamic studies in

- DOCA-salt hypertensive rats after opening of an arteriovenous fistula. Am. J. Physiol. 262 (Heart Circ. Physiol. 31): H1802-H1808, 1992.
5. Huang, M., R. L. Hester, T. G. Coleman, M. J. Smith, and A. C. Guyton. Development of hypertension in animals with reduced total peripheral resistance. Hypertension 20: 828-833, 1992.
  6. Huang, M., M. H. LeBlanc, and R. L. Hester. Evaluation of the needle technique for producing an arteriovenous fistula. J. Appl. Physiol. 77 (6): 2907-2911, 1994.
  7. DeClue, J. W., A. C. Guyton, A. W. Cowley, Jr., T. G. Coleman, R. A. Norman, Jr. And R. E. McCaa. Subpressor angiotensin infusion, renal sodium handling, and salt-induced hypertension in dog. Circ. Res. 43: 503-512, 1978.
  8. Guyton, A. C., T. G. Coleman, A. W. Cowley, Jr., K. W. Scheel, R. D. Manning, Jr., and R. A. Norman, Jr. Arterial blood pressure regulation: overriding dominance of the kidneys in long-term regulation and in hypertension. Am. J. Med. 52:584-594, 1972.
  9. Hall, J. E., A. C. Guyton, M. J. Smith, Jr. And T. G. Coleman. Blood pressure and renal function during chronic changes in sodium intake: role of angiotensin II. Am. J. Physiol. 239: F271-F280, 1980.
  10. Hall, J. E., J. P. Granger, R. L. Hester and J. P. Montani. Mechanisms of sodium balance in hypertension: Role of pressure natriuresis. J. Hypertension 4 (suppl. 4): S57-S65, 1986.
  11. Vaskonen, T., E. Mervaala, T. L. Teravainen, J. Laakso, H. Karppanen, and H. Vapaatalo. Cardiovascular effects of dietary salts and isosorbide-5-mononitrate in spontaneously hypertensive rats. Blood Press 7 (3): 184-192, 1998.
  12. Coleman, T. G. and A.C. Guyton. Hypertension caused by salt loading in the dogs. Circ. Res. 25:153-160, 1969.
  13. Coleman, T.G. Blood Pressure Control. Vol. 1 Eden Press, St. Albans, VT. 1980.
  14. Humphrey, S. J. and G. R. Zins. Whole body and regional hemodynamic effects of minoxidil in the conscious dog. J. Cardiovasc. Pharmacol., 6 (6): 978-988, 1984.
  15. McDonough, J. and C. M. Wilhelmj. The effect of excessive salt intake on human blood pressure. Am. J. Dig. Dis. 21: 180-181, 1954.
  16. Derhaschnig, U., C. Testori, E Riedmueller, E.L. Hobl, F.B. Mayr and B. Jilma. Decreased renal function in hypertensive emergencies. J. of Human Hypertension. Doi: 10.1038: 1-11, 2014
  17. Hall, J. E., A. C. Guyton, T. G. Coleman, L. L. Wood and H. L. Mizelle. Renal excretory function and hypertension. The kidney in Hypertension. Ed. Kaplan NM, Brenner BM and Laragh JH: Raven Press, New York.
  18. Laang, F., D.Y. Huang, V. Vallon. SGK, renal function and hypertension. J. Nephrol. 23 (S16): S124-S129, 2010.
  19. Mattson, D. L. Infiltrating immune cells in the kidney in salt-sensitive hypertension and renal injury. American J. of physiology. 307 (5): F499-F508, 2014
  20. Dickson, K.M., Clifton, P.M., and Keogh, J.B. Endothelial function is impaired after a high-salt meal in healthy subjects. Am J Clin Nutr. 93 (3): 500-5, 2011.
  21. Walsh, K, and Wainford, R. Impaired renal NCC function and expression : a mechanism driving norepinephrine evoked salt-sensitive hypertension? The FASEB journal. 28 (1) Supplement 857.6.
  22. Gavras, H., H. R. Brunner, J. H. Laragh, E.D. Vaughan, M. Koss, L. J. Cote and I. Gavras. Malignant hypertension resulting from deoxycorticosterone acetate and salt excess. Circ. Res., 36: 300-309, 1975.
  23. Hall, J. E., J. P. Granger, R. L. Hester and J. P. Montani. Mechanisms of sodium balance in hypertension: Role of pressure natriuresis. J. Hypertension 4 (suppl. 4): S57-S65, 1986.
  24. Iyer, A., C. Chan, L. Brown. The DOCA-salt hypertensive rat as a model of cardiovascular oxidative and inflammatory stress. Curr Cardiol Rev. 6 (4): 291-297, 2010.
  25. Dzielak, D.J. and R. A. Norman, Jr. Renal nerves are not necessary for onset or maintenance of DOC-salt hypertension in rats. Am. J. Physiol. 249 (Heart Circ. Physiol. 18): H945-H947, 1985.
  26. Gilmore, E., J. weil and C. Chidsey. Treatment of essential hypertension with anew vasodilator in combination with beta-adrenergic blockade. N. Engl. J. Med. 282: 521-527, 1970.
  27. McDonough, J. and C. M. Wilhelmj. The effect of excessive salt intake on human blood pressure. Am. J. Dig. Dis. 21: 180-181, 1954.
  28. Norman, R. A., Jr., J. A. Enobakhare, J. W. Declue, B. H. Douglas and A. C. Guyton. Arterial pressure urinary output relationship in hypertensive rats. Am. J. Physiol. 234: R98-R103.
  29. Michell, H. C., R. M. Graham and W. A. Pettinger. Renal function during long-term treatment of hypertension with minoxidil. Ann. Intern. Med. 93: 676-681, 1980.
  30. Gross, V., A. Lippoldt, C. Jalil, Y. Yalil and F. C. Luft. Pressure natriuresis in salt-sensitive and salt-resistant Sabra rats. Hypertension: 29 (6) : 1252-1259, 1997.
  31. Humphrey, S. J. and G. R. Zins. Whole body and regional hemodynamic effects of minoxidil in the conscious dog. J. Cardiovasc. Pharmacol., 6 (6): 978-988, 1984.

# **STATIN RELEASED BY MEANS OF TRICALCIUM PHOSPHATE LYSINE DELIVERY SYSTEM IN A DEFECT AND SEGMENTAL FEMORAL INJURY IN AN ANIMAL MODEL**

**Felix Adah<sup>1</sup>, Hamed Benguzzi<sup>1</sup>, Michelle Tucci<sup>1</sup>, George Russell<sup>1</sup>, and Barry England<sup>2</sup>**

<sup>1</sup>University of Mississippi Medical Center, Jackson, MS and <sup>2</sup>University of Michigan, Ann Arbor, MI

## **ABSTRACT**

Statins, which are 3-hydroxy-3-methylglutaryl coenzyme A (HMG-CoA) reductase inhibitors are widely used for the treatment of hyperlipidemia, and are largely metabolized in the liver. Recent studies and animal data suggest that statins promote osteogenesis and increase bone strength. Physiologically, marked reduction in total cholesterol level may interfere with the synthesis of reproductive and adrenal hormones. However, little is known about the effects of statins delivered by sustained delivery system to a target site of a defect and segmental bone fractures on the morphology of the liver and adrenal gland. Therefore, the purpose of this study was to develop a targeted statin delivery system using Tricalcium Phosphate Lysine (TCPL) for defect and segmental femoral injuries and evaluate the effects on the injured bones and on the histomorphology of the liver and adrenal after sustained delivery of statin for a period of 30 days and 12 weeks post-surgery. At the end of 30 days (Phase I), and 12 weeks (Phase II), all the animals were euthanized (with overdose of halothane). The vital organs (including the liver and adrenal), reproductive organs, and the femoral bones were collected for histomorphological analysis. Simvastatin used in this study significantly increased fracture healing in both phases. However, in Phase I study, the adrenal wet weight recorded in the statin group was slightly higher than the weights recorded for the sham and the control groups, but the difference was not statistically significant ( $p = 0.157$ ). Also, there was atrophy of the zona fasciculata and the zona reticularis, and compensatory hypertrophy of the medulla of the adrenal glands in the samples taken from two of the rats in Phase I. In addition, the wet weight of the liver in the statin group was not significantly different from the control and the sham groups ( $p = 0.320$ ), although, there was an insignificant decrease of the wet weight compared to the control and sham groups. The histomorphological evaluation by the Image pro digital analysis showed that the liver morphology was different from the control. There appeared to be an atrophy of the liver, with a denser appearance compared to the control and sham groups (Phase I). In Phase II study, there were no significant morphological and wet weight differences of the liver and adrenal glands in the statin group compared to the control and sham groups. In conclusion, sustained delivery of statin in a short period may lead to alteration of the histomorphology of the liver and adrenal gland in a rat model and with adaptation to normal morphology after a long period of sustained delivery of statin.

**Keywords:** Statins, Fracture, Healing, Drug Delivery System, Tricalcium Phosphate Lysine, Simvastatin, morphological changes, biochemical markers.

## **INTRODUCTION**

Reproductive hormonal levels may be influenced by the levels or the bioavailability of cholesterol. Estrogen, progesterone, and testosterone are synthesized from a common cholesterol precursor pathway [4]. There is interrelationship between testosterone (T), estrogen (E), follicle stimulating hormone (FSH), lutenizing hormone (LH), and reproduction. In the males, (LH and FSH) produced from the anterior pituitary gland are involved in stimulating the testes to produce T. The production and the lack of the steroid hormones (reproductive and adrenal hormones) involves cholesterol. Mevalonate pathway is responsible for the production of cholesterol. There is overwhelming evidence in the literature that statin administered orally can reduce cholesterol levels [3, 8, 9]. There is also inconclusive evidence that statin stimulate

bone formation. Some studies have found statin to stimulate new bone formation [3, 30]. However, other studies [1, 2], did not find a link between statin use and bone metabolism. Statins inhibit 3-hydroxy-3 methylglutaryl coenzyme A (HMG Co-A) reductase, an enzyme in mevalonate pathway that is responsible for the production of cholesterol. Several studies in the literature suggested that there were many effects of statin on reproductive hormones [4, 5, 6]. Dobs *et al.* [7] reported small declines in the T levels in the simvastatin treated group without any increase in the serum FSH and LH levels, which is contrary to the normal physiological response. However, oral administration of statin has some systemic side effects. Statin, and other HMG-CoA reductase inhibitors, may cause myotoxicity and rhabdomyolysis [12], especially with patients on multiple drugs [7]. To induce an effect on bone cellular activities, a

large amount of statin may have to be consumed since most of the statin taken orally is metabolized in the liver. The possible reduction in the reproductive hormone levels and the side effects of statin when administered orally may be a major problem in some vital organs such as the liver, and adrenal glands. There is no study in the literature that had investigated the effects of statin on the morphology of the liver and adrenal gland using Tricalcium Phosphate Lysine (TCPL) as a sustained delivery system. The goal of this study was to investigate the effect of vancomycin and statin delivered by TCPL on a defect and segmental bone injuries and the morphology of the liver and adrenal in a rat model. We hypothesized that a sustained delivery of statin by TCPL could facilitate bone healing with no morphological changes of the vital organs including the liver and adrenal.

## MATERIALS AND METHODS

**Experimental Design:** Sprague Dawley rats were purchased from Harlan Supplier and they were used for the study. A total of 33 Sprague-Dawley male albino rats weighing (250 to 300gm) were used for the study. The surgical procedures and maintaining the animals in this study were conducted according to the National Institute of Health (NIH) guidelines and approved according to the protocol by the University of Mississippi Medical Center. The study consisted of two phases. Phase I consisted of a total of 14 rats divided into three groups. Group I animals ( $n = 5$ ) served as the control. Group II animals ( $n = 5$ ) were induced with 2 mm femoral defect on the right side and they subsequently received TCPL loaded with 20 mg vancomycin. Group III animals ( $n = 4$ ) were treated like group II animals but in addition, the TCPL was loaded with 5 mg statin each. Phase II animals consisted of 19 animals which were divided into four groups. Group I animals ( $n = 5$ ) served as intact control with no implant. Group II animals ( $n = 5$ ) served as sham (empty TCPL), Group III animals ( $n = 5$ ) were implanted with TCPL carrying 20 mg vancomycin, and Group IV animals ( $n = 4$ ) were implanted (IM) with TCPL devices loaded with 5 mg statin and 20 mg vancomycin. All animals in Phase II except in group I were surgically induced with 5 mm segmental femoral osteotomy.

**Fabrication of the TCPL Ceramics:** Microcrystals of TCP powder were prepared using standard laboratory procedures outlined in other studies [20, 18, and 19]. The finely milled powder was weighed into units of 1.0 g, combined with 20 mg lysine, 5 mg of statin (simvastatin), and 20 mg of vancomycin for the TCPL-statin-combinations; and another set was made with 1.0 g TCP powder, 20 mg lysine, and 20 mg of vancomycin for the TCPL-vancomycin combinations. The powder was pressed into cylindrical form using a 3/8" die to obtain a

final density of 1.71 gm/cm<sup>3</sup> and surface area of 3.54 cm<sup>2</sup>. A total of 23 sintered capsules were produced and sterilized using ethylene oxide.

**Implantation Procedures:** The procedures for the implantation of the ceramics and other surgical procedures were aseptic and are similar to the procedure described by Conflitti *et al.* [21]. The rats were anesthetized with an intraperitoneal injection of Ketamine (75 mg/kg) and xylazine (10 mg/kg), according to protocol. Following the anesthesia, the right hind limb was shaved, washed with ethanol, and scrubbed with Povidine solution (10%). A palpation was made to isolate the subcutaneous border of the femur. About a 1.5 cm to 2.0 cm incision line was made at the lateral side of the femur through the tensor fascia lata and biceps femoris muscles. A dissection was made through these muscles to expose the femur. A defect using Carbide Burr size # 6 pin (dental burr) was used to produce a defect (2 mm hole), about 50% the width of the cortical bone. After the defect was created, the wounds were irrigated with a sterile saline solution, and the thigh muscles were approximated through the fascia with interrupted 3-0 nylon sutures [21]. Finally, the skin was closed with staples. The rats were monitored while they gradually recovered from the anesthetic effects before being replaced in the cage. Caroprefen (5 mg/kg/day) was given for the first 3 days following surgery. Essentially, the same procedure was used for the Phase II implanted groups except that instead of the defected of 2 mm hole created in Phase I, a 5 mm segmental femoral osteotomy was induced.

**Determination of testosterone, luteinizing hormone (LH), and follicle-stimulating hormone (FSH), and statin levels:** These biochemical markers were determined by standard laboratory procedures. Radioimmunoassay for testosterone (T), luteinizing hormone (LH), follicle-stimulating hormone (FSH), and statin was conducted using standard laboratory protocols (Central Ligand Assay Labs, The University of Michigan, Ann Arbor, MI).

**Weight Recording:** The weight of the rats can be used to know the physiological or metabolic state. Body weights were recorded weekly until the day of termination of the experiment. The wet weights of the vital organs (heart normalized to body weight, kidney normalized to body weight, spleen and adrenal) and reproductive organs (testes, prostate, epididymis, an seminal vesicle) were recorded at the time of termination of experiment.

**Data Analysis:** The data collected from this study were analyzed using Jandel Computer Software, SPSS Guide to Data Analysis and/or the SAS System SAS System the graphs were produced using Slide Write, and the groups were compared using ANOVA at  $p < 0.05$ .

**Histopathological Evaluation of Soft and Hard Tissues:**

The hard tissues (right femur) and soft tissues, vital organs (kidneys, liver, heart, spleen, adrenals, and lungs), reproductive organs (testes, prostate, epididymides, and seminal vesicle) and samples of skeletal muscles were collected, fixed with 10% formalin and later processed according to standard laboratory protocols [22]. Sections were then cut to a thickness of 5  $\mu\text{m}$  using a Leica Microtome, and tissues were stained with hematoxylin and eosin by following standard laboratory procedures.

**Data Analysis:** Statistical analysis was done using Jandel Computer Statistical Analysis Software (Sigma STAT) or SPSS Guide to Data Analysis and/or the SAS System. Slide Write graphic software was used to produce graphical representations of the results. One way analysis of variance was used to compare the groups and significance difference was reported at  $p<0.05$ .

## RESULTS AND DISCUSSION

After 30 days (for Phase I) and 12 weeks (for Phase II), the results were as follows: The body weights of the rats and wet weight of the organs in the vancomycin and statin treated groups were not statistically different from the controls and sham groups in both phases (Tables 1) ( $p>0.05$ ). The T, LH, and FSH also were not statistically different among the groups ( $p>0.05$ ). Qualitative analysis using photomicrographs from the *Image Pro* digital analysis also demonstrated increased bone formation in the vancomycin and statin treated animals in both phases compared to the sham groups and this was presented in our publication [22]. The TCPL can be used to deliver statin and vancomycin in a sustained manner to influence bone growth in a simple (defect) and complex (segmental) fractures. It is important to note that only 5 mg of simvastatin was delivered in a sustained manner for either 30 days or 12 weeks. There was atrophy of the zona fasciculata and the zona reticularis, and compensatory

hypertrophy of the medulla of the adrenal glands in the samples taken from two of the rats in Phase I (Fig. 1).

The adrenal cortex which includes the zona fasciculata and the zona reticularis, is involved in the production of essential hormones such as glucocorticoids and androgens respectively. The result of this study showed that on the third week, there was a reduction ( $p<0.05$ ) in the cholesterol level of the rats (data not presented here). The reduction in cholesterol during the third week of the study may have caused the atrophy of the zona fasciculata and zona reticularis seen in this study as hormonal production activity may have been affected. The hormone production functions of these zones may have been compromised.

Rosol *et.al.* [23], reported that the zona fasciculata and reticularis are more prone to lesion compared to the zona glomerulosa. In this study, the zona glomerulosa appeared intact in the two rats found to have alteration of adrenal gland. Rebiffat, Mazzocchi and Nussdorfer [14] reported morphological changes of the zona fasciculata following a seven day administration of mevinolin-induced inhibition of cholesterol synthesis. Also, Mazzocchi *et al.* [15], reported morphological changes of the zona fasciculata after mevinolin was administered to some rats which the authors attributed to compensatory response to reduced supply of cholesterol. It is also important to note that the wet weight of the adrenal organ in the statin group was higher, but not significant, than the control and sham groups (Table 1). In addition, the wet weight of the liver in the statin group was not significantly different from the control and the sham groups ( $p = 0.320$ ), although, there was an insignificant decrease of the wet weight compared to the control and sham groups (Table 1). The histomorphological evaluation by the Image pro digital analysis showed that the liver morphology was different from the control (Fig. 2).

**Table 1: Rat, Vital and Reproductive Organ weights in Phases I and II (gram) (mean  $\pm$  SE)**

Body Weights in Phase I	Control	Sham	Statin	P-value	
Week 1	$251.22 \pm 5.49$	$255.91 \pm 3.85$	$235.98 \pm 8.45$	$>0.05$	
Week 5	$350.26 \pm 6.22$	$341.60 \pm 6.07$	$338.40 \pm 15.97$	$>0.05$	
Organ Weights in Phase I					
Hearts (mg)	$3.56 \pm 0.36$	$3.63 \pm 0.10$	$4.04 \pm 0.26$	$>0.05$	
Kidneys (mg)	$8.71 \pm 1.42$	$7.27 \pm 0.12$	$7.80 \pm 0.35$	$>0.05$	
Adrenals (g)	$0.12 \pm 0.012$	$0.10 \pm 0.02$	$0.15 \pm 0.00$	$>0.05$	
Spleens (g)	$0.84 \pm 0.05$	$0.87 \pm 0.04$	$0.92 \pm 0.04$	$>0.05$	
Livers (g)	$12.96 \pm 0.44$	$13.72 \pm 0.61$	$12.51 \pm 0.54$	$>0.05$	

Prostates (g)	$0.65 \pm 0.02$	$0.83 \pm 0.07$	$0.86 \pm 0.12$	>0.05	
Testes (g)	$3.94 \pm 0.02$	$3.87 \pm 0.06$	$3.80 \pm 0.05$	>0.05	
Epididymides (g)	$1.72 \pm 0.17$	$1.62 \pm 0.08$	$1.67 \pm 0.11$	>0.05	
Seminal Vesicles (g)	$1.56 \pm 0.14$	$1.02 \pm 0.04$	$1.38 \pm 0.06$	>0.05	
Body Weights in Phase II	Control	Sham	TCPL-AB	Statin	P-value
Week 1	$356.40 \pm 6.05$	$351.80 \pm 7.70$	$342.8 \pm 3.68$	$348.00 \pm 4.56$	>0.05
Week 12	$444.20 \pm 10.06$	$442.00 \pm 23.70$	$431.68 \pm 9.89$	$415.25 \pm 11.01$	>0.05
Organ Weights in Phase II					
Hearts (mg)	$3.96 \pm 0.19$	$3.79 \pm 0.20$	$3.94 \pm 0.23$	$5.31 \pm 0.97$	>0.05
Kidneys (mg)	$7.08 \pm 0.35$	$7.50 \pm 0.14$	$7.98 \pm 0.16$	$7.37 \pm 0.23$	>0.05
Adrenals (g)	$0.09 \pm 0.01$	$0.09 \pm 0.01$	$0.08 \pm 0.01$	$0.08 \pm 0.01$	>0.05
Spleens (g)	$0.86 \pm 0.04$	$0.89 \pm 0.06$	$0.77 \pm 0.07$	$0.95 \pm 0.04$	>0.05
Prostates (g)	$1.42 \pm 0.17$	$1.05 \pm 0.08$	$1.23 \pm 0.13$	$1.20 \pm 0.09$	>0.05
Testes (g)	$3.91 \pm 0.07$	$4.32 \pm 0.10$	$4.25 \pm 0.18$	$3.92 \pm 0.23$	>0.05
Epididymides (g)	$1.78 \pm 0.09$	$1.71 \pm 0.10$	$1.99 \pm 0.10$	$1.61 \pm 0.05$	>0.05
Seminal Vesicles (g)	$1.42 \pm 0.13$	$1.76 \pm 0.32$	$1.39 \pm 0.07$	$1.66 \pm 0.13$	>0.05

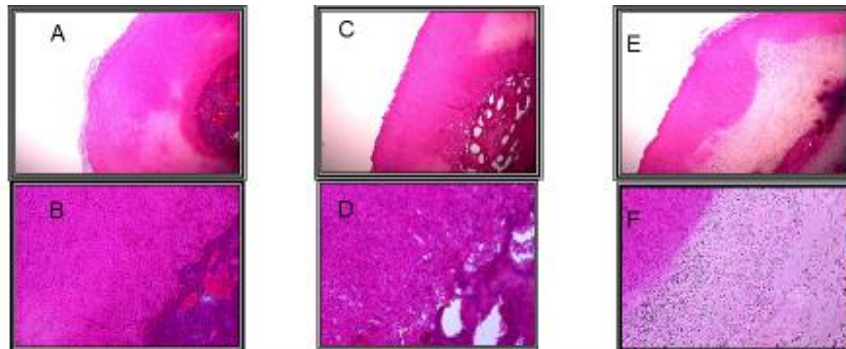


Figure 1: Columns one, two, and three are the control, sham, and statin groups, respectively of Phase I. First row = 100x; and Second row = 400x)

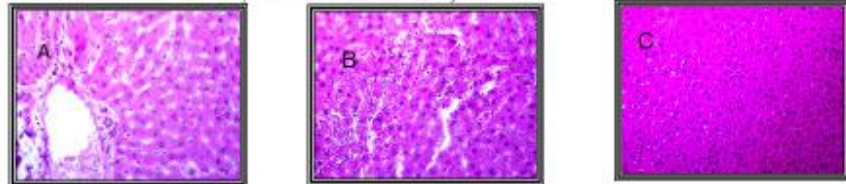


Figure 2: A representative photomicrograph of the liver in all the treatment groups (defect trauma). Figures A, B, and C the control, sham and statin groups, Respectively of Phase I. There are no morphological differences between the sham and the Control groups. However, the statin group morphology tends to be denser with limited spaces (sinusoids) between the hepatocytes. In this group, there was a slight reduction (insignificant) in the weight of the liver compared to the control and sham groups (400x).

There appeared to be an atrophy of the liver, with a denser appearance compared to the control and sham groups. It is reported in the literature [16] that statin intake may cause liver injury, a phenomenon not expected in this study due to the drug delivery system that circumvented the gastrointestinal tract. Horsmans, Desager and Haryengt

associated high dose of simvastatin administration in pig model to alteration of the morphology of the liver [17]. However, in Phase II study, there were no significant morphological and wet weight differences of the liver and adrenal glands in the statin group compared to the control and sham groups (Figs. 3 and 4).

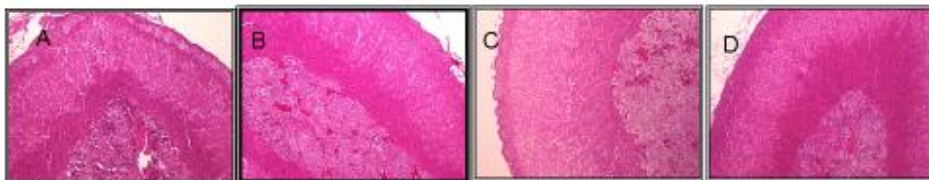


Figure 3: A representative photomicrograph of the adrenals in all the treatment groups (segmental trauma). Figure A, B, C, and D are the control, sham, TCPL AB, and statin groups, respectively of Phase II. There are no morphological differences between the groups. The zones, zona glomerulosa, zona fasciculata, zona reticularis, and the medulla are well defined and normal (20x).

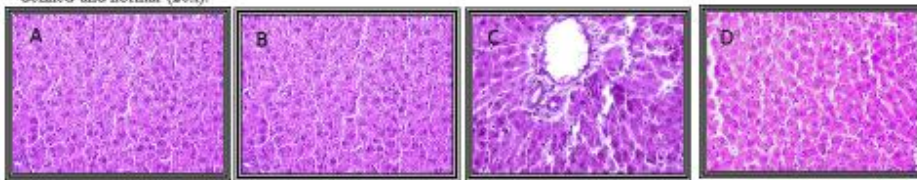


Figure 4: A photomicrograph representation of the liver in all the treatment groups (segmental trauma). Figure A, B, C, and D are the control, sham, TCPL AB, and statin groups, respectively of Phase II. There are no morphological differences in all the groups, the hepatocytes and the sinusoids are clearly defined in all the groups without evidence of any damage (400x).

The positive effects of bone formation by statin found in this study were consistent with many other findings in the literature [3, 26, 8, and 27]. For example, Oxlund *et al.* [30] reported an increase in cancellous bone mass and compressive strength when rats were fed statin orally (10 mg/kg). Clinically, the use of statins as bone forming agents is somewhat controversial. Chan *et al.* [28] found increased serum osteocalcin in individuals on oral 20 mg of statin daily for four weeks. Stein *et al.* [29] found a reduction in the bone formation marker of bone-specific alkaline phosphates in the serum of individuals on oral intake of simvastatin. Edwards *et al.* [31] found that oral intake of statin increased bone mineral density in postmenopausal women.

The statin and vancomycin group, as presented in our previous publication [33], in both phases, produced high density of bone indicating increased osteogenesis and increased angiogenesis compared to the sham group. The increased bone formation in the statin group is in accord with the findings of Oka *et al.* [9], Fukui *et al.* [10], and

Wong and Rabie [24]. Outside osteogenetic tissues, statin also induced angiogenesis. Wu *et al.* [25] reported that statin increased angiogenesis in traumatic brain injury which is speculated to be due to induced activation of the VEGFR-2/Akt/endothelial nitric oxide synthase signaling pathway. However, Zhu *et al.* [32] findings indicate that statin increased angiogenesis in hypoxia state and reduced angiogenesis in inflammatory state by upstream and downstream regulation of HIF-1alpha respectively. In this study, a defect was created in the femur of the rat. Tissues are traumatized during the surgical intervention to create the fracture and this could lead to hypoxia state of the tissues. The hypoxia state of the tissue could trigger the activation of increased angiogenesis for tissue nutrition and removal of debris in the traumatized area.

The impact of statin on vital organs such as adrenal gland and liver could be significant, especially in oral intake as the systemic effect may elicit even greater morphological changes. Imagine oral intake of 5 to 10 mg of statin being taken daily for months and compare this to 5 mg delivered by sustained delivery using TCPL. These

changes noted, especially, in adrenal gland morphology in short duration administration of simvastatin is a signal for caution when this drug is being used therapeutically.

## CONCLUSIONS

In conclusion, the TCPL was able to deliver statin and vancomycin in a sustained level and with positive osteogenesis in both defect and segmental bone traumas leading to accelerated bone healing. It is speculated that sustained delivery of statin using TCPL in short duration may alter the morphology of the adrenal gland, but not a significant change of the liver morphology, in a rat model, an observation not seen during long term sustained delivery of statin. It is possible that these organs in the longer phase experiment were able to recover from the stress present in the first 30 days of injury as the post-surgical weeks increased. It is suggested that, when statin is being considered for therapeutic purposes, extreme caution is to be exerted due to possible morphological changes that may occur in adrenal gland and the liver. Further clinical trial in humans is suggested using TCPL to deliver statin to a target sites and to evaluate the effect on vital organs such as adrenal gland and the liver.

## REFERENCES

- [1] Reid, IR, Hague, W, Emberson, J, Baker, J, Tonkin, A, Hunt, D, MacMahon, S, and Sharpe, N, (2001). Effect of pravastatin on frequency of fracture in the LIPID study: Secondary analysis of a randomised controlled trial. Long term intervention with pravastatin in ischaemic disease. *Lancet*, 357 (9255): 509-512.
- [2] Van Staal, TP, Wegman, S, de Varies, F, Leufkens, B, and Cooper, C, (2001). Use of statins and risk of fractures. *JAMA*, 285: 1850-1855.
- [3] Mundy, G, Garrett, R, Harris, S, Chan, J, Chen, G, Rossini, G, Boyce, B, Zhao, M, and Gutierrez, G. Stimulation of bone formation in vitro and in rodents by statins. *Science*. 1999;286:946-1949.
- [4] Bairly Merz CN, Olson, MB, Johnson, BD, Bittner, V, Hodgson, TK, Berga, SL, Braunstein, GD, Pepine, CJ, Reis, SE, Sopko, G, and Kelsey, SF, (2002). Cholesterol-lowering medication, cholesterol level, and reproductive hormones in women: the Women's Ischemia Syndrome Evaluation (WISE). *Am J Med.* 113(9); 723-727.
- [5] Honjo, H, Tanaka, K, Urabe, M, Naitoh, K, Ogino, Y, Yamamoto, T, and Okada, H, (1992). Menopause and hyperlipidemia: pravastatin lowers lipid levels without decreasing endogenous estrogens. *Clin Ther.*, 14(5): 699-707.
- [6] Ide, H, Fujiya, S, Aanuma, Y, and Agishi, Y, (1990). Effects of simvastatin, an HMG-CoA reductase inhibitor, on plasma lipids and steroid hormones. *Clin Ther*, 12(5): 410-420.  
healing and bone remodeling in dog. *Journal of Orthopaedic Research*. 1996;14(1):74-79.
- [7] Dobs, As, Schrott, H, Davison, MH, Bays, H, Stein, EA, Kush, D, Wu, M, Mitchel, Y, and Illingworth, RD, (2000). Effects of high-dose simvastatin on adrenal and gonadal steroidogenesis in men with hypercholesterolemia. *Metabolism*, 49(9): 1234-1238.
- [8] Ohnaka, K, Shimoda, S, Nawata, H, Shimokawa, H, Kaibuchi K, Iwamoto, Y, and Takayanagi, R. Pitavastatin enhanced BMP-2 and osteocalcin expression by inhibition of Rho-associated kinase in human osteoblasts. *Biochem Biophys Res Commun*. 2001;287(2):337-342.
- [9] Oka, S, Matsumoto,T, Kubo, S, Matsushita, T, Sasaki, H, Nishizawa, Y, Matsuzaki, T, Saito, T, Nishida, K, Tabata, Y, Kurosaka, M, and Kuroda, R. Local administration of low-dose simvastatin-conjugated gelatin hydrogel for tendon-bone healing in anterior cruciate ligament reconstruction. *Tissue Eng Part*. 2013;19(9-10):1233-43.
- [10] Fukui, T, Ii, M, Shoji, T, Matsumoto, T, Mifune, Y, Kawakami, Y, Akimaru, H, Kawamoto, A, Kuroda, T, Saito, T, Tabata, Y, Kuroda, R, Kurosaka, M, and Asahara, T. Therapeutic effect of local administration of low-dose
- [11] Edwards, CJ, and Spector, TD, (2002). Statins and modulators of bone formation. *Arthritis Res*. 2002;4(3):151-153.
- [12] Sica, DA, and Gehr, TW. Rhabdomyolysis and statin therapy: Relevance to the elderly. *Am J Geriatr Cardiol*. 2002;1(1):48-55.
- [13] Corsini, A Bellostas, S, Baetta, R, Fumagalli, R, Paoletti, R, and Bernini, F. New insights into the pharmacodynamic and pharmacokinetic properties of statins. *Pharmacol Ther*. 2000; 84 (3):413-428.
- [14] Rebuffat P, Mazzocchi G, Nussdorfer GG. Effect of long-term inhibition of hydroxy-methylglutaryl coenzyme A reductase by mevinolin on the zona fasciculata of rat adrenal cortex. A combined morphometric and biochemical study. *Virchows Arch B Cell Pathol Incl Mol Pathol*. 1987;54(2):67-72.
- [15] Mazzocchi G, Rebuffat P, Belloni AS, Gottardo G, Meneghelli V, Nussdorfer GG. Effects of mevinolin, an inhibitor of cholesterol synthesis, on the morphological and functional responses of rat adrenal zona fasciculata to a prolonged treatment with 4-aminopyrazolo-pyrimidine. *Anat Rec*. 1988 Jul;221(3):700-6.
- [16] Jose J, Al-Tamimi FA, Helal MM, Jimmy B, Al Riyami Q. Statin associated hepatic adverse effects: a retrospective review from a regional hospital in sultante of oman. *Oman Med J*. 2014 Sep;29(5):351-7. doi: 10.5001/omj.2014.93.
- [17]. Horsmans Y, Desager JP, Harvengt C. Biochemical changes and morphological alterations of the liver in guinea-pigs after administration of simvastatin (HMG Co areductase-inhibitor). *Pharmacol Toxicol*. 1990 Oct;67(4):336-9.
- [18] Benghuzzi, HA, and England, BG. The effect of sustained delivery of danazol and antioxidants on lipoprotein profiles of adult female mice. *Biomedical Sciences Instrumentation*. 1995;31:171-176.

- [19] Nagy, EA, and Bajpai, PK. Development of a ceramic matrix system for continuous delivery of azidothymidine. *Biomedical Sciences Instrumentation*. 1994;30:181-186.
- [20] Benghuzzi, HA, Possley, R, and England, BG. Pulsatile delivery of progesterone and estradiol to mimic the ovulatory surge in adult ewes by means of TCPL implants. *Biomedical Sciences Instrumentation*. 1994;30:187-196.
- [21] Conflitti, J, Graves, M, Russell, G, Tucci, M, and Benghuzzi, H. Plating of rat femoral shaft osteotomies: Report of a technique and preliminary results. *Biomedical Sciences Instrumentation*. 2003;39:278-283.
- [22] Tramontana J, Benghuzzi H, Tucci M, Tsao A, and Hughes J. Morphometric analysis of cortical bone upon the exposure to sustained delivery of anabolic promoting agents using adult male rats as a model. *Biomedical Science Instrumentation*. 2001;37:293-298.
- [23] Rosol TJ, Yarrington JT, Latendresse J, Capen CC. Adrenal gland: structure, function, and mechanisms of toxicity. *Toxicol Pathol*. 2001;29(1):41-8.
- [24] Wong, RW, and Rabie, AB. Early healing pattern of statin-induced osteogenesis. *Br J Oral Maxilfac Surg*. 2005;43(1):46-50.
- [25] Wu, H, Jiang, H, Lu, D, Qu, C, Xiong, Y, Zhou, D, Chopp, M, and Mahmood, A. Induction of angiogenesis and modulation of vascular endothelial growth factor receptor-2 by simvastatin after traumatic brain injury. *Neurosurgery*, 2011;68(5):1363-71.
- [26] Thylin, MR, McConnell, JC, Schmid, MJ, Reckling, RR, Ojha, J, Bhattacharyya, I, Marx, DB, and Reinhardt, RA. Effects of simvastatin gels on murine calvarial bone. *Journal of Periodontology*. 2002;73(10):1141-1148.
- [27] Skoglund, B, Forslund, C, and Aspenberg, P. Simvastatin improves fracture healing in mice. *J Bone Miner Res*. 2002; (11): 2004-2008.
- [28]. Chan MH, Mak, TW, Chiu, RW, Chow, CC, Chan, IH, Lam, CW. Simvastatin increases serum osteocalcin concentration in patients treated for hypercholesterolaemia. *Journal of Clinical Endocrinology and Metabolism*. 2001; 86 (9):4556-4559.
- [29] Stein, EA, Farnier, M, Waldstreicher, J, and Mercuri, M. Efects of statins on biomarkers of bone metabolism: A randomised trial. *Nutrition Metabolism & Cardiovascular Diseases*. 2001;11(2):84-87.
- [30] Oxlund, H, Dalstra, M, and Andressen, TT. Statin given perorally to adult rats increases cancellous bone mass and compressive strength. *Calcified Tissue International*. 2001;69(5):299-304.
- [31] Edwards, CJ, Hart, DJ, and Spector, TD. Oral stains and increased bone-mineral density in post-menopausal women. *Lancet*. 2000;355 (9222): 2218-2219.
- [32] Zhu, XY, Daghin, E, Chade, AR, Lavi, R, Napoli, C, Leman, A, Leman, LO. Disparate effects of simvastatin on angiogenesis during hypoxia and inflammation. *Life Sci*. 2008;5;83(23-24).
- [33]. Adah, F, Benghuzzi, H, Tucci, M, Russell, G, and England, B. Cholesterol Production Inhibitor (Statin) increased bone healing in surgically created femoral defects in an animal model. *Biomedical Sciences Instrumentation*, 43: 95-103.

# **β-ESTRADIOL INDUCES CYTOTOXIC EFFECTS TO HUMAN T-LYMPHOMA (JURKAT) CELLS THROUGH OXIDATIVE STRESS**

**Clement Yedjou, Joseph Cameron, Ariane T. Mbemi, and Paul Tchounwou**

Natural Chemotherapeutics Research Laboratory, NIH-Center for Environmental Health, College of Science, Engineering and Technology, Jackson State University, 1400 Lynch Street, P.O. Box 18540, Jackson, Mississippi, USA.

## **ABSTRACT**

β-estradiol is the most potent estrogen of a group of endogenous estrogen steroids, which includes estrone and estriol. This steroid hormone is the most potent natural estrogen, produced mainly by the ovary, placenta, and is produced in smaller amounts by the adrenal cortex, and the male testes. Although β-estradiol protects the renal and cardiovascular systems, the mechanisms involved remain unclear. In this research, we performed the MTT [3-(4, 5-dimethylthiazol-2-yl)-2,5-diphenyl tetrazolium bromide] assay to evaluate the effect of β-estradiol on human T-lymphoma (Jurkat) cells at 24 and 48 hours, respectively. Lipid peroxidation assay was also performed to estimate the levels of malondialdehyde (MDA) production in β-estradiol-treated cells. The results of MTT assay demonstrated that low, physiological levels of β-estradiol induce cellular proliferation in Jurkat T-cells. At higher dose of exposure, β-estradiol decreases the viability of Jurkat T-cells compared to the control cells. Data generated from lipid peroxidation assay resulted in a significant increase ( $p < 0.05$ ) in MDA production in β-estradiol treated sample. Upon 48 h of exposure, MDA concentrations in the sample [ $\mu\text{M}$ ] (mean  $\pm \text{SE}$ ,  $n = 3$ ) compared to untreated control were  $4.9 \pm 1.7$ ,  $8.1 \pm 1.6$ ,  $11.5 \pm 2.2$ ,  $21.1 \pm 2.3$ ,  $19.5 \pm 1.4$ , and  $21.5 \pm 2.6$  in 0, 1, 2, 4, 8, and  $16 \mu\text{M}$  β-estradiol, respectively. In summary, findings from this study demonstrated that high dose of β-estradiol is cytotoxic to Jurkat T-cells. This cytotoxicity is found to be associated with oxidative stress.

**Keywords:** β-estradiol, MTT assay, Jurkat T-cells, Lipid peroxidation assay

## **INTRODUCTION**

Estradiol is a form of estrogen, and is a female sex hormone produced by the ovaries. Estrogen is necessary for many processes in the body. In vitro studies indicated that the addition of estradiol to cultures of human lymphocytes decreases in CD4+/CD8+ T-cell-subset ratios (Athreya et al., 1993) and enhances immunoglobulin secretion (Kanda and Tamaki, 1999). Studies indicated that estrogens can affect cells of the immune system and may play a role in modulating lymphocyte development and function (Smithson et al., 1998; Grimaldi et al., 2002). Published reports suggest that estrogens may have important actions at other steps in the atherogenic process (Nathan and Chaudhuri, 1997). However, the mechanisms by which β-estradiol-induces cytotoxic effects on cancer cells are not yet completely understood. In the present study, we use the human Jurkat T-lymphoma cell line as a test model to evaluate whether β-estradiol-induced cytotoxicity is associated with oxidative stress.

## **MATERIALS AND METHODS**

### **Chemicals and Test Media**

Growth medium RPMI 1640 containing 1 mmol/L L-glutamine was purchased from Gibco BRL products (Grand Island, NY). Fetal bovine serum (FBS)

and phosphate buffered saline (PBS) were obtained from Sigma Chemical Company (St. Louis, MO).

### **Tissue Culture**

Human T-lymphoma (Jurkat) cells were obtained from American Type Culture Collection (Manassas, VA, USA). In the laboratory, cells were stored in the liquid nitrogen until use. They were next thawed by gentle agitation of their containers (vials) for 2 minutes in a water bath at 37°C. After thawing, the contents of each vial was transferred to a 25 cm<sup>2</sup> tissue culture flask, diluted with up to 10 mL of RPMI 1640 containing 1 mmol/L L-glutamine (GIBCO/BRL, Gaithersburg, MD) and supplemented with 10% (v/v) fetal bovine serum (FBS) and 1% (w/v) penicillin/streptomycin. The 25 cm<sup>2</sup> culture flasks, each containing  $2 \times 10^6$  viable cells, were observed under the microscope, and then placed in a humidified 5 % CO<sub>2</sub> incubator at 37°C. Three times a week, the cells were diluted under same conditions to maintain a density of  $5 \times 10^5/\text{mL}$ , and harvested in the exponential phase of growth.

### **Cell treatment and biochemical test for cell viability**

The *in vitro* cytotoxicity of β-estradiol against Jurkat T-cells was determined by MTT assay as previously described (Yedjou and Tchounwou, 2007). Briefly, to 180 μL aliquots in six replicates of the cell suspension ( $5 \times 10^5$  cells/mL) seeded to 96-well polystyrene tissue culture

plates, 20  $\mu$ L aliquots of stock solutions were added to each well using distilled water as solvent to make-up final  $\beta$ -estradiol concentrations of 1, 2, 4, 8, and 16  $\mu$ M. Control cells received 20  $\mu$ L of distilled water. Cells were placed in a humidified 5% CO<sub>2</sub> incubator for 12 hr at 37°C. After incubation, 20  $\mu$ L aliquots of MTT solution (5 mg/mL in PBS) were added to each well and re-incubated for 4 h at 37 °C followed by low centrifugation at 800 rpm for 5 min. Then, the 200  $\mu$ L of supernatant culture medium were carefully aspirated and 200  $\mu$ L aliquots of dimethylsulfoxide (DMSO) were added to each well to dissolve the formazan crystals after incubation for 10 min to dissolve air bubbles, the culture plate was placed on a Bioteck micro-plate reader and the absorbance was measured at 550 nm. All assays were performed in six replicates for each  $\beta$ -estradiol dose. Statistical analysis was done to determine the means  $\pm$  SDs of cell viability. Cell viability rate was calculated as the percentage of MTT absorption as follows: % survival = (mean experimental absorbance/mean control absorbance  $\times$  100).

#### Biochemical test for oxidative stress by lipid

#### peroxidation assay

Lipid peroxidation is traditionally quantified to measure malondialdehyde (MDA) and 4-hydroxynonenal. The extraction procedure and measurement of the extracted MDA was performed according to the manufacturer's instructions (Calbiochem-Novabiochem, San Diego, CA). Malondialdehydes (MDA) are formed during lipid peroxidation (Halliwell and Gutteridge 1984). Briefly, 2  $\times$  10<sup>6</sup> Jurkat T-cells/mL untreated as a control and cells treated with  $\beta$ -estradiol were incubated in a total volume of 10 ml growth medium for 48 hours. After the incubation period, cells were collected in 15 mL tubes, followed by low-speed centrifugation. The cell pellets were resuspended in 0.5 ml of Tris-HCl, pH 7.4, and lysed using a sonicator (W-220; Ultrasonic, Farmingdale, NY) under the conditions of duty cycle-25% and output control-40% for 5 sec on ice. A 200 $\mu$ l aliquot of the culture medium was assayed for MDA according to the lipid peroxidation assay kit protocol. The absorbance of the sample was read at 586 nm, and the concentration of MDA was determined from a standard curve.

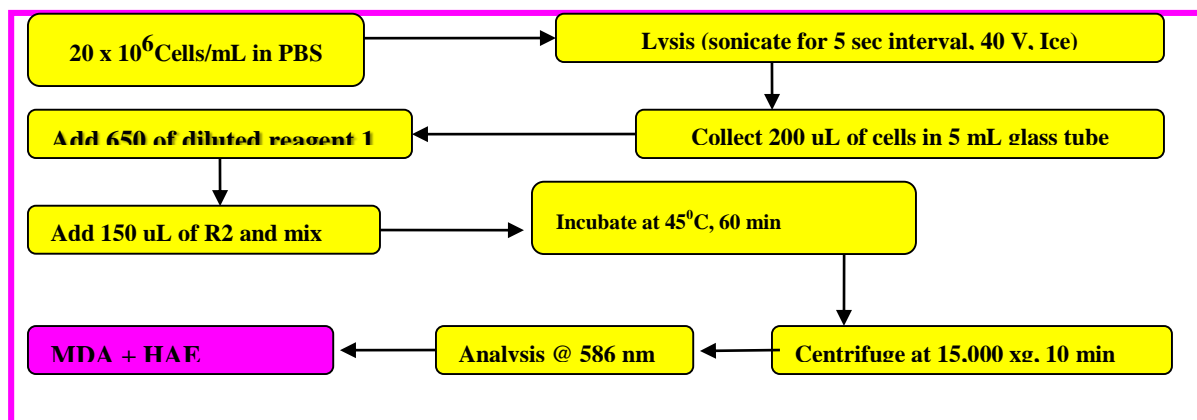


**Figure 1:** Schematic representation of the steps in lipid peroxidation assay

#### Statistical analysis

Experiments were performed at least in triplicates. Data were represented as means  $\pm$  SD. Where appropriate, one-way ANOVA test or paired t-test was performed using SAS Software available in the Bio-statistics Core Laboratory at Jackson State University.

#### RESULTS

##### $\beta$ -estradiol Inhibits Cellular viability of Jurkat T-lymphoma Cells

We used the MTT [3-(4, 5-dimethylthiazol-2-yl)-2,5-diphenyl tetrazolium bromide] assay to examine the cytotoxic effect of  $\beta$ -estradiol on Jurkat T-cells at 24 and 48 hours, respectively (Figure 2). Data generated from these studies clearly showed that  $\beta$ -estradiol exposure

significantly reduces the viability of these cell lines. After 24 and 48 hours of exposure,  $\beta$ -estradiol exerted a significant cytotoxic effect on Jurkat T-cells in dose- and time-dependent, showing a relationship with increasing doses of  $\beta$ -estradiol. We observed a biphasic response where physiological (low) doses of  $\beta$ -estradiol induce cell growth and cellular proliferation of Jurkat T-cells, whereas higher doses inhibit cell growth and induce cell death.

### **$\beta$ -estradiol Induces Oxidative Stress in Jurkat T-lymphoma Cells**

The standard curve generated from lipid

peroxidation assay is presented in Figure 3, and the effect of  $\beta$ -estradiol on malondialdehyde (MDA) production in Jurkat T-cells is presented in Figure 4. MDA is an end product of lipid peroxidation, which is a key determinant of cellular injury. As seen on figure 4, there is a significant increase in MDA level at all doses tested as result of oxidative stress, a biomarker of cellular injury. A maximum level ( $21.5 \mu\text{M}$ ) of malondialdehyde (MDA) production was observed at the highest dose tested compared to ( $4.95 \mu\text{M}$ ) in the control. This increase demonstrates that  $\beta$ -estradiol augments MDA production in Jurkat T-cells.

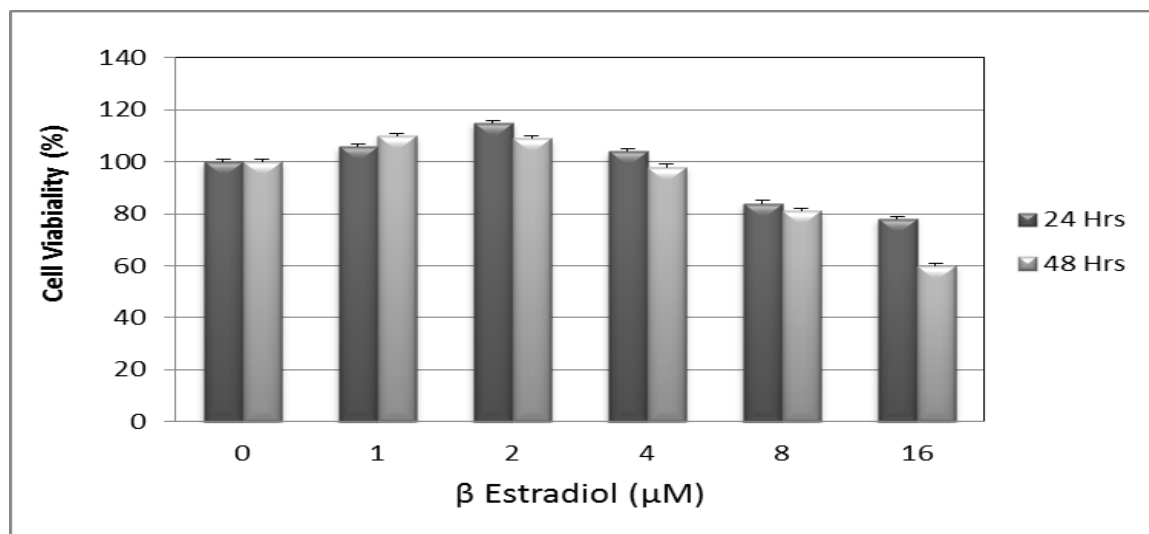


Figure 2:  $\beta$ -estradiol potently induces toxicity to human T-lymphoma (Jurkat) cells. Jurkat T-cells were treated for 24 and 48 hours with medium supplemented with solvent and various doses (1- 16  $\mu\text{M}$ ) of  $\beta$ -estradiol.

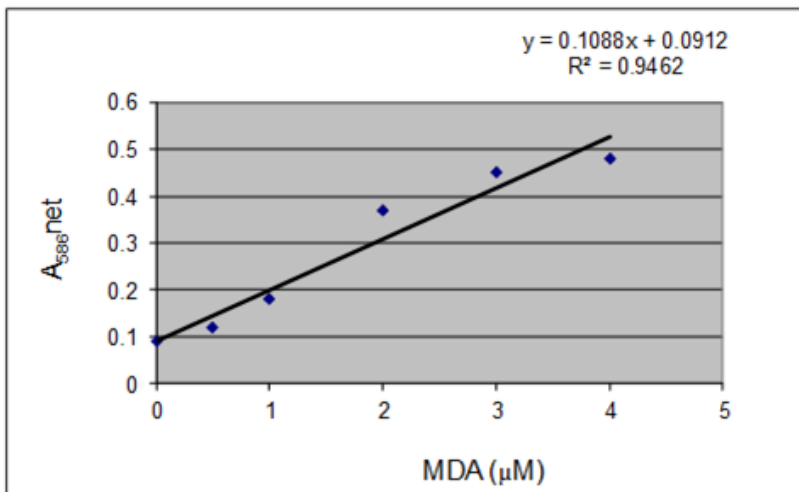


Figure 3: MDA standard curve showing the net absorbance at 586 nm as a function of MDA concentration.

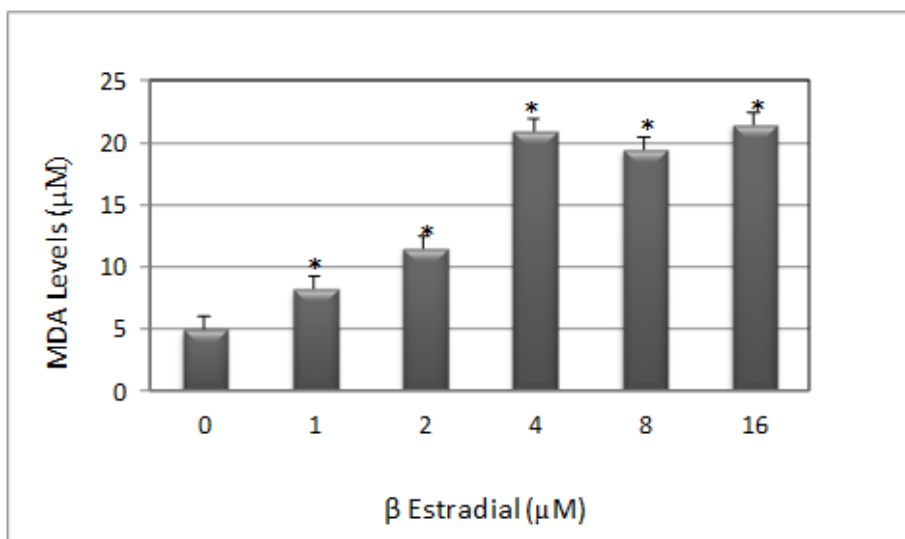


Figure 4:  $\beta$ -estradiol-induced oxidative stress in human T-lymphoma (Jurkat) cells. Cells were incubated for 48 hours with increasing doses of  $\beta$ -estradiol (1, 2, 4, 8, and 16  $\mu\text{M}$ ). Malondialdehyde (MDA) concentrations were determined as described in Materials and Methods. \*Significantly different from the control by ANOVA Dunnett's test;  $p < 0.05$ . Data are representative of 3 independent experiments.

## DISCUSSION

Natural estrogens such as estradiol, estrone, and estriol are produced from natural sources such as the urine of pregnant mares and women, the adrenals and testes of stallions, and the human placenta and amniotic fluid (Roberts, 1986). To prove the cytotoxic efficacy of  $\beta$ -

estradiol in Jurkat T-cell model, cell viability was determined by the MTT assay. As shown in Figure 2,  $\beta$ -estradiol treatment increased the percentage of dead cells in a dose- and time-dependent manner. Consistent with our results, *in vitro* studies indicated that the addition of estradiol to cultures of human lymphocytes causes a decrease in CD4+/CD8+ T-cell-subset ratios (Athreya et al., 1993) and enhances immunoglobulin secretion (Kanda

and Tamaki, 1999). Several scientific reports indicated that estrogen toxicity resulted in the death of the patient (Suess et al., 1992; Sanpera et al., 2002) or in a long recovery period (Hall, 1992; Acke et al., 2003).

To test the hypothesis that oxidative stress may be involved in  $\beta$ -estradiol induced anti-tumor activity in Jurkat T-cells, we performed lipid peroxidation assay. Our result obtained from this assay showed a slight significant ( $p < 0.05$ ) increase in malondialdehydes (a by-product of lipid peroxidation and biomarker of oxidative stress) production in  $\beta$ -estradiol-treated cells compared to the control. Similarly, a recent study in our laboratory indicated that garlic compounds generate MDA production in HL-60 cells leading to phosphatidylserine externalization, caspase-3 activation, nucleosomal DNA fragmentation, and cell death (Yedjou and Tchounwou, 2012). High level of MDA production detected in the Jurkat T-cells may be indicative of the therapeutic mechanisms of action of  $\beta$ -estradiol in human T-lymphoma (Jurkat) cells.

## CONCLUSIONS

Results from this study indicate at the cellular level that  $\beta$ -estradiol significantly reduced the viability of human T-lymphoma (Jurkat) cells in a dose and time-dependent manner. At the molecular level,  $\beta$ -estradiol treatment resulted in a significant increase in lipid peroxidation generation in Jurkat T-cells. Findings from this study indicate that  $\beta$ -estradiol is highly cytotoxic to Jurkat T-cells. This cytotoxicity is found to be mediated through oxidative stress, which is a biomarker of cellular injury.

## ACKNOWLEDGEMENTS

This work was supported by the Mississippi INBRE, funded by an Institutional Development Award (IDeA) from the National Institute of General Medical Sciences of the National Institutes of Health under grant number P20GM103476. We also acknowledge the National Institutes of Health (NIH-NIMHD Grant No. G12MD07581) through the RCMI Center for Environmental Health at Jackson State University (Jackson, Mississippi, USA).

## REFERENCES

Acke E, Money CT, Jones BR. Estrogen toxicity in a

- dog. *Ir Vet J*. 2003;56:465-468.
- Athreya BH, Pletcher J, Zulian F, Weiner DB, Williams WV. Subset-specific effects of sex hormones and pituitary gonadotropins on human lymphocyte proliferation in vitro. *Clinical Immunology and Immunopathology*. 1993; 66 201-211.
- Grimaldi CM, Cleary J, Dagtas AS, Moussai D, Diamond B. Estrogen alters thresholds for B cell apoptosis and activation. *Journal of Clinical Investigation*. 2002; 109 1625-1633.
- Hall EJ. Use of lithium for treatment of estrogen-induced bone marrow hypoplasia in a dog. *J Am Vet Med Assoc*. 1992;200:814-816.
- Halliwell B, Gutteridge JMC. Oxygen toxicity, oxygen radicals, transition metals and disease. *Biochem J*. 1984; 219:1-14.
- Nathan L, Chaudhuri G. 1997 Estrogen and atherosclerosis. *Annual Review of Pharmacology and Toxicology*. 1997; 37:477-515.
- Roberts SJ. The estrogens. In: Roberts SJ, editor. *Veterinary Obstetrics and Genital Diseases*. Woodstock, Vermont: Roberts SJ; 1986. pp. 403–405.
- Sanpera N, Masot N, Janer M, Romeo C, De Pedro R. Estrogen-induced bone marrow aplasia in a dog with a sertoli cell tumour. *J Small Anim Pract*. 2002;43:365–369.
- Smithson G, Couse JF, Lubahn DB, Korach KS, Kincade PW. The role of estrogen receptors and androgen receptors in sex steroid regulation of B lymphopoiesis. *Journal of Immunology*. 1998; 161:27-34.
- Suess RP, Barr SC, Sacre BJ, French TW. Bone marrow hypoplasia in a feminized dog with interstitial cell tumor. *J Am Vet Med Assoc*. 1992;200:1346–1348. [PubMed]
- Yedjou CG, Tchounwou. *In vitro* assessment of oxidative stress and apoptotic mechanisms of garlic extract in the treatment of acute promyelocytic leukemia. *Journal of Cancer Science and Therapy*. 2012; 10(4):1948-1956.
- Yedjou CG, Tchounwou PB (2007) *In vitro* cytotoxic and genotoxic effects of arsenic trioxide on human leukemia (HL-60) cells using the MTT and alkaline single cell gel electrophoresis (comet) assays. *Mol Cell Biochem*. 2007 301:123-130.